The study of *Cellvibrio japonicus* X-domains as potential LPMO redox partners

Jessie Branch

Submitted in accordance with the requirements for the degree of
Doctor of Philosophy

The University of Leeds
Astbury Centre for Structural Molecular Biology

May 2021

Declaration

The candidate confirms that the work submitted is her own and that appropriate credit has been given where reference has been made to the work of others.

Jessie Branch

May 2021

Acknowledgements

Firstly, a very big thank you to my supervisor, Dr Glyn Hemsworth. Thank you for all the help and ideas for the last 4 years, especially in these last few months, it has been invaluable and I appreciate it much more than I can express. Thank you to Professor Alan Berry for his guidance and expertise throughout the PhD. Thank you to our collaborators at the University of Leeds, University of York and University of Maryland, who assisted greatly in work produced in this thesis, particularly, Kristian Want, Kristian Hollingsworth, Nick Yates, Alessandro Paradisi and Peter Lindley, without whom many of these experiments would not have been possible. Thank you to Hemsworth, Berry and Radford members, past and present, for their friendship and useful discussions. Thank you Dan, you have been with me through the highs and the lows, and I am so grateful for your friendship. Thank you to Badri, who helped with so much of this work, thank you for challenging my ideas even when I get angry at you, thank you for the constant support and the many, many cups of tea, I could not have done this without you.

Thank you to Mum, Dad, Jack and Bella for your unwavering support and for always reminding me to believe in myself. Finally, thank you Jord, I could not have done this without your love and support, I hope that I have made you proud.

Abstract

Harnessing energy from recalcitrant polysaccharides is essential for developing new liquid biofuels from non-edible plant biomass. Lignocellulose, the main component of plant cell walls, is the major target for the production of second-generation biofuels. However, a cocktail of degradative enzymes are required to efficiently liberate glucose from lignocellulose in order for it to be fermented into ethanol. Progress in the biomass-breakdown field came with the discovery of a set of novel copper dependent enzymes, lytic polysaccharide monooxygenases (LPMOs), which have been shown to boost polysaccharide degradation from canonical cellulases by increasing the accessibility of polysaccharide chains. LPMOs are proposed to act by an oxidative mechanism, requiring molecular oxygen and a source of electrons, however, the nature of the oxygen species has been debated in recent years. Although several proteins have been established as redox partners to fungal LPMOs, protein partners in bacterial systems are still largely uncharacterised. Previous studies have shown two proteins from *Cellvibrio japonicus* to be important for growth on crystalline cellulose. This thesis has further investigated these proteins: Cbp2D and Cbp2E, which contain several domains with proposed electron transfer functions, and the ability of these domains to act as redox partners to bacterial LPMOs has been examined. This thesis describes the novel crystal structures of the catalytic domain of an LPMO from *C. japonicus*, CjAA10BΔCBM, the X158E domain from Cbp2E and the X183 domain from Cbp2D. Elucidation of these novel crystal structures has allowed functions to be attributed to these previously uncharacterised domains, and, when complemented with biochemical analyses, interdomain electron transfer roles were explored. Most interestingly, the CjX183 domain was able to activate bacterial LPMOs in a manner analogous to small molecule reductants. Experiments performed in this thesis have provided a key starting point for the characterisation of *C. japonicus* Cbp2D and Cbp2E proteins as redox partners to bacterial LPMOs within *C. japonicus*.

Table of Contents

List of Tables

List of Figures

Abbreviations

AA	Auxiliary activity
Amp	Ampicillin
Cam	Chloramphenicol
CAZy	Carbohydrate active enzymes database
CBH	Cellobiohydrolase
CBM	Carbohydrate binding module
CD	Circular dichroism spectrometry
CDH	Cellobiose dehydrogenase
DMSO	Dimethyl sulfoxide
EDTA	Ethylenediaminetetraacetic acid
EPR	Electron paramagnetic resonance spectroscopy
ESI-MS	Electrospray ionisation mass spectrometry
FAD	Flavin adenine dinucleotide
GH	Glycoside hydrolase
HPAEC	High pressure anion exchange chromatography
HRP	Horseradish peroxidase
IPTG	Isopropyl-β-thiogalactopyranoside
ITC	Isothermal titration calorimetry
Kan	Kanamycin
k_{cat}	Catalytic constant
K_m	Michaelis constant
k_{obs}	Observed rate constant
LPMO	Lytic polysaccharide monooxygenase
MALDI-TOF	Matrix-assisted laser desorption/ionisation time of flight
MOPS	3-Morpholinopropane-1-sulphonic acid
MS	Mass spectrometry
MW	Molecular weight
NEB	New England Biolabs
NMR	Nuclear magnetic resonance spectroscopy
OPP	Octaprenyl pyrophosphate
PASC	Phosphoric acid swollen cellulose

PCR	Polymerase chain reaction
PDB	Protein Data Bank
PDH	Pyranose dehydrogenase
PEG	Polyethylene glycol
PIPE	Polymerase incomplete primer extension
PQQ	Pyrroloquinone-quinone
rmsd	Root-mean-square deviation
SDS-PAGE	Sodium dodecyl sulphate polyacrylamide gel electrophoresis
SEC	Size exclusion chromatography
SHE	Standard hydrogen electrode
SoxCD	Sulphane dehydrogenase
T_m	Melting temperature
tNCS	Translational non-crystallographic symmetry
TSBT	Tris-buffered saline Tween
TsdBA	Thiosulphate dehydrogenase/tetrathionate reductase
Ub-8	Ubiquinone-8
Ub-9	Ubiquinone-9
V_{max}	Maximum rate of reaction

Chapter 1

Introduction

1.1 The importance of biofuels from biomass

Depleting levels of fossil fuels combined with increased awareness of the damaging properties of greenhouse gas emissions has fuelled the recent investment in new energy sources. The drive towards using more renewable energy has heightened interest in generating new biofuels. First-generation biofuels derived from starch and sugarcane are already established, but since these rely on feedstocks that are primarily extracted from food sources, the need for biofuels from non-edible biomass is increasingly prevalent (Farrell et al., 2006). Structural polysaccharides contained within lignocellulose are ubiquitous in plant biomass and are rich in glucose. Due to the potential to harness lots of energy from structural polysaccharides, the production of second-generation biofuels is essential, especially in areas where there are food shortages. The ultimate aim of the second-generation biofuels industry is to efficiently liberate as much glucose from plant biomass as possible, to allow its conversion into liquid fuels via microbial fermentation (Himmel et al., 2007). There is large scope for production of useful products from plant biomass, from bioethanol to plastics, therefore, plant biomass represents a yet untapped resource that can feed into the renewable fuels industry (Sheldon, 2014). Liberating sugars from biomass is not without its challenges, to optimally harness the power of second-generation biofuels, substrate recalcitrance must first be addressed.

1.2 Lignocellulose provides structural rigidity in plant cell walls

1.2.1 Lignocellulose

Plant cell walls are rigid, stable structures. They provide structural rigidity to plant cells, protecting them from microbial or mechanical degradation. Lignocellulose, the primary component in plant cell walls, is responsible for this stable structure. Lignocellulose is composed of three components, with typical proportions: 40-50 % cellulose, 20-40 % hemicelluloses and 20-30 % lignin. Lignocellulose also contains a small number of structural proteins, lipids and soluble sugars (Pauly and Keegstra, 2008). The exact composition of lignocellulose is variable, as different plant types have distinct requirements for rigidity depending on plant function. A schematic view of lignocellulose is shown in Figure 1.1 and lignocellulose composition will be discussed further in subsequent sections.

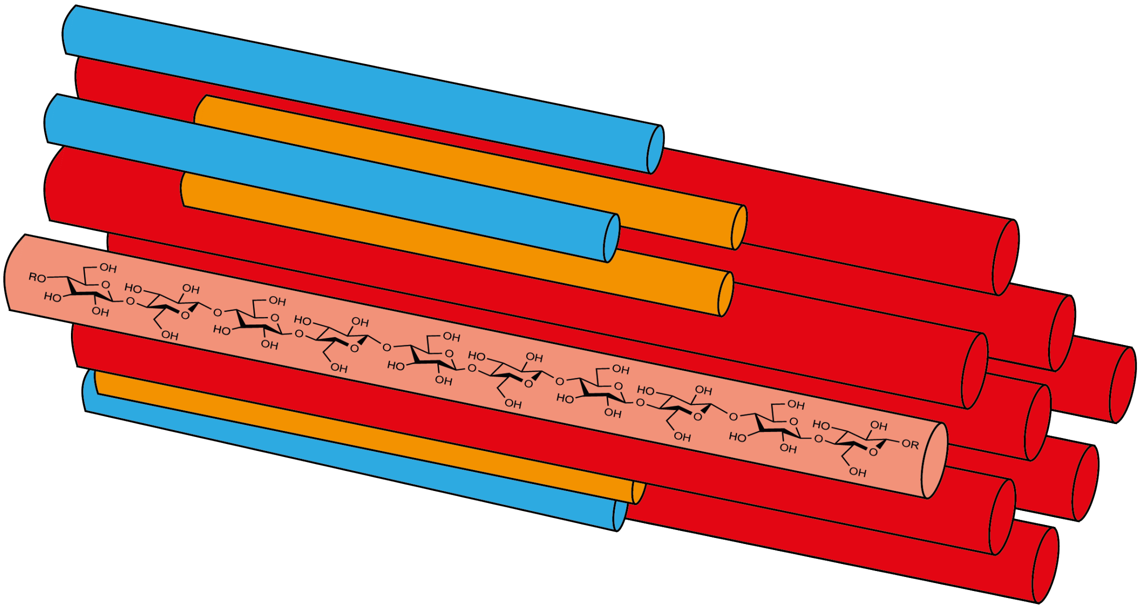

Figure 1.1: Lignin and hemicellulose encase cellulose microfibrils to create a recalcitrant structure. *Schematic representing cellulose strands (red tubes) encased in hemicelluloses (orange tubes) and lignin (blue tubes).*

1.2.2 Cellulose

Cellulose is the primary component of lignocellulose. The homogeneity of cellulose, composed solely of glucose monomers, makes it an ideal target for second generation biofuels, where monomeric glucose can be liberated from the polymer and fermented to ethanol. In cellulose, glucose monomers form chains up to tens of thousands of units long. Within a single cellulose chain, individual β-1,4 linked glucose monomers are rotated 180° relative to each other, making cellobiose the repeating unit (Figure 1.2) (Horn et al., 2012b).

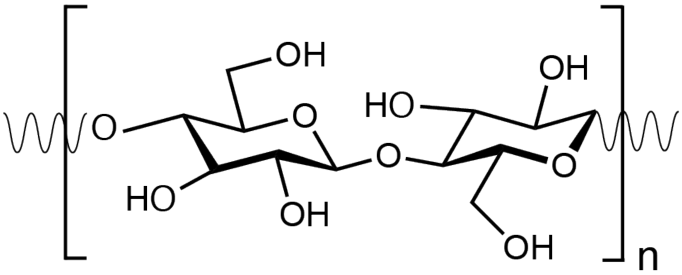

Figure 1.2: Cellobiose forms the repeating unit of cellulose.

Cellulose chains come together to form microfibrils, which are held together by van der Waals forces and a large hydrogen bond network, which forms between the aliphatic hydrogen atoms of one cellulose chain and the hydroxyl groups of another (Figure 1.3) (Kroon-Batenburg and Kroon, 1997; Voet et al., 2008). Hydrophobic and hydrogen bonding interactions bring cellulose microfibrils together to form a highly crystalline structure (Himmel et al., 2007). Within lignocellulose, cellulose is present in well-ordered crystalline regions but there are also areas that have a more amorphous structure. The crystalline nature of cellulose creates a very stable structure, and in plant cell walls cellulose is buried amongst other polymers, such as lignin and hemicelluloses, that bolster its strength and rigidity, creating a highly stable structure.

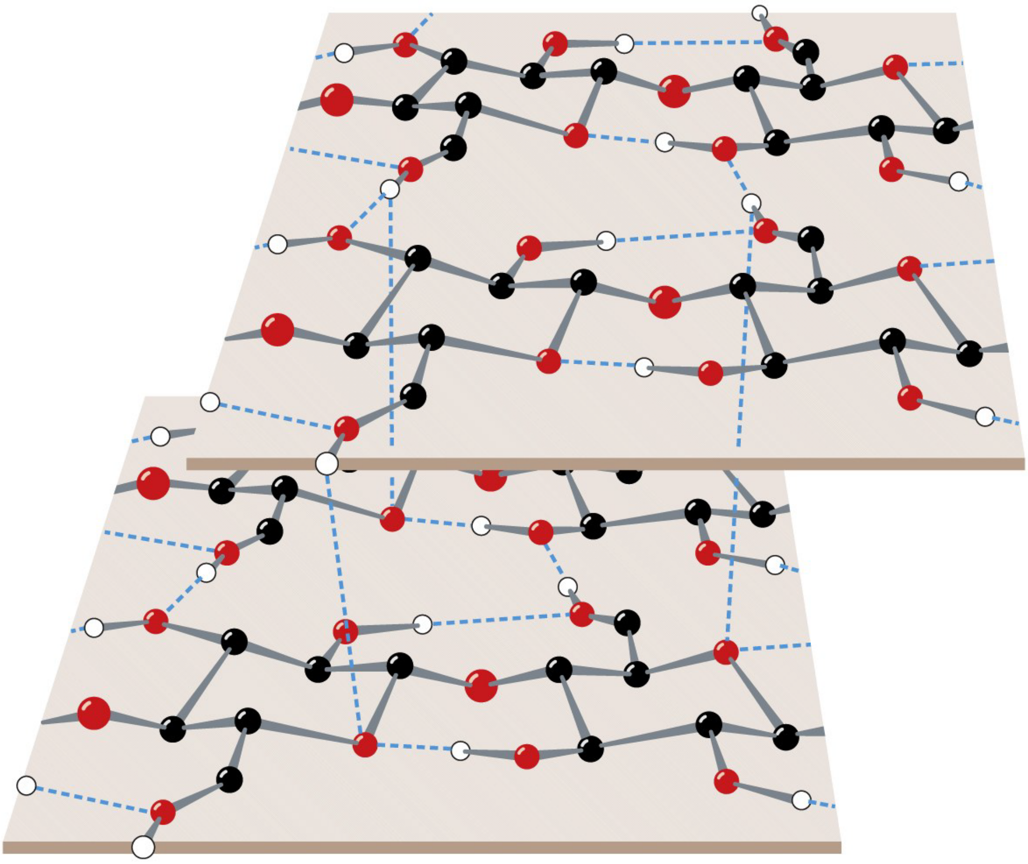

Figure 1.3: Cellulose forms a crystalline structure. *Cellulose chains come together to form a crystalline structure using a network of Van der Waals forces and hydrogen bonds. Atoms are coloured according to atom type with filled lines showing covalent bonds and dashed lines representing hydrogen bonds. Figure from Voet, Voet and Pratt (Voet et al., 2008).*

1.2.3 Hemicellulose

After cellulose, hemicellulose is the second largest constituent of lignocellulose. Hemicelluloses are much shorter polysaccharides than cellulose, and often have branched chains. Hemicelluloses are largely heterogeneous and can be constructed from a large range of monomers in addition to D-glucose, such as arabinose, galactose, mannose and xylose. Complex branching and acetylation patterns among hemicelluloses are thought to contribute to their overall stability. (Johansen, 2016; Jordan et al., 2012; Horn et al., 2012b).

1.2.4 Lignin

Lignin is a key component of lignocellulose and is largely responsible for imparting rigidity into the structure. Unlike cellulose and hemicellulose, lignin is composed entirely of aromatic subunits. It is a heteropolymer formed by the polymerisation of three different phenyl propanoid units: coniferyl alcohol, sinapyl alcohol and coumaryl alcohol (Figure 1.4). The proportions of different lignin units vary dramatically in different types of biomass, with hardwoods containing higher percentages of lignin compared to softwoods (Horn et al., 2012b; Johansen, 2016; Jordan et al., 2012). In lignocellulosic biomass, lignin is cross linked with carbohydrates to increase the rigidity of plant cell walls. The structure of independent components of lignocellulose has been examined at length (Mansfield et al., 1999; Kroon-Batenburg and Kroon, 1997), however, the overall, large scale structure of lignocellulose in the plant cell wall is still largely uncharacterised (Dupree et al., 2015). The complex structure of lignocellulose makes accessing glucose, which is buried in this elaborate structure, particularly challenging.

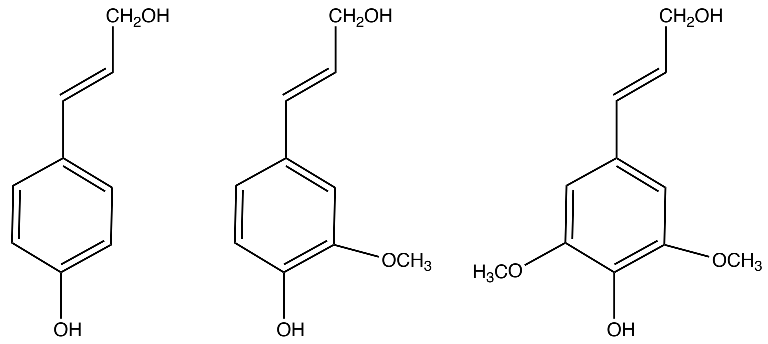

Coniferyl alcohol Sinapyl alcohol Coumaryl alcohol

Figure 1.4: Lignin is composed of aromatic subunits. *The building blocks of lignin are coniferyl alcohol, sinapyl alcohol and coumaryl alcohol.*

1.3 Lignocellulose breakdown is targeted for second generation biofuels

The complex, stable structure of lignocellulose has evolved to ensure the formation of protective and rigid plant cell walls. Lignocellulose stability, coined recalcitrance, has evolved to protect plants against degradation from pathogens (Underwood, 2012). Lignocellulose recalcitrance is the major challenge facing the second-generation biofuels industry, its complex structure requires specific attention to efficiently access the cellulose core, which contains a wealth of untapped resources.

Breaking down lignocellulose into its monosaccharides requires a number of complex industrial processes. The largest contributor to lignocellulose recalcitrance is lignin. Its stable structure is particularly resistant to degradation and, accordingly, biomass with lower lignin content is easier to break down (Ding et al., 2012). Breaking down cellulose and hemicelluloses involves a number of specific enzymes, and can yield a variety of different sugars, which can be problematic for fermentation processes (Jordan et al., 2012; Horn et al., 2012b). To optimally harness the energy that is stored in plant biomass, a collection of industrial processes are used, to overcome substrate recalcitrance and generate bioethanol from plant cell walls.

1.4 Ethanol is generated from lignocellulose in three main steps

A number of approaches have been investigated to degrade lignocellulose to produce liquid biofuels. However, the industry has primarily focussed on the three-step process comprising pretreatment, enzymatic saccharification and fermentation, summarised in the schematic in Figure 1.5.

In order to increase the accessibility of the cellulose core to degradative enzymes, biomass must first be pretreated to break down lignin and hemicelluloses. The pretreatment process requires a combinatorial approach, including physical, chemical and thermal steps. Pretreatment is complex and is often low yield, a trade-off must be struck to remove lignin and hemicelluloses, without releasing large quantities of chemicals that may affect downstream processes (Jordan et al., 2012).

Pretreatment methods to remove lignin have been shown to increase the accessibility of lignocellulose to degradative enzymes (Ding et al., 2012), and typically glucose yields of above 80 % can be achieved following pretreatment, compared to 20% without this stage (Jordan et al., 2012). A typical pretreatment process may use dilute sulphuric acid as a catalyst at temperatures between 150 and 200 °C, along with specific enzymes to depolymerise hemicelluloses and increase the accessibility of the cellulose core (Himmel et al., 2007; Jordan et al., 2012).

Following pretreatment, enzyme saccharification, using a number of different degradative enzymes, is typically used to liberate glucose monomers from cellulose (enzyme cocktails will be explored in more detail in section 1.5). When glucose has been liberated from biomass it is fermented into ethanol. Fermentation is challenging for most microorganisms, tolerance to ethanol, high temperatures and pH variation are required, and for this reason *Saccharomyces cerevisiae* is most commonly used. However, *S. cerevisiae* cannot naturally ferment D-xylose, a product of hemicellulose breakdown, and introduction of this pathway into the organism is still being optimised for efficient fermentation (Jordan et al., 2012). Hexose sugars, such as glucose, are the most easily fermentable sugars by microorganisms, making glucose release from cellulose ideal for this process (Pauly and Keegstra, 2008).

Although pretreatment and fermentation steps are essential for generating liquid fuels, this thesis will focus on the advancements made in the saccharification step. Ensuring that enzymes can efficiently liberate glucose from cellulose is vital for maximal breakdown of lignocellulose. For this process enzyme cocktails, targeting different parts of cellulose breakdown, are commonly used.

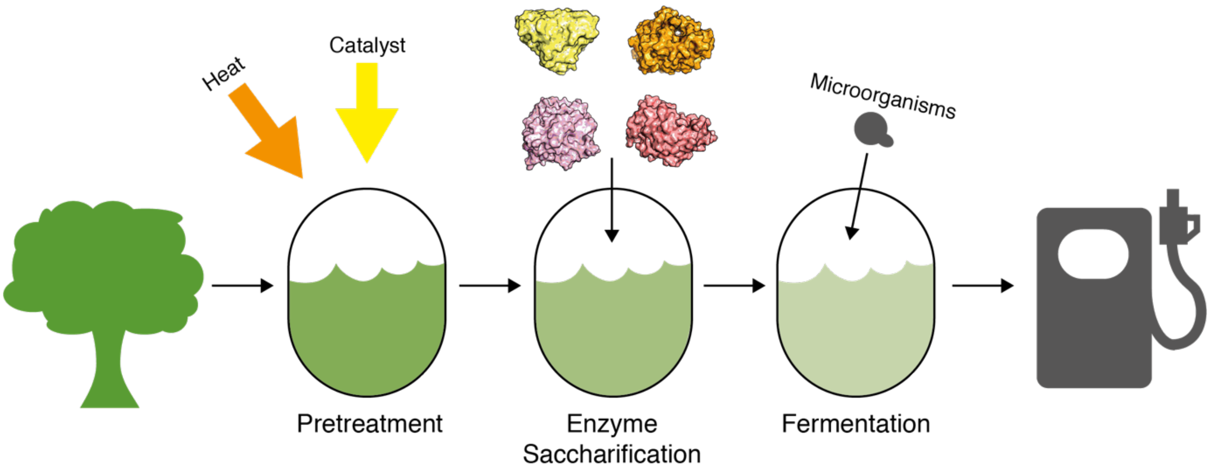

Figure 1.5: Ethanol is generated from lignocellulosic biomass in three main steps. *Lignin is removed during pretreatment, often using high temperatures and sulfuric acid as a catalyst, before glucose monomers can be liberated by enzyme cocktails and fermented into bioethanol.*

1.5 A cocktail of enzymes is required to break down cellulose

Cellulose is an essential component of the carbon cycle, there are many bacterial and fungal saprotrophs that feed on organic matter by targeting the plant cell wall using degradative enzymes to obtain energy from glucose (Lynd et al., 2002; Payne et al., 2015). In Nature, bacteria and fungi have evolved highly specific systems for this process; studying these systems has provided many insights into the optimum enzymes to use in enzyme cocktails.

1.5.1 Cocktails of enzymes are secreted by biomass-degrading organisms

The first system of biomass-degrading enzymes to be studied were discovered from *Trichoderma reesei* (then *Trichoderma viridae*). *T. reesei* is a filamentous fungus, originally isolated on the Solomon Islands for its remarkable cellulose-degrading ability. Cellulase activity was first identified from pioneering work on *T. reesei* (Reese, Elwyn T. and Levinson, 1952), which has laid the groundwork for development of enzyme cocktails and current understanding of cellulase induction and action (Reese, E. T., 1956; Mandels, Mary and Reese, 1957; Mandels, M. and Reese, 1960; Mandels, M. et al., 1962). The cellobiohydrolase (CBH) CBH1 from *T. reesei*, a powerful cellulase that is secreted at high levels, was the first cellulase to be structurally characterised, providing important insight into cellulase action (Divne et al., 1994). Enzyme cocktails used today are largely derived from the research on *T. reesei* cellulolytic systems.

1.5.2 Cellulases

Cellulases are a key component of enzyme cocktails for lignocellulose degradation. They belong to the glycoside hydrolase family of enzymes, which act to degrade polysaccharides and oligosaccharides by the introduction of water molecules into glycosidic bonds. Historically, three main groups of glycoside hydrolases have formed the basis of commercial saccharification cocktails: endo,1-4-β-glucanases, exo-1,4-β-glucanases and β-glucosidases (Horn et al., 2012b). The action of these different enzymes is shown in Figure 1.6.

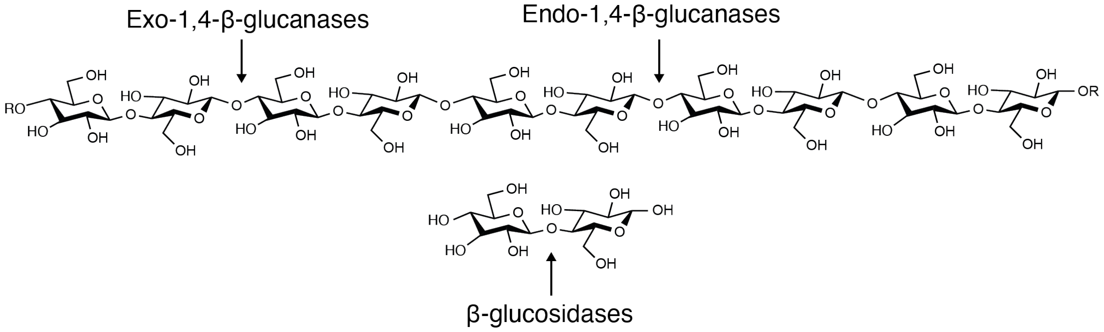

Figure 1.6: Structure of a cellulose chain and action of different cellulases. *The molecular structure of a cellulose chain is annotated with different sites for cellulase action depending on their specificity.*

Endo-1,4-β-glucanases randomly cleave internal bonds within polysaccharide chains (Hatfield and Nevins, 1987). Whereas, exo-1,4-β-glucanases hydrolytically cleave polysaccharide chains from chain ends (Nisizawa and Hashimoto, 1959) (Figure 1.6). Endo- and exo-β-glucanases can act by processive or non-processive mechanisms. Processive enzymes introduce several consecutive cuts following enzyme-substrate association, feeding the polysaccharide chain through the active site and liberating molecules of cellobiose (Horn et al., 2012a; Horn et al., 2006). CBHs are processive exo-1,4-β-glucanases, and it is their processivity that makes them such prolific cellulose degraders. CBHs are the major component of enzyme cocktails, they act in synergy with endo-acting enzymes, which create internal chain breaks for CBHs to initiate their processive action on (Divne et al., 1994).

β-glucosidases act on the products generated by endo- and exo-1,4-β-glucanases, and convert cellobiose, and other cello-oligosaccharides, to monomeric glucose (Conchie, 1954; Chinchetru et al., 1989) (Figure 1.6). These enzymes work in concert to completely break down crystalline cellulose into its glucose monosaccharides (Figure 1.7) (Horn et al., 2012b). Synergy between these groups of enzymes in this system is particularly important to ensure that enzymes are optimally utilised to efficiently break down cellulose.

Although cellulase function, and the synergy between cellulases, in enzyme cocktails is well understood, the quest for further improvements in these systems has resulted in the search for new enzymes that may act to degrade biomass *in vivo*. From these studies, a new class of degradative enzymes was discovered, the lytic polysaccharide monooxygenases (LPMOs) (Harris et al., 2010; Vaaje-Kolstad et al., 2010). LPMOs have been shown to dramatically boost the activity of cellulase cocktails, providing scope for large enhancements in the efficiency of polysaccharide degradation by enzyme saccharification.

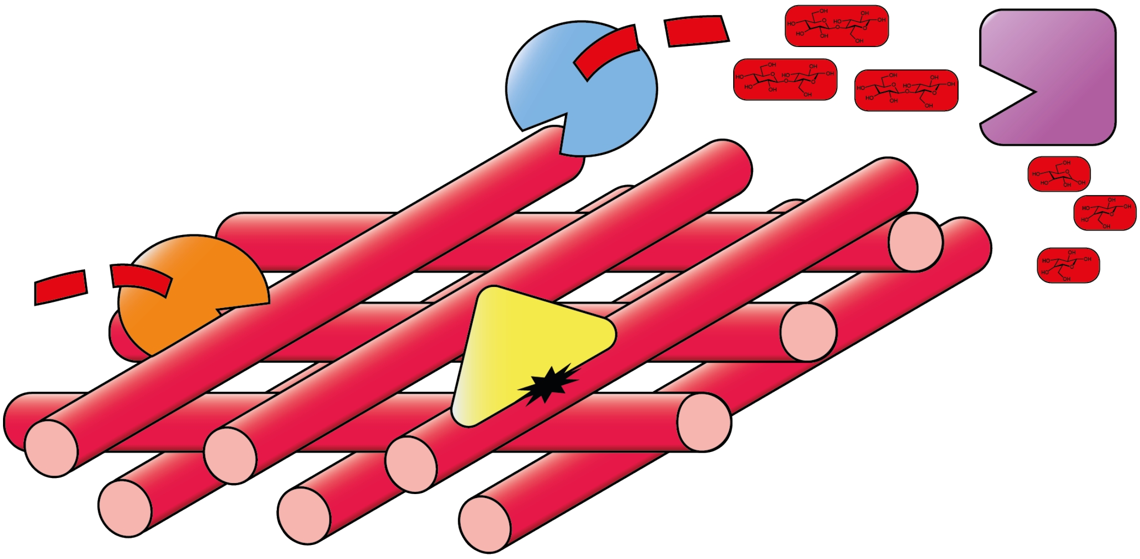

Figure 1.7: A number of degradative enzymes act synergistically to break down cellulose to glucose monosaccharides. *Exo-1,4-β-glucanases (blue), endo-1,4-β-glucanases (orange) and LPMOs (yellow) break down crystalline cellulose (shown as red tubes) β-glucosidases (purple) convert cellobiose to glucose.*

1.6 The discovery of LPMOs

In 2010, a new class of polysaccharide degrading enzymes were discovered. The chitin binding CBP21 protein from *Serratia marcescens*, from the CBM33 family of carbohydrate binding proteins, was shown to cleave glycosidic bonds in crystalline chitin in a metal and reducing agent dependent manner (Vaaje-Kolstad et al., 2010). This suggested an oxidative mechanism distinct from classical glycoside hydrolases, which was confirmed using experiments performed in the presence of ^{18}O. In the same year, a group of fungal enzymes were reclassified, GH61 proteins, which were previously thought to act as glycoside hydrolases, were shown to boost the degradation of polysaccharides by classical cellulases (Harris et al., 2010). It was unclear what the molecular basis for the boosting effect was, but, like CBP21s, it appeared to be metal dependent. The structural similarity between GH61 and CBM33 proteins suggested that these enzymes acted by similar mechanisms. Further investigations into GH61s revealed a catalytic copper ion in the active site (Quinlan et al., 2011), in the original SmCBP21 structure the metal was incorrectly assigned as a sodium ion (Vaaje-Kolstad et al., 2005). The copper active site ion was later confirmed in CBM33s (Hemsworth et al., 2013). These initial studies demonstrated the essential nature of reducing agents, and the active site copper for the generation of oxidised products by these novel enzymes, and showed their capabilities to boost the activity of cellulases on polysaccharide substrates (Forsberg et al., 2011; Beeson et al., 2012; Quinlan et al., 2011). Following the discovery that these enzymes were unique copper dependent monooxygenases, GH61s and CBM33s were reclassified in the Carbohydrate Active enZymes (CAZy) database, as Auxiliary Activity (AA) families 9 and 10 respectively (Levasseur et al., 2013). At this point, LPMOs were deemed to hold great potential to revolutionise enzyme cocktails, their abilities to boost polysaccharide degradation by other cellulases was a key driving force for further research in this area.

To date, there are seven families of LPMO classified in the CAZy database: AA9, AA10, AA11, AA13, AA14, AA15 and AA16 (Levasseur et al., 2013; Hemsworth et al., 2014; Vu et al., 2014b; Lo Leggio et al., 2015; Couturier et al., 2018; Sabbadin et al., 2018; Filiatrault-Chastel et al., 2019). LPMOs have been isolated from fungi, bacteria, viruses, and most recently higher eukaryotes, such as plants and insects (Quinlan et al., 2011; Vaaje-Kolstad et al., 2010; Chiu et al., 2015; Yadav et al., 2019). They act on a wide range of polysaccharide substrates including, but not limited to, cellulose, chitin, starch, and hemicelluloses such as xylan (Vaaje-Kolstad et al., 2010; Quinlan et al., 2011; Vu et al., 2014b; Lo Leggio et al., 2015; Agger et al., 2014; Frommhagen et al., 2015; Couturier et al., 2018). Across these families, LPMOs share low sequence similarities, but are all found to contain the same immunoglobulin-like β-sandwich fold, and a common active site architecture (Beeson et al., 2015; Hemsworth et al., 2015).

1.7 LPMOs cleave crystalline polysaccharides in an oxidative manner

LPMOs are thought to boost cellulase action by cleaving glycosidic bonds within the crystalline region of cellulose, which are difficult for glycoside hydrolases to access (Harris et al., 2010). They, therefore, open up the structure for other degradative enzymes to access the cellulose chains, and hence boost their ability to degrade the substrate (Horn et al., 2012b). LPMOs cause chain breaks by specifically introducing a single atom of oxygen at either the C1 or C4 carbon of the sugar ring, leading to cleavage of the glycosidic bond (Figure 1.8). This was first shown by experiments performed in the presence of $H_2^{18}O$ that showed that the C1 position of chitin oligosaccharides was oxidised to a carboxylic acid with the incorporation of one oxygen atom (Vaaje-Kolstad et al., 2010). Subsequent studies showed that substrate oxidation could occur at the C1 or C4 position of the glycosidic bond, resulting in the formation of lactone or aldonic acid products (Beeson et al., 2012; Vaaje-Kolstad et al., 2010; Forsberg et al., 2011; Langston et al., 2011). Oxidised products liberated by LPMOs are routinely detected by matrix-assisted laser desorption/ionisation time of flight mass spectrometry (MALDI-TOF MS) or by high pressure anion exchange chromatography (HPAEC) (Forsberg et al., 2011; Vaaje-Kolstad et al., 2010; Beeson et al., 2012; Phillips et al., 2011).

LPMO regioselectivity has been grouped into three categories: C1-oxidising, C4-oxidising and C1/C4 oxidising (Vu et al., 2014a). Regioselectivity has been connected to phylogeny, with similar acting enzymes suggested to have evolved from a common ancestor. Additionally, conserved structural features in LPMOs have also been suggested to contribute to regioselectivity (Vu et al., 2014a). Structural studies on LPMOs have been crucial in underpinning the molecular mechanism of LPMOs.

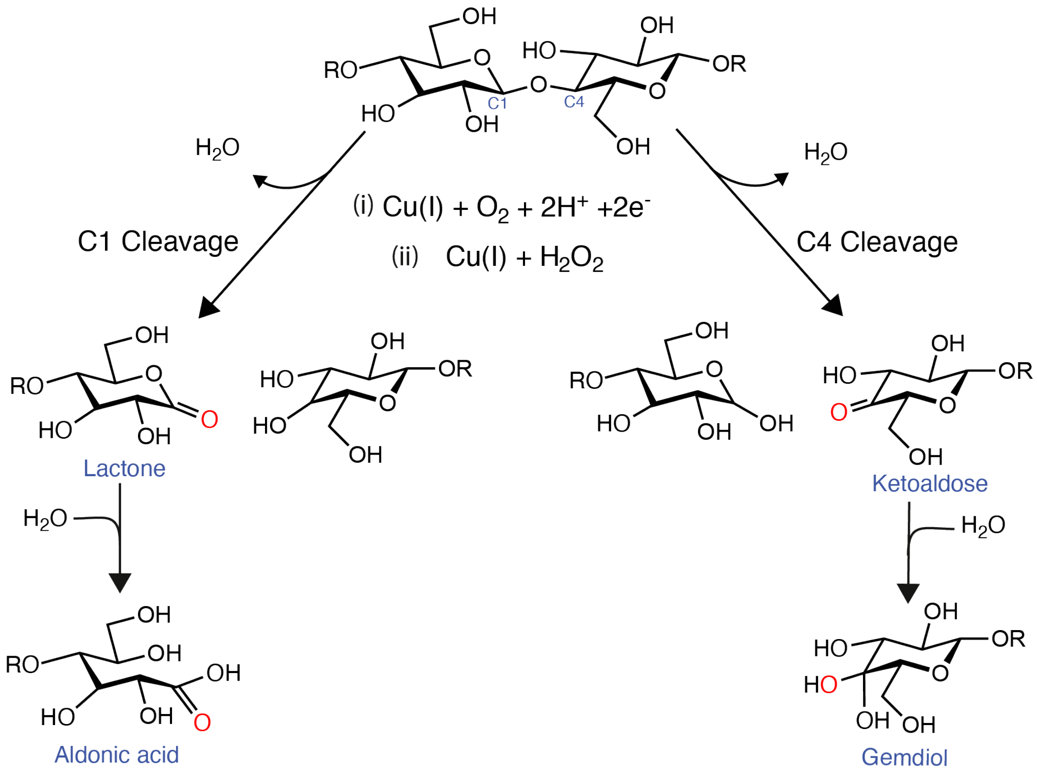

Figure 1.8: LPMO-catalysed C1/C4 cleavage yields lactone and ketoaldose products. *LPMOs act by one of two mechanisms, summarised in (i) and (ii), to cleave crystalline cellulose at C1 and/or C4 positions, generating lactone and ketoaldose products respectively. Hydrated aldonic acid or gemdiol products are also routinely detected.*

1.8 Molecular mechanisms of LPMOs have been highlighted by structural analysis

1.8.1 LPMOs have a common immunoglobulin-like β-sandwich fold

Since the evolution of the LPMO field, structural analyses of LPMOs have been crucial for examining the molecular mechanisms behind their oxidative cleavage. To date there are 223 LPMO structures in the Protein Data Bank (PDB) (PDBe, as of April 2021), which represent structures across all currently known LPMO families and a large number of species. All currently characterised LPMOs share a common immunoglobulin-like β-sandwich core and conserved active site architecture (Beeson et al., 2015; Hemsworth et al., 2015), which is shown in the structure of an LPMO from *Cellvibrio japonicus* CjAA10A in Figure 1.9.

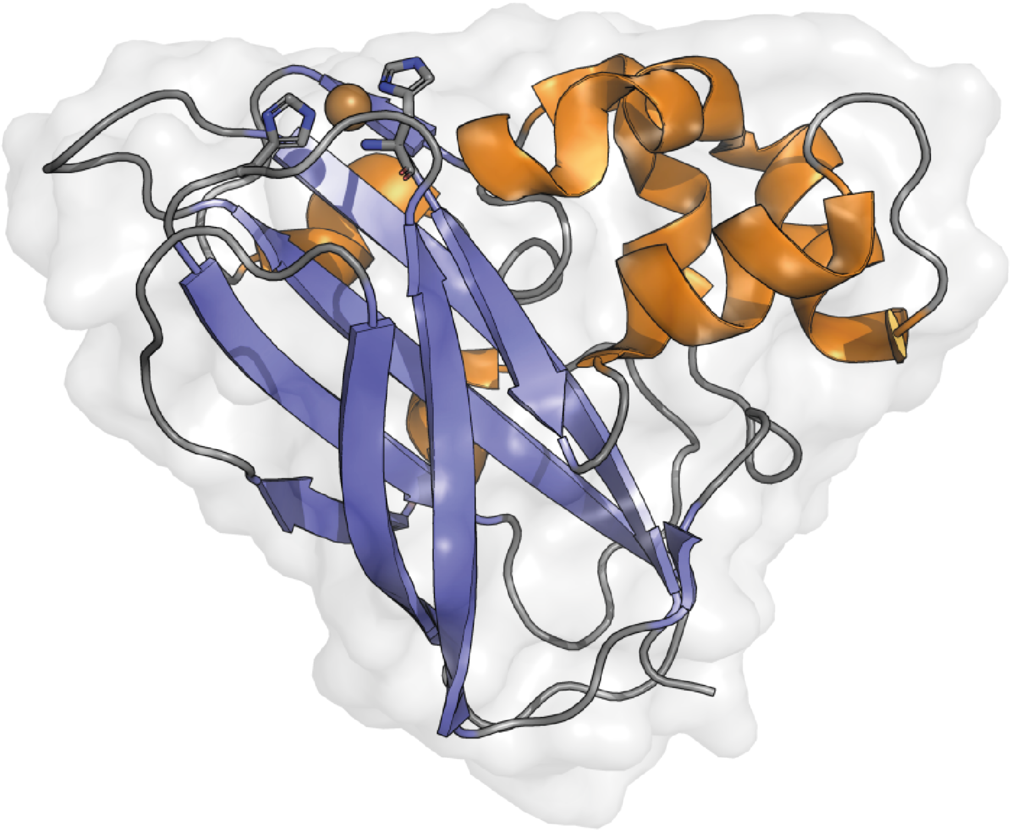

Figure 1.9: LPMOs display a common immunoglobulin-like β-sandwich fold. *The structure of CjAA10A (PDB ref 5FJQ) shown as cartoon, with the active site shown as sticks coordinating a copper ion shown as a brown sphere.*

1.8.2 The LPMO active site

A characteristic feature of all LPMOs is their active site architecture. The active site is formed from a motif that has been termed the histidine brace. This motif consists of two histidine residues, one of which is the N-terminal residue of the protein, which come together to coordinate a single copper ion in a T-shaped geometry. In all LPMOs, the side chain imidazole and amino group of the N-terminal histidine residue act to coordinate the copper ion, along with the side chain of a second histidine residue (see reviews (Ciano et al., 2018; Beeson et al., 2015; Hemsworth et al., 2015)). The copper coordination of CjAA10A is shown in Figure 1.10.

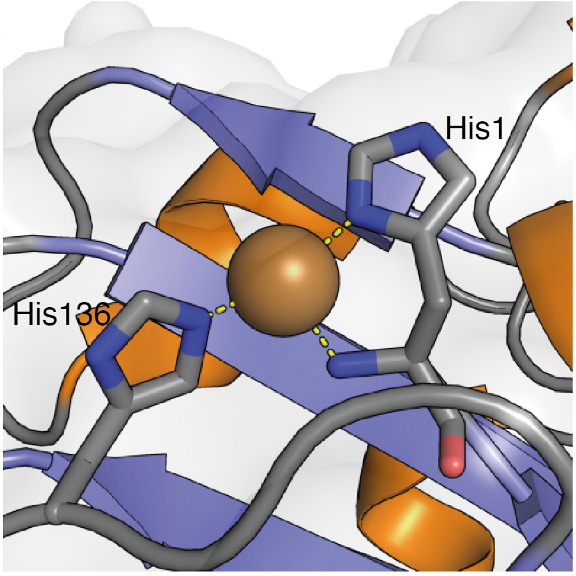

Figure 1.10: The active site copper ion in LPMOs is coordinated in the histidine brace. *The active site of CjAA10A, with active site residues shown as sticks and the active site copper shown as a brown sphere.*

The active site copper ion is now accepted as the catalytic metal, however early studies on LPMOs experienced difficulties with assigning the active site metal ion. In the first crystal structure of an LPMO, CBP21 from *S. marcescens*, the catalytic metal was incorrectly assigned as a sodium ion (Vaaje-Kolstad et al., 2005). In 2011, Quinlan *et al.* correctly assigned the copper active site ion in a GH61 enzyme from *Streptomyces coelicolor* and termed the histidine brace (Quinlan et al., 2011). Isothermal titration calorimetry (ITC), electron paramagnetic resonance (EPR) and X-ray crystallography were used to confirm the presence of the active site copper, demonstrating unambiguously that the catalytic copper ion was bound tightly at the histidine brace, with similar EPR signals to those observed for other copper oxygenases (Quinlan et al., 2011). Similar studies performed on bacterial LPMOs revealed a similar T-shaped coordination of the active site copper ion (Hemsworth et al., 2013). For fungal and bacterial LPMOs, copper binding at the histidine brace was shown to have a significant stabilising effect on proteins, and tight binding, with dissociation constants in the nanomolar range, was measured (Quinlan et al., 2011; Hemsworth et al., 2013).

While the histidine brace is absolutely conserved across all LPMOs that have been biochemically characterised to date, there are some differences that have been noted between enzymes from different species with different substrate specificities. Initial studies on fungal LPMOs observed that the N-terminal histidine was methylated (Quinlan et al., 2011; Li et al., 2012), a feature that is not conserved in bacterial enzymes. The purpose of the N-terminal methylation was initially unclear, however, recent studies have proposed that it could exist to protect the active site from oxidative damage. Methylated and unmethylated AA9 enzymes from *Thermoascus aurantiacus* were compared. Enzyme specificities were unchanged but, interestingly, the methylated enzyme appeared to be active for longer, suggesting that it was less prone to oxidative damage (Petrovic et al., 2018). It is still unclear how the N-terminus of fungal LPMOs is methylated. Interestingly, fungal LPMOs that are recombinantly expressed in bacterial or yeast expression systems lack this feature (Hemsworth et al., 2014; Wu et al., 2013), and this modification has not been observed in other families of LPMO. Consequently, it is interesting that this seemingly protective modification is constrained to only fungal systems.

There has been significant focus on the coordination geometry of the copper in different LPMOs, in a bid to understand the enzymatic properties that tune the copper to activate oxygen for attack of the polysaccharide substrate. Comparison of histidine brace geometries of an AA10 from *Enterococcus faecalis* with an AA9 from *T. aurantiacus* show difference in copper coordination between these two families of LPMO (Figure 1.11). The TaAA9 active site (Figure 1.11B) is typical of a type-II copper centre. In addition to the histidine brace, the Cu(II) ion is coordinated by two water molecules and an axial tyrosine residue (Quinlan et al., 2011), which is conserved in AA9 enzymes. Accordingly, the EfAA10 active site (Figure 1.11A) does not possess the axial tyrosine residue, or methylated N-terminus, and the copper ion is coordinated in the histidine brace and by two additional water molecules (Gudmundsson et al., 2014). Interestingly, coordinating waters are often observed to be lost by photoreduction in the X-ray beam in LPMO structures, suggesting that waters are only present when the active site copper is in the Cu(II) state (Gudmundsson et al., 2014; Gregory et al., 2016).

The EfAA10 structure shows a more distorted active site geometry than the TaAA9 structure (Figure 1.11). EfAA10 is active on chitin, and chitin active AA10s share this distorted active site geometry, and also display more rhombic EPR spectra than cellulose active AA10s (Hemsworth et al., 2013; Forsberg et al., 2014b). Cellulose active AA10s do not show the same distortion in the active site, and resemble the active sites of AA9s more closely (Forsberg et al., 2014a). It is obvious that the distortion is correlated to activity on chitin, however, it is still unclear why the differences in active site geometry alter substrate specificity so dramatically.

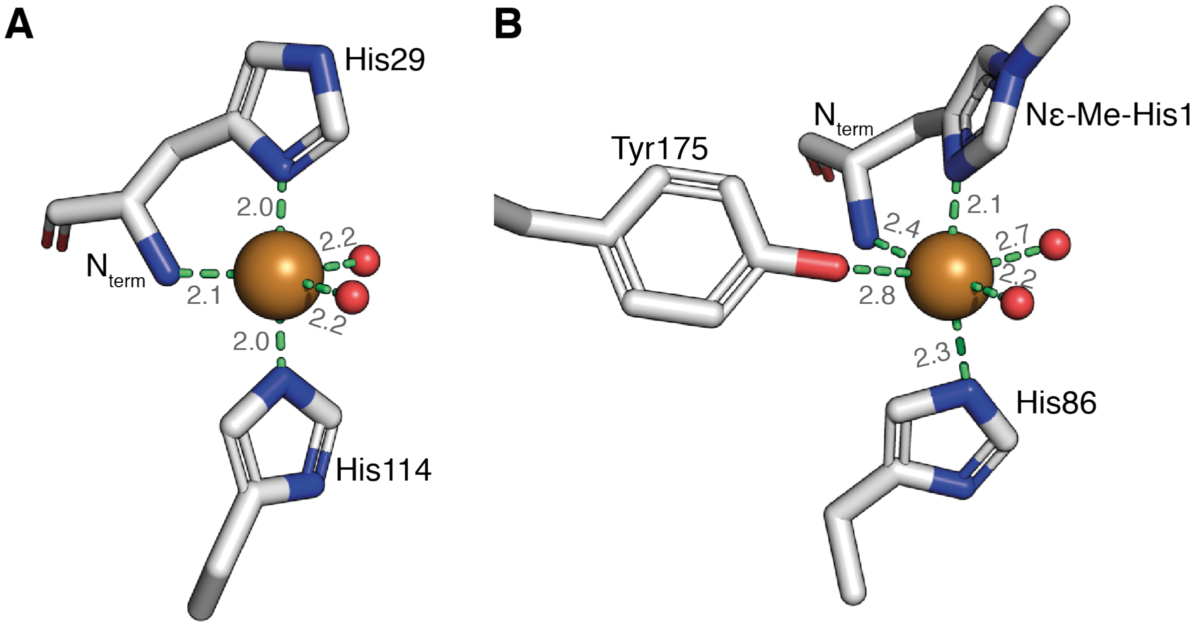

Figure 1.11: Comparison of copper coordination in AA10 and AA9 enzymes. (A) *The Cu(II) ion, shown as a brown sphere, in the E. faecalis AA10 structure (PDB code 4ALC) is coordinated by the histidine brace and two water molecules, shown as red spheres.* ***(B)*** *The copper ion in T. aurantiacus AA9 (PDB code 2YET) is additionally coordinated by a tyrosine residue. Coordinating interactions are shown as green dashes and all distances are in angstroms. Figure adapted from Gudmundersson et al. 2014.*

1.8.3 Second sphere coordination residues do not directly coordinate the copper, but contribute to the stability of the active site

In addition to the histidine brace, the copper ion is surrounded by a number of other residues that form a secondary coordination sphere. These residues are not close enough to the copper to directly coordinate it, but are thought to facilitate the complex oxidative chemistry performed by the copper ion, by providing stabilising interactions within the active site and with catalytic intermediates as the reaction progresses (Span et al., 2017; Forsberg et al., 2019).The secondary sphere residues are largely conserved within LPMO families, but variation between families is common.

The AA9 and AA10 families of LPMOs are the most well characterised, due to their early classification in the field. There are distinct differences (shown in Figure 1.12) between AA9s and AA10s in the second coordination sphere. In the place of the conserved AA9 tyrosine residue, AA10s often have a phenylalanine residue. The phenylalanine is positioned slightly further away from the active site and lacks a polar group, so cannot directly coordinate the copper ion (Hemsworth et al., 2013). The axial tyrosine is generally conserved in AA11, AA13, AA14 and AA15 enzymes and is most commonly found in cellulose specific enzymes (Hemsworth et al., 2014; Lo Leggio et al., 2015; Couturier et al., 2018; Sabbadin et al., 2018). In addition to the axial Phe/Tyr, AA10 enzymes have a conserved axial alanine residue, (Hemsworth et al., 2013; Forsberg et al., 2014b), which can be glycine in some AA10s (Fowler et al., 2019) as shown in Figure 1.12, and has even been seen as a isoleucine in an AA10 from *Photorhabdus luminescens* (Munzone et al., 2020). The axial alanine residue is conserved in AA11 enzymes and was also seen in the structure of an AA15 from *Thermobia domestica* (Hemsworth et al., 2014; Sabbadin et al., 2018). The significance of the axial alanine is unknown, but when present in conjunction with an axial phenylalanine, these residues are thought to be responsible for distortion of the copper coordinating water molecules away from the typical type II copper geometry observed in most fungal LPMOs (Figure 1.11B). The importance of this distortion and its effect on the mechanism of action of LPMOs is still unknown, but these second sphere interactions are likely important in determining the reactivity of the active site copper.

More distant to the copper, all families of LPMOs have a conserved second sphere glutamate/glutamine residue (shown in Figure 1.12), which was shown early on, to be essential for the LPMO reaction (Harris et al., 2010). More recent studies have suggested the second sphere residues to be important for oxygen uptake and product formation (Span et al., 2017; Bissaro et al., 2020b). The Glu/Gln residue has been proposed to gate the active site, restricting access when substrate is bound. This was shown by molecular dynamics simulations, performed by Bissaro *et al.*, which modelled β-chitin binding to an AA10 and showed the second sphere glutamate in different conformations. The different conformations observed for this residue appeared to form a tunnel between the active site and the bulk solvent, which at its widest was 1.6 Å, not wide enough to allow the passage of reducing agents in the substrate bound state (Bissaro, Bastien et al., 2018). In all structurally characterised LPMOs, the Glu/Gln residue is pointing towards the active site (Span et al., 2017), and in the neutron structure of an AA9 from *Neurospora crassa*, the glutamine active site residue is involved in positioning a species thought to represent an equatorially bound oxygen species (O'Dell et al., 2017). Molecular dynamics experiments also suggest that this Glu/Gln residue is directly involved in positioning a key reactive intermediate in the active site during the LPMO reaction (Bissaro et al., 2020a). These studies clearly demonstrate that, in addition to the residues that directly coordinate the copper, secondary sphere residues are imperative to modulating the active site environment and hence LPMO activity.

The variation of secondary sphere residues across AA9s and AA10s is shown in Figure 1.12. The secondary spheres of a cellulose active AA9 from *T. auranticus*, a cellulose active AA10 from *Teredinibacter turnerae* and a chitin active AA10 from *S. coelicolor* demonstrate the variation between families and enzymes that act on different substrates. The conserved axial tyrosine in AA9 enzymes is replaced by a phenylalanine residue in these AA10s. Additionally, the axial alanine is present in the chitin active ScAA10A, but is replaced by glycine in the cellulose active TtAA10. The Glu/Gln residue is conserved in all three enzymes, and is glutamate in the two AA10s and glutamine in TaAA9.

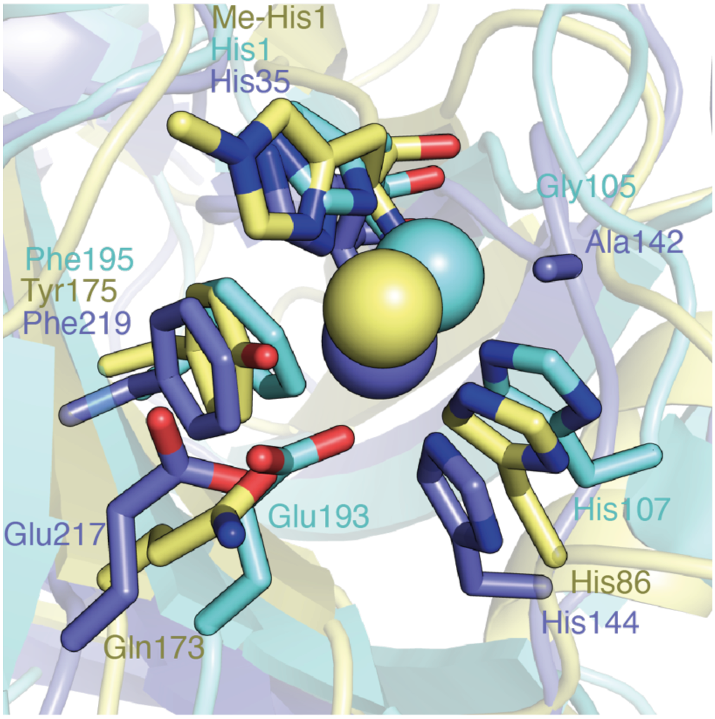

Figure 1.12: Comparison of second sphere coordinating residues in AA9 and AA10 cellulose and chitin active enzymes. *The secondary sphere of cellulose active TaAA9 (yellow) (PDB ref 2YET), cellulose active TtAA10 (cyan) (PDB ref 6RW7) and ScAA10A (blue) (PDB ref 4OY7) shown as sticks with copper atoms shown as spheres.*

1.8.4 Structural features contributing to regioselectivity and substrate specificity

The LPMO active site is located at the centre of a flat substrate binding surface to maximise interactions with crystalline substrates. The lack of a defined substrate binding pocket in LPMOs, in contrast to many enzymes, has made studying substrate specificity and binding challenging. In recent years, large efforts have gone into studying substrate binding by LPMOs to understand how specificity is achieved. LPMOs share very low sequence similarities, with the exception of active site residues (Book et al., 2014). Therefore, identifying residues that are critical for regioselectivity and substrate specificity is difficult. Within families of LPMOs there is higher conservation of these residues, allowing speculation on the importance of structural features for selective oxidation of substrates. In AA10s, most of the structurally conserved residues are surface exposed, in contrast to AA9s, where there is large variation on the substrate binding face (Book et al., 2014). Vu *et al.* classified AA9s into three groups to investigate regioselectivity: C1-, C4- and C1/C4-oxidising enzymes. They showed that removing a small helix from the L2 loop, a highly variable loop at the substrate binding surface, prevented a C1/C4-oxidising LPMO from being able to introduce C4 chain breaks (Vu et al., 2014a). Aromatic residues at the substrate binding surface have also been suggested to contribute to regioselectivity, due to their exposed nature and conservation in LPMOs that show similar regioselectivity (Wu et al., 2013; Vu et al., 2014a). Additionally, Forsberg *et al*. suggested that C4-oxidising activity relies on accessibility of an axial binding site to the copper ion, as many C1-oxidising LPMOs were observed to have an alanine residue blocking this axial binding site (Forsberg et al., 2014a).

LPMOs have been shown to act on a number of different substrates, most commonly cellulose and chitin. The active sites of chitin- and cellulose-specific LPMOs are very similar, however, there are some small differences that could mediate substrate specificity. As mentioned in section 1.8.2, the copper active site of chitin-active enzymes display distorted active site geometries and more rhombic EPR spectra compared to cellulose-active LPMOs (Forsberg et al., 2014b; Hemsworth et al., 2013). Structural comparisons of the active sites have revealed differences in axial residues coordinating the copper ion, although it is not yet fully understood how they influence substrate specificity (Forsberg et al., 2014b). Structural studies have also demonstrated that there is a small cavity adjacent to the active site in chitin specific AA10s that is not present in cellulose specific enzymes, which could accommodate the N-acetyl groups in the repeating unit of chitin (Forsberg et al., 2014b). The differences between chitin and cellulose-specific enzymes have been studied at the residue level, and in 2019, Jenson *et al.* shifted the substrate preference for an LPMO from *S. coelicolor* from cellulose specific to chitin specific (Jensen et al., 2019). A number of site-specific mutations were rationally made at the substrate binding surface, offset from the active site, substituting conserved residues for activity on cellulose for those conserved for chitin activity. Cumulative effects, from the mutation of five residues, were seen to shift the substrate specificity from cellulose to chitin, demonstrating the importance of the entire substrate binding surface, not just the active site, for substrate specificity (Jensen et al., 2019).

Studies on cellulose- and chitin-oxidising enzymes have demonstrated the general principles of substrate specificity, and the importance of the entire substrate binding surface. However, substrate specificity of enzymes that act on different substrates are less well understood. AA13 enzymes are active on starch (Vu et al., 2014b; Lo Leggio et al., 2015), characterisation of an AA13 enzyme from *Aspergillus oryzae* revealed a shallow groove at the substrate binding surface, which has not been seen in LPMOs active on other substrates, and was proposed to favour binding of the helical structure of starch (Lo Leggio et al., 2015). Other LPMOs have been characterised that act on a branched substrates such as xyloglucan (Agger et al., 2014; Isaksen et al., 2014), and factors controlling substrate specificity in these cases are not well understood. Nonetheless, it is well accepted that the extended substrate binding surface of LPMOs is important for positioning the substrate at the active site.

1.8.5 Structural studies to determine residues involved in substrate binding

Due to the crystalline nature of the polysaccharide substrates that LPMOs act on, it is difficult to study enzyme-substrate interactions. Therefore, understanding substrate binding features that are required for regioselectivity or substrate specificity is very challenging. Binding studies using ITC and tryptophan fluorescence quenching have been used to demonstrate increased affinities of LPMOs for their substrates following copper reduction (Kracher et al., 2018; Hangasky and Marletta, 2018; Hedison et al., 2020). The presence of superoxide mimics in the form of chloride or cyanide ions have also been shown to promote substrate binding (Frandsen et al., 2016; Courtade et al., 2016). Additionally, nuclear magnetic resonance spectroscopy (NMR) and molecular dynamics experiments have been used to show that LPMOs form more stable complexes with crystalline substrates in favour of single polysaccharide chains (Aachmann et al., 2012; Zhou, H. et al., 2020). Structurally characterising enzyme-substrate interactions has been challenging due to the insolubility of most LPMO substrates.

Progress in this area came with the characterisation of an AA9 from *N. crassa*, NcAA9C, which was the first LPMO to demonstrate activity on soluble cello-oligosaccharides (Agger et al., 2014; Isaksen et al., 2014). NcAA9C was shown to have a more extended substrate binding site than previously characterised LPMOs, presenting lots of polar residues (Borisova et al., 2015). NMR studies of apo-NcAA9C, performed on the *apo*-protein to avoid masking of active site chemical shifts by the copper ion, showed significant chemical shift differences for the active site residues upon β-glucan binding. Significant perturbations were also observed for a region of the extended substrate binding surface, termed the L3 loop, which is positioned at one end of the substrate binding face and is a feature conserved within xyloglucan active LPMOs (Courtade et al., 2016).

Importantly, the first crystal structure of an AA9 in complex with a soluble cello-oligosaccharide was determined by Frandsen *et al.* (Frandsen et al., 2016). This structure was determined using an AA9 from *Lentinus similis* (LsAA9A) that showed similar substrate specificity to NcAA9C, and has since been used to study its interactions with some substrates other than cellulose (Simmons et al., 2017). Figure 1.13 shows the structure of LsAA9A bound to a cellohexaose molecule (PDB ref 5ACI), the cellohexaose is numbered according to nomenclature defined in Davies *et al.* (Davies et al., 1997), where the glycosidic bond to be cleaved stretches between the -1 and +1 subsite and subsites are labelled from -n, the non-reducing end, to +n, the reducing end. In LsAA9A, the active site copper ion is coordinated in the histidine brace, with the conserved AA9 axial tyrosine residue and a chloride ion occupying the cavity between the active site copper and the bound cellohexaose. Comparison of the substrate-free and -bound structures showed the chloride ion displacing two copper-coordinating waters upon substrate binding (Frandsen et al., 2016).

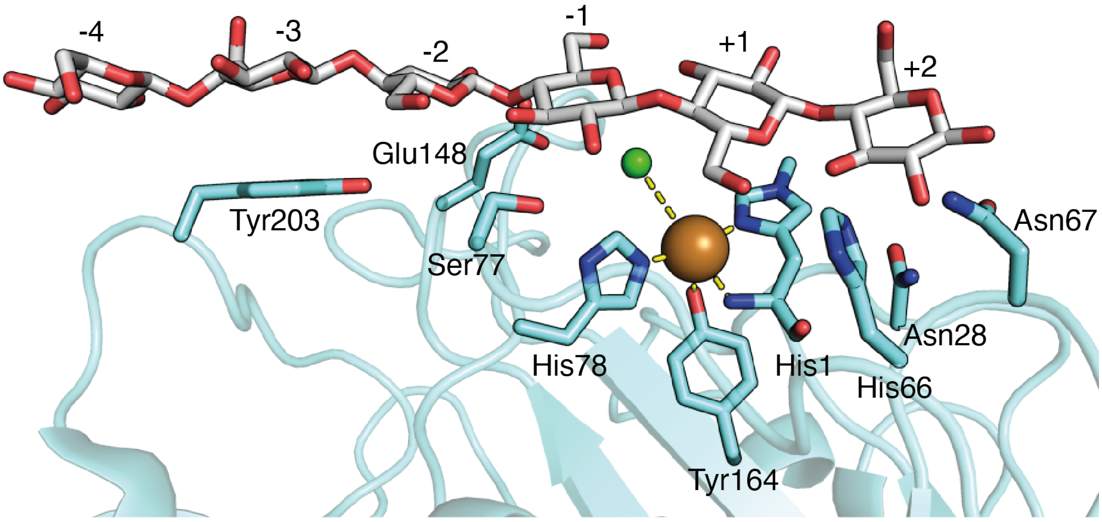

Figure 1.13: The substrate binding face of LsAA9A in complex with cellohexaose. *Cellohexaose is shown in grey and LsAA9A in cyan, with specific atoms coloured by atom type. The copper ion, brown sphere, is shown coordinated by the histidine brace and a chloride ion, green sphere. Important residues and substrate subsites are labelled and active site coordination is shown as yellow dashes.*

A number of residues in LsAA9A are involved in coordinating the cellohexaose molecule. The aromatic ring of Tyr203 is involved in CH-π interactions with the glucosyl unit of the -3 subsite, and hydrogen bonding interactions from Ser77 and Glu148 can be seen stabilising glucosyl oxygen atoms in the -1 subsite. Additionally, a network of hydrogen bonds are believed to form from Asn28, His66 and Asn67 to the O2 and O3 atoms of the +2 subsite. The +1 glycosyl unit at the active site appears to stack directly on top of the methylated His1, in a lone pair-aromatic interaction, which positions the glycosidic bond directly over the proposed oxygen binding site (Frandsen et al., 2016). These interactions are conserved in structures with cellotriose and glucomannan, implying that they are genuine interactions (Frandsen et al., 2016; Simmons et al., 2017), and similar substrate interactions have been seen in a structure of a *Collariella virescens* AA9 with cellohexaose bound (Tandrup et al., 2020). Structures of LsAA9A with glucomannan show the chloride ion displaced towards the glycosidic bond and a water molecule coordinating the copper ion (Simmons et al., 2017). The chloride ion is thought to assist substrate binding, in Figure 1.13 it is bound in the proposed oxygen/superoxide binding site, and is thought to act as an oxygen/peroxide mimic in the LsAA9A structures. EPR experiments with LsAA9A bound to either phosphoric acid swollen cellulose (PASC) or cellohexaose showed similar spectra, indicating that active site geometries were unchanged, which suggests that the interactions observed in these structures are also relevant in the context of enzyme activity on crystalline substrates (Frandsen et al., 2016).

Recently, Zhou *et al.* have investigated LPMO binding to PASC using alanine mutants of MtAA9L from *Myceliophthora thermophia*. Alanine mutants of Asp25, Tyr193 and Tyr194 showed a significant decrease in activity on polysaccharide substrates (Zhou, H. et al., 2020). Molecular dynamics simulations, performed to investigate binding of MtAA9L to PASC, predicted Asp25, Tyr193 and Tyr194 to coordinate the -1, +4 and +5 (of the neighbouring polysaccharide chain) sugar subsites respectively. The decrease in activity on PASC was attributed to a cumulative effect from reduced substrate binding at each of these positions (Zhou, H. et al., 2020).

Overall, these studies stress the importance of synergy between residues in the substrate binding surface to coordinate polysaccharide chains and larger, crystalline polysaccharide surfaces. Structures of AA9 enzymes that act on soluble substrates have been instrumental in this work. However, because sequence conservation between LPMOs is still relatively low, the nature of interactions between enzymes that act on larger, more crystalline, substrates are still largely unknown.

1.8.6 Carbohydrate binding modules direct LPMO binding to polysaccharide substrates

Although the catalytic domains of LPMOs form direct interactions with the substrate surface, substrate binding and specificities of LPMOs are also influenced by carbohydrate binding modules (CBMs). CBMs are additional domains, commonly found appended to enzymes involved in polysaccharide breakdown, they promote enzyme localisation to substrates, making for more efficient breakdown systems (Boraston et al., 2004; Gilbert et al., 2013). Many LPMOs contain C-terminal CBM domains (Book et al., 2014) and searching for novel proteins appended to CBMs is a method that has been used to discover new LPMOs or proteins that may contribute to LPMO action (Hemsworth et al., 2014; Gardner et al., 2014). CBMs, like LPMOs, have flat substrate binding surfaces, to maximise interactions with crystalline polysaccharides. The substrate binding face is comprised of numerous aromatic residues to form strong interactions with crystalline surfaces of polysaccharides (Raghothama et al., 2000; Tormo et al., 1996). There are a number of different families of CBMs that are found appended to LPMOs, the family of CBM can often give an indication of substrate specificity for an LPMO (Boraston et al., 2004). Bacterial cellulose specific LPMOs are often found to have CBM10s, which typically bind to cellulose, or CBM5s or CBM12s in chitin specific enzymes (Crouch et al., 2016). Starch active LPMOs in the AA13 class were identified through their appended CBM20 starch binding domains (Lo Leggio et al., 2015). Interestingly, AA14 enzymes do not appear to contain CBMs, and the reason for this is unknown (Couturier et al., 2018). LPMOs are appended to CBMs via a flexible linker, which often impedes crystallographic studies of LPMOs attached to their CBMs. Therefore, most crystal structures of LPMOs are only representative of the catalytic domain. NMR analysis of a full length modular AA10 from *S. coelicolor* showed large conformational variation in the sample due to a flexible linker with an extended conformation linking the catalytic domain and CBM (Courtade et al., 2018).

Though there is a paucity of structures of LPMOs with appended CBMs, these additional domains have been shown to be important for activity. Deletion of CBMs can impair LPMO activity on polysaccharide substrates. Deletion of the CBM2 domain from the *Cellulomonas fimi* AA10 resulted in a 4-fold decrease in gluconic acid released from bacterial microcrystalline cellulose (Crouch et al., 2016). This effect was attributed to a loss in substrate binding ability, rather than a loss in catalytic activity, as the H_2O_2 generating ability of the truncated enzyme was unchanged (Crouch et al., 2016). The effect of removing the CBM appears to be more prominent when examining substrate binding. In pull down assays with crystalline substrates, truncated variants were not detected in the bound fraction, whereas full length LPMOs were, suggesting stronger binding of the full length proteins (Chalak et al., 2019). The effect of removing the CBM was shown to be more prominent at low substrate concentrations. At these concentrations, a full length AA9 from *Podospora anserina* was shown to liberate more soluble sugars from PASC than a truncated variant, whereas, at high substrate concentrations both enzymes liberated similar amounts of soluble sugars (Chalak et al., 2019). The CBM domain is evidently important for promoting binding of the catalytic domain to polysaccharide substrates especially in environments where the substrate concentration is low.

1.9 Mechanisms of LPMO action

Aside from their industrial applications, there has been considerable interest in understanding the LPMO reaction mechanism. Copper oxidases typically require multiple copper centres to activate molecular oxygen, so how LPMOs can do this using only one metal ion has been a key question in the field (Solomon et al., 2014). Subsequent sections will discuss the various mechanisms that have been proposed for LPMO activity, and recent developments that have suggested that LPMOs may actually act as peroxygenases (Bissaro et al., 2017; Kuusk et al., 2018; Kuusk et al., 2019; Hangasky et al., 2018). The general mechanisms of LPMO action are outlined in Figure 1.14.

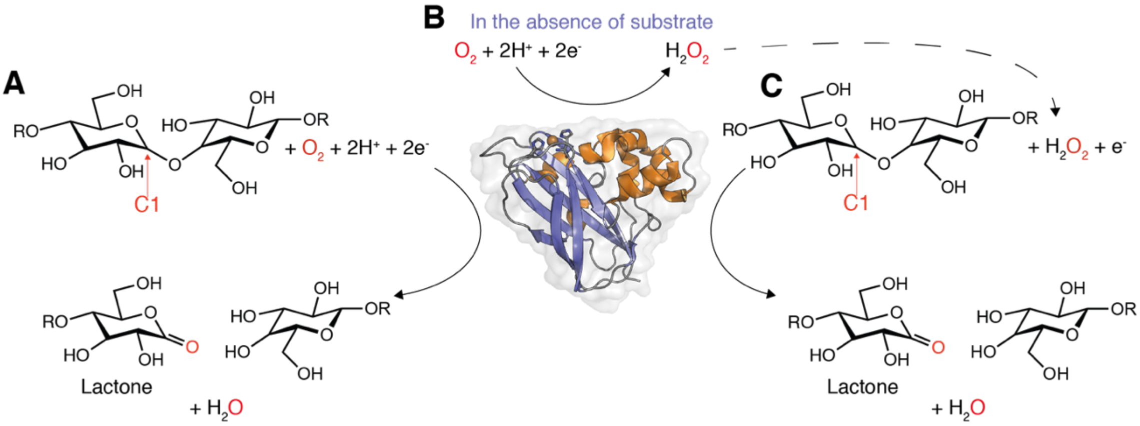

Figure 1.14: Reaction scheme for LPMOs. (A) *The traditionally accepted mechanism that LPMOs use electrons to activate molecular oxygen and introduce chain breaks into polysaccharides.* ***(B)*** *In the absence of substrate, activated LPMOs will generate hydrogen peroxide from oxygen.* ***(C)*** *More recent studies suggest that LPMOs can use hydrogen peroxide as a co-substrate.*

1.9.1 LPMOs as monooxygenases

Upon their discovery, LPMOs were shown to be copper dependent monooxygenases, using molecular oxygen to oxidatively cleave polysaccharides (Figure 1.14A). This was performed using isotope labelling experiments using $H_2{}^{18}O$, which showed that LPMOs introduced a single molecule of oxygen into polysaccharide chains (Vaaje-Kolstad et al., 2010). Experiments showing inhibition of LPMO activity by cyanide and not by catalase, which breaks down H_2O_2, or superoxide dismutase, which breaks down superoxide radicals, suggested that molecular oxygen was important for LPMO action (Vaaje-Kolstad et al., 2010). Using molecular oxygen and an external source of electrons, LPMOs were proposed to introduce a single oxygen atom at the C1 or C4 position resulting in glycosidic bond cleavage, in a copper dependent manner (Quinlan et al., 2011). In this reaction mechanism, the external electron source is used to reduce the active site copper from Cu(II) to Cu(I), then the reduced active site is able to activate molecular oxygen. The identity of the oxidative species that is generated has been a hotly debated topic, with many reaction mechanisms suggested (Hemsworth et al., 2015; Beeson et al., 2015; Ciano et al., 2018).

In attempts to decipher the mechanism of action for LPMOs, observations have suggested oxygen species present at enzyme active sites. Crystallographic studies of NcAA9 enzymes performed by Li *et al.* suggested the presence of a superoxide species (O_2^-) in the LPMO active site, shown to directly coordinate the copper ion in an end-on conformation (Li et al., 2012). Another study of an NcAA9, also showed an end-on oxygen species, equatorially bound at the copper active site. This species was modelled as a peroxo species (O_2^{2-}) (O'Dell et al., 2017). In the structure of a substrate bound LsAA9A (discussed in section 1.8.5), Frandsen *et al.* noted that the axial binding sites of the copper ion were occluded by substrate binding, leaving the equatorial site open for oxygen binding, where a chloride ion was bound in this structure (Frandsen et al., 2016). Therefore, equatorially bound oxygen species, as suggested by studies performed in the absence of substrate, are expected to remain in the substrate-bound state. Computational modelling experiments have shown superoxide binding in an end-on conformation to be more energetically favourable than in a side-on conformation (Cowley et al., 2016).

Kjaergaard *et al.* modelled the end-on binding of the superoxide species, and used a combination of spectroscopic and computational methods to propose a mechanism for superoxide binding and release (Kjaergaard et al., 2014). In this mechanism, copper reduction was shown to drive the loss of an equatorial water molecule, changing the copper coordination from four-coordinate tetrahedral to three-coordinate T-shaped geometry. Rapid oxygen binding at the Cu(I) ion was observed, and the most stably bound oxygen species, determined using computational modelling, was shown to be the superoxide species. The superoxide species was proposed to bind equatorially, and be rapidly displaced upon the binding of an axial water molecule, shown in EPR experiments (Kjaergaard et al., 2014). In the presence of substrate, the axial binding position is occluded, so presumably superoxide will not be released this way (Frandsen et al., 2016). However, it has been disputed whether a Cu-bound superoxide is powerful enough to abstract a hydrogen atom from the C1/C4 position of substrates (Hedegard and Ryde, 2018; Wang, B. et al., 2018). A study by Kim *et al.* proposed hydrogen atom abstraction by a Copper(II)-oxyl species to be more energetically favourable than by a copper(II)-superoxide (Kim et al., 2014). Hydrogen abstraction from the C1/C4 position of the substrate by the reactive copper(II)-oxyl was suggested to form a substrate radical and a copper(II)-hydroxyl, proceeded by rebounding of the hydroxyl group onto the substrate to promote glycosidic bond cleavage (Kim et al., 2014). Subsequent computational modelling experiments have supported the mechanism of glycosidic bond cleavage through the formation of a copper-oxyl or -hydroxyl (Figure 1.15, reaction 1) (Wang, B. et al., 2018; Hedegard and Ryde, 2018). More recent molecular modelling studies have been used to model the transition of the active site through the proposed mechanism, these studies show the formation of a copper(II)-oxyl or -hydroxyl, that is sufficiently reactive to abstract a hydrogen atom from the C1/C4 position of the substrate, one such reaction scheme is shown in Figure 1.15, proposed reactions 1, 3 and 4 (Hedegard and Ryde, 2018).

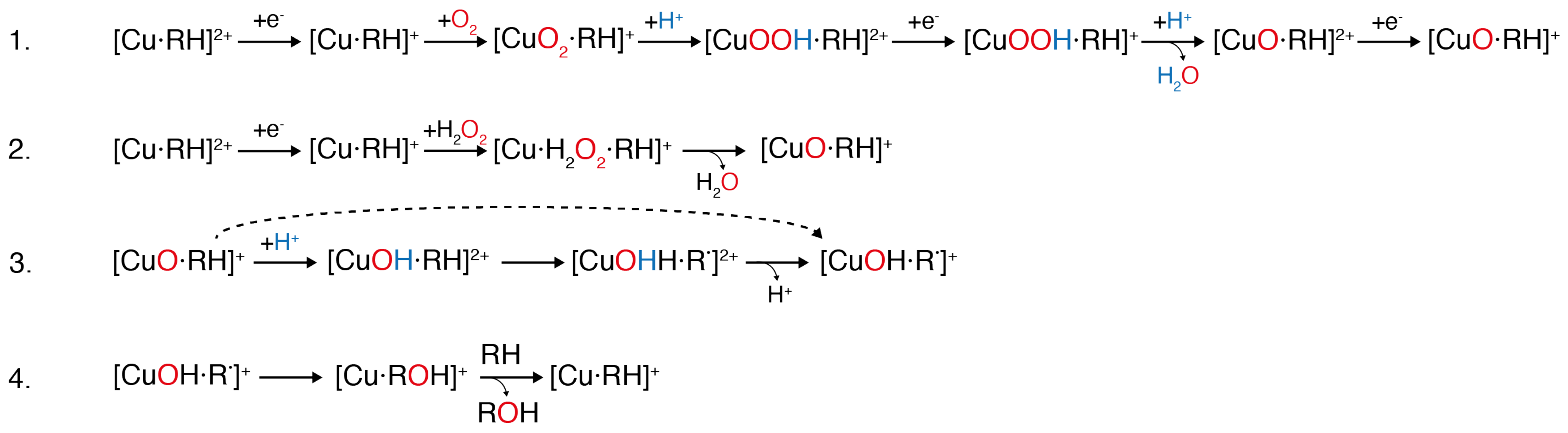

Figure 1.15: Proposed reaction mechanisms for Cu2+-bound LPMOs with O_2 or H_2O_2. *Reaction mechanisms proposed by Hedegård and Ryde for:* ***(1)*** *Reaction of LPMOs with molecular oxygen to generate a reactive copper-oxyl.* ***(2)*** *Reaction of Cu^{2+}-bound LPMOs with H_2O_2 to form a reactive copper-oxyl.* ***(3)*** *Hydrogen atom abstraction from polysaccharide substrates, which may proceed in one step, dashed arrow, or three steps, filled arrows.* ***(4)*** *Hydroxyl rebounding and glycosidic bond cleavage. Reaction scheme adapted from Hedegård and Ryde (Hedegard and Ryde, 2018).*

1.9.2 In the absence of substrate LPMOs generate peroxide

In the absence of substrate LPMOs are known to generate hydrogen peroxide from oxygen (Figure 1.14B) (Kittl et al., 2012). This reaction is useful for the assessment of LPMO activity during expression (Kittl et al., 2012) and has also been used to assess substrate specificity of LPMOs, where a loss of H_2O_2 producing ability was correlated to activity on the substrate (Fanuel et al., 2017). Molecular modelling simulations were used by Wang *et al.* to suggest a mechanism for the formation of H_2O_2 by LPMOs using the small molecule reducing agent ascorbate. In these simulations, the reduced copper ion in LPMOs was proposed to form a copper(II)-superoxide, which then abstracted two hydrogen atoms from two ascorbate molecules to regenerate the copper(I) centre and release H_2O (Wang, B. et al., 2019). Until recently, this system has only been used as a method of assessing LPMO activity, as described above. However, recent studies have suggested the H_2O_2-producing abilities of LPMOs to be a part of the catalytic mechanism, so that H_2O_2 can act as a co-substrate in LPMO-driven catalysis of polysaccharide breakdown (Caldararu et al., 2019; Bissaro et al., 2017; Kuusk et al., 2018).

1.9.3 Recent suggestions that LPMO may act as peroxidases

Recently, there has been much speculation over the true co-substrate of LPMOs. Studies performed by Bissaro *et al.* identified that adding H_2O_2 to reactions boosted liberation of soluble products by LPMOs by 26-fold (Bissaro et al., 2017). It was demonstrated during this work that ^{18}O labelled atoms from hydrogen peroxide were preferentially incorporated into glycosidic bonds, even when a 10-fold excess of oxygen was provided (Bissaro et al., 2017). Subsequent kinetic analyses were performed using H_2O_2 as a co-substrate to LPMOs, which demonstrated that higher rates of LPMO turnover could be achieved when using H_2O_2 compared to O_2, measured by the release of soluble products from crystalline substrates (Kuusk et al., 2018; Hangasky et al., 2018).

A fundamental difference of the H_2O_2 mechanism, compared to the O_2 mechanism, regards the role of the reductant. Reactions performed using sub-stoichiometric concentrations of reducing agents showed that LPMOs activated by H_2O_2 could perform multiple cleavage reactions following an initial priming reduction. This reduction was proposed to convert the Cu(II) ion to Cu(I), but since hydrogen peroxide was the co-substrate, following enzyme turnover the Cu(I) species was regenerated, thereby allowing further turnovers to occur without the requirement of more reducing agents (Bissaro et al., 2017). Kuusk *et al.* recorded that as many as 18 cleavages could be observed for a single priming event (Kuusk et al., 2019). EPR studies have shown the restoration of the copper(I) state after catalysis in the presence of substrates (Hedison et al., 2020). This reaction mechanism negates the need for delivery of a second electron to the copper ion, which has posed questions in the field due to the inaccessibility of the active site when the enzyme is substrate-bound (Bissaro, Bastien et al., 2018).

The mechanism by which hydrogen peroxide fuels polysaccharide cleavage by LPMOs has been the subject of much discussion over recent years (Wang, B. et al., 2018; Hedegard and Ryde, 2018; Bissaro et al., 2020b). Proposals that have contributed to deciphering the mechanism are largely based on computational studies, as has also been seen for the oxidative mechanism. Verifying these results experimentally is very challenging due to the nature of the transient intermediates and fast reaction rates. In these mechanisms, like for the oxidative mechanism, the reaction is proposed to proceed through a reactive copper(II)-oxyl or -hydroxyl (Wang, B. et al., 2018; Bissaro et al., 2020b). In the most commonly proposed mechanism, the primed copper(I) ion, activated by an external electron source, homolytically cleaves a molecule of H_2O_2, forming a copper(II)-hydroxyl and a hydroxyl radical. The hydroxyl radical abstracts a hydrogen atom from the copper(II)-hydroxyl, to release water and form a copper(II)-oxyl (Figure 1.15, reaction 2). As proposed for the oxidative mechanism, the highly reactive copper(II)-oxyl is able to abstract a hydrogen atom from the C1/C4 position of the substrate, forming a copper(II)-hydroxyl and substrate radical (Figure 1.15, reaction 3). Hydroxyl rebounding from the copper ion to the substrate cleaves the glycosidic bond (Figure 1.15, reaction 4) (Bissaro et al., 2020b; Wang, B. et al., 2018). The Cu(I) state is regenerated following substrate cleavage, so the reaction with hydrogen peroxide, unlike the reaction with oxygen, can perform multiple turnovers without requiring further delivery of enzymes to the active site, providing that the Cu(I) state is maintained (Bissaro, B. et al., 2018).

It is clear from these experiments that, at low concentrations, hydrogen peroxide can provide rate enhancements and act as a convincing co-substrate to LPMOs. As a co-substrate, H_2O_2 was shown to be highly advantageous as it limited the need for additional external electron donors. However, at higher concentrations, enzyme inactivity was observed, this activity was shown to be the result of cumulative oxidative modifications to the LPMO, which were primarily detected on the active site histidines and neighbouring residues (Hangasky et al., 2018; Bissaro et al., 2017). It is clear that at high concentrations, H_2O_2 is vastly damaging to LPMOs, feeding H_2O_2 into reactions with LPMOs and substrate, as opposed to adding the co-substrate all in one go, has been shown to provide rate enhancements alongside preserving enzyme stability (Muller, G. et al., 2018). In enzyme cocktails, H_2O_2 can be fed in at a rate that is stoichiometric with product formation, minimising enzyme damage and extending enzyme lifetimes. It appears that, when using LPMOs in enzyme cocktails, there is a trade-off between high catalytic rates, achieved by using H_2O_2, and preserving enzyme lifetimes, which are less affected when oxygen is used as the co-substrate (Muller, G. et al., 2018). However, it is important to note, that the tolerance of cellulases to these concentrations of H_2O_2 has not been measured, in order for this to be effective in commercial enzyme cocktails, the boosting effect of H_2O_2 must outweigh any drawbacks that it may cause. Whether H_2O_2 is the true co-substrate to LPMOs or is just a reaction shunt *in vitro* is still debated, the contributions of these different mechanisms to observed LPMO activity *in vivo* is still largely unknown and will likely be the topic of much discussion for years to come.

1.10 LPMOs require delivery of electrons to the active site

As discussed above, a number of mechanisms have been proposed for LPMO action. However, regardless of the true mechanism of LPMOs, there is still a requirement for an electron source, even a sub-stoichiometric one in the case of H_2O_2 being used as a co-substrate. LPMOs acquire electrons from an external electron source to activate the cleavage reaction. Although this has been known since 2010 (Vaaje-Kolstad et al., 2010), the mechanism of electron transfer remains relatively uncharacterised (Hemsworth et al., 2015). Conventionally in enzyme assays, LPMOs are powered by small molecule electron donors, such as ascorbate, gallic acid or cysteine (Vaaje-Kolstad et al., 2010; Sabbadin et al., 2018; Lo Leggio et al., 2015; Stepnov et al., 2021). This activation by small molecules can provide high initial rates of enzyme turnover but often results in enzyme inactivation (Petrovic et al., 2019). Several other systems for LPMO activation have been explored and a number of enzymes have been implicated in this area.

1.10.1 Cellobiose dehydrogenase as an LPMO activator

Cellobiose dehydrogenase (CDH) is the best characterised enzymatic electron donor to LPMOs. It was first purified from the white-rot fungus *Phanerochaete chrysosporium* in 1993 (Bao et al., 1993), long before the discovery of LPMOs. CDH was shown to oxidise a range of cellobiose-like substrates to their corresponding lactones, using the reducing power of the small molecule cofactor, FAD (Bao et al., 1993; Zamocky et al., 2006). Prior to the discovery of LPMOs, the physiological role of CDH was unclear, it was thought that CDH may drive unspecific degradation of cellulose through the formation of hydrogen peroxide or hydroxyl radicals (Hyde and Wood, 1997; Kremer and Wood, 1992). Following the classification of LPMOs, CDH was also shown to drive their enzymatic turnover on crystalline polysaccharides in place of small molecule reducing agents (Phillips et al., 2011; Langston et al., 2011; Kittl et al., 2012; Sygmund et al., 2012). Deletion of CDH in fungal strains resulted in a significant reduction of cellulase activity, demonstrating its importance in biomass breakdown (Phillips et al., 2011), and direct electron transfer between the cytochrome domain of CDH and LPMOs was measured by monitoring cytochrome oxidation in the presence of a fungal LPMO from the same species (Sygmund et al., 2012). Subsequent studies were used to show that fungal CDHs can activate LPMOs irrespective of family and species. Fungal CDHs have even been shown to activate LPMOs from bacteria (Vu et al., 2014b; Loose et al., 2016). Re-evaluation of the function of CDH as an LPMO activator is supported by regular co-occurrence of CDH and LPMOs in fungal genomes (Phillips et al., 2011; Berrin et al., 2017).

CDH is composed of two domains: an FAD-binding dehydrogenase domain and a haem-binding cytochrome domain, which are connected by a flexible linker (Bao et al., 1993; Tan et al., 2015). At the dehydrogenase domain, CDH catalyses the conversion of cellobiose to cellobiono-1,5-lactone, reducing FAD to $FADH_2$ in the process (Higham et al., 1994). Large scale domain motions have been proposed to facilitate intraprotein electron transfer. The crystal structure of two CDHs from *Myriococcum thermophlum* and *N. crassa* (Figure 1.16) show the closed and open states of CDH, respectively (Tan et al., 2015). These structures demonstrate the large domain motions that are proposed for electron transfer through CDH. In the closed conformation, the cytochrome domain docks to the dehydrogenase domain, positioning the haem-*b* molecule in the cytochrome domain 9 Å from the FADH cofactor in the dehydrogenase domain. These distances are close enough to allow efficient electron transfer from $FADH_2$ to the haem molecule through a shielded electron transfer pathway (Tan et al., 2015). Large scale domain motions have been proposed, to allow the cytochrome to reach away from the dehydrogenase domain and catalyse interprotein electron transfer, facilitated by the flexible linker (Breslmayr et al., 2020; Tan et al., 2015).

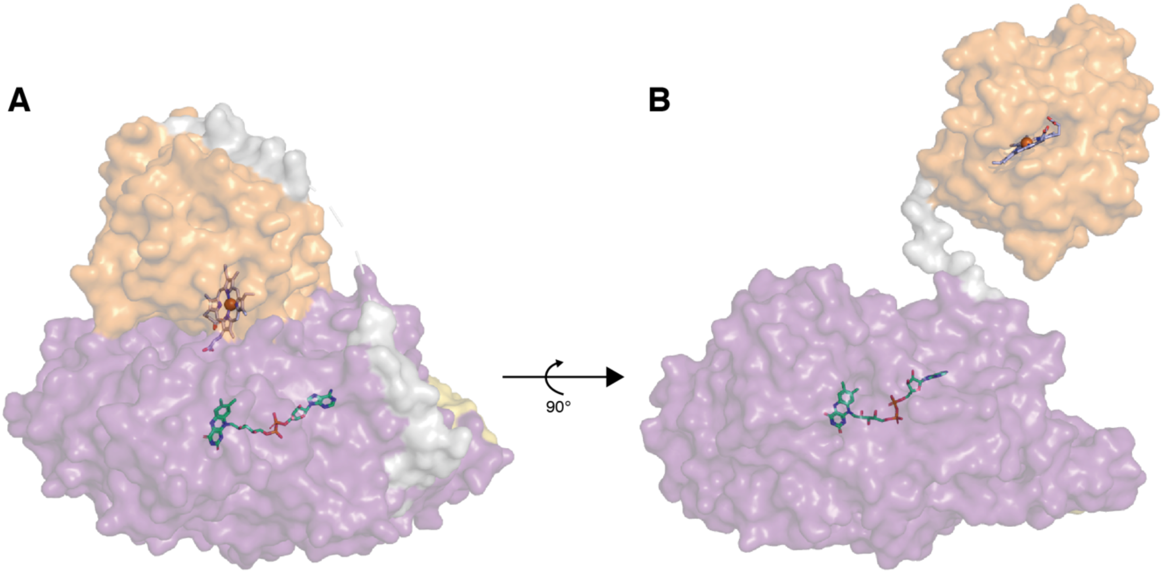

Figure 1.16: CDH undergoes large conformal changes from the closed to open states. (A) *The crystal structure of MtCDH shows the closed conformation (PDB ref 4QI6).* ***(B)*** *NcCDH in the open conformation (PDB ref 4QI7). Protein surfaces are shown, with the dehydrogenase domain in purple, cytochrome domain in orange, CBM in yellow and linker in grey. The haem and FAD molecules are shown as sticks in white and green carbons respectively, with other elements coloured according to atom type.*

Mutagenesis studies on a CDH from *Crassicarpon hotsonii* demonstrated the importance of a conserved tyrosine in the cytochrome domain, Tyr99, for intra- and inter-domain electron transfer. Mutants lacking the conserved tyrosine showed decreased electron intra-domain transfer, and its deletion resulted in a four-fold reduction in electron transfer to an LPMO from *N. crassa* (Breslmayr et al., 2020). Tyr99 is suggested to mediate hydrogen bonding to stabilise the closed conformation, and additionally form polar contacts with the haem-*b* propionate group to correctly orient the haem in interactions with the LPMO (Breslmayr et al., 2020). Domain swapping experiments with chimeric CDHs have also demonstrated the importance of complementarity at the interdomain interface to stabilise the closed conformation. Chimeric CDHs favoured the open state, due to less complementary interfaces, and demonstrated increased interprotein electron transfer rates (Felice et al., 2021).

Interestingly, a recent study using an engineered version of CDH showed enhanced activation of LPMOs (Kracher et al., 2020). In this study, CDH from *C. hotsonii* was engineered to produce more hydrogen peroxide. A double mutant of the enzyme was shown to be 30-times more efficient at driving the *S. marcescens* AA10A than the wild type ChCDH. The engineered CDH showed comparable electron transfer rates to the wild type, suggesting that the increased activity was solely due to its amplified hydrogen peroxide production. Although this enzyme showed increased LPMO activation, as is expected in systems with high concentrations of hydrogen peroxide, there was also significant LPMO inactivation (Kracher et al., 2020).

The characterisation of CDH as a natural redox partner to fungal LPMOs is an important finding to help underpin the mechanisms of LPMOs *in vivo*. However, genes encoding LPMOs are present in in 92 % of fungal genomes, whereas CDH-encoding genes are only present 58 % of the time (Berrin et al., 2017), and in addition to this, there is no bacterial homologue of CDH. Consequently, there may be additional, undiscovered redox partners to LPMOs.

1.10.2 Other proteins have been shown to activate LPMOs

In addition to CDH, a number of other fungal proteins have been shown to activate LPMOs. Fungal flavoenzymes from the AA3 family were suggested to act as LPMO activators due to their occurrence in secretomes of filamentous fungi that had been grown on lignocellulosic biomass (Levasseur et al., 2014). Members of the AA3 family were subsequently shown to activate LPMOs to liberate soluble products from crystalline polysaccharide substrates (Garajova et al., 2016). AA3 enzymes were also shown to activate LPMO turnover in the presence of plant derived phenols and quinones (Kracher et al., 2016). From these results, it was hypothesised that AA3 enzymes could use mediators, in the form of phenols and quinones produced during polysaccharide breakdown, to activate LPMOs (Kracher et al., 2016; Garajova et al., 2016).

Members of the AA12 class of enzymes have also been implicated in LPMO activation. A pyrroloquinone-quinone (PQQ) dependent pyranose dehydrogenase (PDH) from *Coprinopsis cinerea* has been shown to activate LPMOs (Varnai et al., 2018). The CcPDH enzyme comprises an N-terminal cytochrome domain, an AA12 dehydrogenase domain and a C-terminal CBM1 domain (Takeda et al., 2015). CcPDH catalyses the oxidation of monosaccharides at its PQQ binding, dehydrogenase domain, it is suggested to act in a similar manner to CDH, and transfer electrons from the dehydrogenase domain to the cytochrome domain for interprotein electron transfer (Takeda et al., 2015). CcPDH was shown to activate two fungal LPMOs, by the liberation of soluble products from crystalline substrates, addition of excess free PQQ boosted the activity of LPMOs (Varnai et al., 2018), suggesting that PQQ can also act as a redox mediator between CcPDH and LPMOs.

Identification of additional proteins from fungal genomes that act as LPMO activators has built a more comprehensive picture of LPMO activation in fungal systems. The importance of redox mediators in these systems is interesting, and should definitely be considered due to the prevalence of pretreatment of polysaccharides in common biomass breakdown systems.

1.10.3 Lignin and small molecule redox partners

Lignin is a phenolic compound (see section 1.2.4) and has been shown to act as an electron source to LPMOs (Cannella et al., 2012; Dimarogona et al., 2012). Activation of LPMOs by lignin is extremely interesting, lignocellulosic substrates are often pre-treated to remove lignin, which could be unfavourable for LPMO action. Studies on hydrothermally pre-treated substrates showed that the liquid fraction contained enough lignin to drive LPMOs for extended times (Kont et al., 2019). Like reducing agents, these compounds will be depleted over time in LPMO reactions. However, as mentioned in section 1.10.2, plant derived phenols and quinones have sufficient redox potentials and have been shown to act as redox mediators between redox active enzymes and LPMOs (Kracher et al., 2016). Kracher *et al.* demonstrated that glucose oxidase, glucose dehydrogenase and pyruvate dehydrogenase were indeed all capable of reducing quinones derived from lignin, which have appropriate redox potentials to transfer electrons to LPMOs (Kracher et al., 2016). Additionally, aryl-alcohol quinone oxidoreductases and glucose dehydrogenases from *Pycnoporus cinnabarinus* have been shown to activate an LPMO from *Podospora anserina* using anisyl alcohol as a mediator (Garajova et al., 2016). These systems emphasise the ability of lignin and small molecules, which are likely to be present during carbohydrate breakdown, to act as mediators between redox active enzymes, to efficiently transfer electrons to LPMOs.

1.10.4 Unnatural LPMO activation systems

More recently, studies have shown that LPMO activity can be boosted using excited photosynthetic pigments (Cannella et al., 2016; Bissaro et al., 2020a). Thylakoid membranes and a water soluble derivative of chlorophyll, chlorophyllin, were used to boost activity of LPMOs in the presence of ascorbate or lignin. Using these methods, when activated by light, the activity of LPMOs to liberate soluble products from crystalline polysaccharides were boosted by up to 20-fold (Cannella et al., 2016). In this system, light was used to excite the pigment, which transferred an electron to activate the LPMO, the oxidised pigment was then regenerated using an external reductant, such as lignin or ascorbate (Cannella et al., 2016). Light-driven activation was able to occur in the absence of external reductants, however, optimal catalytic rates were observed in the presence of reducing agents (Cannella et al., 2016; Bissaro et al., 2020a). Insights from light-driven activation of LPMOs suggested that large amounts of superoxide were generated in this system. When superoxide dismutase, which converts superoxide to peroxide, was added, increased peroxide production was observed, indicating accumulation of superoxide, produced by the light-exposed photosynthetic pigments (Bissaro et al., 2020b). Superoxide was proposed to directly reduce LPMOs, priming them for further activation by peroxide. The light-activated LPMO showed a more tuneable system, with longer enzyme lifetimes than systems purely activated by ascorbate (Bissaro et al., 2020a), which could be useful in enzyme cocktails to prevent enzyme inactivation and prolong the lifetimes of cocktail components.

1.10.5 Possible electron paths through LPMOs

Mechanisms of electron transfer to LPMOs are of great importance for fully understanding and harnessing LPMO action. The flat substrate binding surface of LPMOs indicates that the active site is likely to be obscured when the enzymes are bound to cellulose, therefore, several studies have attempted to analyse how electron donors may interact with LPMOs. Recent molecular docking studies have suggested that CDH directly contacts the copper ion at the LPMO active site (Laurent et al., 2019). The majority of molecular docking solutions from this study showed the haem-*b* propionate group contacting the copper ion, with surface loops on the LPMO proposed to influence the orientation of the cytochrome domain of CDH (Laurent et al., 2019). These results corroborate findings from previous molecular docking experiments (Tan et al., 2015; Wang, Z. et al., 2021) and observations from NMR experiments (Courtade et al., 2016). Similar chemical shift perturbations were seen for NcAA9C when interacting with CDH and cellohexaose separately, suggesting that they were binding to the same site on the LPMO surface (Courtade et al., 2016). Although these studies suggest that CDH is directly contacting the copper ion, it is difficult to imagine how this interaction would facilitate transfer of multiple electrons to the copper without detachment of the enzyme from the substrate.

Reducing agent delivery to the active site also raises questions regarding the mechanism of activation. When substrate is bound, the active site is obscured. The conserved second sphere Glu/Gln residue is proposed to act as a gate to the active site, restricting access to a 1.6 Å wide tunnel, too small to allow access of reducing agents (Bissaro, Bastien et al., 2018). For efficient enzyme turnover, without requiring unnecessary detachment of LPMO from its substrate, internal pathways to transfer electrons to the active site have been suggested to pass through the core of LPMOs. Li *et al.* suggested two electron transfer pathways, that could be traced from the LPMO surface, through the core of the protein to the catalytic copper ion (Li et al., 2012). For path one, a number of aromatic residues spaced between 3.5 and 4.5 Å apart were identified as candidate electron transfer residues, whilst path two similarly consisted of aromatic residues, but these were slightly closer together at between 3 and 4 Å spacing (Figure 1.17). Significantly, both paths demonstrated some level of conservation, with path one conserved in all fungal cellulose active LPMO, and path two conserved more specifically in fungal C1/C4 cellulose active LPMOs. In both cases the paths were drawn between the active site of the LPMO and a region formed by a Pro-Gly-Pro motif on the enzyme surface, away from the active site, which was suggested as a potential CDH binding site, offering a convenient means of activating the LPMO while bound to a solid substrate (Li et al., 2012; Beeson et al., 2015). Molecular docking studies were investigated for an interaction at this site, although, as described above, the vast majority of solutions showed the haem molecule directly contacting the copper ion (Laurent et al., 2019). However, it is important to note that these studies were not investigated in the presence of substrates, which will likely block direct access of reductants to the copper ion.

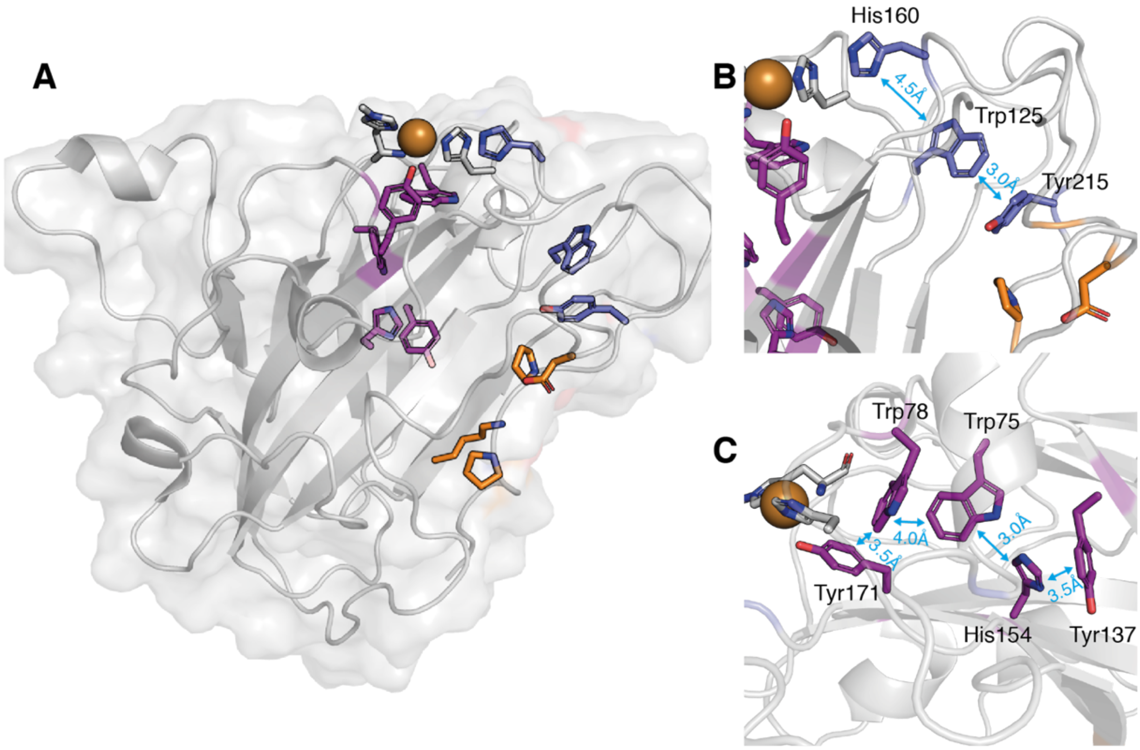

Figure 1.17: Proposed electron transfer paths through N. crassa PMO-3. (A) *N. crassa PMO-3 structure (PDB ref 4EIS) with histidine brace, grey sticks, coordinating the copper ion shown as a brown sphere. The proposed CDH binding site is shown in orange sticks, and path one and path two are shown as blue and purple sticks respectively.* ***(B)*** *Path one links the proposed CDH binding site to the copper site and is conserved in all fungal cellulose active LPMOs.* ***(C)*** *Path two in conserved in C1/C4 cellulose active fungal LPMOs.*

Although docking studies and other approaches have thus far not confirmed the use of electron transfer pathways through the LPMO core, a recent study has provided the first experimental evidence that such a pathway may exist in LPMOs. Paradisi *et al.* observed the development of an unusual, purple coloured, species in LsAA9A that formed when the enzyme was exposed to H_2O_2 at high pH, which was attributed to the formation of a Cu(II)-tyrosyl complex (Paradisi et al., 2019). A putative hole-hopping pathway through the protein was proposed, starting at the active site tyrosine. This pathway was suggested to channel electrons away from the copper ion in the absence of substrate, supported by oxidative modifications found on aromatic residues outside the active site, which made up this proposed pathway. This proposed 'escape-route' for electrons, starting at the active site tyrosine, to prevent LPMO activation in the absence of substrates, could also act as an electron pathway to the active site, if it were reversed

(Paradisi et al., 2019). So far, this study provides the only experimental evidence that internal electron transfer pathways though LPMOs exist.

Most investigations into electron paths through LPMOs have been performed in fungal LPMOs, where there are well defined protein partners. However, recently, an AA10 from *T. turnerae* was shown to have a second non-catalytic copper site, located 14.4 Å away from the active site copper ion. The second copper site was shown to be surface exposed and an internal electron transfer path between the two copper sites was proposed (Fowler et al., 2019). In TtAA10, the second copper could act as a site for a protein partner to bind. However, this additional copper has not been detected in any other characterised LPMOs, so more investigation is required to substantiate the presence of an electron path between the two copper ions in TtAA10. It is thought that bacterial LPMOs will contain similar intraprotein electron transfer paths to those proposed in fungi, however, investigation into redox partners to bacterial LPMOs will greatly assist these analyses.

1.11 Searching for LPMO redox partners in bacteria

As mentioned above, there is no bacterial homologue for CDH, which poses the question: how do LPMOs obtain electrons in bacterial systems? Although bacterial enzymes could obtain their electrons from lignin or organic compounds, there may be similar systems analogous to CDH that may be undiscovered in bacteria. Uncovering the identity and nature of such systems in bacteria will provide fundamental information on how LPMOs are harnessed in biology, whilst also providing further information on how they can be optimally used as enzymatic tools.

Two proteins from *Cellvibrio japonicus* have been proposed as redox partners to bacterial LPMOs (Gardner et al., 2014). Cbp2D and Cbp2E are multidomain proteins (Figure 1.18), both including an N-terminal CBM2 domain. *In vivo* studies have shown the importance of these proteins for bacterial growth on crystalline cellulose, deleting Cbp2D or Cbp2E reduced the ability of *C. japonicus* to grow on crystalline cellulose by 60 % (Gardner et al., 2014). Cbp2D and Cbp2E have since been found in the secretome of *C. japonicus*, where they were significantly upregulated during growth on crystalline chitin, further supporting a role for these proteins in polysaccharide degradation (Tuveng et al., 2016).

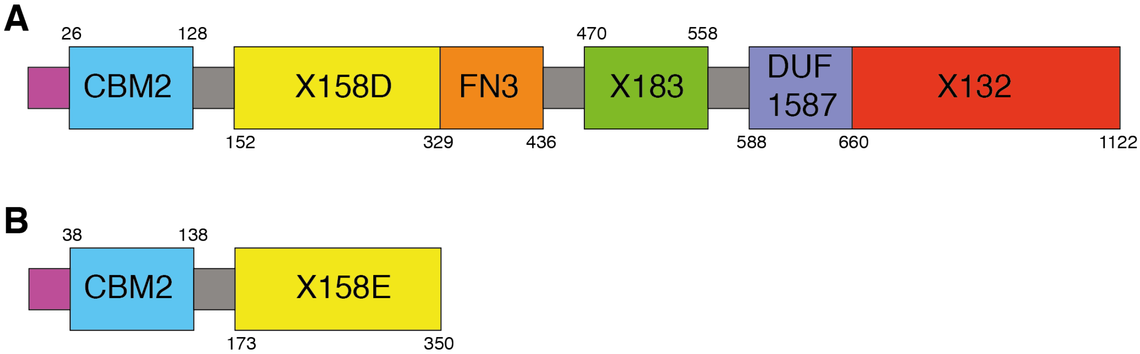

Figure 1.18: Domain organisation of C. japonicus Cbp2D and Cbp2E proteins. (A) *Cbp2D and* ***(B)*** *Cbp2E domains are annotated within the figure, with periplasmic signal sequences in pink and linkers in grey, putative redox domains are X158 domains, yellow, the X183 domain, green, and the X132 domain, red. The FN3 domain represents a fibronectin domain and DUF1587 is a domain of unknown function.*

The domain architecture of these proteins further supports their proposed redox active roles. Cbp2D and Cbp2E are composed of multiple "X-domains", domains of unknown function that, in this case, may act in redox processes (Figure 1.18). Cbp2D is composed of an X158, X183 and X132 domain, whilst Cbp2E contains an X158 domain, with both proteins containing a CBM2 domain at their N-termini with all the domains predicted to be connected through flexible linkers. Homologues of the X158 have been detected in other saprophytic bacteria, often attached to a CBM2. An X158 domain from *Saccharophagus degradans*, SdX158, has been recombinantly expressed and structurally characterised, although its true function remains unclear (Vincent et al., 2010). SdX158 has a lipocalin-like β-barrel fold (Figure 1.19) and has been seen in complex with two different cofactors: octaprenyl pyrophosphate and ubiquinone-8, coordinated at the centre of the β-barrel (Vincent et al., 2010). The coordination of the ubiquinone molecule (Figure 1.19) suggests that the X158 domain may be involved in redox chemistry, as ubiquinone is able to accept two electrons to act as a reductant, and is a key component of many electron transfer chains (Richter and Ludwig, 2009). The SdX158 domain shares 36 % and 46 % sequence identity to CjX158D, from Cbp2D, and CjX158E, from Cbp2E, respectively. Interestingly, CjX158D and CjX158E are only 42 % similar to one another, with the CjX158E protein more alike to the SdX158 domain than it is to the other CjX158 homologue.

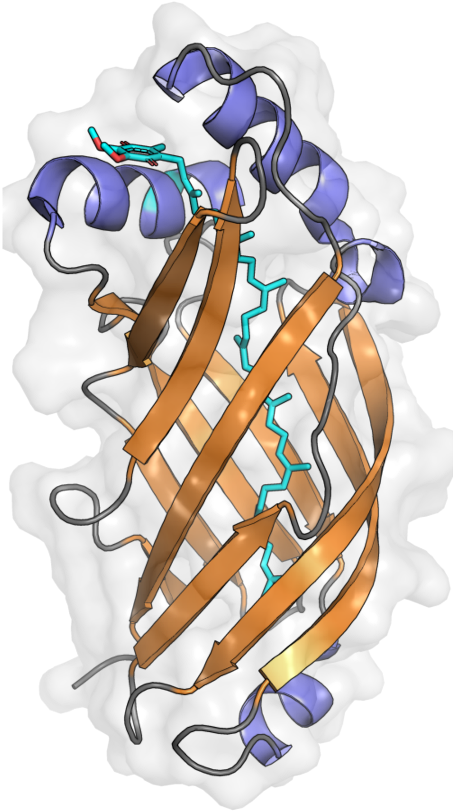

Figure 1.19: Structure of an X158 domain from Saccharophagus degradans with ubiquinone-8. *Structure of SdX158 (PDB ref 2X34) shown as cartoon, with ubiquinone-8 shown as cyan sticks.*

The CjX183 and CjX132 domains, found in Cbp2D, are predicted cytochrome domains, as they both contain one copy of the characteristic haem-*c* binding motif -CXXCH, further indicating a role for these proteins in redox processes. Gardner *et al.* attempted to recombinantly express and purify Cbp2D from *Escherichia coli*, which was not achieved successfully as Cbp2D was retained in the insoluble fraction during purification. However, they report the presence of pink coloured cells, which is a signature of haem containing proteins (Gardner et al., 2014). Cytochrome containing proteins are key components of electron transfer chains in Nature (Richter and Ludwig, 2009), therefore the presence of two proposed cytochrome domains in Cbp2D supports its role as a redox active protein.

1.12 Aims of the thesis

The main aims of this thesis are to investigate the previously uncharacterised Cbp2D and Cbp2E proteins from *C. japonicus*. Better structural and biochemical understanding of these proteins will ultimately help to determine their function within *C. japonicus* and may provide information on how bacterial LPMOs are activated *in vivo*. These efforts will be divided across four results chapters with their specific aims outlined below.

1.12.1 To structurally characterise an LPMO from *C. japonicus*

In the first results chapter, this thesis will describe work conducted to characterise an LPMO from *C. japonicus*, CjAA10B, by removing the C-terminal CBM domain in order to allow structural determination by X-ray crystallography. Chapter 3 details the expression, purification, crystallisation and structure determination of CjAA10BΔCBM, which allowed structural characterisation of the catalytic domain of and investigation into possible redox paths through the protein, prior to experiments with redox partners performed in subsequent chapters.

1.12.2 To characterise the CjX158E domain from Cbp2E

In the second results chapter, efforts were focussed on characterising the CjX158E domain from Cbp2E. Cloning of the CjX158E domain into a suitable vector, followed by protein expression, purification, crystallisation and structure determination will be described a steps taken to structurally characterise CjX158E. These studies were complemented by biochemical experiments to investigate the presence of a cofactor in CjX158E. Structural and biochemical experiments were performed to investigate the function of the CjX158E domain to determine if it had the capacity to act as a redox partner to LPMOs.

1.12.3 To Characterise the CjX183 domain from Cbp2D

In the third results chapter, the CjX183 domain from Cbp2D will be discussed. The CjX183 domain was cloned, expressed, purified and crystallised, and the structure determined to investigate the function of CjX183. Biochemical studies of CjX183 were used to determine its ability to accept and donate electrons and assign a redox potential for the CjX183 domain. This chapter will supplement structural data with biochemical studies, to characterise the CjX183 domain to determine if it had the properties to act as a redox partner to LPMOs.

1.12.4 To determine if CjX183 can act as a redox partner to bacterial LPMOs

In the fourth, and final, results chapter, the ability of CjX183 to donate electrons to and drive the activity of bacterial LPMOs was assessed. This was performed by a number of methods: by studying the oxidation of CjX183 in the presence of LPMOs, and assessing the activity of LPMOs when activated by CjX183 in the absence and presence of crystalline substrates. This chapter also aims to compare the activation of LPMOs by CjX183 and small molecule reducing agents, to build a cohesive picture of how this domain could activate bacterial LPMOs *in vivo*.

Chapter 2

Materials and Methods

2.1 Materials

2.1.1 Chemicals and biological reagents

Unless otherwise stated, all reagents were obtained from Sigma-Aldrich or Fisher Scientific Ltd. Q5 High-Fidelity DNA Polymerase, 1 kb DNA ladder, 6x gel loading dye, Dpn1, KLD Enzyme Mix, Blue Prestained Protein Ladder and anti-mouse IgG horseradish peroxidase conjugate were all obtained from New England Biolabs (NEB). dNTPs and SYBRsafe DNA gel stain were purchased from Invitrogen. GoTaq DNA Polymerase was purchased from Promega. Tryptone and yeast extract, used in growth media, and antibiotics used in this research were purchased from Melford Laboratories Ltd. 3-Morpholinopropane-1-sulphonic acid (MOPS) minimal media components were purchased from Teknova. Isopropyl-β-thiogalactopyranoside (IPTG) was purchased from Generon. Hen egg white lysosome was purchased from Alfa Aesar. Bugbuster was purchased from Merck Millipore. Amplex Red reagent was purchased from Thermo Fisher Scientific. ^{13}C cellobiose was purchased from Omicron Biochemicals.

2.1.2 Kits and chromatography reagents

Miniprep kits were purchased from New England Biolabs and PCR purification kits were purchased from QIAGEN. Vivaspin centrifugal concentrators were purchased from Sartorius. All chromatography columns used for protein purification, His SpinTrap columns and PD10 columns, were purchased from GE Healthcare. Crystallisation conditions were purchased from QIAGEN.

2.1.3 Growth media and antibiotics

Unless stated otherwise, all growth media was made by dissolving all ingredients in deionised water followed by autoclaving at 121 °C, 15 psi for 20 minutes. The composition of growth media used in this thesis can be found in Table 2.1

Media	*Ingredients*	*Preparation notes*
2TY	16 g/L Tryptone 10 g/L Yeast extract 5 g/L Sodium chloride	As above
M9 Minimal Media	**6 g/L Na_2HPO_4** **3 g/L KH_2PO_4** **0.5 g/L Sodium chloride** **1 g/L NH_4Cl** 1 mM/L $MgSO_4 \cdot 7H_2O$ 0.2 %(w/v)/L glucose 0.1 mM/L $CaCl_2$ 10 mL/L BME Vitamins (Sigma-Aldrich B891)	M9 salts, in bold, were added to dH_2O and autoclaved, stock solutions were made and filter sterilised. Prior to inoculation, each litre of M9 was supplemented with the remaining solutions.
MOPS Minimal Media	100 mL/L 10x MOPS mixture 10 mL/L 0.132 M K_2HPO_4 100 mL/L ACGU 200 mL/L 5x supplement EZ 10 mL/L 20 % Glucose 580 mL/L sterile H_2O	Sterile solutions obtained from Teknova Solutions combined aseptically in a sterile container.
Agar Plates	Chosen media 15 g/L agar	Agar was added to chosen media and autoclaved. The solution was allowed to cool before addition of antibiotic(s) and pouring into petri dishes.

Table 2.1: Growth media compositions and preparation notes

Antibiotic stocks were prepared as described in Table 2.2. Antibiotics were weighed out, dissolved, filter sterilised using a 0.22 μm filter and stored at -20 °C

Antibiotic	*Stock solution*	*Working concentration*
Kanamycin (Kan)	50 mg/mL in dH$_2$O	50 μg/mL
Ampicillin (Amp)	100 mg/mL in dH$_2$O	100 μg/mL
Chloramphenicol (Cam)	35 mg/mL in ethanol	35 μg/mL

Table 2.2: Antibiotic solution preparation

2.1.4 Bacterial Strains

E. coli strains used in this thesis are outlined in Table 2.3.

Strain (supplier)	*Purpose*	*Genotype*
5-alpha (New England Biolabs)	DNA manipulation	*fhuA2 Δ(argF-lacZ)U169 phoA glnV44 ϕ80 Δ(lacZ)M15 gyrA96 recA1 relA1 endA1 thi-1 hsdR17*
One Shot BL21(DE3) (Invitrogen)	Protein expression	F^- *ompT hsdS*$_B$(r_B^- m_8^-) *gal dcm* (DE3)
One Shot BL21(DE3) (Invitrogen)*	Protein expression	F^- *ompT hsdS*$_B$(r_B^- m_8^-) *gal dcm rne131* (DE3)
BL21(DE3)-pEC86 (Homemade)	Haem containing protein expression	BL21(DE3) plus *ccm* operon, Cam^R

Table 2.3: E. coli strains used in this research

2.1.5 Oligonucleotides, genes and vectors

Oligonucleotide primers used for this research were obtained from Integrated DNA Technologies. Plasmids obtained before starting this research are shown in Table 2.4.

Plasmid	*Source*	*Features*
pET22-CjAA10B	Gardner *et al.* (Gardner et al., 2014)	Amp^r, cjAA10B gene
pET22-CfAA10	Crouch *et al.* (Crouch et al., 2016)	Amp^r, cfAA10 gene
pET22-cbp2D	Gardner *et al.* (Gardner et al., 2014)	Amp^r, cbp2D gene
pET22-cbp2E	Gardner *et al.* (Gardner et al., 2014)	Amp^r, cbp2E gene
pSF1477	Frey *et al.* (Frey and Gorlich, 2014)	Kan^r, BdSUMO tag
pCW-LIC	A gift from Cheryl Arrowsmith, Addgene plasmid 26098	Amp^r, N-terminal pelB leader
pEC86	A gift from Prof. Lars Jeuken, University of Leeds. Designed by Arslan *et al*. (Arslan et al., 1998)	Cam^r, *ccm* genes for haem maturation

Table 2.4: Plasmids provided at the start of this research

2.2 DNA methods

2.2.1 Primer design

In order to amplify out regions of interest from the pET22-cbp2D and pET22-cbp2E plasmids, primers were designed for polymerase incomplete primer extension (PIPE) cloning (Klock and Lesley, 2009). These primers contained a roughly 15 nucleotide region complementary to the start or end of the region of interest. The primers were designed to include a roughly 10 nucleotide 5’ overhang, complementary to the target vector. Additional primers were designed to linearise target vectors, to create blunt ended linear vectors, where the blunt ends are complementary to the 5’ overhangs on the primers designed for insert amplification.

Primers for deletion of the CBM domain in the pET22-CjAA10B plasmid were complementary to the regions directly flanking the CBM domain. Primers were designed to read outwardly away from the CBM domain in either direction to create a blunt ended linear PCR product of pET22-CjAA10B not including the nucleotide sequence for the CBM domain.

Designed primers, and primers used for sequencing, are shown in Table 2.5.

Table 2.5: Primers used in this thesis. *For primers used for PIPE cloning capital letters represent the oligonucleotide sequence complimentary to the template DNA, lowercase letters represent the region complimentary to the target vector.*

Function	*Primer Name*	*Primer sequence (5’ to 3’)*	*T_m (°C)*
Mutagenesis of CBM domain	CjAA10BΔCBM-F	CAGATTCACCACCACCACCACCACTGA	71
	CjAA10BΔCBM-R	GTGGTGAATCTGCACGTCAATACAA	64
Linearisarion of pSF1477	pSF-F	TAAGGATCTCATCACCATCACCATCA	65
	pSF-BdSUMO-R	GCCACCAGTCTGGTGCAGCA	65
Amplification of CjX158E	BdSUMO- CjX158E-F	tgctgcaccagactggGTGGCGTGGCGAATAACATCAGCTGGG	73
	CjX158-pSF-R	tgatggtgatgagatccttaGCGCGCGTTAAACACAAGCGC	65
Linearisation of pCW-LIC	pCW-F	CACCACCACCACCACCACTGA	65
	pelB-pCW-R	GGCCATCGCCGGCTGGG	65
Amplification of CjX183	pelB-CjX183-F	ctgcccagccggcgatggccGGTTATCTGGTTGGCGATGCAAC	65
	CjX183-pCW-R	cagtggtggtggtggtggtgCCAGGTGCGGATAAAGGCTTCAAT	65
T7 sequencing primers	T7-F	TAATACGACTCACTATAGGG	55
	T7-R	GCTAGTTATTGCTCAGCGG	55
pSF1477 sequencing primers	PQE-F	CGGATAACAATTTCACACAG	55
	PQE-R	GTTCTGAGGTCATTACTGG	55
pCW sequencing primers	pCW-seq-F	ACATCGTATAACGTTACTGG	55
	pCW-seq-R	AGGGAAGAAAGCGAAAGG	55

2.2.2 Polymerase chain reaction

Polymerase chain reaction (PCR) was performed using Q5 DNA Polymerase (NEB) according to manufacturer's instructions. Annealing temperatures for primer pairs used are shown in Table 2.5.

2.2.3 Agarose gel electrophoresis

1 % (w/v) agarose gels were made by combining TAE buffer (40 mM Tris-acetate, 1 mM ethylenediaminetetraacetic acid (EDTA), pH 8) with an appropriate amount of agarose. SYBR safe DNA gel stain was added to molten agarose at 0.001 % (v/v). DNA samples were prepared by the addition of 6x gel loading dye and a 1 kb DNA ladder (NEB) was used to estimate the size of DNA bands. Gels were run at 100 V for 30 minutes in TAE buffer. Resolved DNA was visualised with blue light.

2.2.4 Dpn1 digestion and PCR purification

Template DNA was digested using Dpn1 (NEB) according to the manufacturer's instructions. PCR productions were purified using a QIAquick PCR purification kit (QIAGEN), as per the manufacturer's instructions. Purified DNA was quantified using a Nanodrop Spectrophotometer (ThermoFisher Scientific).

2.2.5 PIPE cloning plasmid assembly

Plasmids were assembled using PIPE cloning (Klock and Lesley, 2009). Purified inserts were mixed with linear vectors in 2:1 concentration ratios then heated at 50 °C for 30 seconds. 1 μL of 25 mM EDTA was added to the ligated vector and left on ice for 5 minutes before transformation into 5-alpha cells.

2.2.6 KLD assembly for site directed mutagenesis

Following site directed mutagenesis of the CBM domain in CjAA10B, the resulted blunt ended PCR product was circularised using the KLD Enzyme Mix (NEB), as per the manufacturer's instructions. Circular plasmids were transformed into NEB 5-alpha cells.

2.2.7 Transformation

Transformations were performed into competent cells as per the manufacturer's instructions. Transformants were plated onto 2TY-agar plates, with the appropriate antibiotic selection marker, and grown at 37 °C for 16 hours.

2.2.8 Colony PCR

Successful transformants from PIPE cloning were picked, using a sterile tip, and checked using colony PCR. Colony PCR was carried out using sequencing primers (Table 2.5) and GoTaq DNA Polymerase (Promega), using the protocol supplied by the manufacturer, where template DNA was replaced by a picked colony.

2.2.9 Plasmid purification and DNA quantification

Plasmid DNA was purified using the Monarch Plasmid Miniprep Kit (NEB) according to the manufacturer's guidelines. DNA concentration was determined using a NanoDrop Spectrophotometer (ThermoFisher Scientific).

2.2.10 DNA sequencing

DNA sequencing was performed by Genewiz. Sequencing primers are listed in Table 2.5. 15 μL samples of minimum 50 ng/μL DNA concentration were provided for sequencing. Results were analysed using the Ape Plasmid Editor Software.

2.3 Protein methods

2.3.1 Recombinant protein expression

2.3.1.1 General notes on culture growth from a single colony

A single colony of *E. coli* cells, transformed with the plasmid of interest, was picked, using a sterile tip, and used to inoculate 5 mL of 2 TY media containing the required antibiotic(s). Cultures were grown at 37 °C shaking at 200 rpm for 6-8 hours, after which 500 μL was used to inoculate a 50 mL overnight culture. After 16 hours, 10 mL of culture was used to inoculate 1 L of 2 TY in a 2.5 L flask. Protein expression conditions varied for different proteins and are outlined below.

2.3.1.2 CjAA10B, CjAA10BΔCBM and CfAA10 protein expression

LPMOs were expressed in *E. coli* BL21(DE3) cells transformed with the pET22-CjAA10B, pET22-CjAA10BΔ-CBM or pET22-CfAA10 plasmid. Cultures were grown in 1 L of 2 TY supplemented with ampicillin in non-baffled 2.5 L flasks for 24 hours at 25 °C shaking at 180 rpm, after 24 hours the temperature was dropped to 16 °C and the shaking speed to 150 rpm and cells were pre-cooled then induced with 1 mM IPTG. Cultures were grown for a further 24 hours before harvesting by centrifugation at 6000 g, and the cell pellets frozen at -80 °C until needed.

2.3.1.3 CjX158E protein expression

BdSUMO-CjX158E was expressed in *E. coli* BL21*(DE3) cells transformed with the pSF1477-CjX158E plasmid. Cells were grown in 1 L of 2 TY (or M9 minimal media) supplemented with kanamycin in 2.5 L baffled flasks at 37 °C and 200 rpm until an OD_{600} of 0.6 was reached. Cultures were then cooled to 20 °C and shaking slowed to 180 rpm before induction with a final concentration of 0.1 mM IPTG. Induced cultures were grown for 16 hours before harvesting at 6000 g and the pellets frozen at -80 °C.

2.3.1.4 CjX183 protein expression

CjX183 was expressed in *E. col* BL21(DE3)-pEC86 cells transformed with the pCW-CjX183 plasmid. Cells were grown in 1 L 2 TY supplemented with ampicillin and chloramphenicol in 2.5 L baffled flasks at 37 °C and 200 rpm until an OD_{600} of 0.6 was reached. Cultures were then cooled to 20 °C and 180 rpm before induction with a final concentration of 0.4 mM IPTG. Induced cultures were grown for 16 hours before harvesting at 6000 g and the pellets frozen at -80 °C.

2.3.2 Protein purification

2.3.2.1 Purification buffer compositions

Protein purification was carried out as described in subsequent sections using buffers outlined in Table 2.6.

Buffer	*Composition*
Sodium phosphate lysis buffer	20 mM Sodium phosphate pH 7, 150 mM sodium chloride, 20 % sucrose
Sodium phosphate buffer A	20 mM Sodium phosphate pH 7, 150 mM sodium chloride, 30 mM imidazole
Sodium phosphate buffer B	20 mM Sodium phosphate pH 7, 150 mM sodium chloride, 300 mM imidazole
Anion exchange buffer A	50 mM Tris-HCl pH 8, 50 mM sodium chloride
Anion exchange buffer B	50 mM Tris-HCl pH 8, 2 M sodium chloride
Copper binding buffer	50 mM Sodium phosphate pH 6, 150 mM sodium chloride
Sodium phosphate SEC buffer	20 mM Sodium phosphate pH 7, 150 mM sodium chloride
Tris lysis buffer	50 mM Tris-HCl pH 8, 200 mM sodium chloride, 20 % sucrose
Tris buffer A	50 mM Tris-HCl pH 8, 200 mM sodium chloride, 30 mM imidazole
Tris buffer B	50 mM Tris-HCl pH 8, 200 mM sodium chloride, 300 mM imidazole
SUMO-tag cleavage buffer	50 mM Tris-HCl pH 8, 200 mM sodium chloride, 5 mM magnesium chloride, 5 mM dithiothreitol
Tris SEC buffer	50 mM Tris-HCl pH 8, 200 mM sodium chloride

Table 2.6: Buffer composition table for purification buffers.

2.3.2.2 Purification of LPMOs

LPMOs were purified from the periplasm of harvested cells by resuspension in 3 volumes of sodium phosphate lysis buffer on ice for 45 minutes. 40 μL of 10 mg/mL hen egg white lysozyme were added per gram of cell pellet during resuspension. After 45 minutes, 60 μL of 1 M $MgSO_4$ were added per gram of cell pellet, and incubated for 15 minutes. Cell debris were pelleted by centrifugation at 75000 g for 10 minutes at 4 °C. The supernatant was retained and the pellet was resuspended in 3 volumes of ice cold water and incubated on ice for a further hour. Cells were pelleted, as above, and the supernatants from both steps were pooled.

All subsequent protein purification steps were performed using an ÄKTA pure protein purification system (GE Healthcare). LPMO samples were initially purified by nickel affinity chromatography, the supernatant was loaded onto a 5 mL HisTrap FF column (GE Healthcare) that had been pre-equilibrated with sodium phosphate buffer A. Following sample loading, the column was washed with 5 volumes of sodium phosphate buffer A, before protein elution with a linear gradient of sodium phosphate buffer B over 10 column volumes. Protein concentration throughout purification was monitored at A_{280}, and LPMO presence was checked using sodium dodecyl sulphate polyacrylamide gel electrophoresis (SDS-PAGE) (method described in section 2.3.4). Protein containing fractions were concentrated (method described in section 2.3.7) in a 10 kDa molecular weight (MW) cut off concentrator (Sartorius) to a volume of 1 mL, then diluted to 20 mL in anion exchange buffer A. Diluted protein sample was loaded onto a 1 mL HiTrap Q HP anion exchange chromatography column (GE Healthcare) pre-equilibrated in anion exchange buffer A. Unbound protein was collected as it flowed through the column, the column was washed with 5 column volumes of anion exchange buffer B, and bound protein was eluted in a linear gradient of 1-25 % buffer B over 10 column volumes. The column was washed to remove any residually bound protein with 5 column volumes of buffer B. Protein presence was confirmed using SDS-PAGE, and the column flow through was concentrated to 1 mL then topped up to 20 mL with copper binding buffer. Protein concentration was determined (method described in section 2.3.6) and the protein was copper loaded using a 1:2 molar ratio of protein to $CuSO_4$. Copper loaded protein was concentrated to 1 mL and further purified by size exclusion chromatography (SEC) on a 16/600 Superdex S75 column (GE Healthcare) equilibrated with sodium phosphate SEC buffer. Fractions of purified LPMOs were checked using SDS-PAGE and concentrated to a volume of 500 μL, protein concentration was determined and protein was flash frozen in 20 μL aliquots in liquid N_2 and stored at -80 °C.

2.3.2.3 CjX158E purification

BdSUMO-CjX158E was purified from *E. coli* by resuspension in 5 volumes of Tris buffer A. Homogenised cells were lysed at 30 kpsi using a Cell Disruptor from Constant Cell Disruption Systems. Insoluble cell debris was pelleted at 75000 g for 20 minutes at 4°C. The supernatant was purified by nickel affinity chromatography with Tris buffer A and Tris buffer B as described in section 2.3.2.2. BdSUMO-CjX158E containing fractions were concentrated to 1 mL in a 10 kDa MW cut off concentrator to a volume of 1 mL. Protein concentration was determined and protein was diluted to 100 μM in SUMO-tag cleavage buffer. To cleave the SUMO-tag, BdSENP1 enzyme (provided by Dr Glyn Hemsworth) was added to a final concentration of 1 μM, and the reaction was incubated at 4 °C for 16 hours. Cleaved CjX158E was purified by nickel affinity chromatography, as described above, and column flow through was collected and retained. Protein presence was checked using SDS-PAGE, and the flow through was concentrated to 1 mL. CjX158E was further purified using size exclusion chromatography, as described in section 2.3.2.2, where the column was equilibrated in Tris SEC buffer. CjX158E was concentred to 500 μL, protein concentration was determined and protein was flash frozen in 20 μL aliquots in liquid N_2 and stored at -80 °C.

2.3.2.4 CjX183 purification

CjX183 cell pellets were resuspended in Tris lysis buffer and were lysed using periplasmic lysis, as described in section 2.3.2.2. Cell lysates were purified using nickel affinity chromatography in Tris buffer A and Tris buffer B, as described in section 2.3.2.2. Protein containing fractions were determined using SDS-PAGE and concentrated to a volume of 1 mL using a 3 kDa MW cut off concentrator (Sartorius). CjX183 was further purified by size exclusion chromatography using Tris SEC buffer, using the method described in section 2.3.2.2. CjX183 was concentrated to 500 μL, protein concentration was determined and protein was flash frozen in 20 μL aliquots in liquid N_2 and stored at -80 °C.

2.3.3 Expression of Cbp2E in *C. japonicus*

Wild type and Cbp2E-6His mutant strains of *C. japonicus* were provided by Jeffrey Gardner (University of Maryland, Baltimore County, USA). Strains were streaked on MOPS-agar plates and grown at 37 °C for 48 hours. A single colony was picked and grown in 5 mL of MOPS media at 37 °C for a further 24 hours. For expression tests, 50 mL non-baffled flasks of MOPS media were inoculated with 500 μL of culture and grown for 24 hours at 30 °C. Cells were harvested by centrifugation at 2500 g for 20 minutes at 4 °C and both the supernatant and pellet were retained.

Cells were lysed with 500 μL Bugbuster (Merck Millipore) on ice for 10 minutes before pelleting of the cell debris by centrifugation in a microcentrifuge at 16000 g for 10 minutes at room temperature. The supernatants were extracted, and the insoluble cell pellets were resuspended in dH_2O. For small-scale nickel affinity experiments, His SpinTrap columns (GE Healthcare) were used according to the manufacturer's instructions. Secreted proteins, the soluble cell lysate and the insoluble cell debris were analysed by SDS-PAGE and Western blot.

2.3.4 Sodium dodecyl sulphate polyacrylamide gel electrophoresis

SDS-PAGE was performed using homemade 12 % (v/v) acrylamide gels, Table 2.7, with a 6 % (v/v) acrylamide stacking layer, Table 2.8.

Reagent	*Volume*
30 % (w/v) acrylamide	5 ml
1 M Tris-HCl pH 8.8	4.7 ml
dH_2O	2.56 ml
10 % (w/v) SDS	125 μl
TEMED	12.5 μl
10 % (w/v) ammonium persulphate	125 μl

Table 2.7: 12 % (v/v) acrylamide resolving gel composition.

Reagent	*Volume*
30 % (w/v) acrylamide	0.75 ml
1 M Tris-HCl pH 6.8	0.47 ml
dH_2O	2.46 ml
10 % (w/v) SDS	37.5 µl
TEMED	3.75 µl
10 % (w/v) ammonium persulphate	37.5 µl

Table 2.8: 6 % (v/v) acrylamide stacking gel composition.

Samples were prepared using 4x loading buffer (200 mM Tris-HCl pH 6.8, 20 % (v/v) glycerol, 8 % (w/v) SDS, 0.4 % (w/v) brilliant blue, 600mM β-mercaptoethanol, 50 mM EDTA) and denatured at 98 °C for 10 minutes. Broad range blue prestained protein standard (NEB) was used to estimate the size of the protein bands. Gels were run at 100 V for 10 minutes and then 200 V for 45 minutes in SDS-PAGE running buffer (25 mM Tris, 250 mM glycine, 0.1 % (w/v) SDS). Gels were stained with InstantBlue (Expedeon).

2.3.5 Western blotting

For Western blots, 12 % acrylamide gels were run with the required protein samples as described in section 2.3.3. Protein samples were transferred to a 0.2 µm polyvinylidene fluoride membrane (Bio-Rad) using a Trans-Blot Turbo Semi-Dry (Bio-Rad). Blocking was performed with 5 % (w/v) milk powder in Tris-buffered saline Tween (TBST) (20 mM Tris-HCl, 150 mM sodium chloride, 0.2 % (v/v) Tween-20). Membranes were incubated overnight with the anti-polyhistidine antibody (Sigma, H1209) diluted 1:10000 in 5 % (w/v) milk powder in TBST. Membranes were washed 3 times for 10 minutes in TBST before incubation with anti-mouse IgG horseradish peroxidase conjugate (NEB, 7076) diluted 1:10000 in TBST. Membranes were washed 3 more times for 10 minutes in TBST before incubation with SuperSignal^{TM} western pico chemiluminescent substrate (ThermoFisher Scientific). The emitted signal was detected using Q9 Alliance.

2.3.6 Protein concentration determination

Protein concentration was determined by measuring the A_{280} or A_{552} (protein dependent) using a Cary 60 UV-Vis spectrophotometer (Agilent). Measurements were taken in a Quartz 10 mm cuvette (Agilent), and were baselined with 200 μL of buffer. Proteins were diluted appropriately to enable accurate measurements. The absorbance value was used in the Beer-Lambert equation: A = εCl (where ε = extinction coefficient ($M^{-1}cm^{-1}$), C = concentration (M), l = path length (cm)) to generate molar concentrations. To convert concentrations to mg/mL the molar concentrations were multiplied by the molecular weight for the protein. Extinction coefficients and molecular weights for proteins measured are shown in Table 2.9.

Protein	*A_{280} Extinction coefficient ($M^{-1}cm^{-1}$)*	*A_{552} Extinction coefficient ($M^{-1}cm^{-1}$)*	*Molecular weight (Da)*
CjAA10B	73505	-	34882
CjAA10BΔCBM	53775	-	23898
CfAA10	81275	-	34701
BdSUMO-CjX158E	9970	-	32081
CjX158E	8480	-	18685
CjX183	19730	27500	10623

Table 2.9: Protein parameters for concentration determination for proteins used in this thesis.

2.3.7 Increasing protein concentration

Protein samples were concentrated using Vivaspin protein concentrators (Sartorius) with molecular weight cut offs at least half the molecular weight of the proteins. Samples were centrifuged at 2500 g until the desired volume was reached.

2.4 Biochemical characterisation

2.4.1 Mass spectrometry

All protein mass spectrometry in this thesis was carried out by Rachel George (Astbury Centre for Structural and Molecular Biology, Leeds, UK). For accurate molecular mass measurement by electrospray ionisation mass spectrometry (ESI-MS), samples were submitted at 20 μM concentration with a minimum volume of 20 μL.

2.4.2 Circular dichroism

Circular dichroism (CD) spectra were recorded between 190 and 260 nm on an APP Chirascan CD spectropolarimeter. 200μL samples were used at 20 μM in buffer containing 10 mM potassium fluoride pH 7 and 50 mM potassium phosphate. For thermal melt experiments spectra were collected every 1 °C from 20 °C to 90 °C. For samples with EDTA, 200 μM EDTA was used to chelate the copper ions. For CjAA10BΔCBM experiments data at 232 nm were extracted and plotted using GraphPad Prism to determine the melting temperatures (T_m) values for both samples. For CjX183 thermal melt experiments the circular dichroism at 222 nm was analysed.

2.4.3 Reduction of CjX183

CjX183 was chemically reduced by the addition of a 10x molar excess of ascorbate. The reduction reaction was left for 1 minute before buffer exchange to remove excess ascorbate using a PD10 desalting column (GE Healthcare) pre-equilibrated in 50 mM sodium phosphate pH 6 buffer. Reduced CjX183 was quantified from the A_{552} peak, extinction coefficient shown in Table 2.9, using UV-Vis spectroscopy on a Cary 60 UV-Vis spectrophotometer.

Electrochemical reduction of CjX183 was performed with the help of Nick Yates and Dr Alison Parkin (University of York, York, UK). A 2 mL solution of CjX183 in a pH 7 mixed buffer solution (consisting of 150 mM of sodium chloride and 50 mM each of acetate, Tris, phosphate and MES) was used at a concentration of 235 μM. A carbon felt working electrode was held at -400 mV vs SHE for 20 minutes at 0 °C and ambient atmospheric pressure in the presence of 2.35 μM of the redox mediator methyl viologen. The oxidative state was monitored by the formation of a peak at 552 nm, indicative of the reduced state, measured by UV-Vis spectroscopy. Electrochemically reduced CjX183 was only used in activity studies described in section 6.3, in all other experiments chemically reduced CjX183 was used.

2.4.4 UV-Vis spectroscopy of CjX183

The redox state of reduced CjX183 was monitored using a Cary 60 UV-Vis spectrophotometer. A wavelength scan from 600 to 400 nm was used to detect the signature haem spectra, baselined against a sample of buffer only. Autoxidation studies were conducted with 10 μM reduced CjX183 in 50 mM sodium phosphate pH 6. Reactions were monitored using wavelength scans between 500 and 600 nm, performed every minute for 250 minutes at room temperature. Data were plotted and analysed using GraphPad Prism.

In experiments with LPMOs. A stock solution of 20 μM reduced CjX183 was prepared, aliquoted and flash frozen in liquid N_2. In this experiment absorbance at 552 nm was monitored for 15 minutes, with readings taken every 0.1 minutes. CjX183 was used at a final concentration of 10 μM and LPMO concentrations were varied between 0 and 50 μM. Reactions were prepared by thawing an aliquot of reduced CjX183 and mixing in a 1:1 ratio with doubly concentrated LPMOs. Reactions were performed in 50 mM sodium phosphate pH 6. Data were plotted and analysed using GraphPad Prism.

2.4.5 Voltammetric electrochemical analysis of CjX183

Electrochemical analyses of CjX183 were performed using cyclic voltammetry with the help of Jake Smith, Nick Yates and Dr Alison Parkin (University of York, York, UK). A Standard 3 electrode set up was used, consisting of: a working pyrolytic graphite edge electrode attached to an Orgiatrod rotator operated in stationary mode; a saturated calomel reference electrode filled with saturated aqueous potassium chloride solution, and a platinum wire counter electrode. The 3 electrodes were contained within a custom-built electrochemical cell (constructed by the University of York Department of Chemistry Glass Workshop). 1 μL of CjX183 was applied onto the surface of a freshly abraded working electrode and left to form an adsorbed film for approximately 1 minute. Measurements were performed in 50 mM sodium phosphate pH 7, 150 mM sodium chloride.

2.5 Crystallographic methods

2.5.1 Crystallography screens

Proteins were set up in crystal screens with four commercially available crystallisation screens: JCSG Core I-IV (QIAGEN). Sitting drop screens were set up in 3-drop MRC 96-well plates using a Mosquito protein crystallisation robot (SPT Labtech). Proteins were initially used at 10 mg/mL, but this was increased in experiments where insufficient protein precipitation was observed at this concentration. Sitting drops contained a total volume of 300 nL, and were set up in 1:1, 2:1 and 1:2 ratios of protein to precipitant. Crystallisation trays were stored at 20 °C and imaged using a Rock Imager 1000 crystal hotel (Formulatrix).

2.5.2 Sample preparation and X-ray diffraction data collection

Crystals were picked and mounted on CryoLoops (Hampton Research), cryo-protected in mother liquor supplemented with 20 % (v/v) ethylene glycol for 30 seconds, and cryo-cooled in liquid N_2. For CjAA10BΔCBM, data were collected on beamline i04 at Diamond Light Source with a wavelength of 0.979 Å. For CjX158E, data were collected on MASSIF-1 beamline at the European Synchrotron Radiation Facility with a wavelength of 0.967 Å. CjX183 diffraction data were collected on beamline i03 at Diamond Light Source with a wavelength of 0.976 Å. For all datasets 1800 images were taken at an oscillation angle of 0.1°.

2.5.3 Data processing, model building and refinement

2.5.3.1 CjAA10BΔCBM

Diffraction data were autoprocessed using the autoPROC software package (Vonrhein et al., 2011). Autoprocessed data were input into CCP4i2 (Potterton et al., 2018) and cut to 1.9 Å (Data were originally collected to 1.75 Å) using data reduction tool Aimless (Evans and Murshudov, 2013) to improve the completeness of data in the highest resolution shells. The space group was determined and the Matthews coefficient (Matthews, 1968) was used to predict the number of monomers in the asymmetric unit using the unit cell dimensions and protein molecular weight. Molecular replacement was initially performed using a single monomer of CjAA10A (PDB ref 5FJQ) as a search model in Phaser (McCoy et al., 2007). Molecular replacement was repeated, replacing the search model for a single monomer of TtAA10 (PDB ref 6RW7). Following molecular replacement, a round of autobuilding using Buccaneer (Cowtan, 2006) was performed. Subsequently, iterative rounds of manual model building, using COOT, and restrained refinement, using REFMAC, were performed (Emsley et al., 2010; Murshudov et al., 2011). The copper ion and water molecules were added manually in COOT (Emsley et al., 2010).

2.5.3.2 CjX158E

Initial processing of CjX158E diffraction data was performed using autoprocessed data using the DIALS pipeline (Winter et al., 2018). To determine the correct space group, diffraction data for CjX158E were processed using XDS (Kabsch, 2010) then input into the CCP4i2 software suite (Potterton et al., 2018). Aimless (Evans and Murshudov, 2013) was used to cut the data to 2.2 Å resolution. The space group was manually set to $P4_3$, and the unit cell dimensions were defined in Aimless. The Matthews coefficient (Matthews, 1968) was used to determine the contents of the unit cell and molecular replacement was performed using a monomer of SdX158 (PDB ref 2X34) as a model in Phaser (McCoy et al., 2007). Density modification was performed using Parrot (Cowtan, 2010), followed by autobuilding using Buccaneer (Cowtan, 2006). Iterative rounds of model building in COOT and refinement using REFMAC were performed (Emsley et al., 2010; Murshudov et al., 2011). The OPP cofactor and water molecules were manually modelled in COOT (Emsley et al., 2010).

2.5.3.3 CjX183

Diffraction data for CjX183 were indexed and integrated using XDS (Kabsch, 2010), then input into the CCP4i2 suite (Potterton et al., 2018). Data reduction were performed in Aimless (Evans and Murshudov, 2013), and data were cut to 1.2 Å (data were initially collected to 1 Å). Aimless was used to predict the space group and unit cell dimensions, subsequently, the Matthews coefficient (Matthews, 1968) was used to predict the number of monomers of CjX183 in the asymmetric unit. Anomalous diffraction from the haem iron atom was used for phasing, using the SHELXC/D/E pipeline (Sheldrick, 2008).

Model refinement was performed using iterative cycles of model building and restrained refinement using COOT and REFMAC, respectively (Emsley et al., 2010; Murshudov et al., 2011). The haem cofactor and water molecules were manually modelled in COOT, the model was validated using MolProbity (Chen et al., 2010).

2.6 LPMO activity assays

2.6.1 LPMO activity assays and MALDI-TOF analysis

Activity assays were set up with PASC. PASC was prepared as described by Wood (Wood, 1988) and was stored at 4 °C. Prior to use, PASC was pelleted, washed and resuspended in the required assay buffer by centrifugation at 16000 g. Activity assays comprised: 10 % (v/v) PASC, 1 μM CjAA10BΔCBM or CfAA10, 1 mM ascorbate or 150 mM reduced CjX183, and were conducted in 5 mM ammonium acetate pH6 buffer, with the exception of the assays with electrochemically reduced CjX183, which was performed in 50 mM sodium phosphate pH 6 buffer. Assays were performed using either chemically or electrochemically reduced CjX183, as described in section 2.4.3. Reactions were incubated for 16 hours in a head over tail rotator. Remaining substrate was pelleted by centrifugation at 16000 g for 10 minutes at room temperature, and the supernatant was analysed using a matrix-assisted laser desorption ionization-time-of-flight/time-of-flight (MALDI-TOF/TOF) instrument (Bruker). MALDI-TOF MS was performed by Peter Lindley and Alessandro Paradissi (University of York, York, UK) using methods described in Hemsworth *et al.* (Hemsworth et al., 2014). Peak analysis was performed using flexAnalysis software.

2.6.2 Activity measurements using the H_2O_2 Amplex Red assay

2.6.2.1 A note on reagent concentrations used for the Amplex Red assay

Detection of H_2O_2 production from LPMOs was determined using a coupled assay with Amplex Red. The product of this reaction, resorufin, was detected by fluorescence spectroscopy using a FLUOstar Galaxy microplate reader (BMG Labtech) using an excitation filter of 570 nm and an emission filter of 595 nm. Experiments were carried out in 96-well black polystyrene microplates and the gain was calculated each day from a concentration curve of known H_2O_2 concentrations.

A 20 mM stock of Amplex Red was prepared by dissolving 5 mg of Amplex Red reagent (ThermoFisher Scientific) in dimethyl sulfoxide (DMSO), which was aliquoted and frozen at -20 °C. A 10 U ml^{-1} stock of horseradish peroxidase (HRP) was made by dissolving lyophilised HRP (Merck) in dH_2O, aliquoted and frozen. For the coupled assay stock solutions of 500 μM Amplex Red reagent and 2 U mL^{-1} HRP were made by dilution in Amplex Red assay buffer (50 mM sodium phosphate pH 6). Working concentrations of 50 μM Amplex Red and 0.2 U mL^{-1} HRP were used in all assays.

2.6.2.2 Concentration curve determination

Concentration curves were generated using stock solutions of 2, 4, 6, 8, 10 μM H_2O_2, prepared by the dilution of 30 % (w/w) hydrogen peroxide into Amplex Red assay buffer. 50 μL of stock solutions were mixed with 12 μL reaction mix containing HRP and Amplex Red and incubated for 10 minutes at room temperature before heating at 95 °C for 10 minutes. Heated samples were centrifuged briefly to collect any condensation from the lid. 62 μL of samples were pipetted into a 96-well microplate, and the remaining 38 μL of buffer (for CjX183-lacking samples) or reduced CjX183 (prepared as described in section 2.4.3) were added. Concentration curves were conducted at each concentration of CjX183 used in subsequent assays to account for inner filter effects (discussed further in section 6.4.2). Resorufin concentration was measured using fluorescence spectroscopy. Data were analysed using GraphPad Prism, and ensured to fit to a linear dependence before further assays were conducted.

2.6.2.3 Measurement of H_2O_2 production from LPMOs

Amplex red assays were used to compare the production of H_2O_2 by different LPMOs with different reductants. Reduced CjX183 was used at 50 μM, ascorbate at 25 μM and LPMOs at 2 μM. Reactions were started with the addition of reduced CjX183 or ascorbate with a multichannel pipette. Enzyme-free and reductant-free controls were performed every time and reactions were performed in triplicate. Reactions were monitored using fluorescence spectroscopy and readings were taken every minute for 60 minutes. Data were plotted and analysed using GraphPad Prism.

In assays used to determine kinetic parameters for LPMOs, the LPMO concentration was held constant at 2 μM and the CjX183 or ascorbate concentration was varied about calculated K_m values. Optimisation was required to obtain initial values for K_m to allow this. In final assays, reductants were used at ¼ , ½ , 1, 2 and 4 times the K_m value. Data were analysed using GraphPad Prism and were fitted to the Michaelis-Menten equation and kinetic parameters were extracted using the Michaelis-Menten function on GraphPad.

2.6.3 Glycoside hydrolase boosting activity assays

Glycoside hydrolase assays were set up on PASC (preparation described in section 2.6.1) or Avicel, for which a 50 % (w/v) stock was made by suspending Avicel in dH_2O. PASC and Avicel were used at a final concentration of 10 % (v/v) in boosting assays. Boosting assays were set up in 50 mM sodium phosphate pH 6 and included LPMOs at 2 μM, endo-1,4-β-D-glucanase from *T. longibrachiatum* (Megazyme) at 1 U mL^{-1}, and CjX183 at 150 μM or ascorbate at 75 μM. Reactions were incubated at room temperature on a head over tail rotator for 8 hours, for PASC reactions, or 16 hours, for Avicel reactions. Reactions were stopped by heating at 95 °C for 10 minutes, and insoluble material was pelleted by centrifugation. Soluble material was retained and diluted 10-fold into water. For quantification, diluted reactions were combined in a 1:1 ratio with 100 μM ^{13}C-labelled cellobiose (Omicron Biochemicals) and analysed by positive mode ESI-MS. Quantification of cellobiose by this method was performed with the help of Dr Kristian Hollingsworth (Astbury Centre for Structural and Molecular Biology, Leeds, UK). Cellobiose production from boosting assays was measured by comparing the intensity of the $[\text{cellobiose-Na}]^+$ peak at 365 Da with that of the $[^{13}\text{C-cellobiose-Na}]^+$ peak at 377 Da.

2.6.4 ESI-MS protein oxidation experiments

Protein damage experiments were set up in 50 mM sodium phosphate pH 6 using LPMOs at 1 μM, ascorbate at 100 μM or CjX183 at 200 μM. Samples were taken upon mixing, to reflect the 0 hour timepoint, and reactions were incubated at room temperature with further samples taken after 1 hour, for the CfAA10 enzyme, or 2 hours, for the CjAA10BΔCBM enzyme, and after 24 hours, for both enzymes. Samples were run and analysed by Rachel George (Astbury Centre for Structural and Molecular Biology, Leeds, UK). Protein damage was assessed by analysing the formation of +16 Da peaks relative to wild type peaks.

Chapter 3

CjAA10BΔCBM: a cellulose active LPMO from *C. japonicus*

3.1 Introduction

C. japonicus expresses a wide range of secreted proteins for polysaccharide breakdown (Tuveng et al., 2016). Included in these proteins are two LPMOs: CjAA10A and CjAA10B, which have been shown to be critical for growth on crystalline polysaccharides (Gardner et al., 2014; Forsberg et al., 2016). CjAA10A is active on chitin and is composed of a catalytic domain appended to two C-terminal chitin binding domains by flexible linkers. The catalytic domain of CjAA10A has been structurally characterised, and shows similar copper coordination to other C1-oxidising AA10s (Forsberg et al., 2016). CjAA10B has been previously characterised to show activity on cellulose (Gardner et al., 2014), but its structure is currently unknown.

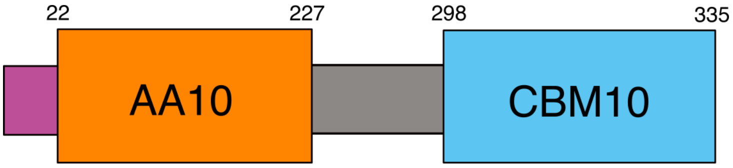

Figure 3.1: Domain annotation for CjAA10B. *Numbers indicate domain annotation at the amino acid level. Domains are labelled, with signal sequence shown in purple and linker region in grey.*

CjAA10B is composed of an AA10 domain connected to a CBM10 domain by a flexible linker, which is 70 residues long and serine rich (Figure 3.1). The CBM10 domain is proposed to mediate tight binding to cellulose, and the polypeptide has a signal peptide for extracellular export, consistent with detection of LPMOs in secretomes. Degradative enzymes frequently contain CBMs, and in LPMO action CBMs have been suggested to facilitate tight binding to crystalline substrates, aiding localisation of the catalytic domain to the substrate (Courtade et al., 2018; Crouch et al., 2016). The flexible linker connecting the domains is thought to impede crystallisation of full length LPMOs, and most LPMO crystal structures are representative of separate domains only. Only one crystal structure has been solved with additional domains at the C-terminus, the *Vibrio cholerae* GbpA protein, which has an N-terminal domain that is structurally similar to

LPMOs, and in these studies they emphasise difficulties experienced with crystallising the full length protein (Wong et al., 2012). High levels of flexibility between the domains were shown in an NMR structure of a full length LPMO (Courtade et al., 2018), highlighting the importance of truncating these proteins in order to study their structures using X-ray crystallography.

This chapter will describe the steps taken to study the structure of the catalytic domain of CjAA10B. Characterisation of CjAA10B was desired to inform studies with putative redox partners, performed later in this thesis. In order to do this, the CBM and flexible linker of CjAA10B were deleted, subsequent studies in this chapter were performed using the CBM-lacking mutant, henceforth called CjAA10BΔCBM.

3.2 Mutagenesis was used to delete the C-terminal CBM domain

The pET22-CjAA10BΔCBM construct was generated by deletion of the coding region for the CBM domain and flexible linker from the pET22-CjAA10B construct. The resulting vector is shown in Figure 3.2. The CjAA10B coding region is flanked by an N-terminal pelB leader, for expression in the periplasm, and a C-terminal 6His tag, to allow for efficient purification. Analysis of the sequence of the CjAA10B catalytic domain shows that it has 6 cysteine residues, that may form disulphide bonds to stabilise the protein. Therefore, for correct folding, the protein was expressed periplasmically, as has been done for this protein previously (Gardner et al., 2014) and for other LPMOs expressed in bacteria (Vaaje-Kolstad et al., 2005; Hemsworth et al., 2013; Forsberg et al., 2014a).

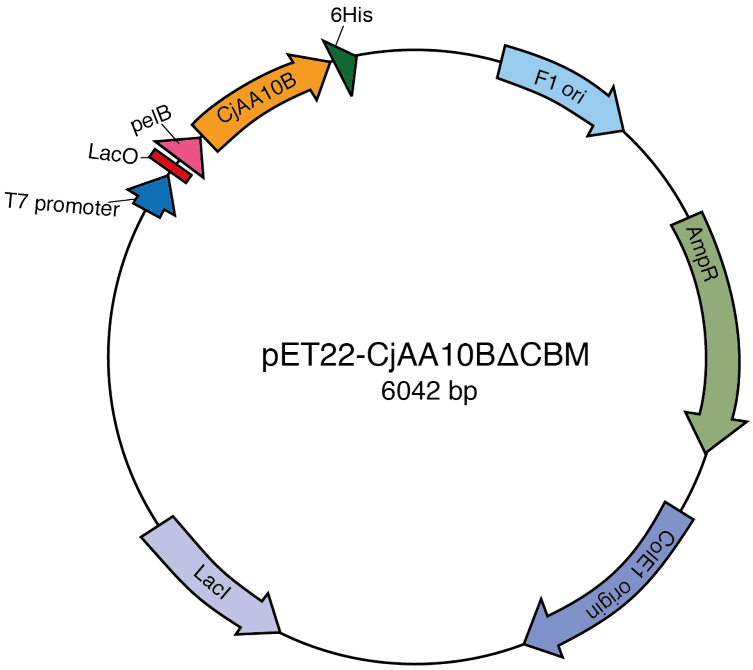

Figure 3.2: Plasmid map for the pET22-CjAA10BΔCBM construct. *The CjAA10B domain is shown in orange and is flanked by a pelB leader and a 6His tag.*

3.3 Expression and purification of CjAA10BΔCBM

CjAA10BΔCBM was expressed in BL21(DE3) cells following IPTG induction. Purified protein was extracted from the periplasm and obtained by a three-step purification method, involving nickel affinity, anion exchange and size exclusion chromatography. The protein was copper loaded prior to size exclusion chromatography to provide the catalytic copper required for enzyme activity. Protein presence was checked throughout using SDS-PAGE (Figure 3.3A, B and C).

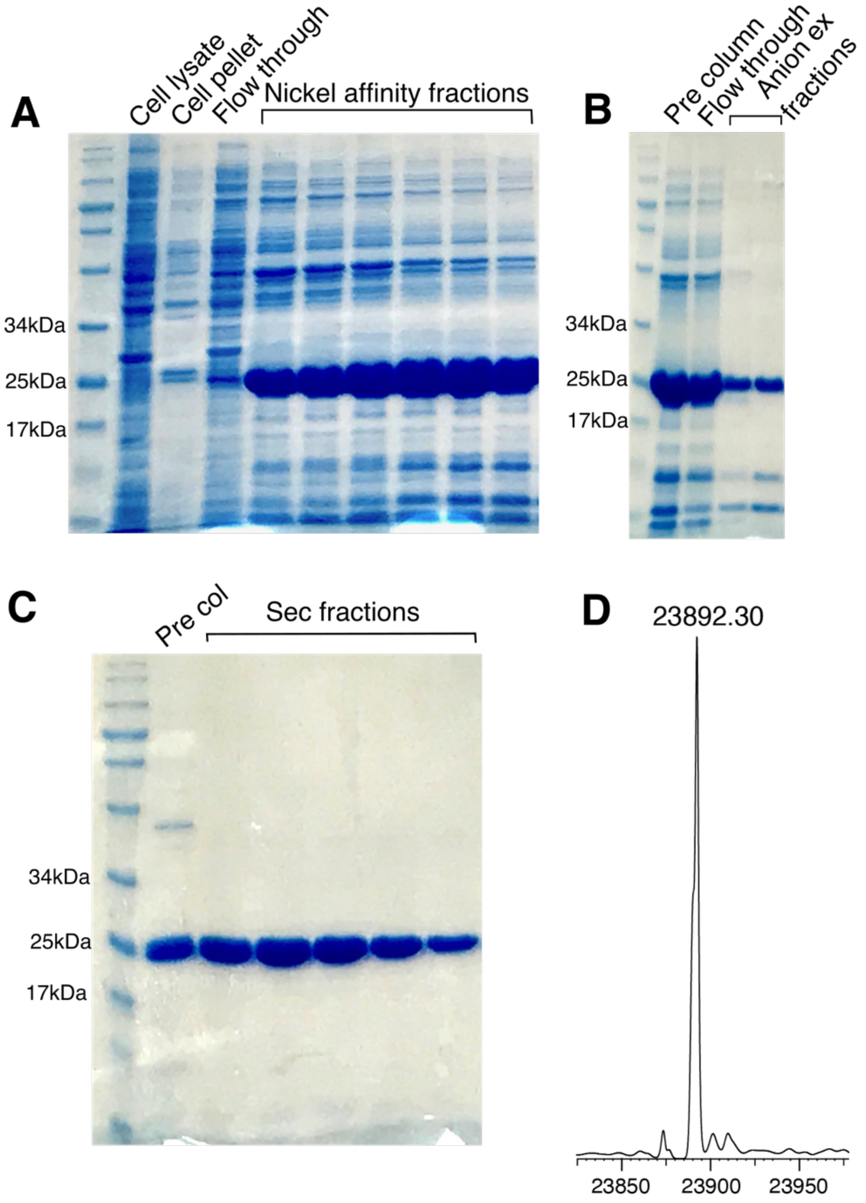

Figure 3.3: Purification of CjAA10BΔCBM. *SDS-PAGE gels showing the purification of the 23.9 kDa CjAA10BΔCBM by **(A)** nickel affinity chromatography **(B)** anion exchange chromatography and **(C)** size exclusion chromatography. A protein of roughly 25 kDa was observed throughout. **(D)** ESI-MS showing a peak at 23892 Da, CjAA10BΔCBM has a predicted mass of 23898 Da and was assumed to lose 6 Da through the formation of 3 disulphide bonds.*

Purified protein was analysed using ESI-MS to confirm the successful purification of CjAA10BΔCBM (Figure 3.3D). ESI-MS results showed a peak of 23892 Da for CjAA10BΔCBM. The expected mass of CjAA10BΔCBM is 23898 Da based on the amino acid sequence of the protein. CjAA10BΔCBM has 6 cysteine residues, were these to form 3 disulphide bonds, then the actual mass would be -6 Da, due to the loss of 6 protons.

Therefore, the peak at 23892 Da confirmed that CjAA10BΔCBM had been successfully isolated.

3.4 Circular dichroism of CjAA10BΔCBM shows that copper binding stabilises the protein

Copper loading of LPMOs is essential for enzyme activity. For CjAA10BΔCBM, enzymes were copper loaded during protein purification, prior to size exclusion chromatography. Copper binding at the histidine brace is known to significantly stabilise LPMOs (Gregory et al., 2016; Hemsworth et al., 2013). CjAA10BΔCBM stability was assessed by circular dichroism, where a thermal melt was used to observe protein unfolding. Figure 3.4A shows the full spectrum for the thermal melt, where spectra were collected every 1 °C between 200 and 260 nm. Examining the spectra, there is a pronounced negative peak at 232 nm, which allowed protein unfolding to be studied. Data were extracted for the 232 nm peak and converted to fraction folded, using the equation $F_F=(\theta_t-\theta_U)/(\theta_F-\theta_U)$, where F_F is the fraction unfolded, θ_t is the observed ellipticity at any temperature, θ_U is the average ellipticity of the final unfolded values and θ_F is the average of the initial folded values (Greenfield, 2006a). The thermal melts of CjAA10BΔCBM, with and without EDTA, are plotted in Figure 3.4B. Data were fitted to the Boltzmann sigmoid distribution using GraphPad Prism using the equation $Y=LL+((UL-LL)/1+e((T_m-X)/slope)$, where LL is the lower limit, UL is the upper limit and T_m is the temperature where X=0.5.

The T_m for copper loaded CjAA10BΔCBM, defined as the temperature when half of the protein was unfolded, was compared to that of a sample where excess EDTA was added to chelate the copper ions (Figure 3.4). The copper-bound enzyme had a T_m of 61 °C, 7 °C higher than the EDTA-treated sample, which had a T_m of 54 °C, results which are comparable with those from similar studies on LPMOs (Hemsworth et al., 2013; Gregory et al., 2016). These results verified that CjAA10BΔCBM was copper bound, and showed that binding had an advantageous effect on protein stability.

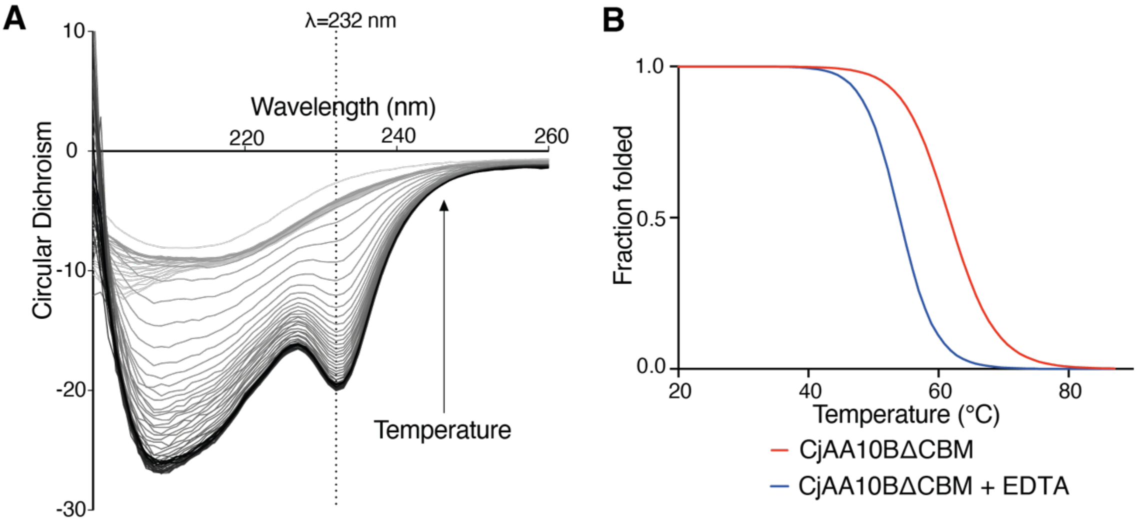

Figure 3.4: Thermal melt for apo- and copper-bound CjAA10BΔCBM. (A) *CjAA10BΔCBM unfolding was monitored by circular dichroism at wavelengths between 200 and 260 nm. The spectra for copper loaded CjAA10BΔCBM, where data was collected every 1 °C, is shown as lines, coloured by a gradient from dark to light with increasing temperature.* ***(B)*** *The circular dichroism at 232 nm was converted to fraction folded, showing a* T_m *of 61 °C for copper loaded CjAA10BΔCBM (red), which was reduced to 54 °C in the presence of EDTA (blue).*

3.5 Crystallisation of CjAA10BΔCBM

CjAA10BΔCBM was crystallised using JCSG Core I-IV screens, and crystals formed in 0.1 M Tris pH 8.5 and 1 M diammonium hydrogen phosphate (Figure 3.5). X-ray diffraction data were collected at Diamond Light Source on beamline i04. Diffraction from the crystal showed some anisotropy, and after processing displayed some signs of translational non-crystallographic symmetry (tNCS). tNCS occurs when there are multiple copies of a protein in the asymmetric unit that adopt the same orientation but are not related by a crystallographic symmetry operator, resulting in systematic interference that can make the measurements of intensities inaccurate. Autoprocessing performed in ISPyB struggled to define the dimensions of the unit cell, which may have been a result of the tNCS. Autoprocessed data, processed using the autoPROC software package (Vonrhein et al., 2011), were input into CCP4i2 and further processed (Potterton et al., 2018), the statistics for this dataset are shown in Table 3.1.

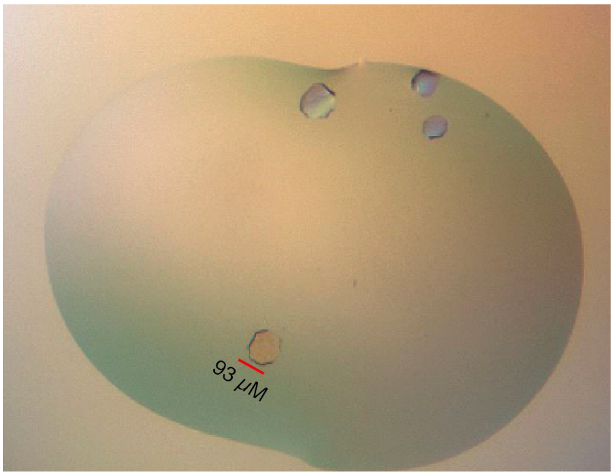

Figure 3.5: Crystals of CjAA10BΔCBM. *Crystals formed in 0.1 M Tris pH 8.5 and 1 M diammonium hydrogen phosphate.*

Dataset		*CjAA10BΔCBM*	
Space Group		P1 2_1 1	
Cell dimensions			
a	α	76.8 Å	90°
b	β	74.9 Å	102°
c	γ	137.5 Å	90°
Resolution		10.41-1.90 Å (1.93-1.90 Å)	
Rmerge		0.077 (0.832)	
Rpim		0.040 (0.452)	
Observed/ unique reflections		548904/25490	
Mean I/σ		11 (1.4)	
Half set correlation CC(1/2)		0.999 (0.950)	
Completeness		99.5 % (98.5 %)	
Multiplicity		4.6 (4.4)	

Table 3.1: Statistics for the CjAA10BΔCBM dataset. *Statistics for the highest resolution shell are shown in parentheses.*

Initial molecular replacement searches were performed using the *C. japonicus* AA10A structure (PDB ref 5FJQ) (Forsberg et al., 2016), as this was the closest homologue available at the time. Using the CjAA10A structure, a molecular replacement solution was not found. The catalytic domains of CjAA10A and CjAA10B are only 29 % identical, and with the quality of the diffraction data, molecular replacement was not successful. In September 2019, the structure of an AA10 catalytic domain from *T. turnerae* was published (PDB ref 6RW7) (Fowler et al., 2019). CjAA10B shares 57 % sequence identity with TtAA10, considerably more than with CjAA10A, therefore, molecular replacement was performed using the TtAA10 structure. From this, a solution was achieved, modelling eight monomers in the asymmetric unit. Iterative rounds of model building and refinement produced a structure with a final resolution of 1.9 Å. The final statistics for the model are shown in Table 3.2.

Dataset	*CjAA10BΔCBM*
Resolution	75.23-1.90 Å
Number of reflections (working/free sets)	118690/5863
R-factor/R-free	0.230/0.281
RMS deviations	
Bonds	0.0077
Angles	1.530
Average B factors	29.0
B-average -protein	27.8
B-average -Cu	23.6
B-average -waters	29.3

Table 3.2: Summary of the final refinement statistics for the CjAA10BΔCBM structure.

3.6 The structure of CjAA10BΔCBM shows a typical immunoglobulin fold

The crystal structure of CjAA10BΔCBM (Figure 3.6) is typical of an LPMO. It exhibits an immunoglobulin-like fold, composed of eight anti-parallel β-strands and has a flat substrate binding surface. During model building, strong density supporting the presence of an active site copper ion was seen in each monomer (Figure 3.7). To account for this density, the copper ion was built into the model in COOT (Emsley et al., 2010).

The copper ion is presented at the active site in the histidine brace, as was expected from its coordination in other LPMO structures (Quinlan et al., 2011; Hemsworth et al., 2013).

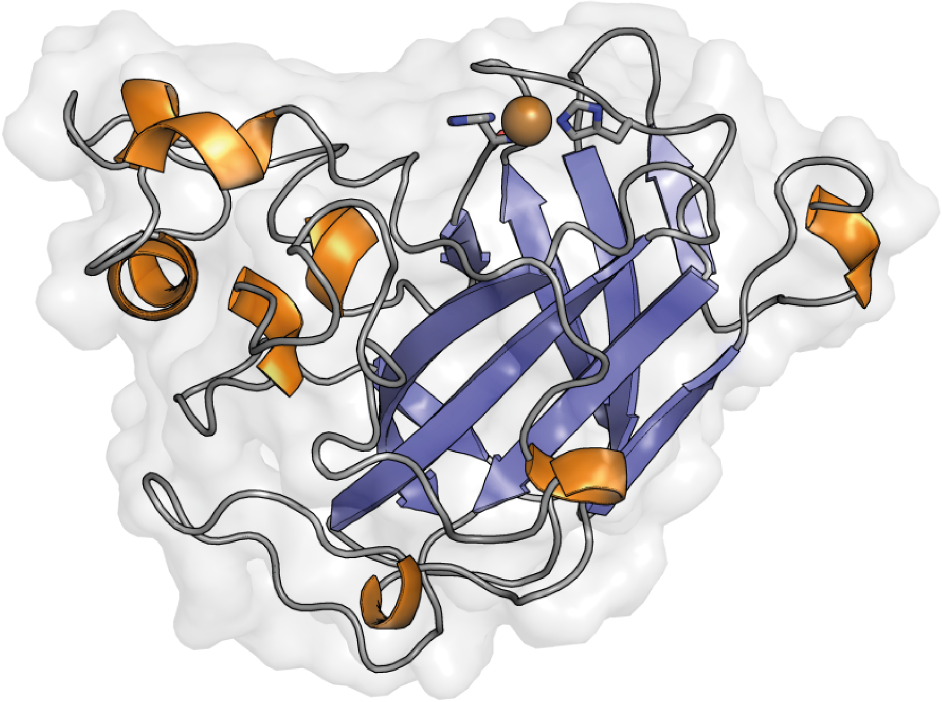

Figure 3.6: The crystal structure of CjAA10BΔCBM shows a typical immunoglobulin fold. *The histidine brace is shown as sticks coordinating the copper atom, shown as a brown sphere.*

The active site copper ion is coordinated at the histidine brace motif, using the side chain and amino group of the N-terminal histidine and the side chain of His109. This catalytic motif is critical for LPMO activity and is believed to be the site of oxygen (or peroxide) activation (Quinlan et al., 2011; Hemsworth et al., 2015; Forsberg et al., 2019). During model building and refinement, additional density was observed at the active site, after the copper ion was modelled. This additional density was too large to be from a water molecule, so a phosphate ion, assumed to be an additive from the crystallisation condition, was modelled into the density. The phosphate ion (shown as sticks in Figure 3.7) was present in all chains, and in some chains an additional water molecule was also modelled into the copper coordination sphere. There was some variation observed between the copper coordinating residues in the eight chains. In three chains (chains A, D and F) there was electron density to support the presence of an equatorial water molecule additionally coordinating the copper ion. In the remaining five chains, the density was not strong enough to support the presence of the water molecule. The copper coordination in chains F and G, representing the two different coordination states, are shown in Figure 3.7. Photoreduction of the copper ion by the X-ray beam is often seen in crystal structures of LPMOs (Gudmundsson et al., 2014; Gregory et al., 2016). The loss of the coordinating water molecule in five monomers of CjAA10BΔCBM may imply that the copper has been photoreduced. In the remaining three chains, the copper-water bond is longer than would be expected, which could also suggest some photoreduction. However, the phosphate ion is still present in all chains, and would likely be lost following full reduction of the copper ion, therefore, partial reduction of the copper ion is proposed to have occurred in the X-ray beam.

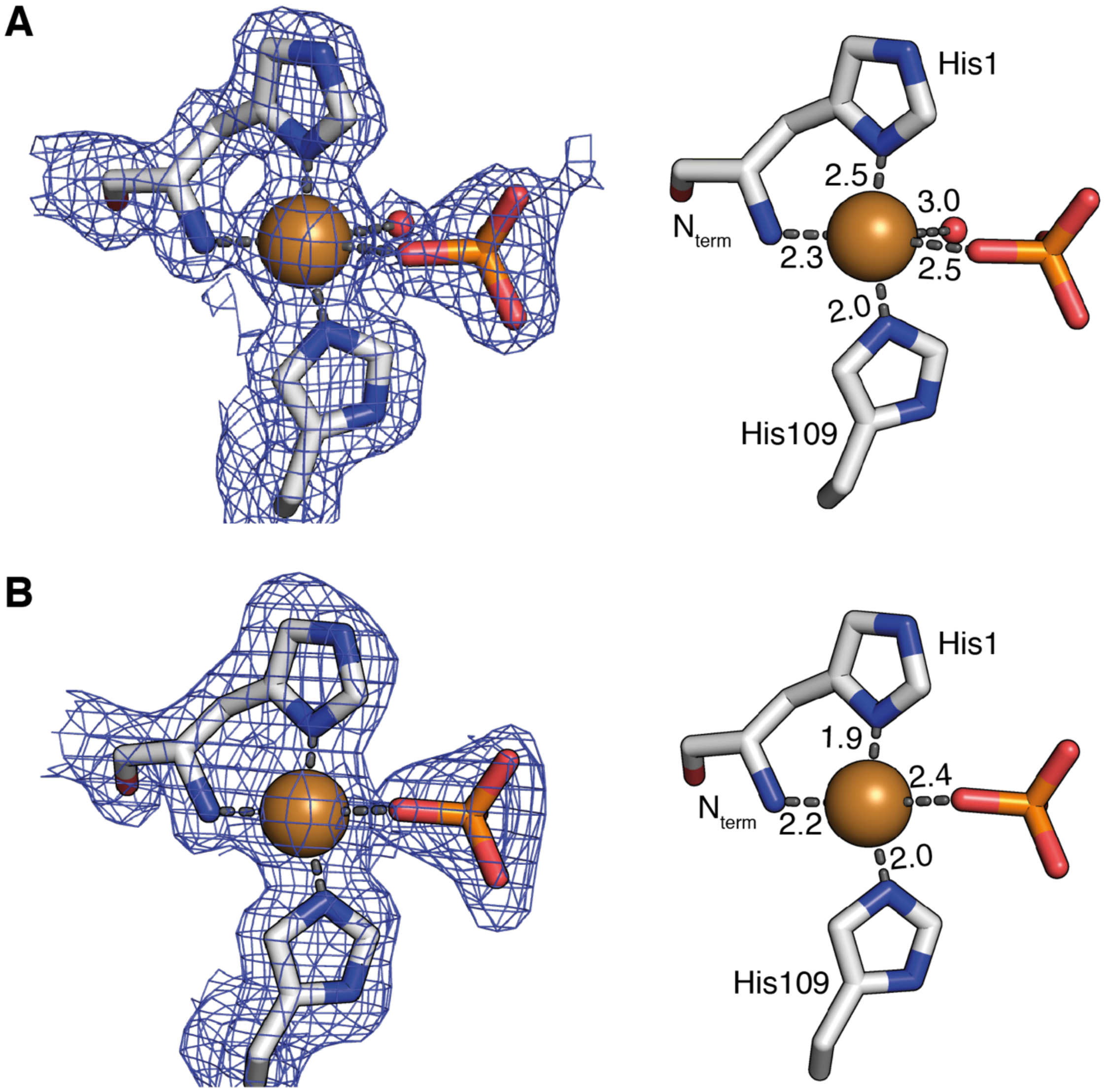

Figure 3.7: The copper ion is coordinated in the histidine brace. (A) *Electron density for chain F shows copper coordination by His1, His109, a phosphate ion and a water molecule. The 2Fo-Fc map is shown as blue mesh and is contoured at 1σ, the copper ions are shown as brown spheres with coordinating residues shown as sticks coloured by atom type. Distances (measured in angstroms) are labelled.* ***(B)*** *Electron density for chain G shows that the equatorial water molecule has been lost.*

The environment of the copper ion is additionally influenced by residues in the second coordination sphere, which are too distant to directly coordinate the copper, but contribute to the overall environment of the active site (Span et al., 2017; Forsberg et al., 2019). The second coordination sphere of AA10 enzymes typically comprise conserved phenylalanine, alanine and glutamate/glutamine residues. CjAA10BΔCBM shares the conserved axial phenylalanine residue (Phe197) and has a glutamate residue

(Glu195) at the conserved Glu/Gln position, which are located 3.5 Å and 3.6 Å from the copper ion respectively. Additionally, CjAA10BΔCBM has a glycine (Gly107) residue, which is 4 Å away from the copper ion (Figure 3.8). Interestingly, the glycine residue is in the place of the typically conserved alanine in AA10s. An axial glycine residue has also been observed in the structure of the *T. turnerae* AA10, the closest structural homologue to CjAA10B, and has been suggested to contribute to cellulose-specific activity. As mentioned in Chapter 1, the axial alanine in AA10 enzymes has been proposed to cause a distorted active site geometry, which has been linked to activity on chitin (Hemsworth et al., 2013; Forsberg et al., 2014b). The axial Ala/Gly is surface exposed, and could be involved in mediating substrate interactions, the additional space provided by the glycine residue could influence substrate specificity, promoting interactions with cellulose over chitin. Interestingly, in CjAA10BΔCBM, Gly107 has an unusual conformation, exhibiting unusual torsion angles, that do not occupy energetically favourable positions on a Ramachandran plot. The copper ion is most likely responsible for this unusual conformation. The glycine residue arcs directly around the copper ion, which could force a conformation that would otherwise not be favourable. This unusual glycine conformation may be involved in modulating the active site environment to allow CjAA10B to act on cellulose.

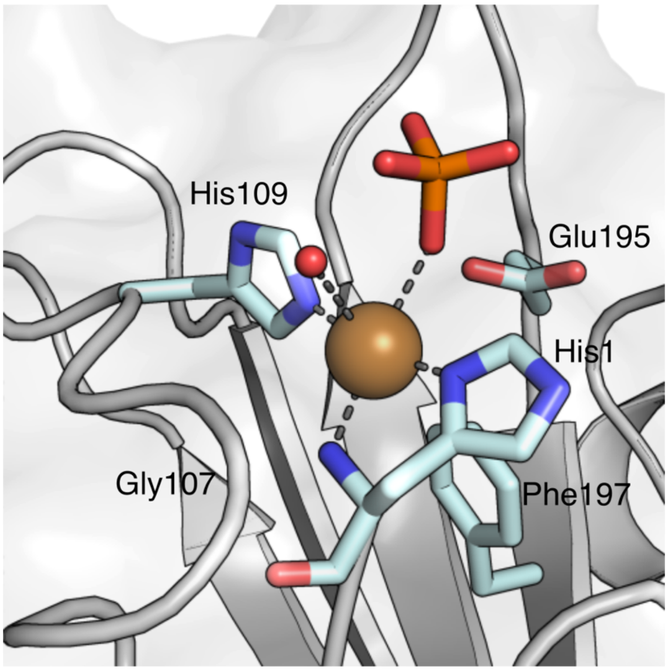

Figure 3.8: The copper ion in CjAA10BΔCBM is additionally coordinated by residues in the second sphere. *Residues within 5 Å of the active site copper are labelled and shown as sticks, a copper coordinating water molecule is shown as a red sphere, and the phosphate ion is also shown as sticks coloured by atom type. The copper ion is shown as a brown sphere. Dashes represent direct coordination of the copper ion by active site residues.*

3.7 Structural comparisons show residue conservation in the second coordination sphere

Structural comparisons against the PDB were performed using the protein comparison server DALI (Holm, 2019). The AA10 from *T. turnerae* had the highest structural similarity to CjAA10BΔCBM (PDB ref 6RW7) (Fowler et al., 2019). TtAA10 is active on cellulose, like CjAA10BΔCBM, but has structural similarity to a number of chitin active LPMOs, such as CjAA10A. The superposition (Figure 3.9), of the 53 % structurally similar proteins, spans 208 residues with a root-mean-square deviation (rmsd) of 1.2 Å. The two proteins share the same overall structure, with core immunoglobulin fold and flat substrate binding face.

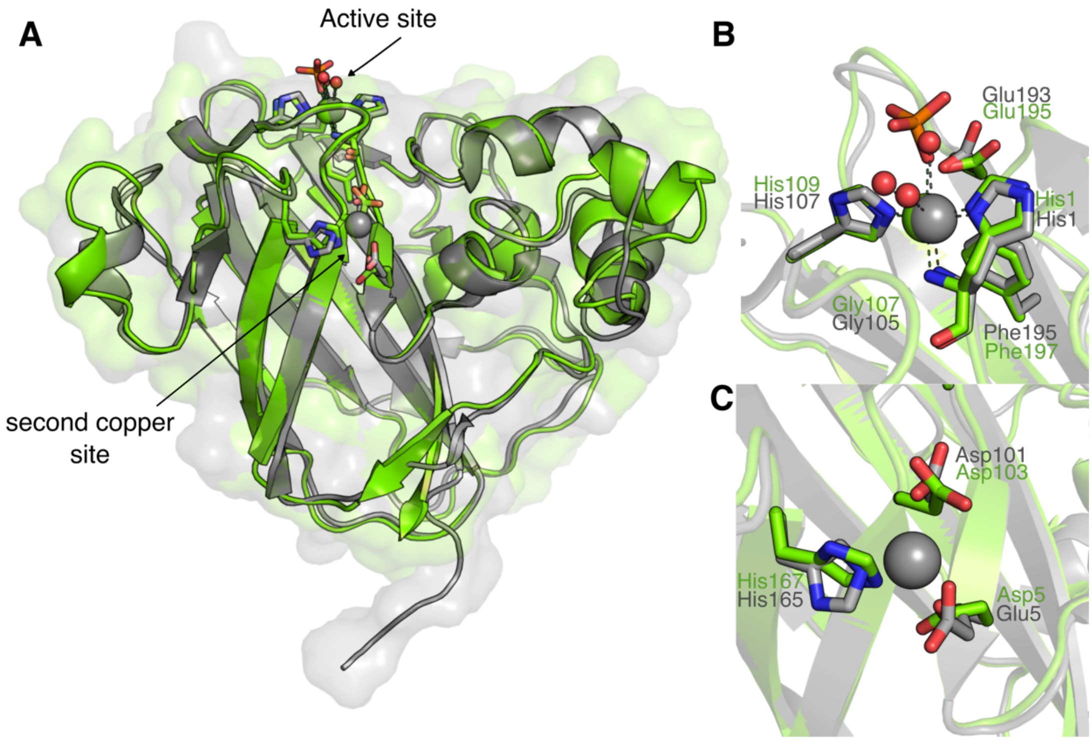

Figure 3.9: Superposition of CjAA10BΔCBM with TtAA10. (A) *CjAA10BΔCBM (green) aligns well with TtAA10 (grey).* ***(B)*** *The second sphere coordination in the active site is conserved between both enzymes.* ***(C)*** *Residues coordinating the TtAA10 second copper ion are conserved in CjAA10BΔCBM. Protein structures are shown as cartoons, with copper ions shown as green (CjAA10BΔCBM) or grey (TtAA10) spheres. Residues coordinating the copper ions are shown as sticks with green or grey carbons and other atoms coloured according to atom type. Water molecules are shown as red spheres. Atoms are labelled in green for CjAA10BΔCBM, or grey for TtAA10.*

The active site geometry is conserved between the two enzymes, both exhibiting the histidine brace and glycine, phenylalanine and glutamate secondary sphere residues, occupying equivalent positions in both crystal structures (Figure 3.9B). The only notable difference in the active site, is the replacement of one axial water molecule in TtAA10 with the phosphate ion in CjAA10BΔCBM, however, this is most likely an artefact from the crystallographic conditions, and is expected to be a water molecule in Nature. Interestingly, TtAA10 has a second, non-catalytic copper site, located 14.4 Å from its active site, a feature that has not been observed in any other LPMO structures. The second copper was not present in all enzyme batches, showing unpredictable variation.

It was suggested that the second copper site in TtAA10 could act to receive electrons and shuttle them to the catalytic copper at the histidine brace, however it has not been experimentally shown to be functional (Fowler et al., 2019). In TtAA10, the non-catalytic copper is coordinated by Glu5, Asp101 and His165. The functional groups of these residues are conserved in CjAA10BΔCBM, with the only residue change being Glu5 for Asp5, and the residues occupy similar geometries (Figure 3.9C). However, in CjAA10BΔCBM there was no electron density to support the presence of a second copper ion. The lack of a second copper ion in CjAA10BΔCBM is not surprising, so far TtAA10 is the only LPMO that has shown this feature, and is inconsistent between batches. However, due to the high similarity of these enzymes and conservation of residues, the structure of CjAA10BΔCBM raises more questions regarding the purpose of the second copper ion in TtAA10.

The closest homologue to CjAA10B and TtAA10 is CjAA10A, the second *C. japonicus* LPMO. CjAA10A is active on chitin, whereas CjAA10B and TtAA10 are active on cellulose (Fowler et al., 2019; Forsberg et al., 2016). The active site and second sphere geometries are similar between these three enzymes (Figure 3.10), with a notable difference that Gly107 (Gly105 in TtAA10) is replaced with an alanine residue, Ala134, in CjAA10A. The conserved alanine in chitin active AA10s has been suggested to create a distorted active site geometry that facilitates chitin cleavage (Hemsworth et al., 2013; Forsberg et al., 2014a; Forsberg et al., 2014b). Therefore, the substitution of this alanine for a glycine residue in both CjAA10B and TtAA10 could explain their different substrate preferences.

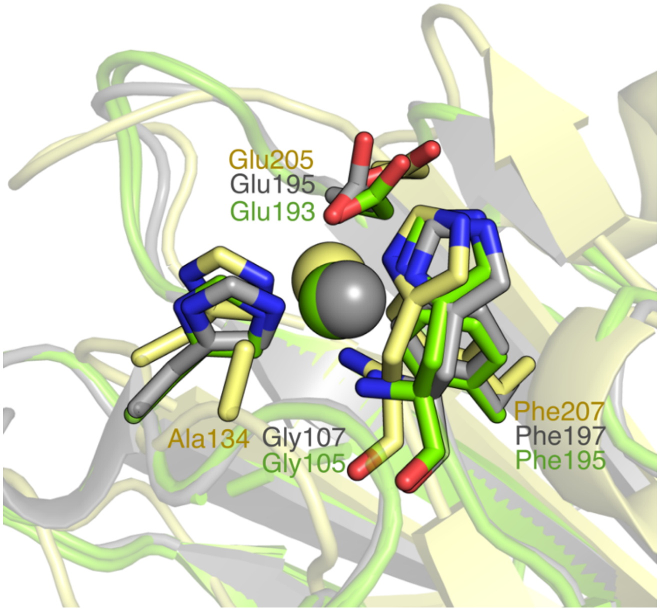

Figure 3.10: Second sphere conservation of residues between CjAA10BΔCBM, CjAA10A and TtAA10. *CjAA10BΔCBM (green) and TtAA10 (grey) have a second sphere glycine residue, whereas CjAA10A (yellow) has a second sphere alanine residue in its place. Amino acids within 5 Å of the active site copper are shown as sticks, with second sphere coordinating residues labelled in yellow (CjAA10A), green (CjAA10BΔCBM) and grey (TtAA10), active site copper ions are coloured consistently and are shown as spheres.*

3.8 Possible electron paths through CjAA10BΔCBM

A number of studies on LPMOs have used crystal structures to analyse potential electron transfer paths through proteins (see section 1.10.5) (Li et al., 2012; Paradisi et al., 2019; Beeson et al., 2015), although, this work has primarily been conducted in fungal AA9s. Although it is well known that LPMOs require delivery of electrons to the active site, the mechanism by which the electrons are delivered is largely unknown. As mentioned in Chapter 1, molecular docking studies have probed interactions between CDH and LPMOs, which have largely predicted the cytochrome domain of CDH interacting directly with the copper ion of LPMOs (Laurent et al., 2019; Felice et al., 2021). However, during activity on substrates, the active site is presumed to be obscured, preventing direct electron transfer to the copper ion in the substrate bound state. Therefore, it has been hypothesised that electron paths through LPMOs could supply electrons to the copper ion when enzymes are substrate-bound.

Knowledge of the structure of CjAA10BΔCBM has enabled putative electron paths through the protein to be studied. Examining possible electron paths could indicate mechanisms by which CjAA10BΔCBM could receive electrons from a protein partner. Possible electron paths were probed computationally by a final year undergraduate student, Kristian Want. Using the computer program EHPath (Teo et al., 2019), hole hopping pathways through the CjAA10BΔCBM structure to the catalytic copper were examined. EHPath identifies hole hopping pathways through redox active amino acids, tyrosine, tryptophan, cysteine and methionine, based on the mean residence time of charge transfer through these pathways (Teo et al., 2019). Efficient electron transfer relies on close proximity between redox active amino acids, most commonly tryptophan and tyrosine, and favourable orientation of aromatic rings. For CjAA10BΔCBM, Trp187 was defined as the terminal electron acceptor, and the EHPath algorithm ranked pathways to this residue using chains of redox amino acids as an electron hopping ‘bridge’.

From these analyses, two electron transfer paths were proposed. The mean residence times calculated using EH Path are shown in Table 3.3. These paths have been outlined in Figure 3.11, where distances have been defined as the shortest separation between aromatic side chains of Trp and Tyr residues. In the first path, shown in pink in Figure 3.11, electrons are proposed to be accepted by Trp135 and channelled through Trp119, Tyr118 and Trp102 to Trp187. Trp187 is proposed as the terminal residue in both paths and is positioned 5.4 Å from the copper ion, well within the distance required for efficient electron transfer. Path two, shown in blue in Figure 3.11, proposes electron transfer from Tyr156 to Trp187 via Tyr148. Distances between residues in path one are shorter on average, but distances between residues in both paths are sufficiently short to ensure efficient electron transfer between redox active residues, and both paths propose electron hopping routes that could efficiently provide electrons to the catalytic copper ion when CjAA10BΔCBM is bound to polysaccharide substrates. The presence of these paths in TtAA10 and CjAA10A were investigated (Figure 3.11B). Interestingly, path one is largely conserved between all three enzymes, however, path two is not conserved at all in TtAA10 or CjAA10A. Conservation of residues involved in the proposed path one in other AA10s substantiate hypotheses that this path could act to perform intraprotein electron transfer.

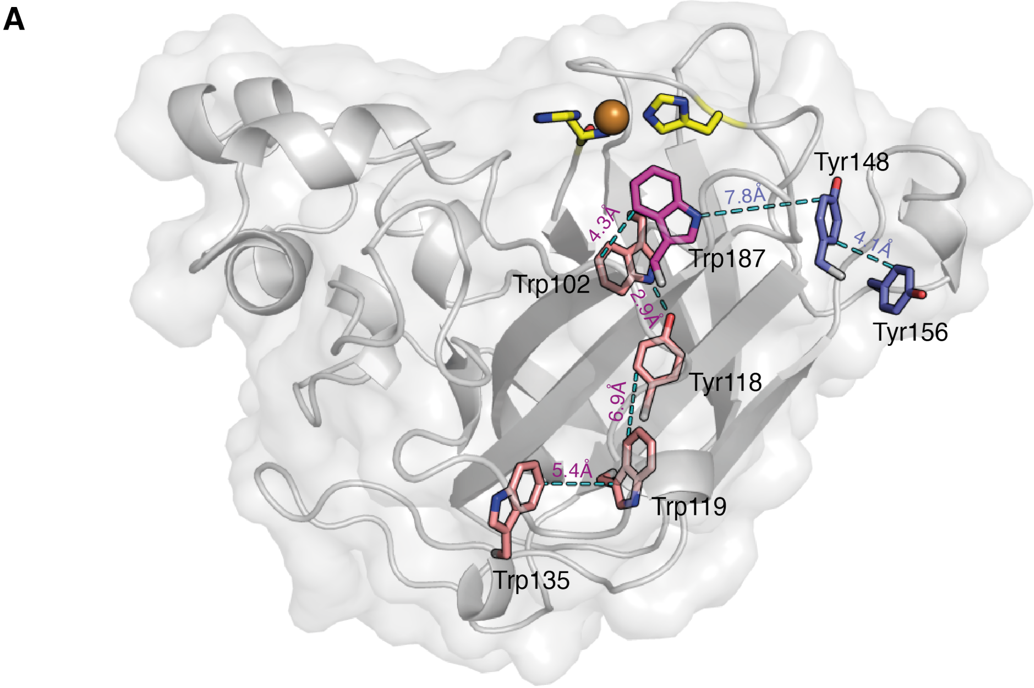

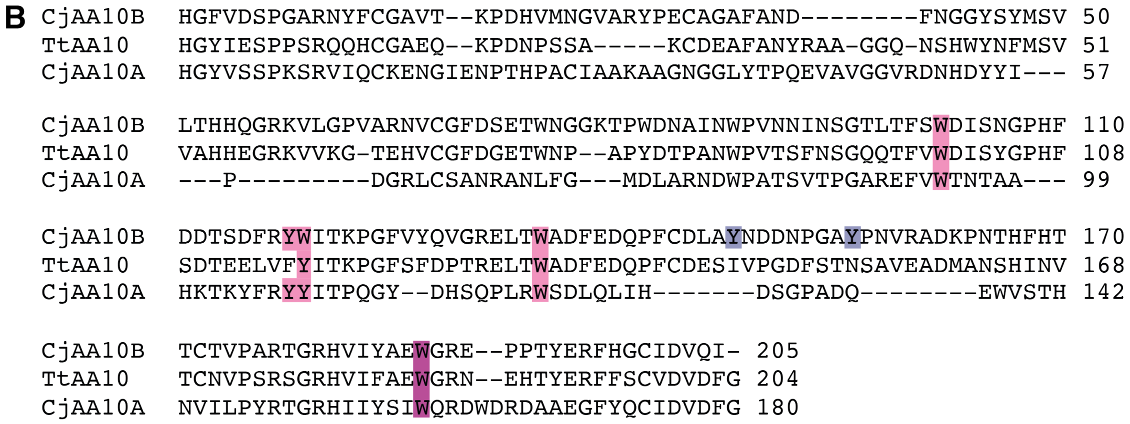

```
CjAA10B   HGFVDSPGARNYFCGAVT--KPDHVMNGVARYPECAGAFAND--------FNGGYSYMSV 50
TtAA10    HGYIESPPSRQQHCGAEQ--KPDNPSSA-----KCDEAFANYRAA-GGQ-NSHWYNFMSV 51
CjAA10A   HGYVSSPKSRVIQCKENGIENPTHPACIAAKAAGNGGLYTPQEVAVGGVRDNHDYYI--- 57

CjAA10B   LTHHQGRKVLGPVARNVCGFDSETWNGGKTPWDNAINWPVNNINSGTLTFSWDISNGPHF 110
TtAA10    VAHHEGRKVVKG-TEHVCGFDGETWNP--APYDTPANWPVTSFNSGQQTFVWDISYGPHF 108
CjAA10A   ---P---------DGRLCSANRANLFG---MDLARNDWPATSVTPGAREFVWTNTAA--- 99

CjAA10B   DDTSDFRYWITKPGFVYQVGRELTWADFEDQPFCDLAYNDDNPGAYPNVRADKPNTHFHT 170
TtAA10    SDTEELVFYITKPGFSFDPTRELTWADFEDQPFCDESIVPGDFSTNSAVEADMANSHINV 168
CjAA10A   HKTKYFRYYITPQGY--DHSQPLRWSDLQLIH-------DSGPADQ--------EWVSTH 142

CjAA10B   TCTVPARTGRHVIYAEWGRE--PPTYERFHGCIDVQI- 205
TtAA10    TCNVPSRSGRHVIFAEWGRN--EHTYERFFSCVDVDFG 204
CjAA10A   NVILPYRTGRHIIYSIWQRDWDRDAAEGFYQCIDVDFG 180
```

Figure 3.11: Possible electron transfer paths through CjAA10BΔCBM. **(A)** *Two possible paths are shown in pink and blue, both terminating at Trp187, shown in purple. Labelled residues are shown as sticks with blue dashes showing distances for electron transfer, defined as the shortest distances between aromatic side chain residues, the active site is shown as yellow sticks and the active site copper as a brown sphere.* **(B)** Multiple sequence alignment for proposed electron paths in CjAA10B, with CjAA10A and TtAA10. Conserved residues are coloured according to (A).

Electron Pathway	*Mean residence time (s)*
Y156-Y148-W187	1.1 x 10^{-3}
W135-W119-Y118-W102-W187	6.5 x 10^{-3}

Table 3.3: Mean residence times for hole-hopping pathways calculated by EH Path. *The first residue of each path is the electron acceptor and the terminal residue in both paths is W187, which is the terminal electron acceptor before the copper ion.*

Li *et al.* proposed a number of electron transfer paths through a *N. crassa* AA9, shown in Figure 1.17, one of which links a proposed CDH binding site to the catalytic copper ion. The sequence and structure of CjAA10BΔCBM are significantly different to those of NcAA9, so it was not possible to perform alignments to detect conserved residues between the two proteins. However, Tyr156 in CjAA10BΔCBM appears to be located at a similar position to Tyr215 in NcAA9, which is proposed to transfer electrons from a putative CDH binding site on the NcAA9 surface (Li et al., 2012). The electron paths between the tyrosine residues and the copper ions are not conserved between these two enzymes, but it is interesting that these similarly positioned surface exposed tyrosines are both proposed to be involved in electron transfer paths through LPMOs. However, as shown in Figure 3.11B, Tyr156 is not conserved in two structurally similar AA10s, so these hypotheses may not hold up in other AA10s. The proposed electron paths within CjAA10BΔCBM are only putative, and are not backed up experimentally, but they serve to demonstrate the potential electron hopping paths that could be used to deliver electrons to the active site from binding of protein partners to the protein surface away from the active site.

3.9 Summary

This chapter has described the structure of CjAA10BΔCBM, a truncated variant of CjAA10B that is lacking the C-terminal CBM domain. CjAA10B has been biochemically characterised in previous work (Gardner et al., 2014), but this chapter represents the first structural study of this enzyme.

The catalytic domain of CjAA10B, CjAA10BΔCBM, was expressed and purified from *E. coli*. The crystal structure of CjAA10BΔCBM showed a typical LPMO structure, with an immunoglobulin-like fold and histidine-brace coordination of the copper ion. Analysis of residues surrounding the active site showed a second sphere glycine in an unusual conformation, which could be linked to enzyme activity on cellulose. Structural comparisons with the structure of a cellulose active AA10 from *T. turnerae* show very similar active site and second sphere geometries. Both enzymes contain a second sphere glycine residue, reaffirming the importance of this residue for activity on cellulose. Interestingly, TtAA10 has a second non-catalytic copper ion, the copper coordinating residues are conserved in CjAA10BΔCBM, however, a second copper ion was not observed in CjAA10BΔCBM.

The structure of CjAA10BΔCBM was probed for possible electron paths that could allow speculation on electron transfer to the active site through the protein. These paths may allow electron transfer to the active site from a protein partner when LPMOs are substrate bound and the active site is obscured, so are of great importance. Two putative pathways were proposed that could act to transfer electrons from the protein surface, which would be accessible when substrate was bound to the active site. Residues for one of these paths were shown to be conserved in structurally similar AA10s, supporting these predictions. The presence of these possible pathways support hypotheses that binding sites may exist for protein partners in LPMOs.

Subsequent chapters will describe investigations of other proteins, or domains, that may act as LPMO activators in *C. japonicus*. The characterisation of CjAA10BΔCBM described here could help to inform LPMO-redox partner experiments in the future.

Chapter 4

CjX158E: a polyisoprenoid binding domain from Cbp2E

4.1 Introduction

As the LPMO field develops and more information is discovered on the mechanism of LPMO action, deciphering the true redox partner to LPMOs remains a key priority. As discussed in section 1.10, small molecule reducing agents are routinely used in enzyme cocktails as LPMO-activators, however, these can cause enzyme inactivation if enzymes are activated in the absence of substrate. The use of a protein partner to activate LPMOs may reduce non-specific activation and protein damage, and therefore prolong enzyme lifetimes.

As discussed in Chapter 1, CDH has been shown to act as a redox partner to fungal LPMOs (Phillips et al., 2011; Loose et al., 2016), additionally, glucose-methanol-choline oxidoreductases (Kracher et al., 2016; Garajova et al., 2016) and AA12 PQQ-dependent pyranose dehydrogenases (Varnai et al., 2018) have also been used as LPMO activators. There is no bacterial homologue of CDH, and so far, no protein partners to bacterial LPMOs have been characterised, despite the prevalence of LPMOs in biomass-degrading bacteria. Cbp2D and Cbp2E are two proteins from *C. japonicus* that have been proposed as LPMO redox partners (Gardner et al., 2014). Chapter 3 described the structure of an AA10 domain from the *C. japonicus* CjAA10B protein, subsequent work in this thesis will explore domains from Cbp2D and Cbp2E as LPMO redox partners, to characterise their function and investigate whether they can act as redox partners to CjAA10B.

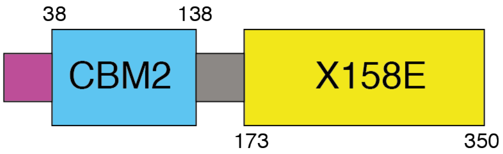

Figure 4.1: CjX158E is a domain from the Cbp2E protein. *Numbers indicate the domain boundaries at the amino acid level. Putative linkers are shown in grey and the signal sequence in purple*

Cbp2E is a secreted protein from *C. japonicus* that has been shown to be upregulated during growth on crystalline polysaccharides (Tuveng et al., 2016). Its deletion impeded bacterial growth on filter paper by up to 60 % (Gardner et al., 2014), suggesting a role in polysaccharide degradation. Cbp2E comprises an N-terminal signal peptide followed by a CBM2 domain which is connected to CjX158E via a flexible linker. A similar protein, with the same configuration of modules, exists in *Saccharophagus degradans*, Sde-1182 also contains a signal peptide, CBM2 and X158 domain (Vincent et al., 2010; Gardner et al., 2014). CjX158E is the C-terminal, 177 residue long domain of Cbp2E (Figure 4.1), which shares 46 % sequence similarity with SdX158 described by Vincent *et al.* (Vincent et al., 2010). The structure of the SdX158 domain has been solved, revealing an 8-stranded, antiparallel, β-barrel (Vincent et al., 2010). Two structures of SdX158 were determined with different cofactors, ubiquinone-8 (Ub-8) and octaprenyl pyrophosphate (OPP), both bound through the centre of the barrel using hydrophobic and Van der Waals forces (Vincent et al., 2010). SdX158 has been likened to the YceI family of proteins, a family of pH-induced periplasmic proteins that have also been found to associate with members of the Ub-8 biosynthetic pathway (Stancik et al., 2002).

The implication that CjX158E could associate with Ub-8, which is redox active and is a key electron transfer molecule in electron transport chains, would support a role for Cbp2E as an LPMO redox partner *in vivo*. This chapter will describe the steps taken to express, purify and solve the structure of the CjX158E domain of Cbp2E, in order to determine whether it has the biochemical properties to act as a redox partner to bacterial LPMOs.

4.2 Generation of the pSF1477-CjX158E construct

The coding region for CjX158E was amplified from the pET22-cbp2E plasmid and inserted into the pSF1477 vector using PIPE cloning (Klock and Lesley, 2009), the resulting vector is shown in Figure 4.2. The pSF1477 vector was used as it encodes an N-terminal SUMO tag from *Brachypodium distachyon* (BdSUMO). Solubility was a large problem when expressing the X-domain proteins and the addition of N-terminal SUMO domains is a common approach to encourage soluble protein expression. SUMO proteins are well-folding and are thought to enhance soluble protein expression through promoting correct folding of their appended proteins (Muller, S. et al., 2001). The BdSUMO tag encoded by this vector was chosen for a number of reasons, it has been shown to provide high expression and solubility enhancements on challenging proteins, but crucially, it can be cleaved very efficiently by the BdSENP1 protease following a glycine-glycine motif (Frey and Gorlich, 2014). Advantageously, cleavage with SENP1 does not leave any residual amino acids on the protein, which could impede further analysis. The BdSUMO tag is expressed with a N-terminal 14His tag, which is useful for purification, but can be cleaved off with the BdSUMO tag, resulting in untagged protein for analysis.

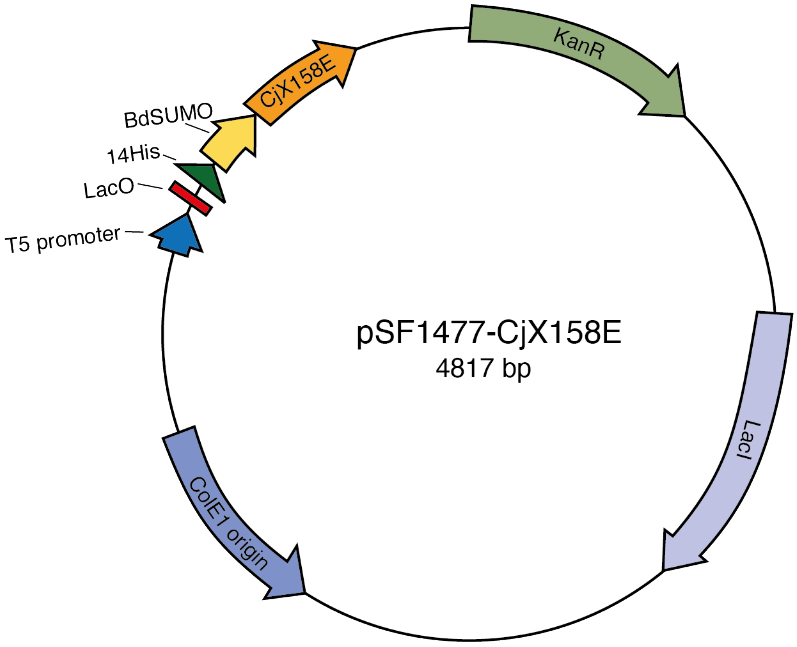

Figure 4.2: Plasmid map for the pSF1477-CjX158E construct. *The coding region for CjX158E is shown in orange, and is preceded by the BdSUMO tag, yellow, and the 14His tag, green.*

4.3 Recombinant expression and purification of CjX158E

BdSUMO-tagged CjX158E was expressed in BL21*(DE3) cells by induction with IPTG. Purified protein was obtained by nickel affinity chromatography, the BdSUMO tag was cleaved with BdSENP1 protease and CjX158E was further purified by nickel affinity chromatography followed by size exclusion chromatography. The presence of CjX158E (or BdSUMO-CjX158E) was confirmed throughout by SDS-PAGE (Figure 4.3A), and purified protein was further validated using ESI mass spectrometry. ESI-MS showed a peak at 18685 Da (Figure 4.3B), which is the expected molecular weight of CjX158E, confirming the production of the target protein.

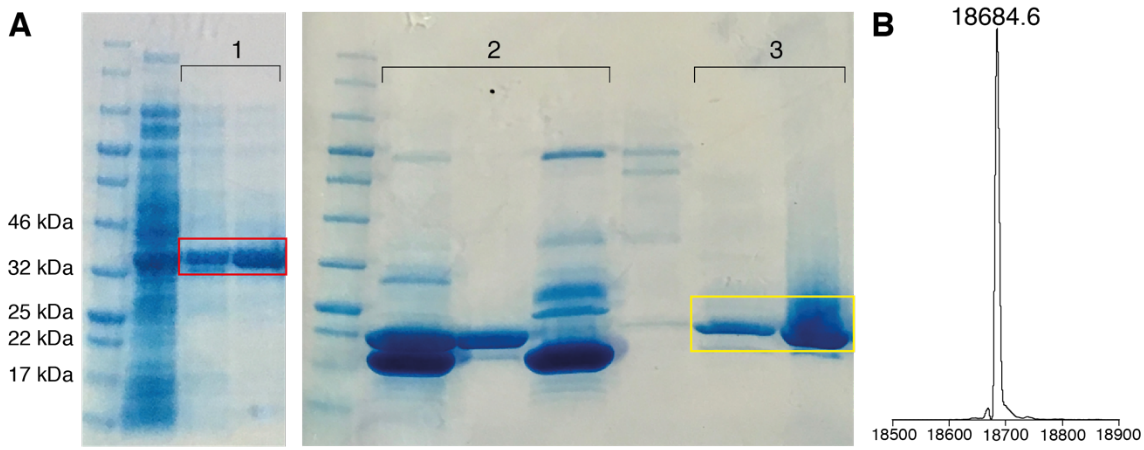

***Figure 4.3: Purification of CjX158E. (A)** SDS PAGE was used to check for protein presence: after nickel affinity chromatography (1), after tag cleavage (2), and after gel filtration (3). A band suspected to be the 32.1 kDa BdSUMO-CjX158E is shown in red, and the 18.7 kDa CjX158E is shown in yellow. **(B)** ESI-MS showed a peak at 18695 Da for CjX158E, confirming the exact expected mass of the protein.*

4.4 CjX158E exhibits interesting spectral properties

Interestingly, purified protein had a slightly yellow colour, which intensified with protein concentration (Figure 4.4). A previous study by Agrawal *et al.* recorded observations of a yellow colour corresponding to a pure sample of oxidised Ub-8, which disappeared following reduction (Agrawal et al., 2017). Additionally, ubiquinones have been shown to absorb at wavelengths within the 270-290 nm visible region, 275 nm for the oxidised ubiquinone and 290 nm for the reduced ubiquinol, and thus can be detected by UV-vis spectroscopy (Agrawal et al., 2017; Morton, 1958). Purified samples of CjX158E, in addition to displaying a vivid yellow colour, absorbed strongly in the 280 nm region when probed using UV-vis spectroscopy. It was difficult to determine whether this absorbance was due to high protein concentration or presence of a cofactor as large variations were seen between protein batches and the strong yellow colour diminished over time, resulting in inconsistencies in these observations. It could be hypothesised that the presence of a quinone molecule, as indicated by the yellow colour, was interfering with the typical absorbance spectrum expected from aromatic rings in the protein, however, these claims could not be consistently substantiated. The presence of a ubiquinone cofactor would not be surprising, as discussed in section 4.1, a structure of an X158 domain from *S. degradans* has been solved with a Ub-8 cofactor (Vincent et al., 2010). The spectroscopic observations noted here, although speculative, suggest the presence of a quinone molecule associated with the CjX158E domain, however, to substantiate these observations, experiments were subsequently conducted to investigate the presence of a quinone molecule.

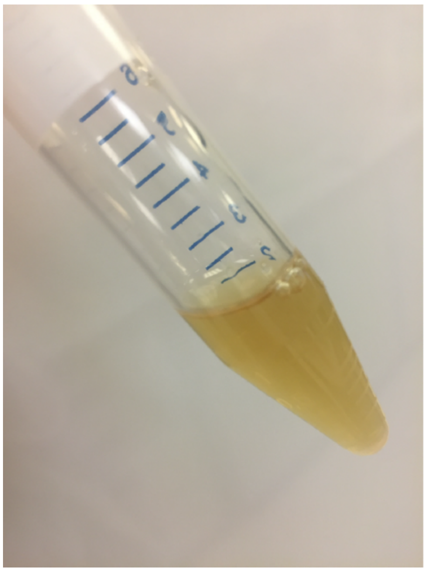

Figure 4.4: CjX158E exhibits a strong yellow colour*. A sample of CjX158E during purification at approximately 1 mg/mL in buffer comprising 50 mM Tris pH8, 200 mM NaCl.*

4.5 Native ESI-MS shows OPP as the cofactor

Following the interesting spectral observations of CjX158E, the presence of a cofactor was investigated using native MS. Cofactors detected in the *S. degradans* X158 domain were non-covalently associated at the centre of the β-barrel protein (Vincent et al., 2010), thus native MS was used to avoid displacement of a possible cofactor in CjX158E. The native MS spectrum of CjX158E (Figure 4.5) showed two peaks, one at 18682 Da, representing apo-CjX158E, which has an expected mass of 18685 Da, and the other at 19405 Da. The mass difference between the two peaks is 723 Da. Ub-8 (Figure 4.6A) has a molecular weight of 727 Da, whereas OPP (Figure 4.6B), a quinone precursor, has a molecular weight of 722 Da. From this, it appears there is a mixed population of apo- and bound protein, and the bound fraction represents protein with the pyrophosphate precursor, OPP. These results do not support the observations outlined in section 4.4, as the OPP molecule is not expected to be coloured. It could be that a small portion of protein contains the Ub-8 cofactor, but the bulk of protein contains the OPP cofactor due to slow biosynthesis of Ub-8 in *E. coli*, resulting in accumulation of the isoprenoid precursor. In the *S. degradans* X158 structure, Vincent *et al*. only observed the Ub-8 molecule after growth in minimal media (Vincent et al., 2010). It could be that in minimal media, where the growth of the bacteria is slowed, the Ub-8 biosynthetic pathway is not limited, therefore, the process is not halted at the pyrophosphate precursor. However, at this point, with the exception of the yellow colour, which has only been loosely associated with Ub-8, there was no other evidence to support the presence of a Ub-8-bound species.

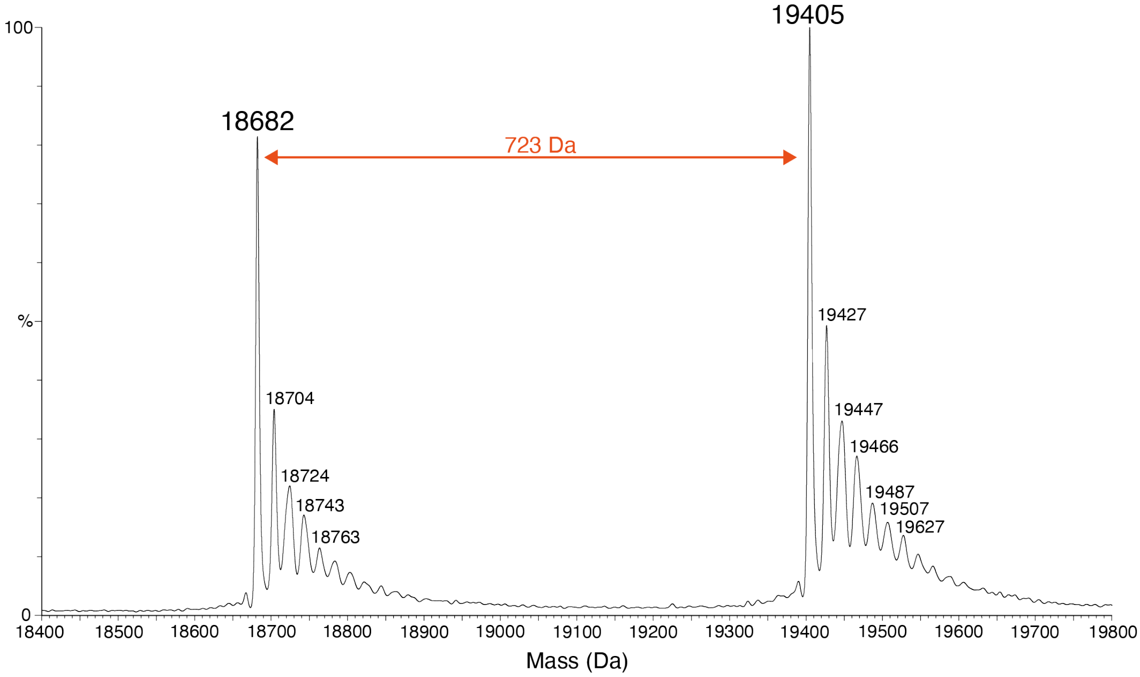

Figure 4.5: Native mass spectrum for CjX158E. *Two prominent peaks were present, at 18682 Da corresponding to apo-CjX158E, and one at 19405 corresponding to the OPP-bound form of CjX158E.*

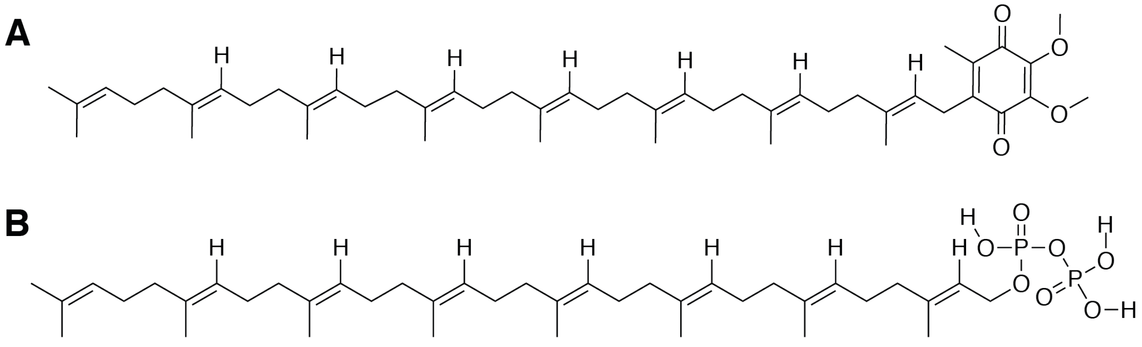

Figure 4.6: Chemical structures of possible CjX158E cofactors. (A) *Ubiquinone-8.* ***(B)*** *Octaprenyl pyrophosphate.*

4.6 Crystallisation of CjX158E and diffraction data collection

CjX158E was crystallised using JCSG Core I-IV screens. Crystals formed in a number of conditions, and multiple crystals were exposed to X-rays. In many of the crystals screened, diffraction data was weak and low resolution, with some crystals exhibiting considerable anisotropy. The best data set was determined by examining statistics for signal to noise (I/σ), R-factors and completeness. For the chosen data set, crystals, shown in Figure 4.7, formed in 0.1 M sodium acetate pH 4.5 and 20 % polyethylene glycol (PEG) 3000. Diffraction data were collected from these crystals at the European Synchrotron Radiation Facility on beamline MASSIF-1. Crystals diffracted to roughly 2.2 Å.

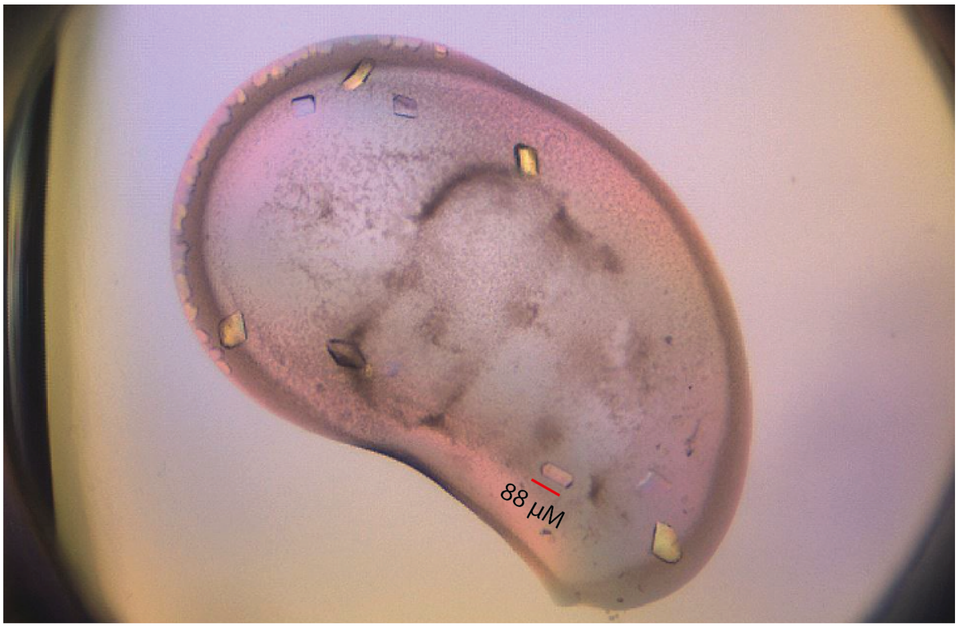

Figure 4.7: Crystals of CjX158E. *Crystals formed in 0.1M sodium acetate pH 4.5 and 20 % PEG 3000.*

To solve the structure of CjX158E, reflection data were initially processed using the CCP4i2 suite of programmes (Potterton et al., 2018). Initial analyses of the CCP4i2-processed data revealed problems with the CjX158E data set, the space group was predicted as $P4_1\ 2\ 2$ and L-tests performed in AIMLESS consistently showed warnings of twinning (Figure 4.8A). L-tests examine the cumulative probability distributions for reflections close together in reciprocal space, which can be indicative of twinned data sets (Padilla and Yeates, 2003). Following data processing in $P4_1\ 2\ 2$, a molecular replacement solution could not be reached. However, closer inspection of the diffraction data showed close together, overlapping spots (Figure 4.8B). This pattern was attributed to orientation of the unusually long unit cell (Figure 4.8C) in the X-ray beam, with the axis aligned with the beam, resulting in overlapping spots, since there is an inverse relationship between the cell dimensions and distance between spots. The closely-packed spots were misinterpreted by the software as twinned data. Following this, data were reprocessed using XDS (Kabsch, 2010), which indicated strongly that the space group was $P4_3$, and the XDS-processed data were re-input into CCP4i2 (statistics shown in Table 4.1). Despite the difficulties resulting from the long unit cell, after reindexing with XDS, the data were taken forward to achieve a convincing molecular replacement solution.

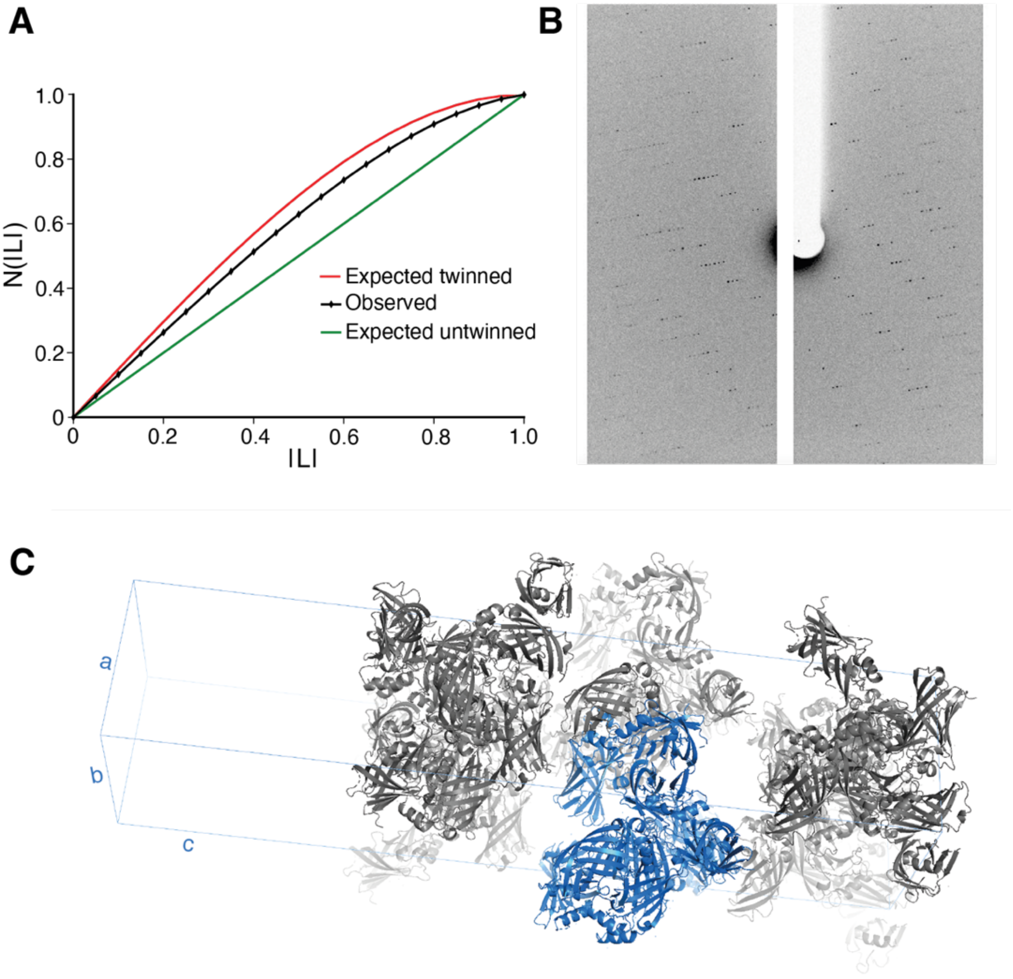

Figure 4.8: Indications during data processing suggesting data were twinned. (A) *L-tests performed in AIMLESS plot the cumulative probability distribution, N(|L|) of the parameter |L|, where L is defined as the difference between two intensities divided by their sum.* ***(B)*** *Diffraction data showed close together, overlapping spots.* ***(C)*** *The unit cell, shown as a blue rectangle, was unusually long. Cartoon representation of molecules in the unit cell are shown, with one asymmetric unit shown in blue. 10 molecules are expected to occupy the asymmetric unit, and for simplicity, 6 are shown here.*

Dataset		*CjX158E*	
Space Group		$P4_3$	
Cell dimensions			
a	α	74.9 Å	90°
b	β	74.9 Å	90°
c	γ	339.1 Å	90°
Resolution		12.05-2.20 Å (2.24-2.20 Å)	
Rmerge		0.073 (0.743)	
Rpim		0.033 (0.497)	
Observed/ unique reflections		534698/92808	
Mean I/σ		16 (1.4)	
Half set correlation CC(1/2)		0.997 (0.739)	
Completeness		98.8 % (90.6 %)	
Multiplicity		5.8 (2.9)	

Table 4.1: Statistics for the CjX158E dataset. *Statistics for the highest resolution shell are shown in parentheses.*

For molecular replacement, the X158 domain from *S. degradans* (PDB ref 2X32) was used as the search model. SdX158 was the most similar model available within the PDB, with CjX158E and SdX158 sharing 46 % sequence similarity. The model was constructed within CCP4i2 using Chainsaw (Stein, 2008) to prune non-conserved residues back to the peptide backbone. The molecular replacement solution, which presented 10 molecules of CjX158E in the asymmetric unit (Figure 4.9), in line with expectations from the unit cell dimensions, required density modification followed by model rebuilding to generate an acceptable starting model. The starting model was deemed workable, as monomers were sensibly modelled, with no clashes, and R-factors were seen to decrease as more of the structure was built. Following density modification and model rebuilding, 9 and a half monomers were rebuilt, the 10th monomer showed only partial density, mainly for the well-ordered β-sheet regions. Iterative rounds of model building and refinement produced a structure with a final resolution of 2.2 Å. The final refinement statistics are shown in Table 4.2. In the finished model only one monomer, chain I, was completely modelled, other chains lacked density for some flexible loop regions, which will be discussed further later. Although a model for the structure of CjX158E was achieved, throughout the map, especially in less-ordered regions, there were areas of low data quality, indicated by poor electron density. In order to obtain a better structure, more crystals would be needed, and data collection optimised to orient the crystals in the X-ray beam. However, due to reproducibility issues with CjX158E crystallisation, it was not possible to recrystallise the protein to obtain a better data set.

Dataset	*CjX158E*
Resolution	42.43-2.20 Å
Number of reflections (working/free sets)	92690/4745
R-factor/R-free	0.258/0.318
RMS deviations	
Bonds	0.0098
Angles	1.790
Average B factors	38.4
B-average -protein	40.3
B-average -ligand	43.7
B-average -waters	27.6

Table 4.2: Summary of the final refinement statistics for the CjX158E structure.

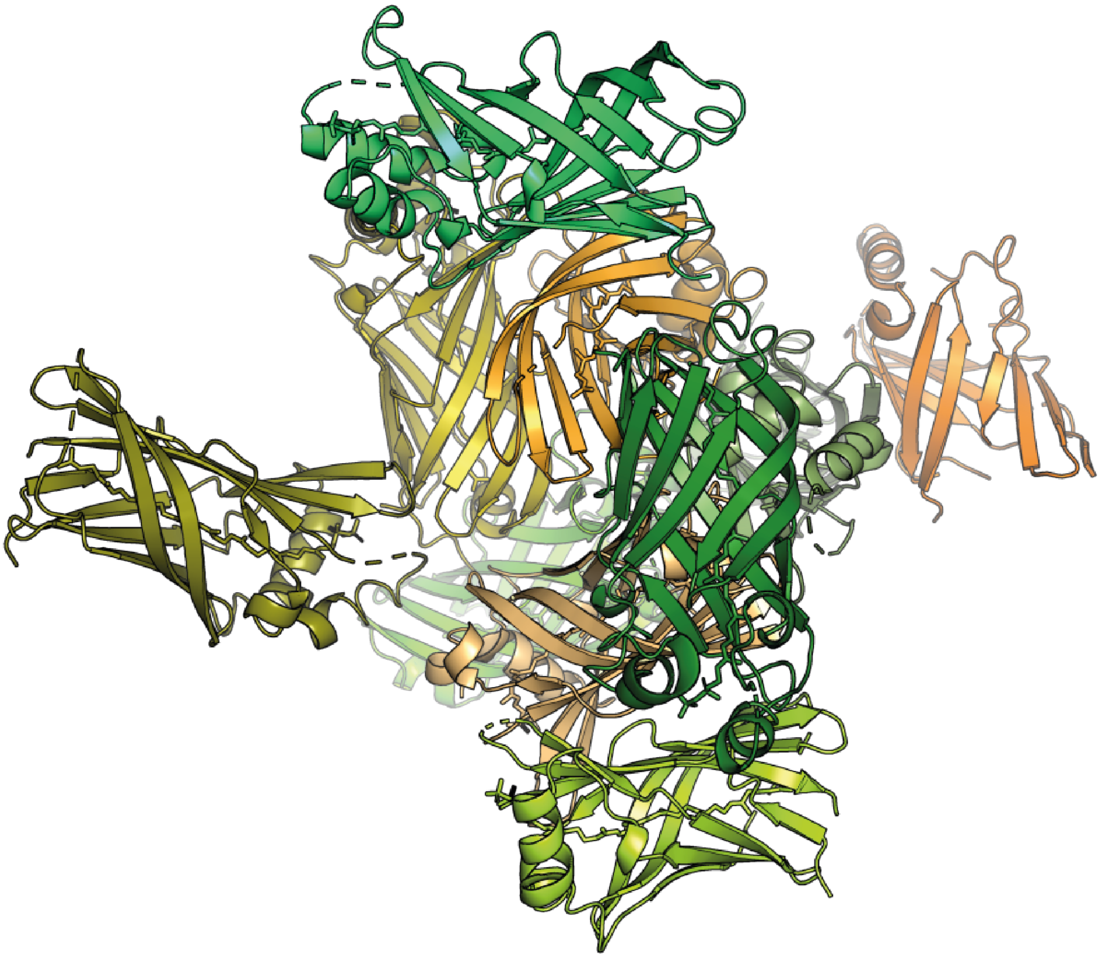

Figure 4.9: The asymmetric unit contained 10 molecules of CjX158E. *9 molecules of CjX158E were almost entirely modelled, shown as cartoons, with the OPP molecule shown as sticks. The 10th molecule was only partially modelled and is shown on the extreme right in orange.*

Throughout refinement and molecular modelling processes, additional density was seen within the map (shown in Figure 4.11), in the same position for each monomer of CjX158E, with the exception of the partially modelled tenth chain. This extra density was in the same position as the cofactor in the SdX158 structure, with a long stretch of density running down the middle of the β-barrel protein. A molecule of OPP was modelled into this density in nine chains, density at the tenth chain was too weak to support the presence of a cofactor. In the nine well-modelled chains, the density for the head group strongly supported the presence of the pyrophosphate precursor instead of the ubiquinone molecule, supporting the results seen by native MS (section 4.5).

4.7 CjX158E is a β-barrel protein with an OPP cofactor

The final structure of CjX158E (Figure 4.10) shows it to be a β-barrel protein, like SdX158 and other YceI-like proteins. The barrel is made up of β-sheets, with a series of loops and helices forming the barrel opening. The sheets are well ordered, with hydrophobic residues pointing into the centre of the cavity, and polar residues on the external faces. Hydrophobic residues within the barrel appear to be responsible for coordinating the isoprene tail of OPP, and the phosphate head groups are coordinated by residues at the barrel opening (Figure 4.11).

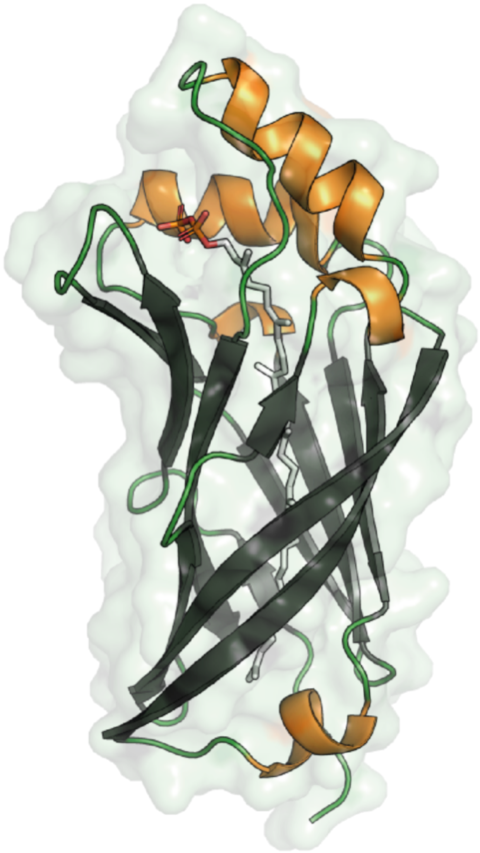

Figure 4.10: CjX158E is a β-barrel protein. *CjX158E forms a β-barrel (grey) with α-helical regions (orange) at the opening to the barrel. A molecule of OPP, shown as white sticks, spans the inside of the barrel.*

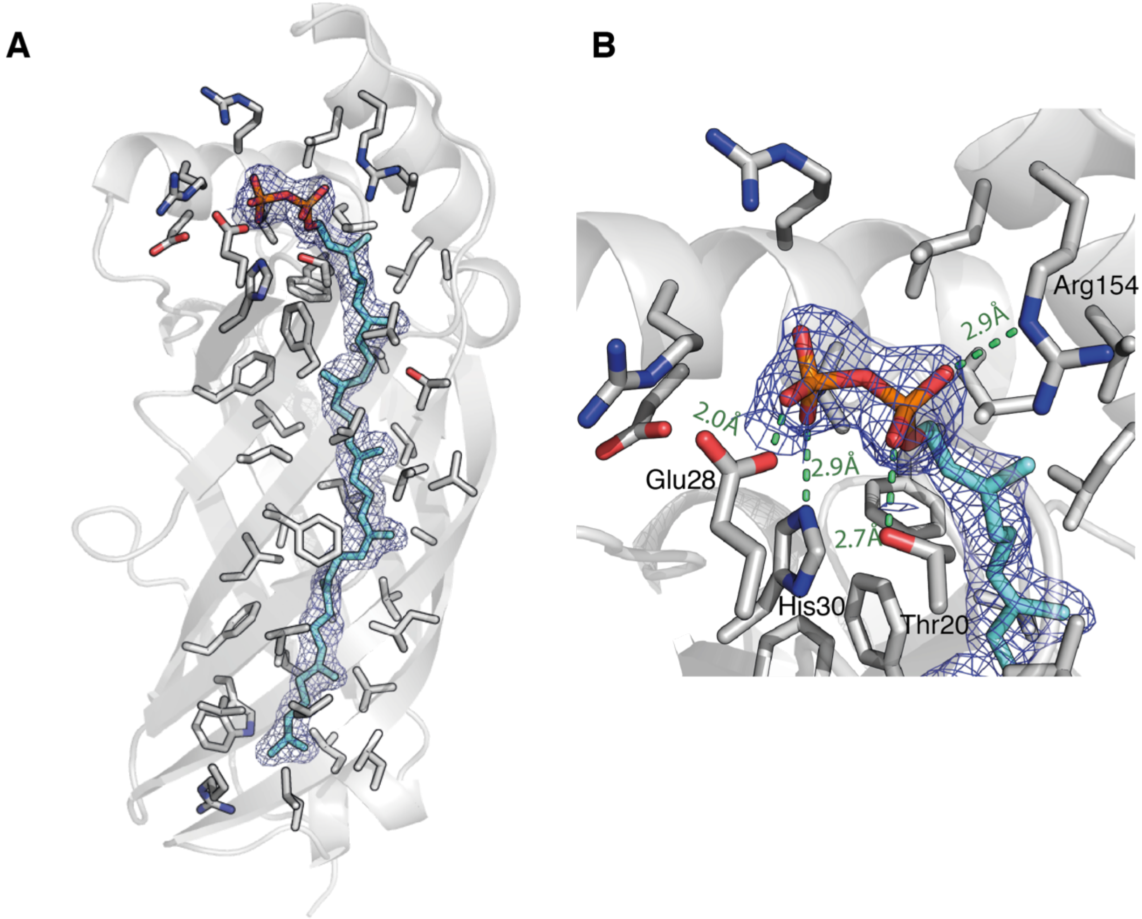

Figure 4.11: Electron density supports the presence of a non-covalently bound OPP molecule. (A) *The cavity of the β-barrel is lined with hydrophobic residues. The OPP molecule is shown as sticks with cyan carbons and other atoms coloured according to atom type. CjX158E is shown in grey and residues within 5 Å of the cofactor are shown as sticks. Electron density for the OPP molecule, represented by the 2Fo-Fc map, is shown as blue mesh.* ***(B)*** *The pyrophosphate head group is coordinated by residues in α-helices at the top of the barrel. Proposed interactions are shown as green dashes with distances labelled.*

The OPP cofactor was modelled into the cavity of the β-barrel. The electron density for the cofactor, shown in Figure 4.11, spans the length of the molecule and strongly supports the presence of the pyrophosphate cofactor. The polyisoprene tail comprises 8 repeating units that run though the length of the barrel. Nonpolar residues span the central cavity of CjX158E and coordinate the isoprene tail through hydrophobic interactions. The coordination of the pyrophosphate cofactor is shown in Figure 4.11B. In chain I, the only fully modelled chain, it appears that Thr20, Glu28, His30 and Arg154 are involved in coordinating the pyrophosphate head group. It is important to note that, due to the weak density at the top of the β-barrel across all ten chains, the interactions with the head group cannot be predicted with certainty. However, it is evident, that at the opening of the barrel, a large number of charged and polar residues are present, which could play a role in coordinating the pyrophosphate head group.

As mentioned above, the helices and loops, which form the opening of the barrel, showed less well defined electron density in the maps relative to the well-structured core. These regions were only fully modelled in chain I, which is shown in structural figures throughout this chapter. The regions that showed significant flexibility, indicated by drastic variations between molecules in the asymmetric unit and high B-factors, occurred around three loops at the opening of the β-barrel (Figure 4.12). Loop one spans residues 21-29 and connects sheets two and three. Loop two, residues 58-65, comprises the top of a loop, moving into the start of the first helix, and contains Arg61, which is found in close proximity to the pyrophosphate head groups in most monomers. Loop 3, residues 148-163, forms the upper most part of the protein, this region showed the weakest electron density across the ten monomers, suggesting that it is highly flexible. The position of these three flexible regions, at the barrel opening and near the pyrophosphate head group, could imply a role in restricting access of to the cavity, and stabilising the non-covalently bound cofactor.

The presence of the OPP molecule in the crystal structure, corroborates the native MS data (section 4.5). Additionally, the SdX158 structure solved with the OPP molecule was from protein grown in rich media, like CjX158E. Only when grown in minimal media was the Ub-8 molecule observed in SdX158 (Vincent et al., 2010). Therefore, the presence of the OPP in CjX158E was not entirely surprising given the conditions under which the protein was expressed.

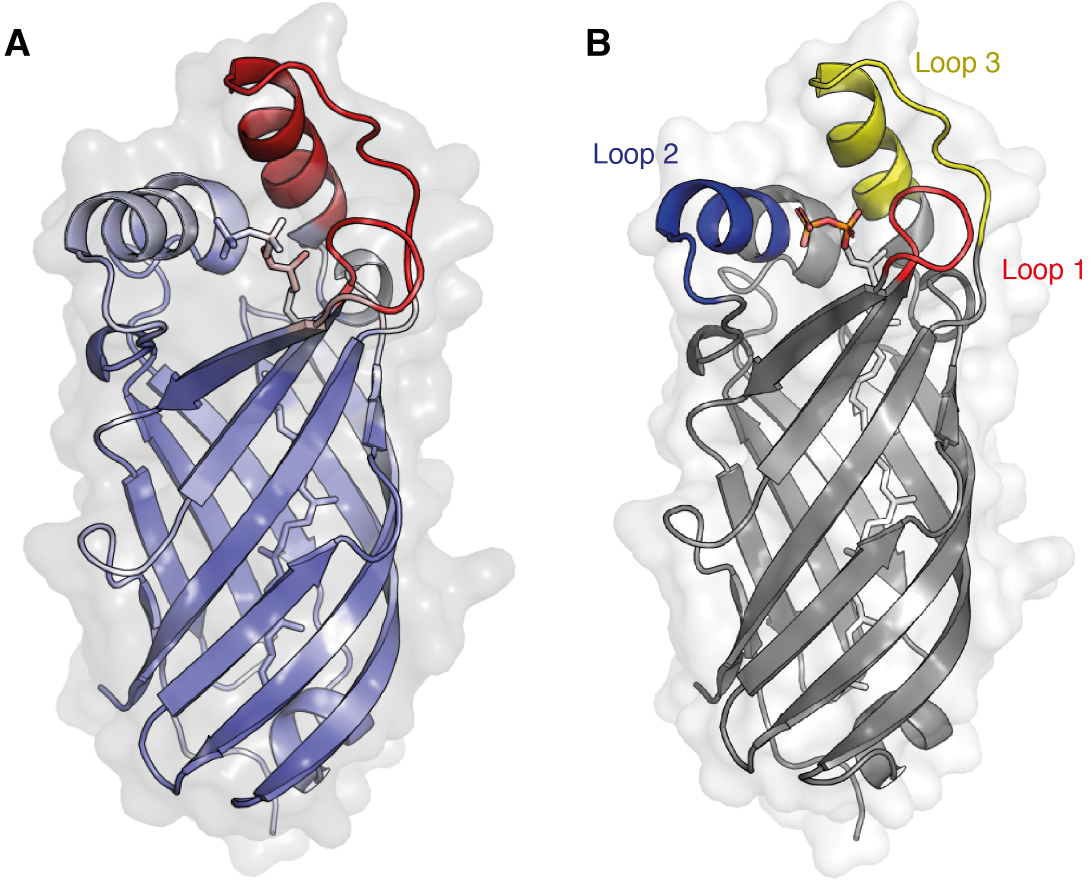

***Figure 4.12: Flexible regions of CjX158E. (A)** CjX158E chain I coloured according to B-factors, from low to high B-factors on a gradient of blue, white, red. **(B)** Three flexible regions of CjX158E are shown in red, blue and yellow. Protein structures are represented as cartoons with OPP molecules shown as sticks*

4.8 Structural comparison with the PDB

The protein comparison server DALI was used to perform structural comparisons against the PDB (Holm, 2019). As expected, CjX158E aligned most closely with the structures of the X158 domain from *S. degradans*. From these structures, the highest similarity was for the OPP-bound structure (PDB ref 2X32). The superposition of CjX158E with SdX158 is shown in Figure 4.13. The two proteins superpose well, spanning 174 residues with an rmsd of 1.1 Å. The configuration of the β-barrels appear very similar, with only minor differences and a large conservation of hydrophobic residues within the cavity. Interestingly, the most prominent difference is in the positioning of the cofactor. The units of the C40 isoprene tail of CjX158E occupy almost identical positions within the barrel, however, the tail is shifted an entire unit into the cavity in the structure of CjX158E (Figure 4.13B). In the SdX158 structure there is a valine residue, Val85, at the bottom of the barrel, blocking the OPP molecule from moving further into the cavity. Val85 is replaced by a leucine residue in CjX158E and is positioned differently in the channel (Figure 4.13C). As a result of the different cofactor positions, the phosphate head groups of the CjX158E cofactor are positioned further into the cavity and make different contacts to those observed in the SdX158 structure (Figure 4.13D). The SdX158 pyrophosphate head group is suggested to form contacts with Lys18 and Arg57 (Vincent et al., 2010), and this arginine residue is conserved across other homologues and is involved in coordinating the cofactor in other OPP-bound β-barrel proteins (Handa et al., 2005). Although the lysine and arginine residues are conserved in CjX158E (Arg61 and Lys22 in CjX158E), they do not appear to be involved in coordinating the head group of the OPP molecule, due to its different position in the crystal structure. In the CjX158E crystal structure, Thr20, His30, Glu28 and Arg154 are within hydrogen bonding distances of the phosphate oxygen atoms. The glutamate, histidine and arginine residues are conserved in SdX158. The glutamate and histidine residues show similar rotamers, but are not involved in coordinating the phosphate groups due to the different positioning of the OPP molecule within the cavity.

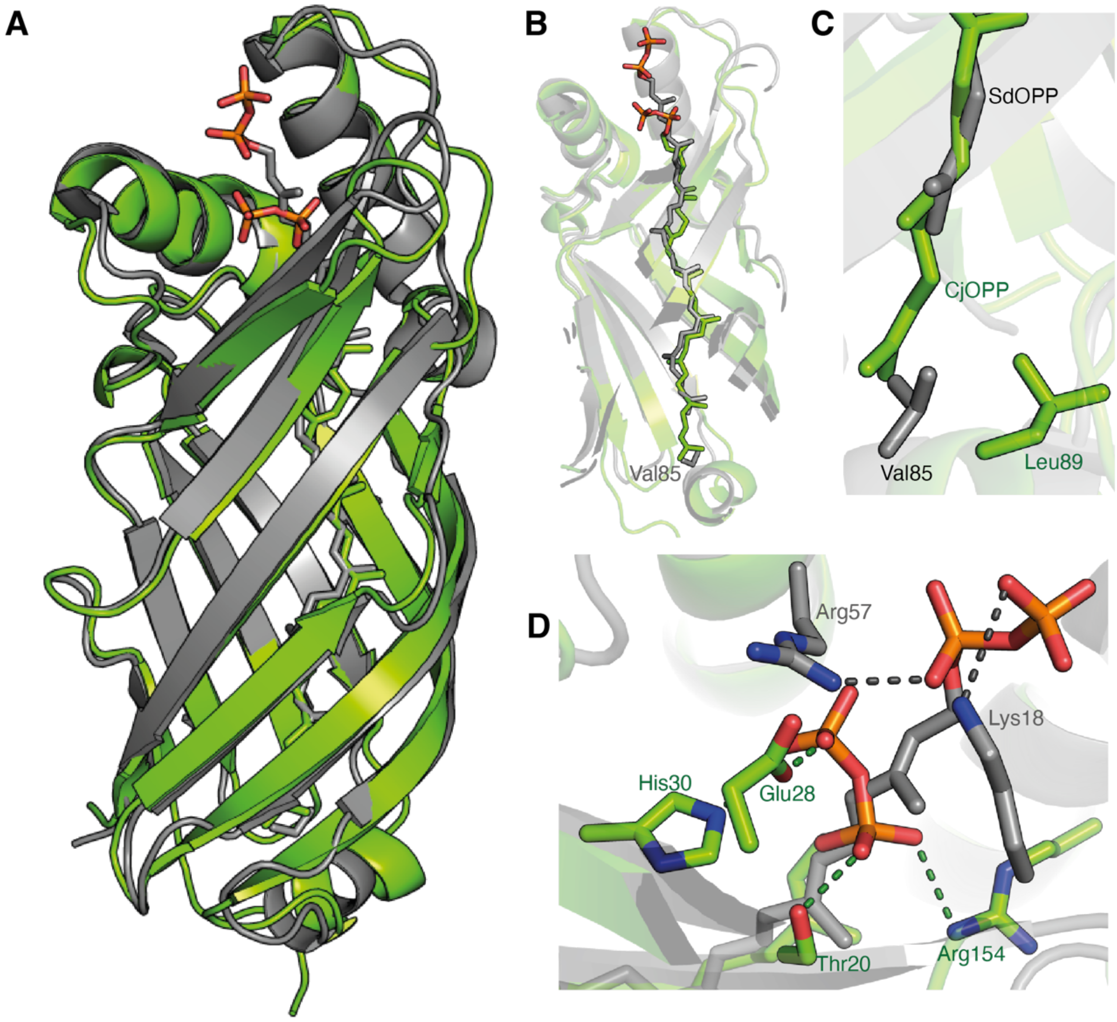

Figure 4.13: Structural comparison of CjX158E with SdX158-OPP bound structure. ***(A)*** *Superposition of CjX158E (green) with OPP-bound SdX158 (grey) (PDB ref 2X32), OPP molecules are shown as sticks, with green or grey carbon atoms and other atoms coloured according to element type .* ***(B)*** *OPP molecules occupy similar conformations in the CjX158E and SdX158 structures, however, in CjX158E the cofactor is shifted one isoprene unit further into the barrel.* ***(C)*** *Residues at the bottom of the barrel allow different positioning of the OPP cofactor in the two structures.* ***(D)*** *Coordination of the phosphate head groups is mediated by different residues due to the different cofactor positions in the barrel.*

CjX158E also aligned with a number of other β-barrel proteins, mostly from the YceI protein family, which are putative periplasmic proteins thought to bind lipids or isoprenoids (Stancik et al., 2002; Handa et al., 2005). The next best alignment was with a YceI protein from *Pseudomonas syringae*, which has a molecule of Ub-8 bound (PDB ref 3Q34). Although there is no publication linked to this PDB entry, it is clear that this structure was solved with selenomethionine residues, implying that the protein had been expressed in minimal media supplemented with selenomethionine. The presence of Ub-8 in this structure supports the hypothesis that the Ub-8 cofactor is only present in the protein when expressed in minimal media. The structures of PsYceI, and a number of other proteins that came up in the structural alignment, all contain cofactors with eight-unit isoprene tails (Ub-8, OPP, octaprenylphenol), and show the cofactor bound in the same position as the SdX158 cofactors, with no structures showing the cofactor positioning shown in CjX158E (Handa et al., 2005; El-Halfawy et al., 2017). Figure 4.14 shows CjX158E aligned to PsYceI and SdX158, the two structural alignment hits that had a bound Ub-8 molecule. The head groups of the Ub-8 molecules of SdX158 and PsYceI exhibit very similar conformations, which are very different to the head group position in CjX158E. The cofactors are both shifted one isoprene unit higher in the β-barrel relative to the cofactor seen in the CjX158E structure. The bottom of the β-barrel in these structures appear to be more closed, often a valine or isoleucine residue occupies the position that the terminal end of the OPP molecule in the CjX158E structure does.

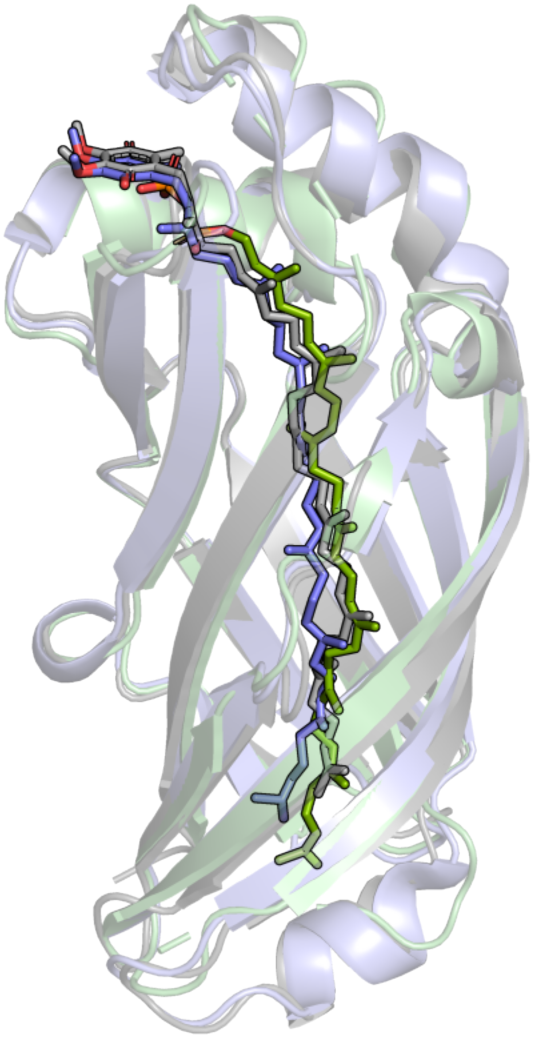

Figure 4.14: Multi-alignment of CjX158E to other proteins. *CjX158E (green) aligns to SdX158E (grey) (PDB ref 3X34) and PsYceI (blue) (PDB ref 3Q34). Protein structures are shown as cartoons and cofactors are shown as sticks with green, grey or blue carbons and other residues coloured according to atom type.*

4.9 Attempts to obtain the quinone cofactor

Ubiquinone-8 bound structures of CjX158E homologues have resulted from proteins expressed in minimal media (Vincent et al., 2010). It was hypothesised that overexpression in *E. coli* could lead to a larger population of the OPP-bound species, due to shortages of the quinone head group required for the biosynthesis of Ub-8. Therefore, slower expression in minimal media may result in lower protein expression levels, and potentially a larger proportion of Ub-8-bound protein. To investigate this further, CjX158E was expressed in M9 minimal media. Unfortunately, although cell growth was slowed, protein expression levels were not dampened. Purified protein was also yellow and native MS analysis showed the presence of a +723 Da cofactor, in agreement with results seen from protein expression in rich media. From these experiments, it was not possible to obtain a Ub-8 bound form of CjX158E

Following these difficulties to obtain quinone-bound CjX158E, the nature of the true cofactor was considered. These failures, combined with structural comparisons that showed the CjX158E OPP shifted down one isoprene unit in the β-barrel, prompted discussions over whether Ub-8 was the natural cofactor of CjX158E. Although the structures of a number of similar proteins have been determined, the true physiological cofactor of these proteins have not been confirmed either (Vincent et al., 2010; Handa et al., 2005; El-Halfawy et al., 2017). Although *E. coli* predominantly uses Ub-8 (Collins and Jones, 1981), less is known about the preferred ubiquinone tail length in *C. japonicus*. *C. japonicus* was originally characterised as a strain of *Pseudomonas fluorescens*, before recharacterisation as *C. japonicus* (Humphry et al., 2003). Although the ubiquinone preference of *C. japonicus* is uncharacterised, it is known that *P. fluorescens* uses ubiquinone-9 (Ub-9) (Collins and Jones, 1981). Through conversations with collaborators (Jeffrey Gardner, University of Maryland) it was suggested that *C. japonicus* may also use Ub-9. *E. coli* do not make Ub-9 (Collins and Jones, 1981), therefore this cofactor would not be expected to be present following protein expression in *E. coli*. Substitution of a 9-unit long isoprene cofactor for an 8-unit long cofactor could explain the unusual positioning of the OPP cofactor in CjX158E. If the true cofactor were to be Ub-9, then the extra isoprene unit could position the head group further out of the barrel in a similar configuration to those seen in the structure of similar YceI-like proteins. Following these hypotheses and discussions, expression of CjX158E from *C. japonicus* was proposed, as a method to obtain the natural cofactor of CjX158E.

4.10 Isolation of Cbp2E from *C. japonicus*

In order to probe the natural cofactor of CjX158E, protein purification from *C. japonicus* was proposed. For this, a *C. japonicus* strain containing a constitutively expressed Cbp2E followed by a C-terminal 6His-tag (a kind gift from Jeffrey Gardner, University of

Maryland, Baltimore) was used. Cbp2E has an extracellular localisation signal, therefore it was expected to be secreted from *C. japonicus*. The 6His-Cbp2E *C. japonicus* strain was grown in MOPS minimal media, shown to be optimal for *C. japonicus* growth (Gardner and Keating, 2012), alongside wild-type *C. japonicus* and the cellular compositions and secretomes were compared using SDS-PAGE (Figure 4.15A). From SDS-PAGE, it was not clear if Cbp2E-6His, which has a predicted molecular weight of 37.2 kDa, was expressed, and there were no discernible differences between the wild-type and mutant strains. Subsequently, these experiments were repeated and the presence of a 6His-tagged protein was examined using a Western blot, in which the gel was probed with an anti-his antibody (Figure 4.15B). The Western blot clearly showed the presence of a 6His tagged protein, which was present in the Cbp2E-6His strain and not the wild-type. These result suggest that the Cbp2E-6His strain expressed some 6His-tagged protein, most likely Cbp2E, that was present in the media, cell lysate and cell pellet. Attempts were made to scale up the growth of the Cbp2E-6His *C. japonicus* strain to purify Cbp2E-6His by affinity chromatography. Unfortunately, it was not possible to scale up the growth of *C. japonicus* sufficiently to make enough protein to purify using affinity chromatography, and all attempts resulted in the purification of other *C. japonicus* contaminant proteins that were more strongly expressed than Cbp2E-His.

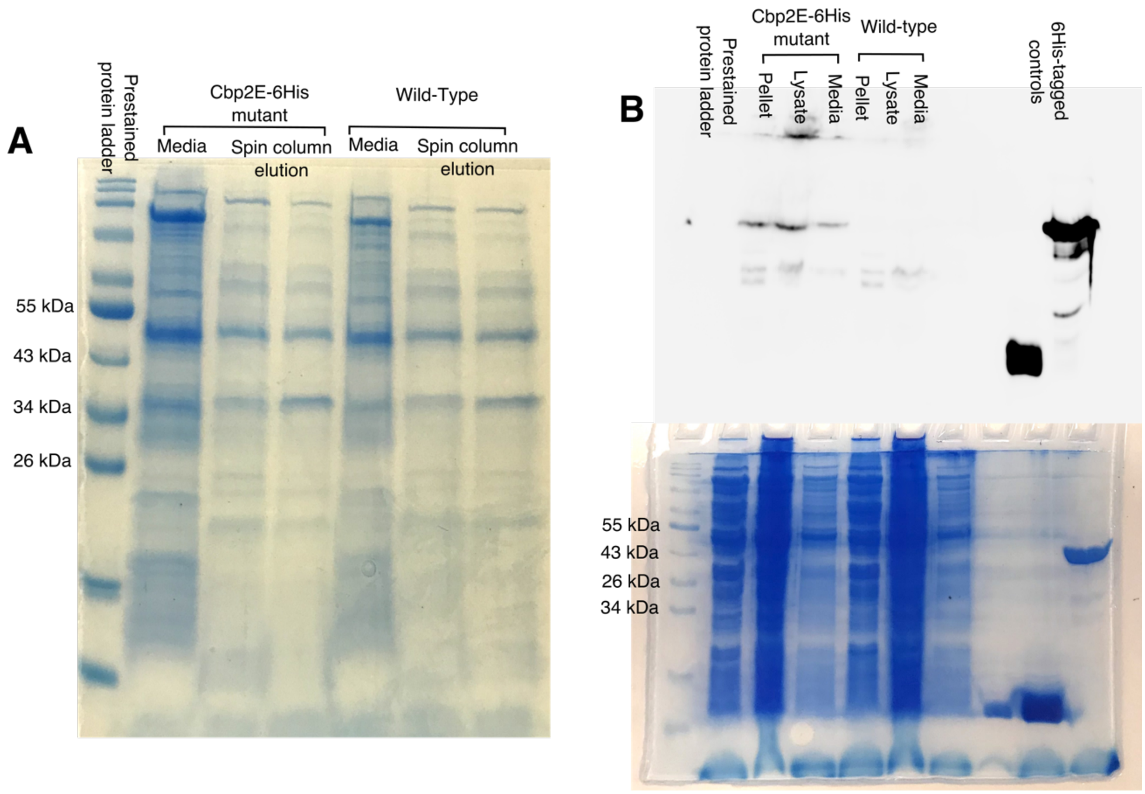

Figure 4.15: Detection of Cbp2E from C. japonicus. ***(A)*** *SDS-PAGE gel following using nickel affinity spin columns to purify proteins from the C. japonicus growth media.* ***(B)*** *Western blot using anti-his antibodies and SDS-PAGE gel to show presence of 6His-tagged proteins from 6His-Cbp2E and wild type C. japonicus strains.*

4.11 Molecular docking of proposed CjX158E cofactors

Despite utilising a variety of methods, attempts to isolate quinone-bound CjX158E, or Cbp2E from *C. japonicus*, were unsuccessful. Therefore, molecular docking studies were performed to investigate how different cofactors would occupy the β-barrel cavity if they were to bind CjX158E. Docking was performed using Autodock Vina (Trott and Olson, 2010), using an apo-chain I model for CjX158E. OPP, Ub-8 and Ub-9 were docked into the model and the structures were visualised using PyMol. The structures were manually inspected, and the most probable conformations were chosen by eye, eliminating any unlikely conformations (Figure 4.16). These models show the cofactor binding through the β-barrel, but all predictions show the cofactor positioned lower in the cavity than would be expected from the observed binding of OPP in the CjX158E crystal structure. Additionally, these structures show cofactors binding significantly lower into the β-barrel than are seen for other protein structures like this in the PDB.

Although these models show predictions for the binding of different cofactors in CjX158E, they do little to inform the nature of the protein-cofactor interaction, or shed light on the true cofactor of CjX158E. The poor quality of these predictions could be due to the poor data quality for the regions at the opening of the β-barrel, where the head group is predicted to form interactions with side chains. In order to perform more reliable molecular docking, a higher quality crystal structure would be beneficial for better resolution of residues involved in head group association.

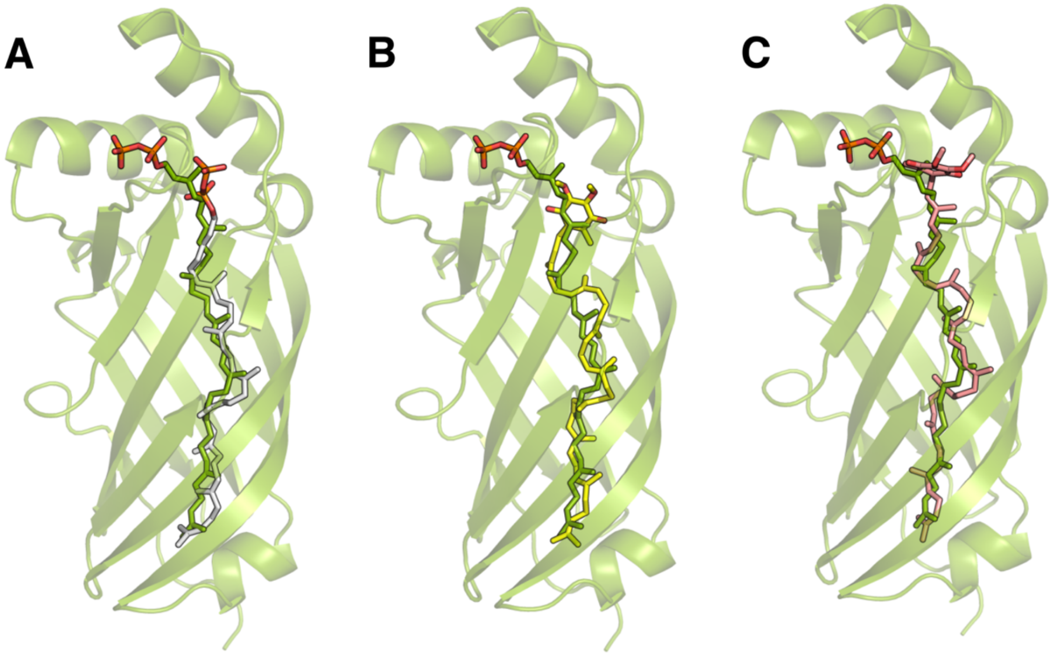

Figure 4.16: Molecular docking of CjX158E cofactors. *CjX158E chain I, green, with the original OPP molecule shown as green sticks, docked with **(A)** OPP, grey sticks, **(B)** Ub-8, yellow sticks, and **(C)** Ub-9, pink sticks.*

4.12 Summary

This chapter describes the steps taken to clone, express and purify the CjX158E domain of unknown function from the larger *C. japonicus* protein, Cbp2E. Prior to this work CjX158E was an uncharacterised, predicted quinone-binding domain, due to its similarity to the *S. degradans* X158 domain, which binds a Ub-8 cofactor (Vincent et al., 2010).

CjX158E was expressed and purified from *E. coli*. Purified protein exhibited a strong yellow colour and native MS analyses showed the presence of a non-covalently bound

OPP cofactor. The crystal structure of CjX158E showed it to be a β-barrel protein and confirmed its association with a molecule of OPP within the β-barrel. The OPP molecule was coordinated by hydrophobic interactions within the cavity and by a number of polar residues in loops at the opening of the barrel. However, precise interactions were difficult to predict due to poor quality maps, most likely caused by a higher degree of flexibility at the barrel opening.

Comparisons between the structure of CjX158E and similar proteins demonstrated subtle differences in coordination of isoprenoid molecules. The OPP molecule in CjX158E appeared to be shifted one isoprene unit further into the β-barrel compared to similar isoprenoid binding proteins. These observations prompted discussions regarding the true cofactor of CjX158E, suggesting that it may naturally associate with Ub-9 over Ub-8. Trying to resolve the true cofactor of CjX158E was particularly challenging, and ultimately unsuccessful. However, this work has provided a starting point for the characterisation of the CjX158E domain, and structural analyses have shown that it is likely to be capable of coordinating a ubiquinone molecule. Although a redox active form of CjX158E domain was not obtained in these studies, they have provided a framework for recombinant CjX158E production and have revealed a novel structure of the previously uncharacterised domain.

Chapter 5

CjX183: a *c*-type cytochrome domain from Cbp2D

5.1 Introduction

Cbp2D is a protein implicated in polysaccharide degradation. As mentioned in Chapter 4, Cbp2D and Cbp2E were shown to be important for growth of *C. japonicus* on crystalline cellulose in a study performed by Gardner *et al.* (Gardner et al., 2014). Chapter 4 focussed on the X158E domain from the Cbp2E protein, this chapter will investigate the function of the X183 domain from Cbp2D.

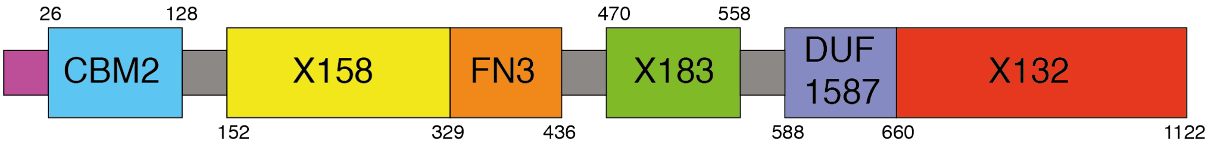

Figure 5.1: Domain annotation for Cbp2D performed by HMM analysis. *Numbers indicate the domain boundaries at the amino acid level. X domains represent CAZy domains of unknown functions whereas FN3 and DUF1587 are annotated by pfam, proposed linker regions are shown in grey and N-terminal signal sequence in purple.*

The CjX183 domain is an 89-amino acid region of the larger Cbp2D protein, shown in Figure 5.1. Sequence analysis of CjX183 suggests that it may act as a cytochrome protein. The domain contains a CXXCH motif, which is essential for *c*-type cytochromes as it is required for covalent attachment of a haem molecule. In *c*-type cytochromes, the two cysteine residues from this motif form thioether bonds with carbon atoms from the haem vinyl groups, haem coordination in this way is suggested to have a significant stabilising effect on *c*-type cytochrome proteins (Kranz et al., 2009).

LPMOs require an electron source to oxidatively cleave polysaccharides (Vaaje-Kolstad et al., 2010). As mentioned in Chapter 1, CDH has been shown to act as a redox partner to LPMOs, and fungal CDHs are able to activate both bacterial and fungal LPMOs (Loose et al., 2016). CDH generates electrons at its dehydrogenase domain and shuttles them to a *b*-type cytochrome domain via large scale domain motions (Tan et al., 2015; Breslmayr et al., 2020). The role of CjX183 as a cytochrome domain within Cbp2D would endorse the hypothesis that Cbp2D could act in a similar manner to CDH, forming an electron relay to bacterial LPMOs.

This chapter will describe the steps taken to express, purify and solve the structure of the CjX183 domain. It will explore how obtaining the structure of this domain may provide clues to CjX183 function, and will describe results from other biochemical experiments used to fully characterise the redox properties of this small X-domain. Results from this chapter laid the groundwork for the biochemical analysis discussed in Chapter 6. The role of CjX183 as a cytochrome domain corroborates our hypothesis that it acts as a redox partner to bacterial LPMOs *in vivo*.

5.2 Generation of the pCW-CjX183 construct

The coding sequence for CjX183 was amplified from the pET22-cbp2D plasmid and was cloned into the pCW-LIC vector using PIPE cloning (Klock and Lesley, 2009), the resulting construct is shown in Figure 5.2. Previous studies have detected Cbp2D in the secretome of *C. japonicus*, suggesting that it is likely to be exported from cells following production (Tuveng et al., 2016). Additionally, *c*-type cytochromes require periplasmic export in order to fold correctly. Incorporation of the haem molecule, which promotes folding in *c*-type cytochromes, occurs in the periplasm in prokaryotes, where the oxidising environment is required for thioether bond formation to the conserved cysteine residues within the protein (Kranz et al., 2009). Adhering to these requirements, an N-terminal pelB leader, provided by the vector, was used to direct expressed proteins to the periplasm using the SEC system. The pCW-LIC plasmid also provided a C-terminal 6His tag, which was used for protein purification. An advantage of using PIPE cloning meant that no additional codons were included between the end of the coding region for CjX183 and the 6His tag.

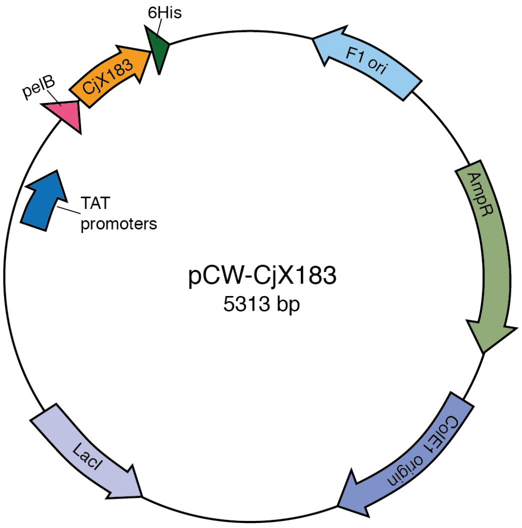

Figure 5.2: Plasmid map for the pCW-CjX183 construct. *The coding region for CjX183 is shown in orange and is flanked by a pelB leader sequence and a C-terminal 6His tag.*

5.3 Recombinant expression of CjX183 using the pEC86 plasmid for haem maturation

The pCW-CjX183 plasmid was transformed into BL21(DE3) cells previously transformed with the pEC86 plasmid. There are three main processes for haem incorporation into proteins, and in Gram-negative bacteria the ccm system is predominantly used. The ccm system operates a two-step process, coordinating oxidation and reduction of a haem molecule to export it to the periplasm, localise it to the CXXCH motif, and catalyse the formation of thioether linkages between the protein and the haem (Kranz et al., 2009). The pEC86 plasmid contains the 8 cytochrome *c* maturation genes used in the ccm system, *ccmABCDEFGH*. It has been shown to increase recombinant expression levels of cytochrome *c* proteins, facilitating haem incorporation, which is required for protein folding and soluble expression of bacterial cytochrome *c* proteins (Arslan et al., 1998). CjX183 expression was achieved by IPTG induction, and presence of a pink cell pellet indicated that a cytochrome protein with a covalently bound haem molecule had been expressed. This result was verified by SDS-PAGE, where a protein of roughly 11 kDa, CjX183 was predicted to be 10.6 kDa, was observed in the cell lysate (Figure 5.3A).

5.4 Purification of CjX183

Pure protein was obtained using nickel affinity chromatography and size exclusion chromatography. The presence of CjX183 was checked throughout purification by monitoring the absorbance at 280 nm and 410 nm, where the haem molecule absorbs. Protein presence was also validated by SDS-PAGE, and a protein at roughly 11 kDa was observed throughout (Figure 5.3A). Purified protein was indicative of a cytochrome protein, with a strong red colour (Figure 5.3B) that intensified with protein concentration. ESI-MS analysis was used to determine an accurate mass for the protein, revealing a peak at 11237 Da (Figure 5.3C). The predicted mass of CjX183 is 10623 Da based on the ProtParam (www.expasy.org) analysis of the amino acid sequence of the domain. Haem *c* has a mass of 618 Da , so the combined mass of the CjX183-haem *c* complex was therefore expected to be 11241 Da. CjX183 has four cysteine residues, two of these were predicted to be involved in coordinating the haem by a thioether bond, losing two protons, for a mass of 11239 Da. The observed mass appeared to be 2 Da lighter than expected, therefore, we reasoned that the two other cysteines in CjX183 likely formed a disulphide bond which would result in the loss of a further two protons and hence 2 Da of mass. Combined with the visible evidence of haem incorporation from the sample's red colour, it was concluded CjX183 had been successfully purified for further characterisation.

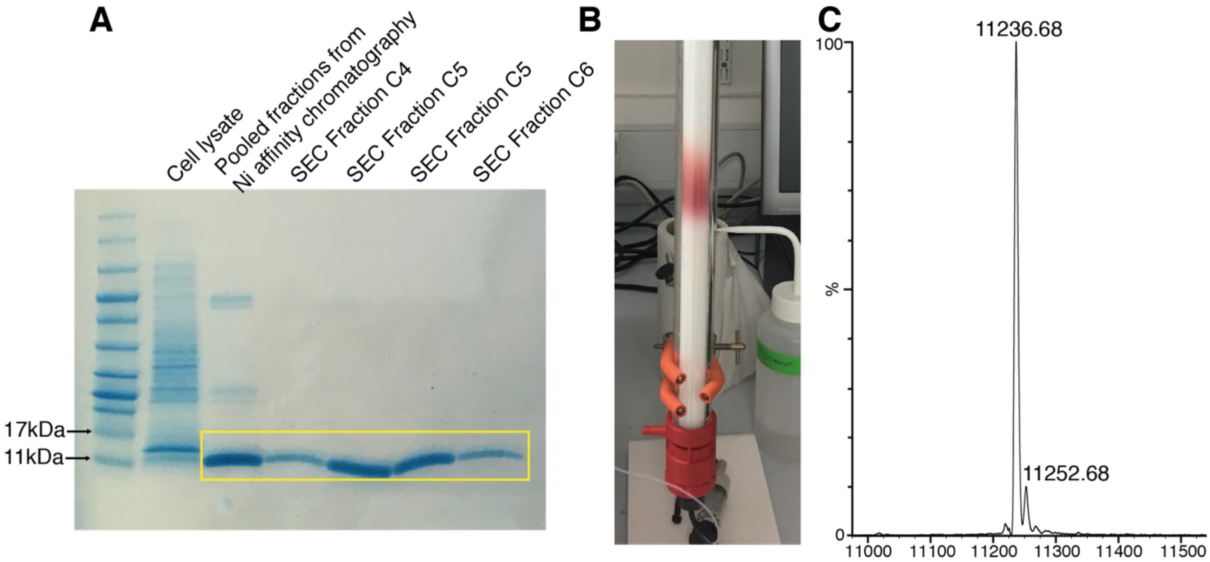

Figure 5.3: Purification of CjX183. (A) *Purification of CjX183 by nickel affinity chromatography followed by size exclusion chromatography. SDS-PAGE showed a pure protein at roughly 11 kDa, highlighted in yellow.* ***(B)*** *Bright red protein, indicative of a haem-bound protein, was clearly visible on the size exclusion column.* ***(C)*** *ESI mass spectrometry showed a peak at 11237 Da, this equates to the haem bound CjX183 protein with two protons lost from the formation of a disulphide bond.*

5.5 Examination of protein stability using circular dichroism

Following protein purification, circular dichroism was used to confirm that CjX183 was stably folded. Circular dichroism measures the difference in absorbance of left- and right-circularly polarised light absorbed by a protein, and this can be used to deduce secondary structure. For best secondary structure predictions, the spectrum should span wavelengths from 180 nm to 260 nm, however in this experiment, the data below 200 nm was extremely noisy, due to salt in the buffer conditions, as salts absorb strongly below 200 nm. Salt was kept at physiological concentrations in the buffer to ensure protein stability, as the spectrum above 200 nm was clear, data below 200 nm were excluded. From the data, CjX183 appeared to be well folded and showed α-helical characteristics with well-defined peaks at 207 nm and 226 nm (Figure 5.4A), in line with negative peaks at 208 nm and 222 nm that are characteristic of α-helical proteins (Greenfield, 2006b). The stability of CjX183 was also examined using this technique in a thermal melt experiment in which the CD spectrum was monitored as the temperature was raised to 90°C in 1°C increments (Figure 5.4B). Circular dichroism at 222 nm was monitored, to study the unfolding of the protein from α-helical to random coil. Data at 222 nm were converted into fraction unfolded, fitted to a Boltzmann sigmoidal curve (shown in Figure 5.4B), and T_m values extracted using equations described in section 3.4. The T_m was calculated to be 64.3°C. These results indicated that the protein was well folded and highly stable, and is therefore suitable for further structural and functional studies.

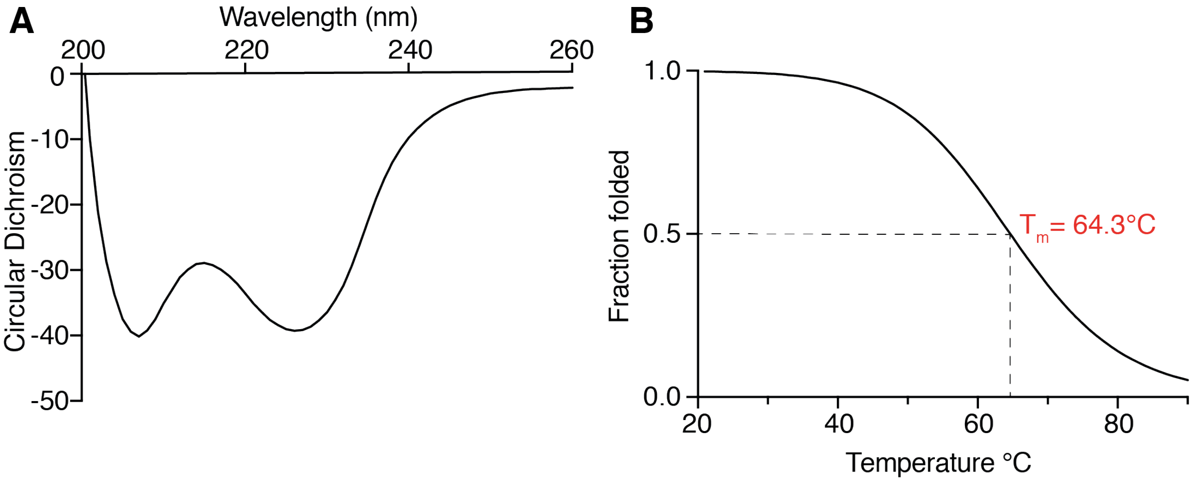

Figure 5.4: Circular dichroism data for CjX183. (A) *CjX183 exhibited typical α-helical character over a wavelength scan from 200 to 260 nm with absorbance minima at 226 and 207 nm.* ***(B)*** *A thermal melt of CjX183 following the circular dichroism at 222 nm gave a melting temperature of 64.3 °C.*

5.6 Structural determination of CjX183 by X-ray crystallography

5.6.1 Protein crystallography and data collection

CjX183 was screened for crystallisation using JCSG core screens I-IV, and crystals were successfully obtained in 0.1 M HEPES pH 7.5, 20 % PEG 4000 and 10 % propan-2-ol. Crystals, shown in Figure 5.5, were formed in 1:2 and 2:1 ratios of protein to precipitant. Crystals were harvested from initial screens without optimisation and were cryo-cooled in the crystallisation condition supplemented with 20 % ethylene glycol. Diffraction data were collected at Diamond Light Source on beamline i03.

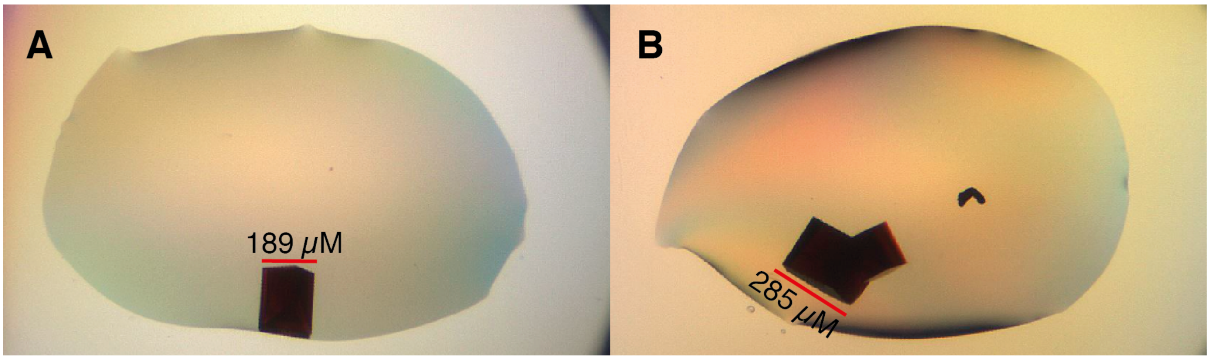

Figure 5.5: Crystals of CjX183. *Crystals of CjX183 were formed in 0.1 M Hepes pH 7, 20 % PEG 4000 and 10 % propan-2-ol, crystals were formed in* ***(A)*** *2:1 and* ***(B)*** *1:2 ratio of protein: precipitant*

To solve the structure of CjX183, data were processed using programmes from the CCP4i2 suite (Potterton et al., 2018), the statistics for the dataset are shown in Table 5.1. On the beamline, data diffracted to 1 Å, but high resolution data was only measured on the corners of the detector due to limits of the detector movement at the beamline. Therefore, data were cut to 1.2 Å to improve the completeness of the high resolution shell. The space group was predicted as P2 2_1 2_1 and the Mathews coefficient predicted one monomer in the asymmetric unit (Matthews, 1968). The structure was solved by anomalous diffraction from the haem iron atom using the SHELX-C/D/E pipeline (Sheldrick, 2008). There was a strong signal for the iron atom in the dataset collected at 0.976 Å, so data sets collected at additional wavelengths were not required.

Electron density maps from the SHELX solution showed well defined electron density modelling one copy of the protein in the asymmetric unit. The initial maps showed density for additional features that were not included in the SHELX model, such as side chains, water molecules and the haem, suggesting that the solution had been successful. Clear density was seen for the haem molecule, which was built into the model in COOT (Emsley et al., 2010). The SHELX pipeline produced a model with an R factor of 0.32 and an R-free of 0.34, iterative rounds of refinement produced a final structure with an R factor of 0.12 and an R-free of 0.13, final statistics for the structure solution are shown in Table 5.2. The final model was validated using the MolProbity server (Williams et al., 2018; Chen et al., 2010), which corroborated the model showing no Ramachandran or rotamer outliers, output from MolProbity analysis is shown in Table 5.3.

Dataset		*CjX183*	
Space Group		$P2\ 2_1\ 2_1$	
Cell dimensions			
a	α	28.5 Å	90°
b	β	55.4 Å	90°
c	*γ*	55.9 Å	90°
Resolution		6.57-1.20 Å (1.22-1.20 Å)	
Rmerge		0.059 (0.105)	
Rpim		0.027 (0.046)	
Observed/ unique reflections		170527/28435	
Mean I/σ		48.3 (21.7)	
Half set correlation CC(1/2)		0.997 (0.990)	
Completeness		100 % (99.6 %)	
Multiplicity		6.0 (6.0)	

Table 5.1: Statistics for CjX183 dataset. *The statistics for the highest resolution shell are shown in parentheses.*

Dataset	*CjX183*
Resolution	55.85-1.2 Å
Number of reflections (working/free sets)	28390/1404
R-factor/R-free	0.122/0.132
RMS deviations	
Bonds	0.0173
Angles	1.532
Average B factors	10.3
B average -protein	11.3
B average -haem	9.5
B average -waters	23.6

Table 5.2: Summary of the final refinement statistics for the CjX183 structure.

Dataset	*CjX183*	
Poor rotamers	0	0 %
Favoured rotamers	77	98.8 %
Ramachandran outliers	0	0 %
Ramachandran favoured	87	96.7 %
Bad Bonds	0/754	0 %
Bad angles	0/1032	0 %

Table 5.3: Molprobity analysis of CjX183 coordinates

5.6.2 The structure of CjX183 shows it to be a small *c*-type cytochrome

The crystal structure of CjX183, shown in Figure 5.6, shows it to be an α-helical *c*-type cytochrome with a covalently bound haem molecule. Clear electron density (Figure 5.7) showed that the haem molecule was bound to Cys19 and Cys22, from the conserved CXXCH motif, by thioether linkages. The central iron atom is coordinated by a proximal histidine residue, His23, and a distal methionine residue, Met66, which are 2.0 Å and 2.3 Å from the iron atom respectively (Figure 5.7). His/Met iron coordination is typical for electron transferring *c*-type cytochromes, therefore, these observations are in line with CjX183 being an electron transferring cytochrome protein. Unusually for *c*-type cytochromes, CjX183 has two additional cysteine residues, which form a disulphide bond on the protein's surface, perhaps to stabilise the protein in an extracellular environment. Disulphide bonds are uncommon in cytochrome *c*s, but have been observed previously in another electron transferring cytochrome *c*, cytochrome *c*6A from *Arabidopsis thaliana* (Marcaida et al., 2006).

Visualising the protein surface shows that the edges of the haem molecule are solvent exposed, with the propionate groups, the likely site for electron transfer, pointing outwards along the solvent exposed edge of the haem binding pocket. However, these propionate groups appear to form hydrogen bonds with Arg44 and Ser50 residues from a surface loop that extends around this part of the molecule. This interaction could account for the relative stability of the reduced state of the haem molecule, which is discussed later. It is likely that electron transfer into the haem occurs directly through the propionate groups, due to their largely solvent exposed nature and the lack of an alternative electron transfer pathway through the protein.

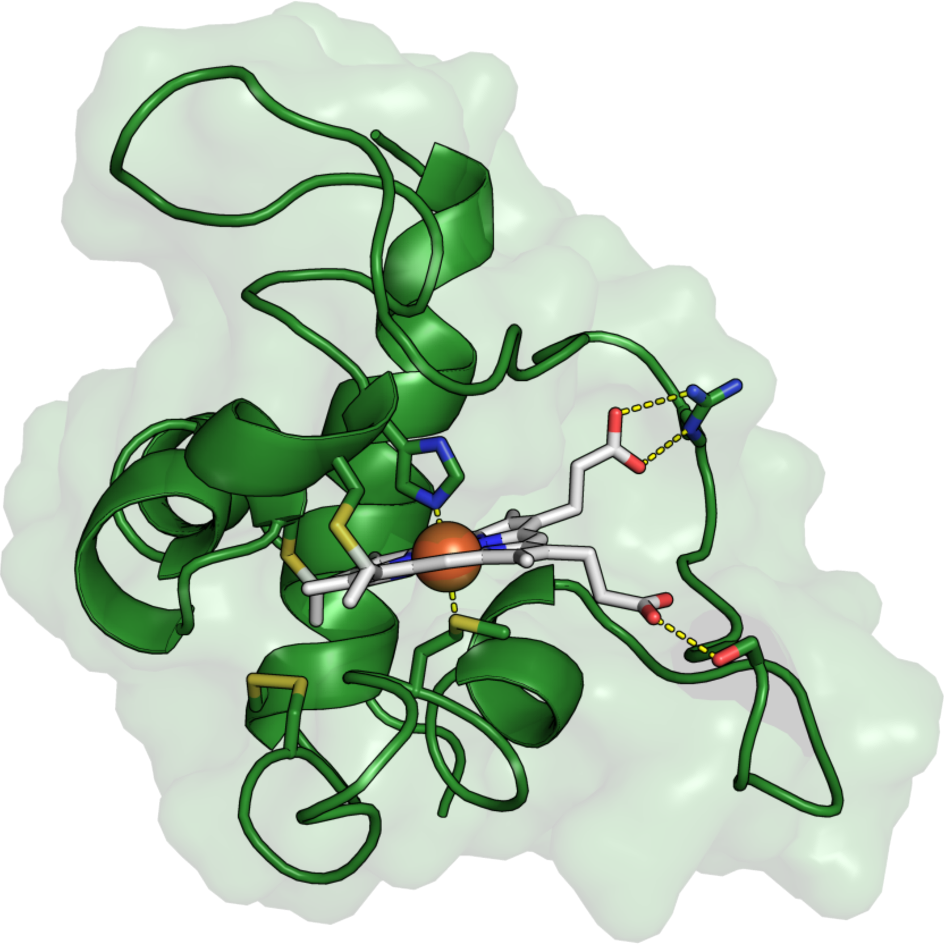

Figure 5.6: The crystal structure of the CjX183 domain. *The overall structure of CjX183 revealed it to be a* α*-helical c-type cytochrome exhibiting typical haem coordination. The protein is represented as a cartoon with the surface shown in green, the haem molecule is shown as sticks with white carbons, with other atoms coloured by atom type and with the central iron atom shown as an orange sphere. Residues coordinating the haem molecule and disulphide bond forming residues are shown as sticks, and coloured by atom type with the carbon atoms shown in green.*

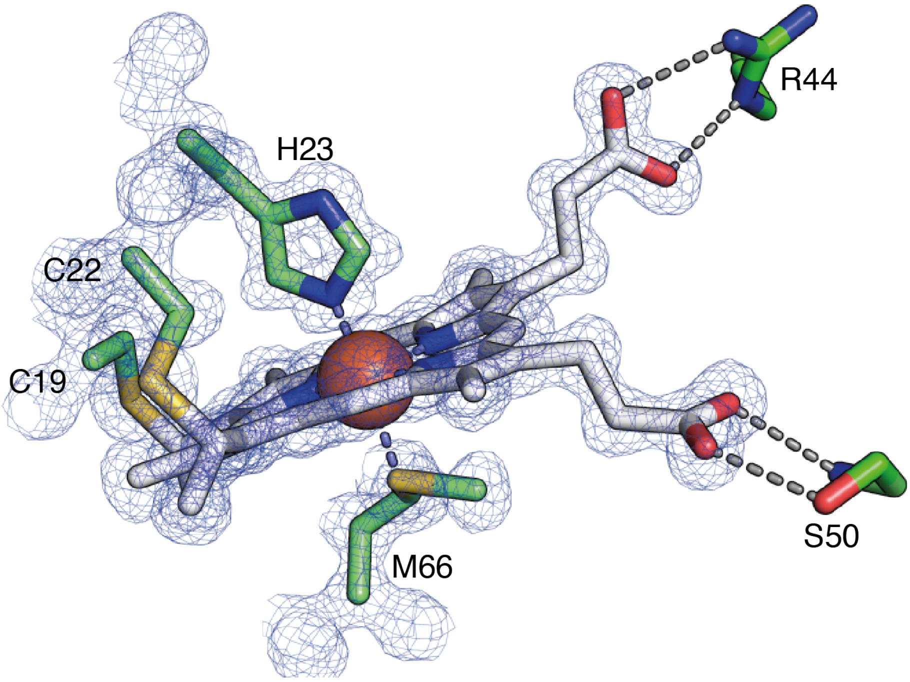

Figure 5.7: CjX183 coordinates a haem molecule. *A close-up view of the haem molecule and its coordinating residues from the CjX183 molecule, the 2Fo-Fc map is shown as blue mesh around the molecule and contoured at 1σ. Dashes represent hydrogen bonding interactions to the propionate groups.*

5.7 Structural comparison with the PDB reveals similarities with domains in other electron transfer proteins

5.7.1 Structural alignment with the thiosulphate dehydrogenase/ tetrathionate reductase, TsdBA

Structural comparisons against the PDB were performed using the protein comparison server DALI (Holm, 2019). As expected, CjX183 aligns with a number of other *c*-type cytochrome domain containing proteins. The closest structural alignment was with a single domain of the thiosulphate dehydrogenase/tetrathionate reductase (TsdBA) from *Marichromatium purpuratum* (PDB code 5LO9) (Kurth et al., 2016). The superposition, shown in Figure 5.8, spans 72 residues with an rmsd of 2.3 Å, and the two domains have a sequence identity of only 31 %. The TsdBA protein in this organism has resulted from an unusual gene fusion event, resulting in expression of the two proteins in a single polypeptide chain. Both proteins contain two cytochrome domains. In TsdA, the active site haem shows His/Cys haem coordination, with the cysteine residue covalently bound to a molecule of thiosulphate. The second haem in TsdA shows His/Met coordination, and it is to this domain that CjX183 has the highest structural similarity. Similarly, the two haems in TsdB are coordinated by His/Met ligands. It is thought that the oxidation of two molecules of thiosulphate at the catalytic site in TsdA generates one molecule of tetrathionate and two electrons (Kurth et al., 2016). The electrons are shuttled away from the catalytic domain, through the second haem of TsdA and to the two TsdB haems. These electrons are suggested to feed into aerobic respiratory or photosynthetic pathways, either directly or through small electron transfer proteins (Kurth et al., 2016). As CjX183 aligns to the electron transfer domain of TsdA, it is plausible that the CjX183 domain exists as part of a larger electron transfer chain, either within Cbp2D or with other protein partners that may play a catalytic role to act as an electron source.

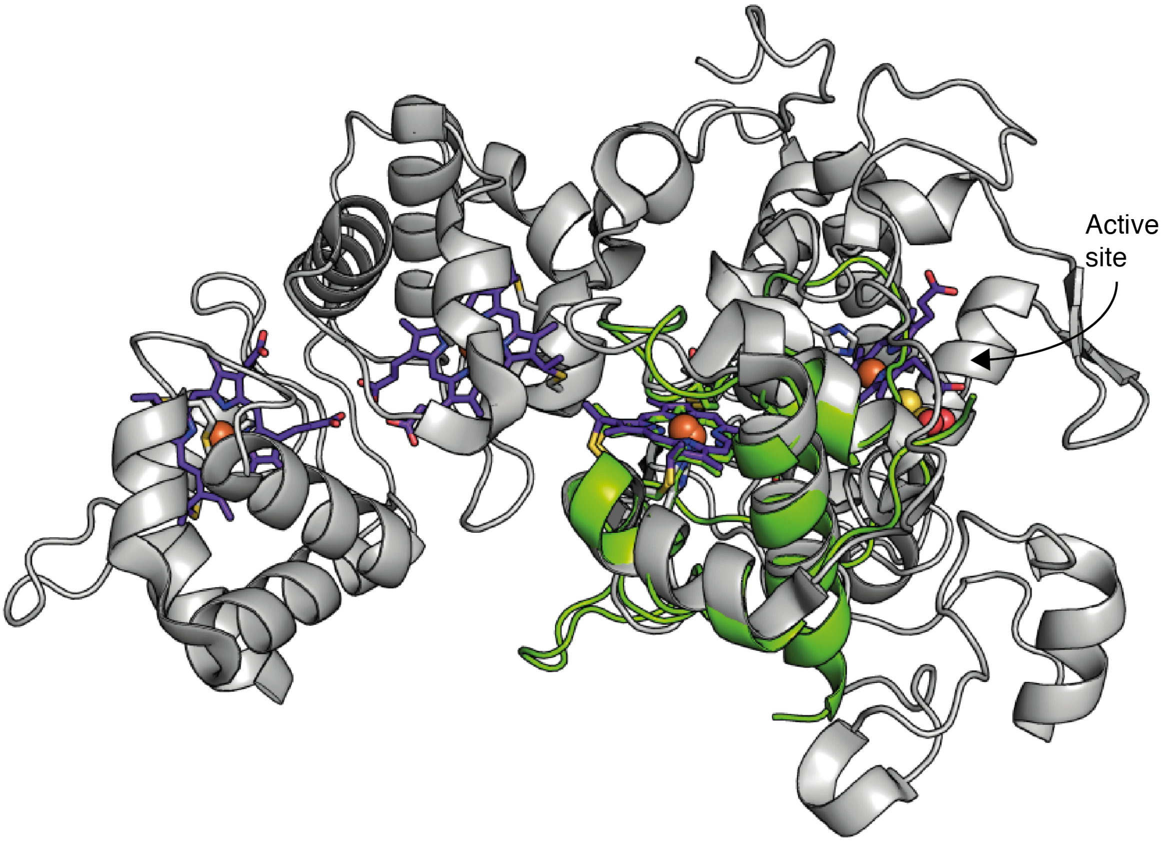

Figure 5.8: Superposition of CjX183 with TsdBA from Marichromatium purpuratum. *Protein structures are shown as cartoons with CjX183 in green and TsdBA in grey, the haem molecules of TsdBA are shown with blue carbons and orange spheres representing the iron atoms, they act to shuttle electrons away from the active site, where the molecule of thiosulphate is shown as spheres.*

5.7.2 Structural alignment with the sulphane dehydrogenase, SoxCD

A further structural comparison, revealed using the DALI server (Holm, 2019), was with the sulphane dehydrogenase, SoxCD, from *Paracoccus pantotrophus* (PDB code 2XTS). SoxCD is a dimer of the molybdoprotein SoxC with the dihaem cytochrome protein SoxD. For crystallographic analysis the second haem domain of SoxD was deleted by the authors as it was not required for the sulphur oxidising activity (Zander et al., 2011). CjX183 aligns to the crystallised cytochrome domain of SoxD. The superposition, shown in Figure 5.9, spans 203 residues with an rmsd of 2.1 Å, despite a sequence identity of only 22 %.

SoxCD is involved in a six electron transfer reaction to convert a protein bound sulphur to its sulphone state. Electrons are shuttled from the sulphane group on the sulphur carrier protein SoxYZ through a molybdenum cofactor in SoxC to a haem *c* molecule in SoxD, where they are transferred to an external protein partner (Zander et al., 2011). The structural similarity between CjX183 and the electron transferring SoxD domain reaffirms hypotheses suggesting that CjX183 may be involved in a larger electron transfer chain.

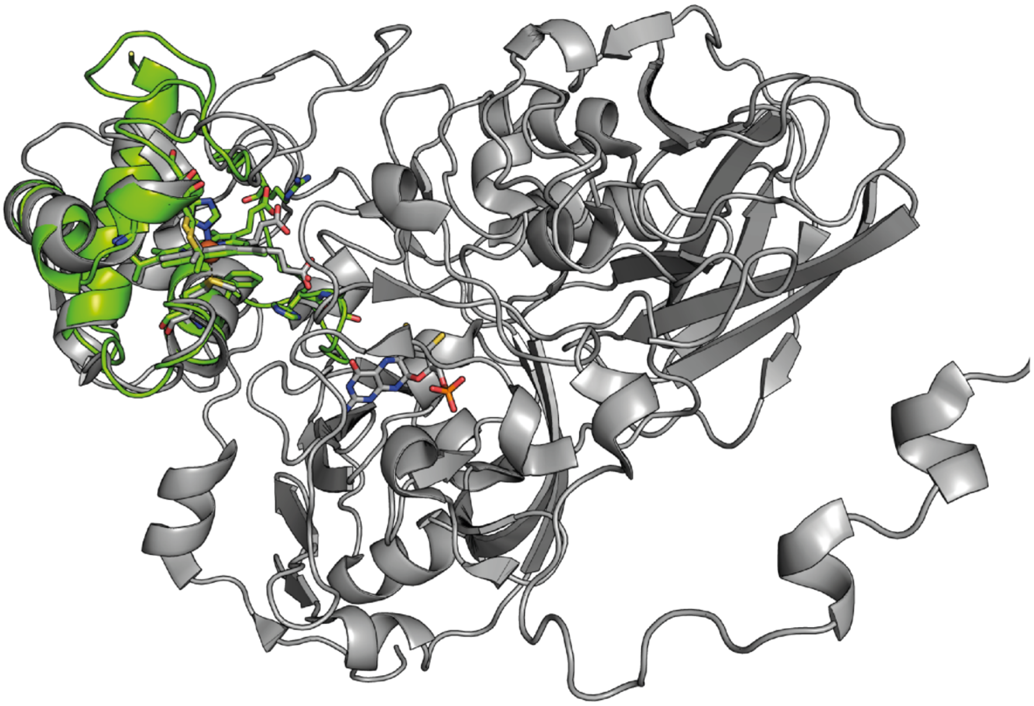

Figure 5.9: Superposition of CjX183 with SoxCD from Paracoccus pantotrophus.
Protein structures are shown as cartoons, with CjX183 in green and SoxCD in grey, the CjX183 haem is shown as green sticks, and molybdenum and haem cofactors for SoxCD are shown as grey sticks, iron atoms are shown as orange spheres.

5.8 Redox properties of CjX183

5.8.1 UV-Visible spectroscopy to monitor the redox state of CjX183

Haem molecules have a characteristic absorbance spectrum. The redox state of *c*-type haems can be studied spectroscopically between 410-420 nm and 500-600 nm (Moore, 1990). *C*-type cytochromes have three peaks that are indicative of their reduced state: the Soret peak, which is the highest intensity band of cytochrome UV-Vis spectra, absorbs between 410 and 420nm and shifts its maxima between the oxidised and reduced states, and the α and β peaks, which form two sharp peaks between 500 and 600 nm in the reduced state and merge to a single broad peak following oxidation (Moore, 1990). The Soret peak and the α and β peaks are a result of electron excitation from the π-bonding to π^*-antibonding orbitals of the porphyrin ring. Absorption at the Soret peak is a result of the transition to the second excited state, whereas the α and β peaks are formed by transitions to the first excited state (Moore, 1990).

The UV-Vis spectrum of CjX183 is characteristic of those of *c*-type cytochromes. To measure spectra for fully oxidised and reduced CjX183, potassium ferricyanide and ascorbate were used respectively. In these spectra (Figure 5.10) the reduced state of CjX183 displayed a strong signal at 419 nm for the Soret peak, which shifted to 413 nm in the oxidised protein. The α and β peaks showed maxima at 552 nm and 520 nm in the reduced state, and flattened to a single broad peak in the oxidised protein (Figure 5.10), such absorbance maxima are typical for *c*-type cytochromes. The spectroscopic properties of CjX183 enabled the redox state of the haem to be easily measured, and facilitated subsequent experiments to monitor the rate of CjX183 oxidation.

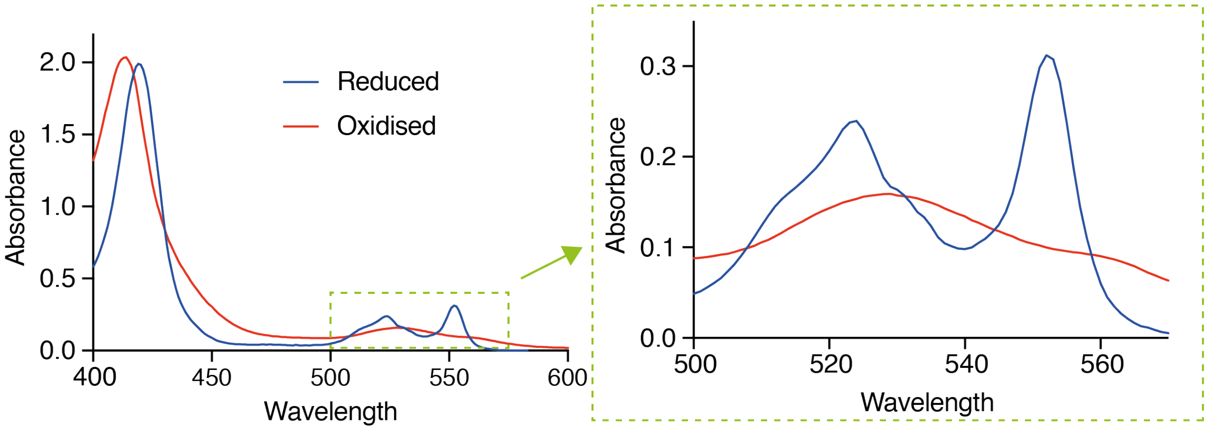

Figure 5.10: UV-Vis spectrum for CjX183 between 400 and 600nm. *In the oxidised state the Soret peak was at 413 nm and there was one broad peak between 500 and 570 nm, expanded in the green box. After reduction, the Soret peak moved to 419 nm and α and β peaks formed at 552 and 520 nm.*

The stability of the reduced state of redox proteins can be probed by monitoring autoxidation, the rate at which electrons are lost to atmospheric oxygen. To track the autoxidation of CjX183, the protein was reduced with ascorbate and passed down a PD10 desalting column to remove excess reductant. The UV-Vis spectrum was then monitored over time between 500 and 600 nm to track the decrease of the peaks at A_{520} and A_{552}. By tracking the A_{552}, it was clear to see that the majority of protein was oxidised after 2 hours (Figure 5.11), which was deemed sufficiently stable for use in further experiments with LPMOs, which are explored in Chapter 6.

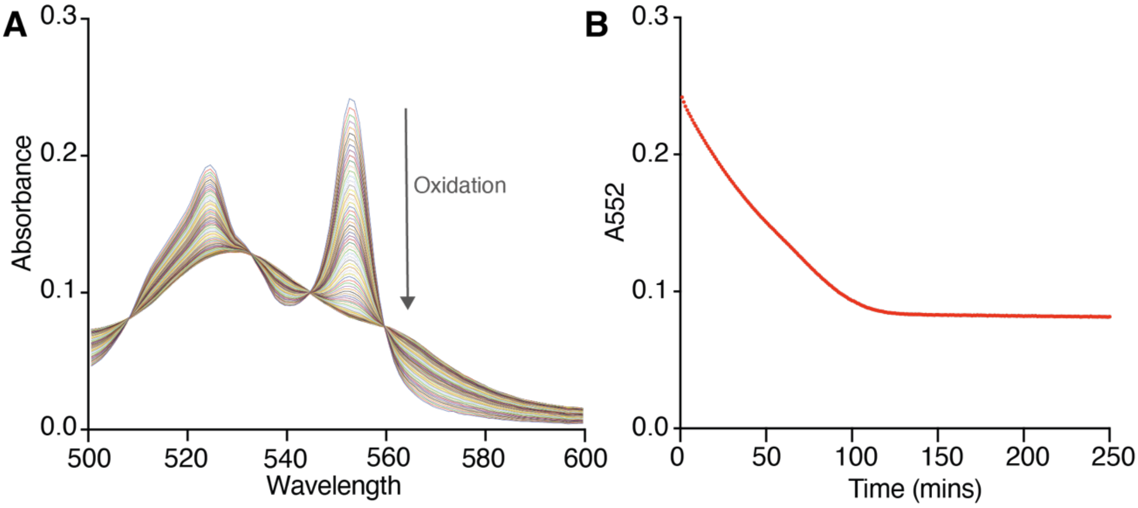

Figure 5.11: Autoxidation of the CjX183 domain can be tracked spectroscopically. (A) *Absorbance at the α and β peaks of the protein at A_{520} and A_{552} decrease as CjX183 undergoes autoxidation.* ***(B)*** *Plotting the decrease in absorbance at 552 nm shows that CjX183 takes approximately 120 minutes to undergo full autoxidation.*

5.8.2 Cyclic voltammetry gives a redox potential for CjX183

Knowledge of the redox potentials of electron transfer proteins is useful to determine the path of electrons travelled in any electron transfer chain. In Cbp2D, assigning redox potentials to individual domains will build a more complete picture of the putative electron transfer chain. The redox potential of CjX183 could provide information on where the protein sits in this electron transfer chain, therefore cyclic voltammetry was used to examine this. The protein was applied to a carbon electrode in an anaerobic chamber and allowed to form a film before submerging in buffer. A voltage was applied and varied between -0.5 and +0.5 V vs the standard hydrogen electrode (SHE) and the current was measured against a reference electrode. CjX183 gave a clear and reproducible voltammogram, shown as an average of four traces in Figure 5.12. With clear peaks centred around +0.2 mV for oxidation, seen at positive currents, and reduction, seen at negative currents. From this, the midpoint potential was measured to be +193 mV vs SHE at pH 8. LPMOs, however, have been more challenging to probe using cyclic voltammetry. Therefore, efforts to determine the redox potentials of LPMOs have been performed using the small molecule electron transfer mediator tetramethyl-1,4-phenylenediamine, who's redox state can be quantified spectroscopically (Aachmann et al., 2012). From studies using this method, LPMO redox potentials have been shown to be greater than +220 mV (Hemsworth et al., 2013; Aachmann et al., 2012; Borisova et al., 2015). Therefore, it seems plausible that CjX183 could activate LPMOs, as electrons move towards more positive reduction potentials. CjX183 was therefore examined in this context, which will be discussed in further in Chapter 6.

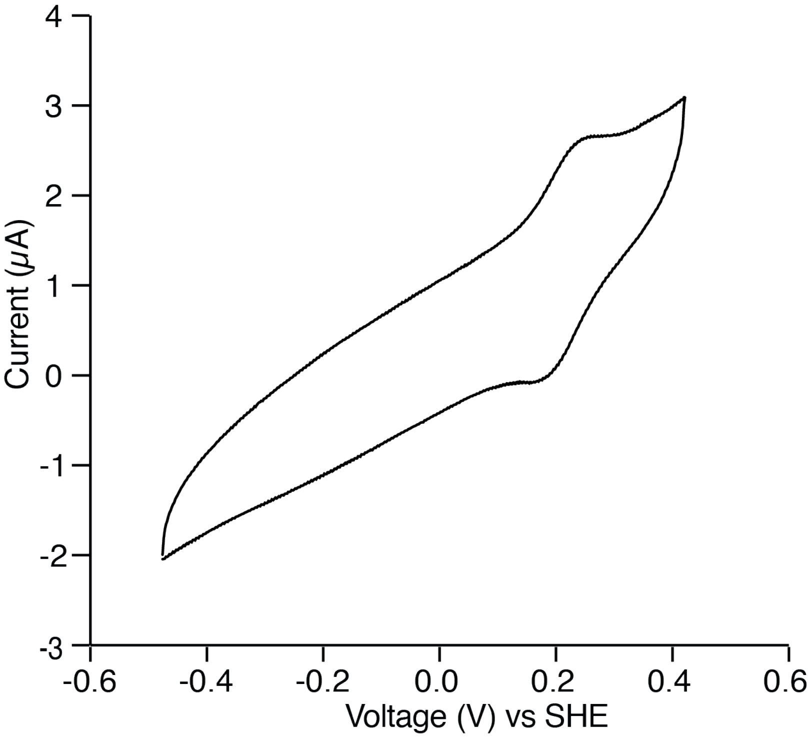

Figure 5.12: Cyclic voltammetry data for CjX183 measured on a carbon electrode. *The midpoint potential at pH 8 was measured to be +193 mV (vs SHE).*

5.9 Summary

This chapter describes the steps taken to isolate, express and characterise the CjX183 domain of unknown function from Cbp2D. Prior to this project, knowledge of CjX183 was limited to sequence analyses, which predicted it to be a *c*-type cytochrome domain.

CjX183 was expressed and purified from *E. coli* with the aid of the pEC86 vector. The crystal structure showed an α-helical protein covalently bound to haem *c*. The haem molecule formed covalent bonds to two cysteine residues in the protein and the iron atom showed His/Met coordination, which is typical for *c*-type cytochromes. The propionate groups of the haem are largely solvent exposed, allowing speculation of direct electron transfer directly to and from the propionate groups. Structural comparison against the PDB linked CjX183 to cytochrome domains in multidomain electron transfer proteins, suggesting a role for CjX183 as part of a larger electron transfer chain. CjX183 exhibited typical spectroscopic characteristics for a *c*-type haem and was easily reduced and oxidised using small molecules. Complete oxidation of fully reduced CjX183 with atmospheric oxygen was recorded to take approximately two hours. The redox potential of CjX183 was measured as +200 mV (vs SHE) using cyclic voltammetry, which is sufficient to activate LPMOs. Characterisation of CjX183 as a redox active cytochrome domain supports the role of Cbp2D as a redox partner to bacterial LPMOs.

This chapter provided a novel structure of a the previously uncharacterised CjX183 domain, and performed analyses suggesting that CjX183 should be capable of activating LPMOs, in line with the original hypothesis for the function of Cbp2D. These studies provided a starting point for the investigation of CjX183 as a redox partner to bacterial LPMOs, which is probed further in Chapter 6.

Chapter 6

CjX183 can activate LPMOs

6.1 Introduction

A large number of LPMOs have been discovered and characterised over the last decade (Beeson et al., 2015; Hemsworth et al., 2015). LPMOs require electrons and molecular oxygen in order to break glycosidic bonds, many sources of these electrons have been proposed, however there are open questions regarding the native electron source, especially in bacterial systems. Although mechanisms of activation have been hypothesised, there has been little progress made to decipher whether there is a protein based redox partner for bacterial LPMOs. In fungal systems, the enzyme CDH has been shown to act as an LPMO redox partner (Phillips et al., 2011), however, a bacterial redox partner is yet to be identified. Small molecule reductants, typically used in lab-based experiments are very good LPMO activators and produce high turnover rates, however they have also been shown to generate high concentrations of H_2O_2, which is very damaging to enzyme cocktails, causing oxidative damage to active site residues (Bissaro et al., 2017; Hangasky et al., 2018). Use of specific protein partners, could subvert this problem and activate LPMOs in a more specific and controlled manner, which may reduce non-specific LPMO activation and prolong the lifetime of enzymes.

Chapter 5 characterised CjX183, a small cytochrome domain from the *C. japonicus* Cbp2D protein. CjX183 was shown to be redox active with a redox potential of +193 mV vs SHE. With a redox potential capable of activating LPMOs, which typically have redox potentials larger than +220 mV (Hemsworth et al., 2013; Aachmann et al., 2012; Borisova et al., 2015), reduced CjX183 could act to transfer electrons to bacterial LPMOs.

Measuring the activity of LPMOs is not straightforward. Due to the insoluble nature of the cellulosic substrates that they act on it is often hard to measure and assign rates to the activity of an LPMO. This chapter will utilise methods that are currently used in the field, such as measuring H_2O_2 production from a substrate-free side reaction of LPMOs (Kittl et al., 2012), and measuring the boosting effect of LPMOs on canonical cellulases (Quinlan et al., 2011; Lo Leggio et al., 2015; Sabbadin et al., 2018), to compare the activation of two bacterial LPMOs by reduced CjX183 and small molecule electron donors. The aim of work performed in this chapter was to unravel the potential for the CjX183 domain to act as an electron donor to LPMOs. Furthermore, given that the domain in isolation acts as a finite electron source, similar to small molecule reducing agents, this chapter probes the underlying differences in the mode of LPMO activation when a small molecule is used compared to a protein based partner.

6.2 Addition of LPMOs accelerates CjX183 oxidation in a concentration dependent manner

Cytochrome proteins display characteristic spectroscopic properties that allow interconversion between the reduced and oxidised states to be measured. The spectroscopic characteristics of CjX183 were outlined in section 5.8.1. Oxidation of CjX183 was tracked by monitoring the absorbance decrease of the 552 nm peak indicative of the haem reduced state, and in Chapter 5, it was shown that complete oxidation for CjX183 took approximately 2 hours.

To determine if electron transfer between CjX183 and LPMOs could be monitored, depletion of the CjX183 A_{552} peak, corresponding to loss of the reduced state, was tracked in the presence of LPMOs. CjX183 was reduced using ascorbate, as described in section 5.8.1, and LPMO concentrations were varied to establish a concentration dependence, linking CjX183 oxidation to LPMO presence. These experiments were performed with an LPMO from *C. japonicus*, CjAA10BΔCBM (structurally characterised in Chapter 3), and an LPMO from *Cellulomonas fimi*, CfAA10, obtained from Crouch *et al*. (Crouch et al., 2016), to observe if CjX183 could activate LPMOs in an intra- and interspecies manner. LPMOs for this experiment were used at a 1.25, 2.5 and 5-fold molar excess and CjX183 concentration was held constant. Data (shown in Figure 6.1) were fitted to an equation for single exponential decay in Graphpad prism, using the equation $Y=(Y0\text{-plateau})*e^{-KX}+\text{plateau}$, where Y0 is the Y value when X (time) equals zero, plateau is the Y value where the curve flattens off (corresponding to full protein oxidation) and K is the rate constant.

CjX183 oxidation was accelerated by LPMOs in a concentration dependent manner (Figure 6.1). Autoxidation of the CjX183 domain occurred slowly, comparable to results from Chapter 5. As increasing concentrations of CjAA10BΔCBM or CfAA10 were titrated into the reaction, the rate of CjX183 oxidation increased in a linear fashion. Linear relationships between CjX183 oxidation and LPMO concentration were seen for both enzymes, suggesting intra- and interspecies activation of LPMOs. Interestingly electron transfer from CjX183 was faster to the CfAA10 enzyme than to the CjAA10BΔCBM enzyme, this was unexpected as interspecies electron transfer was expected to proceed through a less specific protein interaction. Following these studies, LPMO activities when activated with CjX183 were probed, to determine whether electron transfer to LPMOs was causing enzyme turnover.

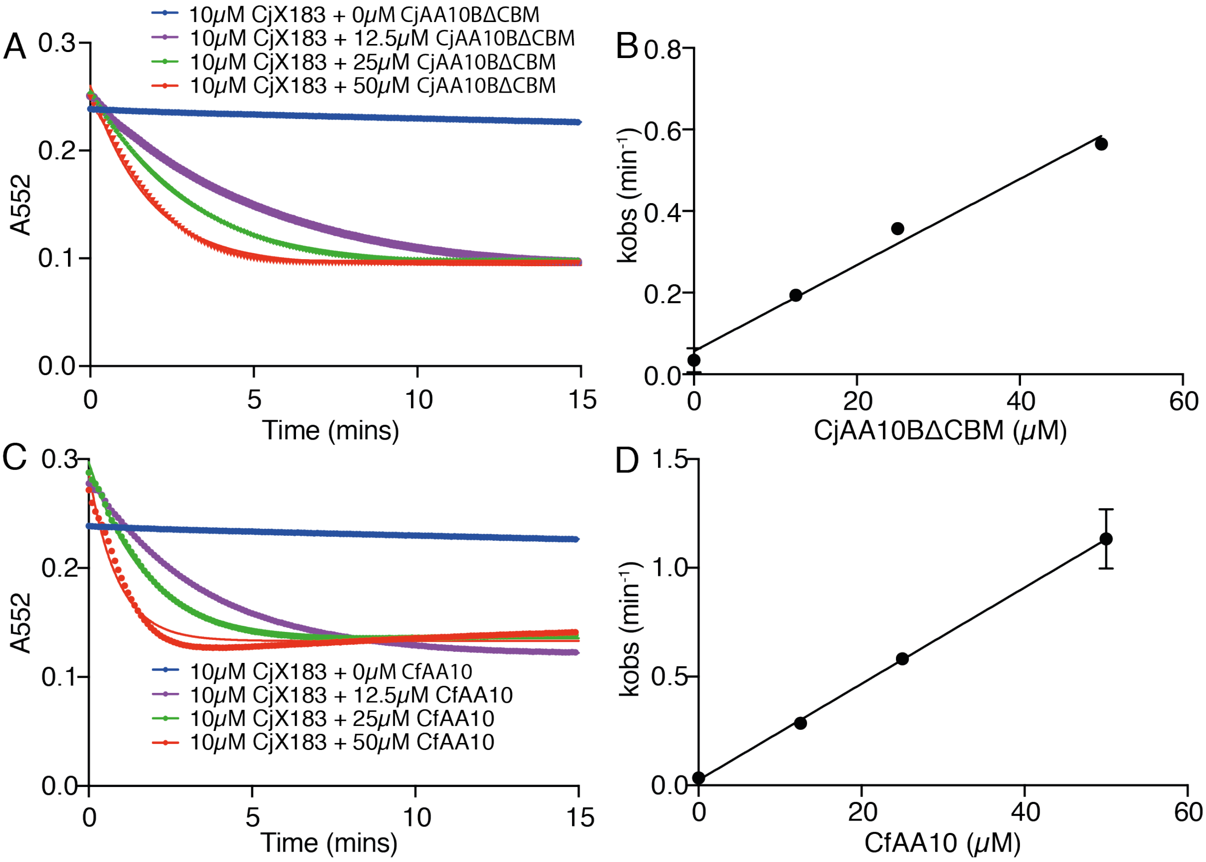

Figure 6.1: Oxidation of CjX183 is accelerated by CjAA10BΔCBM and CfAA10. (A) *Monitoring of the decrease of the reduced state of CjX183 with 0 (blue), 1.25 (purple), 2.5 (green) and 5 (red) fold excess of CjAA10BΔCBM.* ***(B)*** *Plot of oxidation rates of CjX183 against CjAA10BΔCBM concentration shows a linear relationship.* ***(C)*** *and* ***(D)*** *Equivalent graphs to (A) and (B) to show CjX183 oxidation rates with CfAA10. Data in (A) and (B) were fitted to the equation for single exponential decay* ($Y=(Y0\text{-plateau})*e^{-KX}+\text{plateau}$)*, and (C) and (D) to a straight line (Y=mx+c).*

6.3 CjX183 can activate turnover of LPMOs on cellulosic substrates

The oxidation experiments, described above, indicated that CjX183 can donate electrons to LPMOs in a concentration-dependent manner. Following this, the ability of CjX183 to drive LPMO activity on substrate was tested. Activity assays were carried out to detect oxidised products following incubation of both LPMOs on PASC using ascorbate or reduced CjX183 as the electron source. Breakdown products were analysed by MALDI-ToF MS, which is commonly used to detect the oxidised oligosaccharides released by LPMOs (Vaaje-Kolstad et al., 2010; Forsberg et al., 2011; Lo Leggio et al., 2015). Controls for this experiment using ascorbate to activate CjAA10BΔCBM or CfAA10, clearly show the generation of lactone and aldonic acid terminated oligosaccharides (Figure 6.2), in line with results previously seen from these LPMOs (Gardner et al., 2014; Crouch et al., 2016).

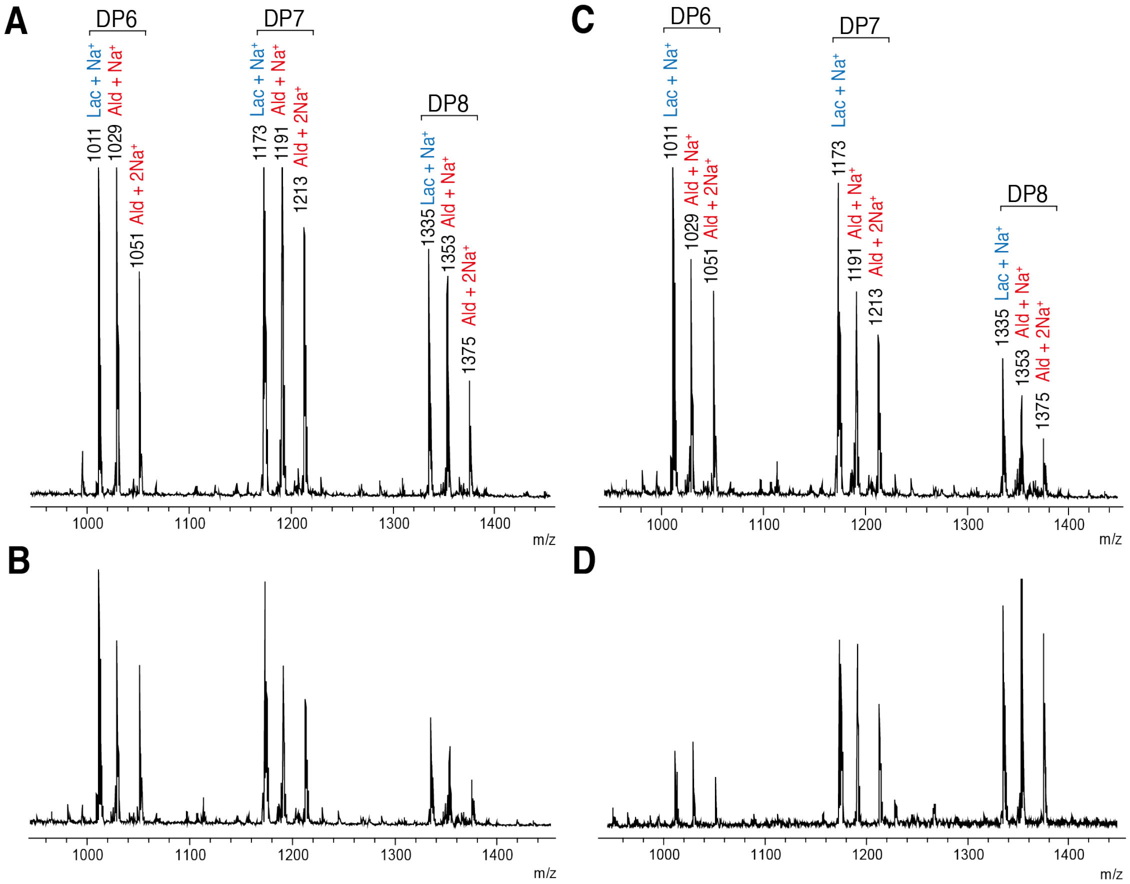

Figure 6.2: MALDI-ToF MS detection of oxidised products from CjAA10BΔCBM and CfAA10. (A) *Oxidised oligosaccharides released from CjAA10BΔCBM when ascorbate is used as a reducing agent. Peaks have been annotated such that DPX (where X is an integer) represent the length of the oligosaccharide, and lac and ald have been used to indicate the lactone or aldonic acid forms of the oligosaccharides respectively.* ***(B****) Oxidised oligosaccharides released by CjAA10BΔCBM driven by chemically reduced CjX183. Equivalent spectra for* ***(C)*** *ascorbate activated CfAA10 and* ***(D)*** *CfAA10 and chemically reduced CjX183.*

To confirm that LPMOs were powered by reduced CjX183 and not residual ascorbate in chemically reduced samples, activity assays were set up with chemically and electrochemically reduced CjX183 and CfAA10. CjX183 was chemically reduced using ascorbate, as described in section 5.8.1. Electrochemically reduced CjX183 was prepared using a graphite mesh electrode and 1 % methyl viologen as a mediator. Both chemically and electrochemically reduced CjX183 activated CfAA10 to produce oxidised products from PASC, which were not seen in reductant-free control samples, confirming that reduced CjX183 alone is acting as the reductant (Figure 6.3).

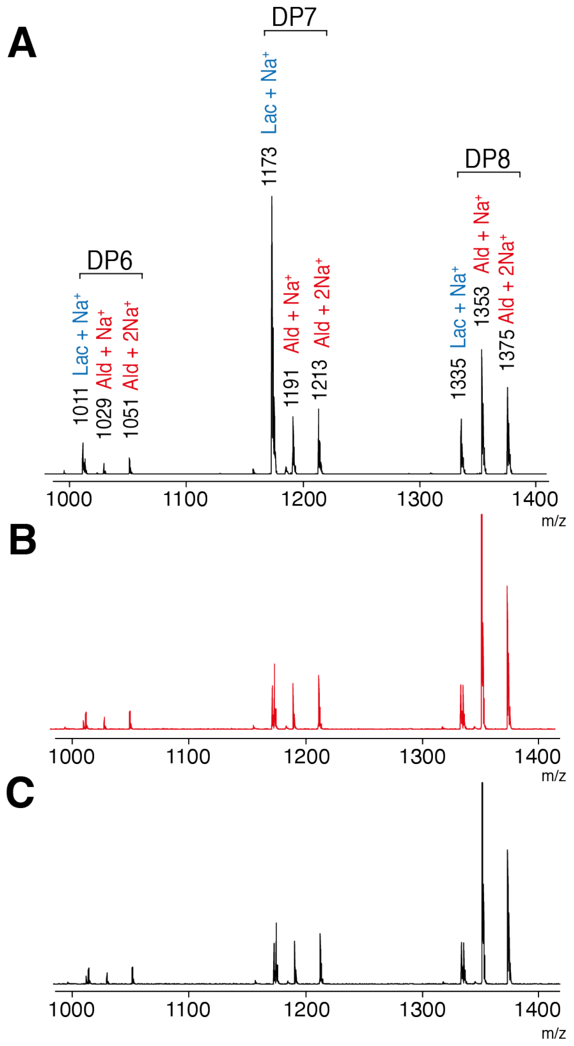

Figure 6.3: CfAA10 activation by electrochemically and chemically reduced CjX183. (A) *CfAA10 activated by ascorbate.* ***(B)*** *CfAA10 activated by electrochemically reduced CjX183* ***(C)*** *CfAA10 activated by chemically reduced CjX183. Peaks have been annotated to represent the degree of polymerisation (DP) of the oligosaccharide, and lactones and aldonic acid terminated oligosaccharides are annotated ald and lac respectively.*

These results clearly demonstrate that the reduced CjX183 domain is able to activate LPMOs on crystalline substrates. However, as these results are not quantitative, they do not provide insight into the activities of LPMOs when driven by different reductants. Following this evidence that CjX183 can act as an LPMO activator, subsequent studies were conducted to explore whether there were any significant differences between activation by reduced CjX183 or ascorbate.

6.4 LPMO activity can be tracked by measuring peroxide production

Measuring enzyme activity is crucial for assessing how effective an enzyme system is. For LPMOs, this is challenging, due to the insolubility of their polysaccharide substrates, which makes product detection difficult. To date, only a handful of LPMOs have been found to act on smaller, more soluble polysaccharides (Isaksen et al., 2014; Borisova et al., 2015; Frandsen et al., 2016; Simmons et al., 2017), and CjAA10B and CfAA10 are not included in these. For this reason, it is difficult to generate accurate kinetic data for activities of these LPMOs on their main substrate, crystalline cellulose. However, LPMOs have a side reaction that can be exploited for this purpose. In the absence of substrates, LPMOs will generate hydrogen peroxide from oxygen and the rate of H_2O_2 production from this side reaction can be correlated to LPMO activity (Kittl et al., 2012; Bennati-Granier et al., 2015; Isaksen et al., 2014). H_2O_2 production can be quantified using a coupled assay with Amplex Red reagent (Zhou, M. et al., 1997), schematic shown in Figure 6.4, horseradish peroxidase (HRP) converts Amplex Red reagent to resorufin through the conversion of H_2O_2 to O_2. Through the Amplex Red H_2O_2 assay the activities of CjAA10BΔCBM and CfAA10 were determined and the ability of ascorbate and CjX183 to act as a reducing agents were compared.

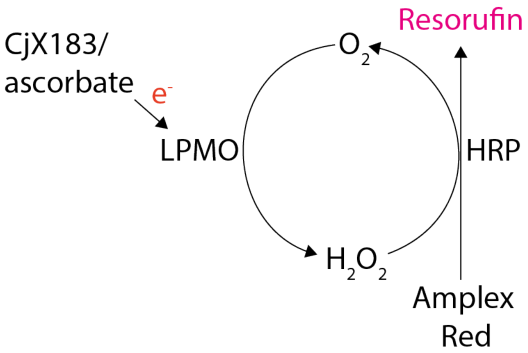

Figure 6.4: Schematic of the coupled assay with Amplex Red to measure H_2O_2 production by LPMOs. *HRP uses H_2O_2 to convert Amplex Red reagent to the colorimetric resorufin.*

The formation of resorufin, which has a red/pink colour, from Amplex Red reagent, colourless, can be measured by UV-Vis spectroscopy between 550 and 600nm. It can also be monitored using fluorescence spectroscopy with excitation and emission maxima at 571 and 585 nm respectively. Preliminary experiments were performed to detect resorufin formation using both absorbance and fluorescence spectroscopy, however, fluorescence readings showed higher sensitivity, and were less affected by absorbance of the CjX183 haem, discussed further later. For subsequent experiments fluorescence spectroscopy was performed using an excitation filter of 570 nm and an emission filter of 595 nm.

6.4.1 Assay conditions were optimised

Initially, this assay was designed using instructions from the Amplex Red Hydrogen Peroxide/Peroxidase Assay Kit (Thermofisher, cat no. A22188), and HRP and Amplex Red concentrations were used as suggested in this kit. To detect resorufin using fluorescence spectroscopy, an emission filter of 570 nm and an excitation filter of 595 nm were used. The 570 nm excitation filter did show some overlap with the absorbance region of the haem *c* in CjX183 (see Figure 5.11 for reference), however, effects caused by haem absorbance were accounted for using a series of concentration curves, discussed in subsequent sections.

Based on previous studies using LPMOs in this assay (Kittl et al., 2012; Bennati-Granier et al., 2015; Isaksen et al., 2014), LPMO concentration was used at 2 μM, this gave a suitable signal, which allowed differentiation between enzyme-driven and enzyme-free controls. CjX183 and ascorbate concentrations in this assay were optimised over time. Prior to this study there was no information on the kinetic parameters of the CjAA10BΔCBM or CfAA10 enzymes with CjX183 or ascorbate, so these values were determined using subsequent experiments.

6.4.2 Inner filter effects were considered to account for light absorption from the CjX183 haem

As mentioned above and in section 5.8.1, due to its characteristic cytochrome protein spectrum, CjX183 absorbs light strongly at points between 500 and 600 nm. Although the 570 nm excitation filter was chosen to avoid the 552 nm absorbance peak from the reduced CjX183 haem molecule, at 570 nm there is still some absorbance from the haem, which could interfere with fluorescence readings in CjX183-containing samples. In order to probe the effects resulting from CjX183 absorbance, a concentration curve of known H_2O_2 concentrations was performed in the presence of different concentrations of reduced CjX183 (Figure 6.5). As predicted, CjX183 absorption detracted from emitted fluorescence signals in a concentration dependent manner, an effect that is subsequently termed inner filter effects. Following these observations, equivalent concentration curves were performed prior to each assay, containing CjX183 at each concentration required for the ensuing experiment. Concentration curves were fitted to straight lines using Graphpad Prism, using Y=mx+c, where m is equal to the gradient and c to the Y-intercept. Gradients from generated concentration curves were used to convert fluorescence readings obtained in assays to hydrogen peroxide concentrations, taking into account inner filter effects resulting from the presence of CjX183.

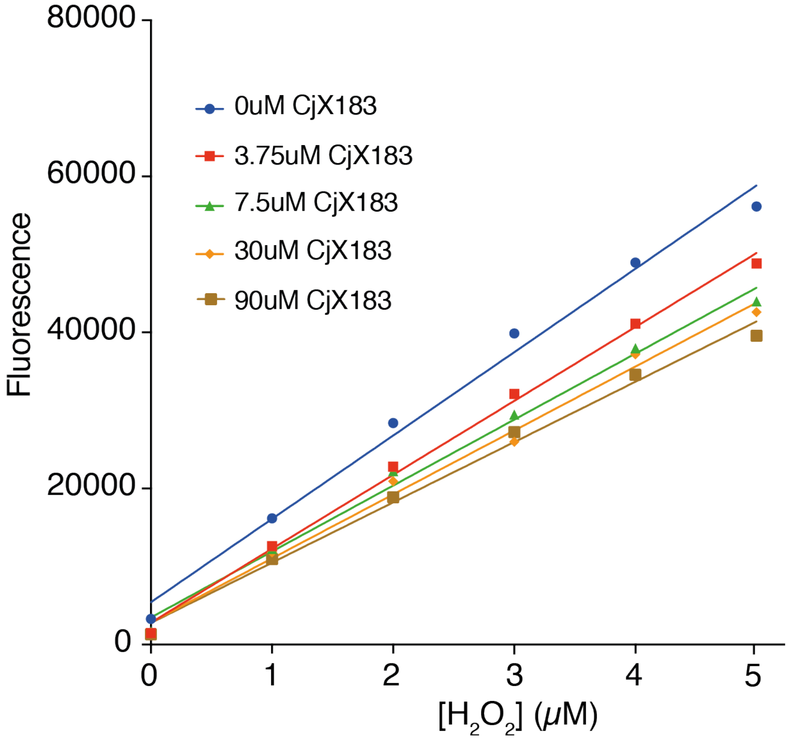

Figure 6.5: Absorbance from CjX183 exhibits inner filter effects. *H_2O_2 concentration curve showing fluorescence of resorufin measured at H_2O_2 concentrations from 0-5 μM, concentrations of CjX183 used as indicated in the inset.*

6.4.3 LPMOs produce less H_2O_2 when activated with CjX183 compared to ascorbate

The activities of CjAA10BΔCBM and CfAA10 to generate H_2O_2 were measured using the Amplex Red H_2O_2 assay. Both enzymes were active in samples where an electron source, either reduced CjX183 or ascorbate, was supplied, indicated by a steady production of peroxide to reach a plateau (Figure 6.6), presumably a result of depleted reducing agent or enzyme inactivity. Control samples comprised of LPMOs without reducing agents did not generate any background H_2O_2. In reductant-supplied reactions, reduced CjX183 was used at twice the concentration of ascorbate, as ascorbate is a two electron donor and CjX183 was assumed to be a single electron donor, ensuring delivery of the same number of electrons to LPMOs.

Results from these experiments enabled the activities of CjAA10BΔCBM and CfAA10 to be compared when activated by different electron sources. Figure 6.6 shows that significantly more H_2O_2 was produced when ascorbate was used as an electron donor to CjAA10BΔCBM or CfAA10 compared to using reduced CjX183. It is important to note, that in the absence of LPMOs, autoxidation of ascorbate or CjX183 will also generate H_2O_2 from oxygen. Production of H_2O_2 by ascorbate was significantly larger than from reduced CjX183, in line with observations from other studies that suggest H_2O_2 production by ascorbate to be beneficial to the LPMO reaction (Kittl et al., 2012; Stepnov et al., 2021; Bissaro et al., 2017). However, it appears that in the presence of LPMOs, H_2O_2 is produced more rapidly and reductants are depleted faster than in LPMO-free controls. Therefore, it was assumed that the vast majority of H_2O_2 produced in assays with LPMOs was a result of LPMO activity rather than from reductant autoxidation.

Each combination of LPMO and redox partner exhibited a different propensity to produce H_2O_2 (Figure 6.6). For the CjAA10BΔCBM enzyme: 2.56 μM of H_2O_2 was produced after an hour of activation with ascorbate, which was reduced to 0.56 μM when CjX183 was used instead. For the CfAA10 enzyme: with ascorbate, 1.60 μM H_2O_2 was produced by the enzyme after an hour, reduced to 0.75 μM with the use of CjX183. These results showed that both LPMOs, CjAA10BΔCBM and CfAA10, produced significantly less H_2O_2 when a protein partner, CjX183, was used as an electron source compared to a small molecule reductant, ascorbate.

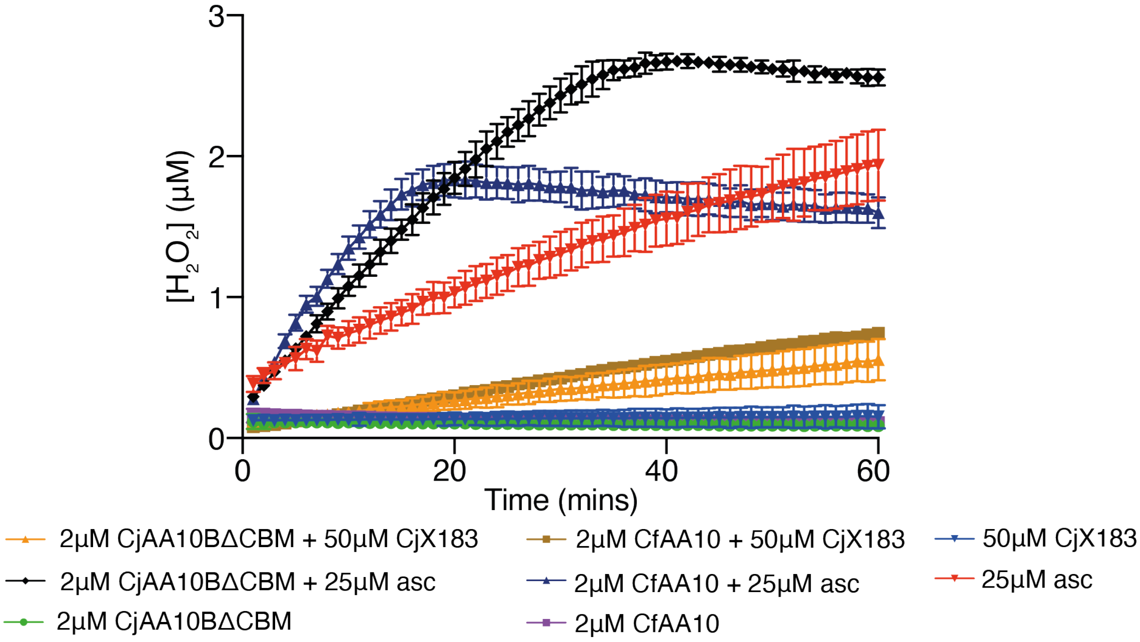

Figure 6.6: Analysis of H_2O_2 production by CjAA10BΔCBM and CfAA10 enzymes using the Amplex Red H_2O_2 assay. *LPMOs were powered by ascorbate or reduced CjX183, samples are annotated in the inset.*

6.4.4 Kinetic parameters of CjAA10BΔCBM and CfAA10 enzymes were measured using the Amplex Red H_2O_2 assay

The Amplex Red H_2O_2 assay enabled determination of kinetic parameters for the H_2O_2 producing reaction of CjAA10BΔCBM and CfAA10 with both redox partners. In order to do this, LPMO concentrations were held constant and reductant concentrations were varied to enable kinetic analyses. For this reaction, CjX183 and ascorbate were assumed to act as the substrate, donating a finite number of electrons as they were not being regenerated. Therefore, varying the reductant concentration was analogous to varying the substrate concentration for classical Michaelis-Menten kinetics. These experiments enabled the extraction of values for the Michaelis constant (K_m) and maximum enzymatic rate (V_{max}) for each enzyme-substrate pair, utililising the Michealis-Menten equation: $V=(V_{max}[S])/(K_m+[S])$, where V is the observed rate, V max is the maximum enzymatic rate, [S] is the substrate concentration and K_m is the substrate concentration where half of the maximum rate is achieved.

Calculated parameters fitted to predictable Michaelis-Menten kinetics for the LPMO-ascorbate reactions. However, for the CjX183-driven reactions, a significant amount of substrate inhibition was observed, shown in Figure 6.7. When the rates of H_2O_2 production were analysed using a Lineweaver-Burk plot, substrate inhibition was obvious at higher CjX183 concentrations (Figure 6.7 B and D). The Lineweaver-Burke plot is a double reciprocal plot, where the reciprocal of the observed rate for each substrate concentration is plotted against the reciprocal of the substrate concentration. In this plot the gradient of the straight line should be equal to the K_m value. Although substrate inhibition must be occurring whenever substrates are present, it is particularly prominent at higher concentrations, indicated by these values not conforming to a linear trend in Figure 6.7 B and D. Therefore, in subsequent experiments, points at saturating conditions, that could be seen to deviate from the linear trend, were excluded during analysis as they impeded the fitting process.

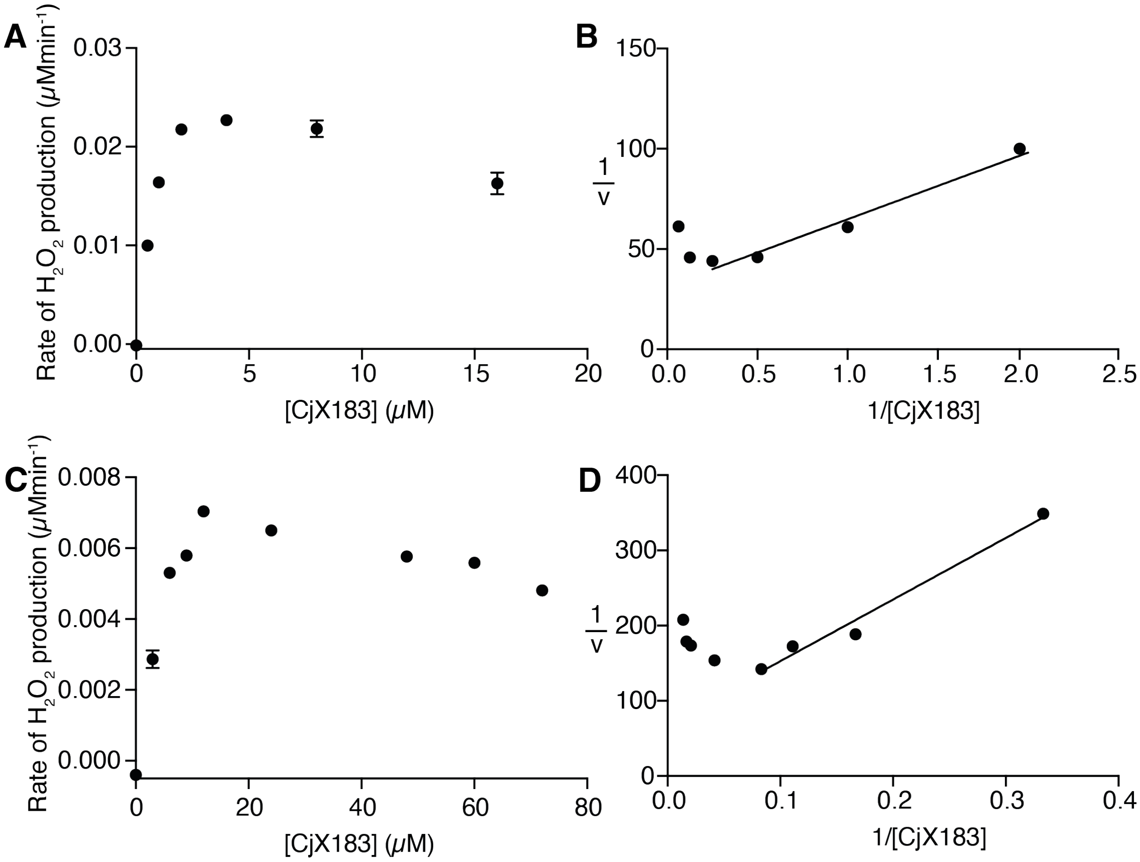

Figure 6.7: Substrate inhibition observed for LPMOs activated by CjX183 in the Amplex Red H_2O_2 assay. (A) *Rate of H_2O_2 production by CjAA10BΔCBM using CjX183 at concentrations from 0-16 μM.* ***(B)*** *Lineweaver-Burk plot for CjAA10BΔCBM activated by CjX183, where v represents rate of H_2O_2 production* ***(C)*** *Rate of H_2O_2 production by CfAA10 using CjX183 at concentrations from 0-72 μM.* ***(D)*** *Lineweaver-Burk plot for CjAA10 activated by CjX183.*

Fitting of these data sets was performed using the Michaelis-Menten equation: $V=(V_{max}[S])/(K_m+[S])$, where V is the observed rate, V max is the maximum enzymatic rate, [S] is the substrate concentration and K_m is the substrate concentration where half of the maximum rate is achieved, inbuilt in GraphPad, for the graphs shown in Figure 6.8. Fitting generated values for V_{max}, the maximum rate of H_2O_2 production by the enzyme, and the K_m, the Michaelis Constant: the substrate concentration at which ½ V_{max} is achieved, which can be reflective of the affinity of an enzyme for its substrate. For both the CjAA10BΔCBM and CfAA10, the V_{max} values were highest for the ascorbate activated enzymes (Figure 6.8), supporting the results seen in section 6.4.3. For CjAA10BΔCBM, the V_{max} was reduced nearly 2-fold when ascorbate was replaced with reduced CjX183, and this change was 10-fold lower for the CfAA10 enzyme. For both LPMOs the apparent K_m values for the CjX183 domain were lower than for ascorbate. The lowest K_m values were seen when the CjAA10BΔCBM enzyme was activated with reduced CjX183, with a K_m of 0.78 μM. Since K_m is often correlated to binding affinity, this could imply that the binding affinity of the CjAA10BΔCBM-CjX183 pair is greater than with ascorbate, or for the CfAA10 enzyme with CjX183. Speculation of a specific interaction between the two proteins of the same species could support a role for CjX183 as an LPMO activator in *C. japonicus*. However, in order to correlate low K_m values with affinity, protein-protein interactions would have to be investigated further.

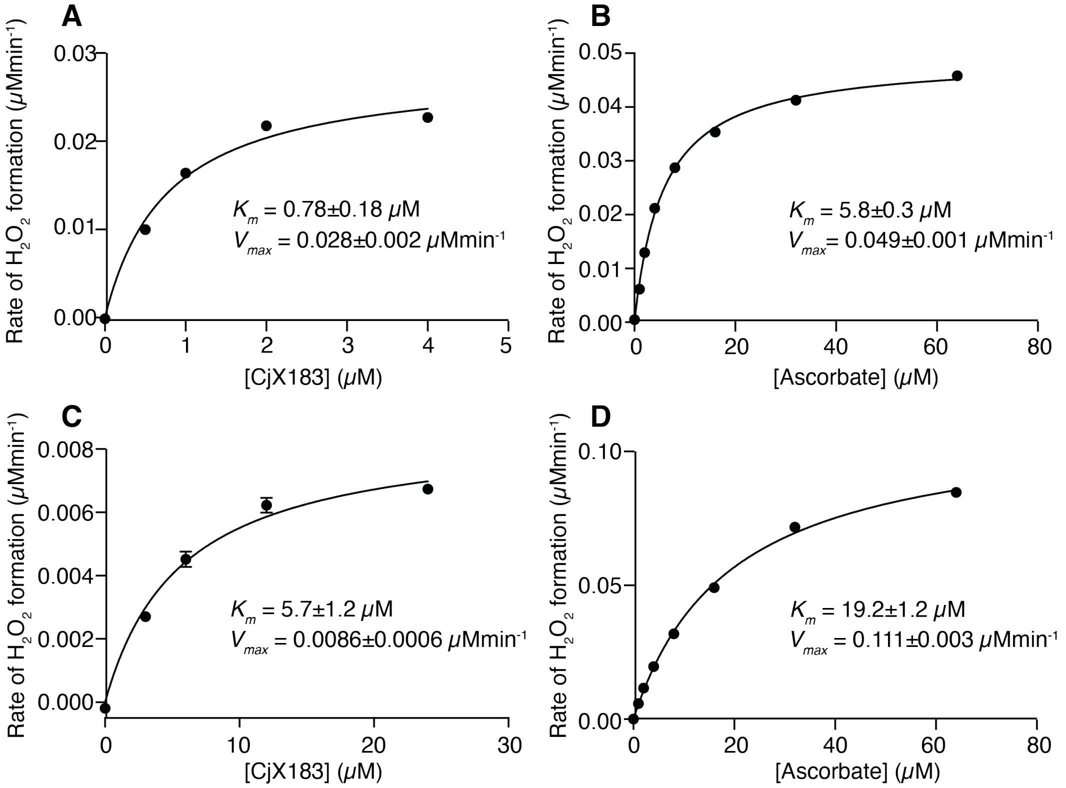

Figure 6.8: Kinetic comparison of LPMOs activated by reduced CjX183 or ascorbate using the Amplex Red assay. (A) *Plot of the rate of H_2O_2 production by CjAA10BΔCBM at different concentrations of CjX183, data were fitted to the Michaelis-Menten equation to generate annotated values. Equivalent plots in* ***(B)*** *for CjAA10BΔCBM activated by ascorbate.* ***(C)*** *for CfAA10 activated by CjX183.* ***(D)*** *CfAA10 activated by ascorbate.*

The calculated parameters of V_{max} and K_m were used to define a value for the observed rate constant (k_{obs}) and the catalytic efficiency for each enzyme-substrate pair. These parameters for the CjAA10BΔCBM and CfAA10 enzymes with both electron partners are shown in Table 6.1. k_{obs} was defined as the number of molecules of substrate an enzyme could turnover in one minute at its maximum speed, akin to the catalytic constant (k_{cat}). However, due to the many complexities of LPMO activation, the rate limiting step is undefined, so k_{obs} may not be equal to k_{cat} and could represent a range of potential rates, from oxygen binding at the histidine brace, electron transfer from ascorbate or CjX183 or conversion of oxygen to H_2O_2. Despite issues defining the precise rate that k_{obs} corresponds to, it is clear that these rates are drastically lowered when ascorbate is replaced with reduced CjX183. Additionally, catalytic efficiency of each reductant-LPMO combination was analysed, defined as k_{obs}/K_m, which indicated that the pair with the highest catalytic efficiency was the combination of CjAA10BΔCBM activated by reduced

CjX183. Although there are many complications in this assay, due to the complex nature of LPMO activation and the multiple variables within these reactions, it is clear that there are interesting differences between how different reductants may interact and activate LPMOs. However, further investigation is required to probe these intricacies and assess differences in enzyme activation on crystalline substrates.

	K_m *(μM)*	V_{max} *(μM min^{-1})*	k_{obs} *(min^{-1})*	*Catalytic efficiency (μM^{-1} min^{-1})*
CjAA10BΔCBM + CjX183	0.78 ± 0.18	0.028 ± 0.002	0.014	0.018
CjAA10BΔCBM + ascorbate	5.8 ± 0.3	0.049 ± 0.001	0.0245	0.0042
CfAA10 + CjX183	5.7 ± 1.2	0.0086 ± 0.006	0.0043	0.00075
CjAA10 + ascorbate	19.2 ± 1.2	0.111 ± 0.003	0.0555	0.0029

Table 6.1: Kinetic parameters for CjAA10BΔCBM and CfAA10 enzymes calculated in the Amplex Red H_2O_2 assay following activation with reduced CjX183 or ascorbate.

6.5 LPMO activity on cellulosic substrates was analysed using boosting experiments

Following on from the Amplex Red H_2O_2 assay, which showed that CjAA10BΔCBM and CfAA10 both produced significantly less H_2O_2 when activated by reduced CjX183 compared to ascorbate, boosting experiments were performed to compare activities of LPMOs on cellulosic substrates when activated by different reductants. Boosting assays have been widely used in the LPMO field (Quinlan et al., 2011; Lo Leggio et al., 2015; Sabbadin et al., 2018), and examine an LPMO's ability to boost polysaccharide degradation by other degradative enzymes. Glycoside hydrolase enzymes release cellobiose, which is soluble and detectable by a number of methods, whereas most LPMO breakdown products are long polysaccharides that are not easily quantified. Most boosting studies performed previously have used high pressure anion exchange chromatography, HPAEC, to quantify cellobiose (Forsberg et al., 2011; Cannella et al., 2012) however, HPAEC facilities are not available in Leeds, so a new method was developed for these studies.

6.5.1 Cellobiose was quantified using ESI-MS

For these studies, a method of detecting and quantifying cellobiose from boosting experiments was developed. With the help of Dr Kristian Hollingsworth (University of Leeds, Leeds, UK), cellobiose was quantified by positive mode ESI-MS. In order to quantify the cellobiose produced, a known amount of ^{13}C cellobiose was spiked into the reaction. The spectrum for one such reaction is shown in Figure 6.9. The peak height at 365 on the m/z scale, corresponding to cellobiose-Na$^+$, was compared to the peak at 377, for the ^{13}C cellobiose-Na$^+$ ion, and from this the concentration of cellobiose produced in the reaction was calculated.

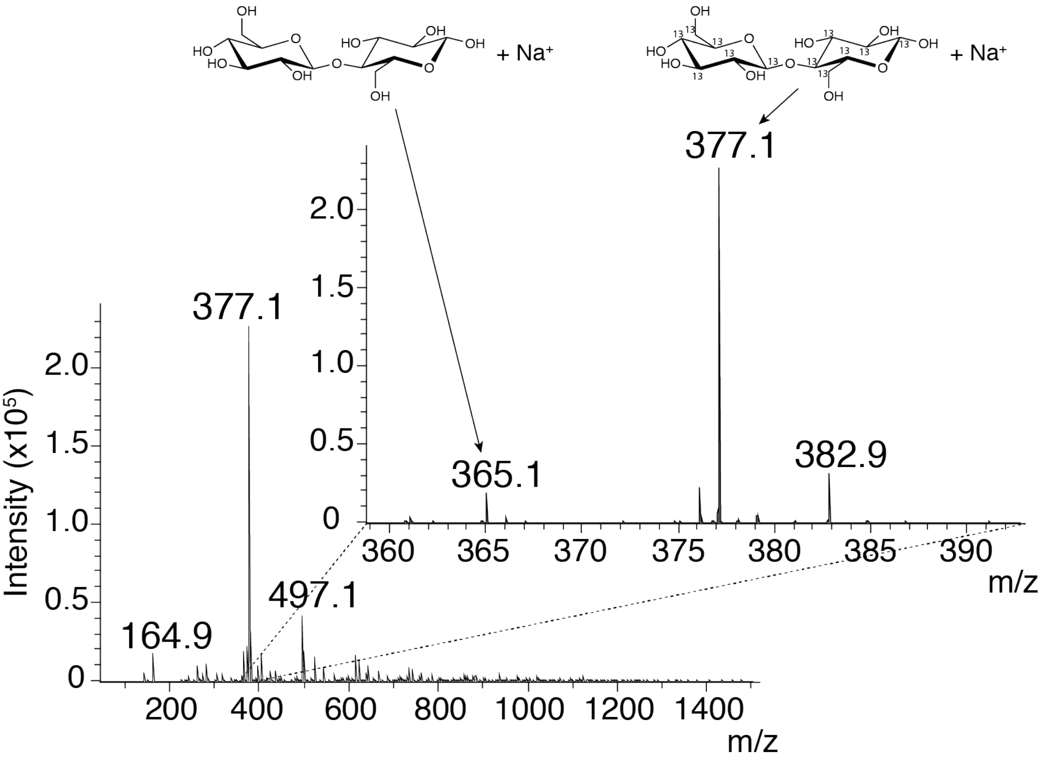

Figure 6.9: ESI-MS spectrum showing quantification of cellobiose from boosting experiments. *The 360-390 m/z region is highlighted allowing the cellobiose-Na+ peak at 365 to be compared to the spiked ^{13}C cellobiose-Na+ peak at 377.*

6.5.2 CjX183 boosts LPMO activity to the same extent as ascorbate

Boosting experiments were set up using a GH7 CBH from *Trichoderma longibrachiatum* on two cellulosic substrates: Avicel, a crystalline cellulose substrate, and PASC. Boosting was performed for CjAA10BΔCBM and CfAA10 with both redox partners: reduced CjX183 and ascorbate, where the ascorbate was used at half the concentration of CjX183, consistent with previous experiments, to ensure equivalent amounts of electrons were supplied. Avicel has a more crystalline structure than PASC, which has some amorphous regions due to its acid pretreatment, therefore the Avicel boosting reactions were incubated for longer than the reactions on PASC to allow for slower breakdown on Avicel.

Results from the boosting experiments (Figure 6.10) showed that both CjAA10BΔCBM and CfAA10 enzymes were able to boost degradation of PASC and Avicel by the GH7 from *T. longibrachiatum*. It appears that on both substrates, LPMOs from *C. japonicus* and *C. fimi* were able to boost degradation to the same extent when activated by reduced CjX183 or ascorbate. These results were more consistent in the experiments tested on PASC, the nature of these insoluble substrates often make them hard to work with, a combination of this and the longer incubation time of the reaction could explain the higher error levels seen in the Avicel reactions. These results suggest that, although conclusions from the Amplex Red assay suggested enzymes were more active when activated by ascorbate, on crystalline substrates in the boosting experiments, the LPMOs appeared to be equally active with either redox partner.

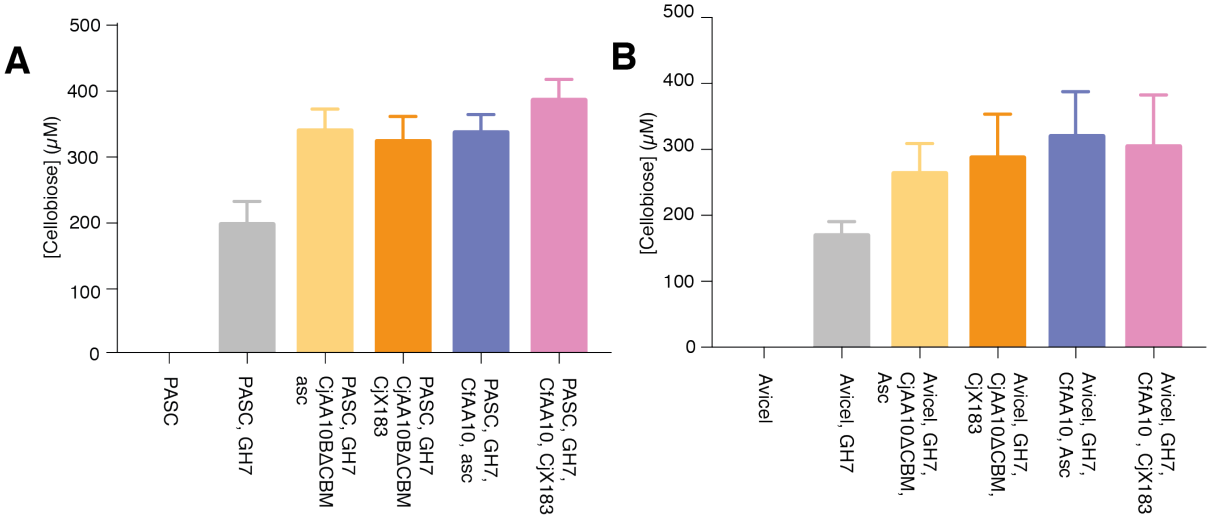

Figure 6.10: Boosting experiments using CjAA10BΔCBM and CfAA10. *Enzymes were activated by reduced CjX183 or ascorbate with a GH7 from Trichoderma longibrachiatum on **(A)** PASC for 8 hours and **(B)** Avicel for 16 hours.*

6.6 Activation by CjX183 reduces protein damage to LPMOs compared to ascorbate activation

Oxidative damage to LPMOs, as a result of H_2O_2 production in the absence of substrates, has been shown to lead to enzyme inactivation over time (Hangasky et al., 2018; Bissaro et al., 2017). Recent studies have investigated oxidative damage in experiments using H_2O_2 as a co-substrate to LPMOs, and have used mass spectrometry to map adducts on the enzymes corresponding to oxidative modifications. Mapping of these oxygen adducts revealed that they were largely found on the catalytic histidine residues and to a smaller degree on the neighbouring active site residues (Bissaro et al., 2017; Hangasky et al., 2018).

In the Amplex Red H_2O_2 assay, it was shown that both CjAA10BΔCBM and CfAA10 produced more H_2O_2 over time when activated by ascorbate compared to with reduced CjX183. Consequently, it was investigated whether increased H_2O_2 production was causing more oxidative damage to enzymes activated by ascorbate. ESI-MS was used to assess the level of oxidation occurring to the enzymes themselves over time. In the absence of substrate, LPMOs were incubated with equivalent amounts of ascorbate or reduced CjX183, under the same conditions used for the cellulose degradation and Amplex Red assays. Accurate ESI-MS spectra were taken for each sample at a number of time points: upon mixing, after 1 hour for CfAA10 or 2 hours for CjAA10BΔCBM reactions, and at 24 hours. Over time, species at +16 Da from the wild type peak appeared, these peaks were assumed to be a result of direct oxidation to the LPMOs. Comparison of the abundance of the unmodified protein peaks, at the expected molecular weight, to the oxidised peaks allowed the ratio of wild type to damaged protein to be approximated.

The ESI-MS spectra, shown in Figure 6.11, showed clear differences in oxidative damage to LPMOs when ascorbate was replaced with reduced CjX183. The CfAA10 enzyme appeared to be much more sensitive to damage, with peaks for the singly oxidised protein appearing after 1 hr with both electron donors (Figure 6.11C and D). For the CfAA10 enzyme, there was significantly more damage when activated by ascorbate, with a peak appearing after 24 hours for the doubly oxidised enzyme. The CjAA10BΔCBM enzyme, on the other hand, showed much less oxidative damage (Figure 6.11A and B). For the CjX183-activated sample there were no significant peaks after 24 hours to suggest the presence of the +16 Da species. There was some oxidative damage in the ascorbate-driven sample after 24 hours, demonstrated by the presence of the singly oxidised species, and a small amount of doubly oxidised species.

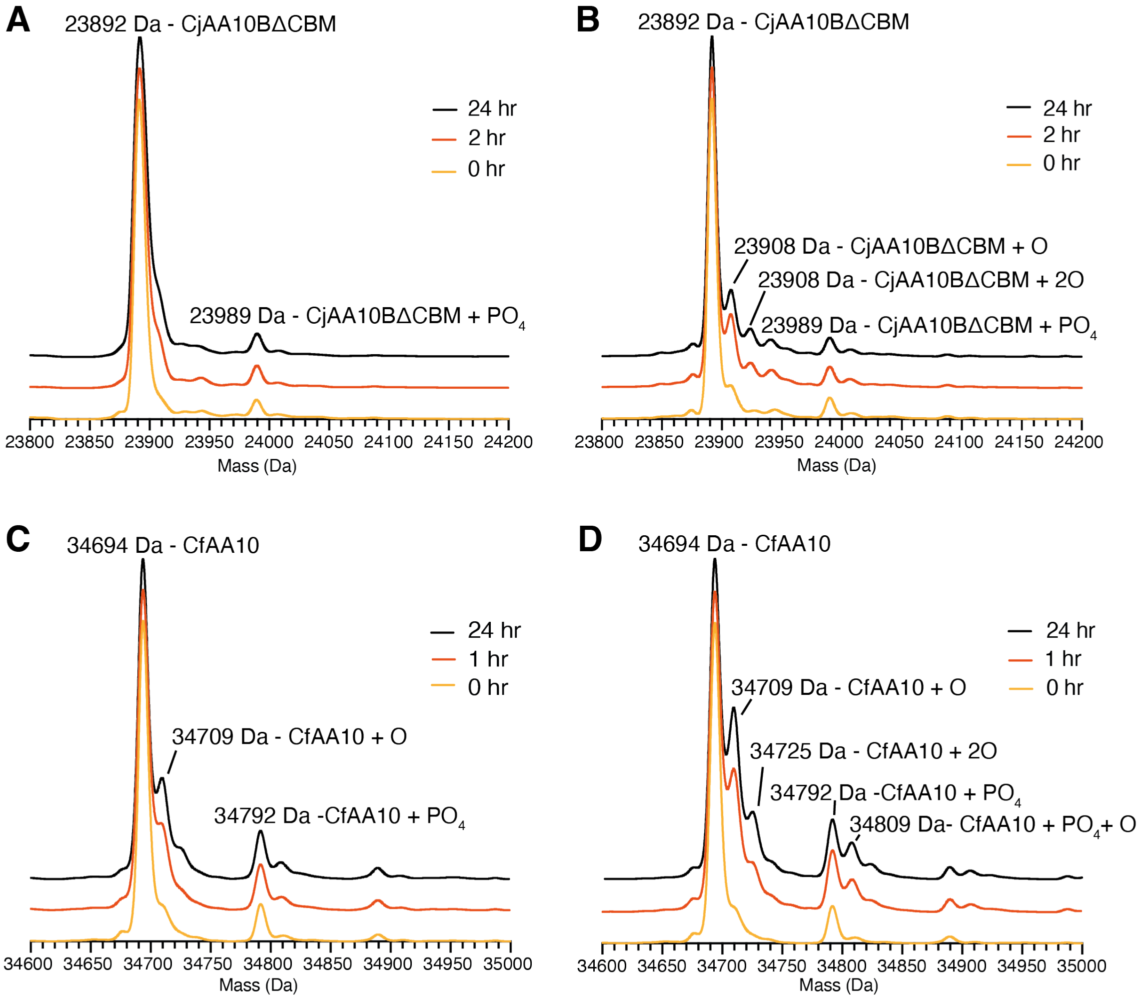

Figure 6.11: ESI mass spectrometry data to show oxidative damage to LPMOs. (A) *CjAA10BΔCBM activated by reduced CjX183 at time points 0, 1 and 24 hours, peaks at relevant masses are annotated.* ***(B)*** *CjAA10BΔCBM activated by ascorbate, annotated in the same manner as (A).* ***(C)*** *CfAA10 activated by reduced CjX183 at time points 0, 2 and 24 hours, with relevant peaks labelled.* ***(D)*** *CfAA10 activated by ascorbate, annotated as in (C).*

For both LPMOs, oxidative damage to the enzymes was significantly lower when ascorbate was replaced with the reduced CjX183 domain. These results correlate well with observations from the Amplex Red H_2O_2 assay, which showed increased H_2O_2 by LPMOs activated by ascorbate instead of reduced CjX183. From these observations, accumulation of H_2O_2 can be directly associated with oxidative damage to LPMOs, in line with previous studies (Bissaro et al., 2017). These results present the deleterious effect of H_2O_2 on LPMOs and raise further questions about the use of H_2O_2 as a co-substrate to LPMOs.

6.7 Summary

This chapter has demonstrated the ability of the small cytochrome domain, CjX183, from *C. japonicus* protein Cbp2D, to act as a redox partner to bacterial LPMOs. Experiments explored here have presented evidence for activation of two bacterial LPMOs: CjAA10BΔCBM and CfAA10 by reduced CjX183, and have performed comparisons between activation by small molecule reductants or a protein partner.

Reduced CjX183 was demonstrated to transfer electrons to both bacterial LPMOs in this study, however, faster electron transfer was observed from CjX183 to CfAA10, not the LPMO from *C. japonicus*. Speculation on this subject could hypothesise that the more specific interaction between CjAA10BΔCBM and CjX183 could represent a higher affinity and longer lived complex. Were this to be the case, a longer interaction would result in slower electron transfer in the higher affinity pair. Interestingly, measured electron transfer rates were also slower than those that have been observed for CDH. Studies here with CjX183 present electron transfer rates in the order of min^{-1}, equivalent studies on *Mt*CDH to an LPMO from *S. coelicolor* measured rates in the order of sec^{-1} (Loose et al., 2016). Whether rate differences observed in this study, and comparisons with other studies, are directly related to LPMO activity and affinities, or a function of surface interactions between different proteins, is unclear without evidence for the nature of such interactions.

Reduced CjX183 was able to activate CjAA10BΔCBM and CfAA10 to generate oxidised products from PASC, in a manner mirroring activation by ascorbate, confirming enzymatic turnover following electron transfer. Additionally, the H_2O_2 producing abilities of LPMOs were also measured using the Amplex Red H_2O_2 assay. Interestingly, significantly less H_2O_2 was produced when reduced CjX183 was used in place of ascorbate. The kinetic data from this assay were complicated and caution was applied to data interpretation. However, comparisons of apparent K_m values for LPMOs activated by ascorbate or CjX183 showed consistently lower values for CjX183 activation, which could support formation of higher affinity interactions between LPMOs and a protein partner compared to a small molecule if K_m is reflective of protein affinities. Compiled with findings above, these results could suggest the presence of a higher affinity interaction between CjX183 and CjAA10BΔCBM. If a specific interaction could be measured, then this may lend further support to the function of the CjX183 domain to activate LPMOs.

Further experiments were performed to assess LPMO activity on cellulosic substrates. Both ascorbate and CjX183 were able to activate LPMOs to boost degradation of substrate by a GH7 endocellulase to an equal extent, suggesting that LPMOs were equally active irrespective of redox partner, despite results from the Amplex Red H_2O_2 assay suggesting that enzymes were more active when activated by ascorbate. Examining protein damage showed that the reduced H_2O_2 production, resulting from CjAA10BΔCBM activation by CjX183, also resulted in less oxidative damage. These observations were in line with studies that have demonstrated the damaging effects of overaccumulation of H_2O_2 on LPMOs (Bissaro et al., 2017; Muller, G. et al., 2018; Kuusk et al., 2018; Kuusk et al., 2019).

This chapter has ascertained the ability of CjX183 to act as a protein partner to bacterial LPMOs, in direct comparison with the small molecule reductant, ascorbate. These results feed into current discussions in the field concerning the importance of H_2O_2 in LPMO activation. While H_2O_2 can contribute to significant boosts in LPMO activity, it is also strongly correlated to protein damage, as has been shown here. The role of protein partners in LPMO activation is still largely uncharacterised, and the work presented here highlights the delicate balance between enzyme turnover and inactivation. Whether Cbp2D is involved in activating LPMOs *in vivo* is still unclear, however, this chapter has shown that CjX183 is certainly capable of performing electron transfer to bacterial LPMOs to initiate oxidative breakdown.

Chapter 7

Concluding remarks and future perspectives

7.1 Summary

This thesis has described the progress made in characterising the previously unexplored Cbp2D and Cbp2E proteins from *C. japonicus*, and assessment of their individual domains as LPMO redox partners.

Chapter 1 introduced second-generation biofuels and the challenges involved in lignocellulose degradation, which must be overcome to liberate glucose monomers for their fermentation into ethanol. LPMOs are copper-dependent monooxygenases, and of great importance in biomass breakdown, due to their ability to boost the activity of canonical cellulases (Harris et al., 2010). Protein partners are largely thought to be responsible for transferring electrons to LPMOs, to initiate their catalytic mechanism, and this topic is the primary subject of this thesis. The fungal enzyme CDH has been extensively characterised for this purpose (Phillips et al., 2011; Tan et al., 2015; Loose et al., 2016), and a number of electron-transferring proteins partners have been identified to fungal LPMOs (Kracher et al., 2016). However, there is no known CDH equivalent in bacteria, and bacterial protein partners to LPMOs are largely uncharacterised. Cbp2D and Cbp2E from *C. japonicus* are two proteins that have been suggested to act as bacterial redox partners, and this thesis set out to investigate this hypothesis.

In Chapter 3 the structure of an LPMO from *C. japonicus* was determined. Although this protein has been biochemically characterised previously (Gardner et al., 2014), prior to this work the structure of CjAA10B was unknown. The structure of the catalytic domain of CjAA10B was used to explore the relationship between electron transfer and LPMO activation. Electron transfer to LPMOs is complicated, the active site is likely to be obscured by substrate binding during catalysis, and intraprotein electron transfer pathways may act to deliver electrons to the active site. Two potential electron transfer paths through CjAA10B were identified, providing electron hopping routes through the protein to the catalytic copper ion. The presence of these pathways supports hypotheses that binding sites, away from the active site, may exist for protein partners to activate bacterial LPMOs.

Chapters 4 to 6 focussed on characterisation of domains from Cbp2D and Cbp2E, which may be potential electron donors to the LPMOs in *C. japonicus*. Chapter 4 determined the novel structure of the X158E domain from Cbp2E. Although the X158E domain was a predicted ubiquinone-binding domain, these studies were unable to obtain a quinone-bound form of CjX158E. Comparisons of CjX158E with structurally similar proteins revealed altered cofactor binding relative to other family members. These observations questioned the true cofactor of CjX158E, with indications that it may bind ubiquinone-9 instead of ubiquinone-8, as originally thought. Although a redox-active form of CjX158E was not obtained, these studies have provided a crucial starting point for the characterisation of Cbp2E.

Chapters 5 and 6 investigated the role of the X183 domain from Cbp2D. The structure of CjX183 confirmed predictions that it was a *c*-type cytochrome and subsequent biochemical studies showed it to be redox active, with a redox potential capable of activating LPMOs. Since the reduced state of CjX183 was stable in an aerobic environment, activation of bacterial LPMOs by reduced CjX183 was able to be studied. As the CjX183 domain was not thought to have enzymatic activity, it was used as a finite electron source and its activation of LPMOs was compared with activation by the small molecule reductant ascorbate. LPMOs activated by reduced CjX183 and ascorbate were able to liberate soluble oxidised products from crystalline cellulosic substrates, demonstrating that reduced CjX183 was able to initiate LPMO turnover. By assessing the ability of these reductants to activate LPMOs to produce H_2O_2, it was clear that LPMOs produced significantly less H_2O_2 when activated by reduced CjX183 compared to ascorbate. Interestingly, apparent K_m values for enzyme-reductant pairs were also consistently lower when CjX183 was used as a redox partner. Although kinetic analyses from these experiments were complex, the apparent K_m values may be considered to report on protein affinities. If this is the case in these studies, then a lower K_m value may reflect a higher affinity between LPMOs studied here and CjX183, supporting the formation of specific interaction between the two proteins, which would not be expected for LPMOs and ascorbate. If a specific interaction could be confirmed, then this may further support a function for Cbp2D to activate LPMOs *in vivo*.

Boosting experiments were performed to assess the ability of LPMOs to boost the activity of a GH7 endocellulase on cellulosic substrates. LPMOs appeared to be equally active when activated by reduced CjX183 or ascorbate, which was interesting following previous observations that suggested that enzymes may be more active with ascorbate. Considering the variations in H_2O_2 production from LPMOs when activated by different reductants, prompted experiments to examine oxidative damage to the enzymes. LPMOs showed significantly more oxidative damage when activated by ascorbate compared to reduced CjX183, in line with other studies that have demonstrated the damaging effects of overaccumulation of H_2O_2 on enzyme lifetimes (Bissaro et al., 2017; Muller, G. et al., 2018; Kuusk et al., 2018; Kuusk et al., 2019). Taken together, the results from Chapters 5 and 6 contribute important information on the activation of LPMOs using protein partners compared to small molecules. These results suggest that a protein partner may activate LPMOs in a more specific manner, reducing the build-up of damaging H_2O_2 and increasing enzyme lifetimes. Demonstration that reduced CjX183 can activate bacterial LPMOs lends further support to the role of Cbp2D as an LPMO activator within *C. japonicus*.

7.2 Future perspectives

This thesis has structurally characterised an LPMO from *C. japonicus* and has explored the X158E and X183 domains from *C. japonicus* Cbp2D and Cbp2E proteins as potential LPMO activators. This work has demonstrated novel research linking the CjX183 domain to LPMO activation. However, these domains only represent two of four X-domains present in Cbp2D and Cbp2E, investigation into the roles of the other domains is essential in order to decipher the true function of the proteins.

During this project, efforts were made to recombinantly express the full length Cbp2D and Cbp2E proteins in *E. coli*, however, soluble protein expression was never achieved through these methods. Expressing the X132 domain of Cbp2D individually was also challenging, due to significant protein expression problems. The X132 domain is the most unique domain of the X-domains, it has no sequence similarly to any characterised domains or proteins, and is proposed to act as a cytochrome domain due to the presence of a haem binding motif -CXXCH in its sequence, however, its true role is unknown. A number of different vectors for protein expression, with various N-terminal signal sequences, were trialled, and were co-expressed with the pEC86 plasmid to assist haem incorporation. In these attempts, CjX132 was seen to be overexpressed, by analysis of the insoluble fraction of cells following IPTG induction. However, soluble expression of CjX132 was never achieved. Expressed CjX132 did not appear to bind haem, indicated by the absence of red coloured cells following protein expression, therefore CjX132 was assumed to be in stored inclusion bodies following protein misfolding. Unfortunately, problems with CjX132 expression were never overcome, so CjX132 was not biochemically characterised. Expression of the X158D domain from Cbp2D was also affected by insolubility. Efforts were made to improve soluble expression of CjX158D, but were unfortunately unsuccessful and soluble protein was not obtained. Expression and characterisation of the X158D and X132 domains from Cbp2D, and the full length Cbp2D and Cbp2E proteins, should be a priority in future work. Solubility problems could be circumvented by purifying full length proteins from *C. japonicus*. Although this process would be lower yield than recombinant expression in *E. coli*, the structure of these larger proteins could be studied using cryo-electron microscopy, which requires much lower protein concentrations compared to X-ray crystallography. Characterising the full Cbp2D and Cbp2E polypeptides will allow the domains to be probed in concert, to assess whether they can work together to activate LPMOs.

It is still important to determine the true cofactor of CjX158E. If CjX158E does indeed require Ub-9, then these studies should be performed in *C. japonicus* and further efforts should be focussed on scaling up the growth of *C. japonicus* cells to produce sufficient protein. For CjX183, interactions between the cytochrome and the LPMO should be studied. Unfortunately, determining interactions between LPMOs and redox partners is challenging due to the transient nature of interactions required for electron transfer. However, work is ongoing in the Hemsworth lab to trap this transient interaction between CjX183 and CjAA10BΔCBM using a novel chemical crosslinker (Horne et al., 2018). Analysis of the interaction between CjX183 and CjAA10BΔCBM at the residue level will help to elucidate the mechanism by which CjX183 is able to activate LPMOs, and provide key information on LPMO activation by protein partners.

Additionally, although these domains have been suggested to form larger redox active proteins, the initial source of electrons to these proteins is still uncharacterised. CDH has been shown to generate electrons at its dehydrogenase domain and shuttle them to LPMOs through its cytochrome domain (Tan et al., 2015). Cbp2D and Cbp2E are not predicted to contain enzymatic domains that could generate electrons, unless the elusive X132 domain can perform this role. Therefore, searching for the initial source of these electrons is imperative. It could be that additional dehydrogenases could be at play, using the redox domains of Cbp2D and Cbp2E as mediators, as has been seen in work with small molecule activators of LPMOs (Kracher et al., 2016). In order to understand the role of Cbp2D and Cbp2E within *C. japonicus*, this initial electron source must be identified.

7.3 Concluding remarks

This thesis has characterised domains from *C. japonicus* proteins Cbp2D and Cbp2E to assess their ability to act as redox partners to bacterial LPMOs. Three novel crystal structures have been proposed, providing crucial functional information about CjAA10B, Cbp2D and Cbp2E. In doing so, the CjX183 domain has been proposed as a novel redox partner to bacterial LPMOs, and has been shown to be less damaging to enzymes than small molecule reductants that are commonly used in enzyme cocktails. This work has provided the first comprehensive characterisation of domains from Cbp2D and Cbp2E, and is an important starting point in identifying *C. japonicus* LPMO redox partners.

Prior to this work, little information was available on the activation of LPMOs from *C. japonicus in vivo*, this research has provided the starting point for these investigations, which will be critical in understanding the mechanism of LPMO activation to allow enzymes to be optimally harnessed for biomass breakdown.

List of References

Aachmann, F.L., Sorlie, M., Skjak-Braek, G., Eijsink, V.G. and Vaaje-Kolstad, G. 2012. NMR structure of a lytic polysaccharide monooxygenase provides insight into copper binding, protein dynamics, and substrate interactions. *Proceedings of the National Academy of Sciences.* **109**(46), pp.18779-18784.

Agger, J.W., Isaksen, T., Varnai, A., Vidal-Melgosa, S., Willats, W.G., Ludwig, R., Horn, S.J., Eijsink, V.G. and Westereng, B. 2014. Discovery of LPMO activity on hemicelluloses shows the importance of oxidative processes in plant cell wall degradation. *Proceedings of the National Academy of Sciences.* **111**(17), pp.6287-6292.

Agrawal, S., Jaswal, K., Shiver, A.L., Balecha, H., Patra, T. and Chaba, R. 2017. A genome-wide screen in *Escherichia coli* reveals that ubiquinone is a key antioxidant for metabolism of long-chain fatty acids. *Journal of Biological Chemistry.* **292**(49), pp.20086-20099.

Arslan, E., Schulz, H., Zufferey, R., Kunzler, P. and Thony-Meyer, L. 1998. Overproduction of the *Bradyrhizobium japonicum c*-type cytochrome subunits of the cbb3 oxidase in *Escherichia coli*. *Biochemical and Biophysical Research Communications.* **251**(3), pp.744-747.

Bao, W., Usha, S.N. and Renganathan, V. 1993. Purification and characterization of cellobiose dehydrogenase, a novel extracellular hemoflavoenzyme from the white-rot fungus *Phanerochaete chrysosporium*. *Archives of Biochemistry and Biophysics.* **300**(2), pp.705-713.

Beeson, W.T., Phillips, C.M., Cate, J.H. and Marletta, M.A. 2012. Oxidative cleavage of cellulose by fungal copper-dependent polysaccharide monooxygenases. *Journal of the Americal Chemical Society.* **134**(2), pp.890-892.

Beeson, W.T., Vu, V.V., Span, E.A., Phillips, C.M. and Marletta, M.A. 2015. Cellulose degradation by polysaccharide monooxygenases. *Annual Review of Biochemistry.* **84**, pp.923-946.

Bennati-Granier, C., Garajova, S., Champion, C., Grisel, S., Haon, M., Zhou, S., Fanuel, M., Ropartz, D., Rogniaux, H., Gimbert, I., Record, E. and Berrin, J.G. 2015. Substrate specificity and regioselectivity of fungal AA9 lytic polysaccharide monooxygenases secreted by *Podospora anserina*. *Biotechnology for Biofuels.* **8**, p90.

Berrin, J.G., Rosso, M.N. and Abou Hachem, M. 2017. Fungal secretomics to probe the biological functions of lytic polysaccharide monooxygenases. *Carbohydrate Research.* **448**, pp.155-160.

Bissaro, B., Isaksen, I., Vaaje-Kolstad, G., Eijsink, V.G.H. and Røhr, Å.K. 2018. How a Lytic Polysaccharide Monooxygenase Binds Crystalline Chitin. *Biochemistry.* **57**(12), pp.1893-1906.

Bissaro, B., Kommedal, E., Rohr, A.K. and Eijsink, V.G.H. 2020a. Controlled depolymerization of cellulose by light-driven lytic polysaccharide oxygenases. *Nature Communications.* **11**(1), p890.

Bissaro, B., Rohr, A.K., Muller, G., Chylenski, P., Skaugen, M., Forsberg, Z., Horn, S.J., Vaaje-Kolstad, G. and Eijsink, V.G.H. 2017. Oxidative cleavage of polysaccharides by monocopper enzymes depends on H2O2. *Nature Chemical Biology.* **13**(10), pp.1123-1128.

Bissaro, B., Streit, B., Isaksen, I., Eijsink, V.G.H., Beckham, G.T., DuBois, J.L. and Rohr, A.K. 2020b. Molecular mechanism of the chitinolytic peroxygenase reaction. *Proceedings of the National Academy of Sciences.* **117**(3), pp.1504-1513.

Bissaro, B., Varnai, A., Rohr, A.K. and Eijsink, V.G.H. 2018. Oxidoreductases and Reactive Oxygen Species in Conversion of Lignocellulosic Biomass. *Microbiology and Molecular Biology Reviews.* **82**(4).

Book, A.J., Yennamalli, R.M., Takasuka, T.E., Currie, C.R., Phillips, G.N., Jr. and Fox, B.G. 2014. Evolution of substrate specificity in bacterial AA10 lytic polysaccharide monooxygenases. *Biotechnology for Biofuels.* **7**, p109.

Boraston, A.B., Bolam, D.N., Gilbert, H.J. and Davies, G.J. 2004. Carbohydrate-binding modules: fine-tuning polysaccharide recognition. *Biochemical Journal.* **382**(Pt 3), pp.769-781.

Borisova, A.S., Isaksen, T., Dimarogona, M., Kognole, A.A., Mathiesen, G., Varnai, A., Rohr, A.K., Payne, C.M., Sorlie, M., Sandgren, M. and Eijsink, V.G. 2015. Structural and Functional Characterization of a Lytic Polysaccharide Monooxygenase with Broad Substrate Specificity. *Journal of Biological Chemistry.* **290**(38), pp.22955-22969.

Breslmayr, E., Laurent, C., Scheiblbrandner, S., Jerkovic, A., Heyes, D.J., Oostenbrink, C., Ludwig, R., Hedison, T.M., Scrutton, N.S. and Kracher, D. 2020. Protein Conformational Change Is Essential for Reductive Activation of Lytic Polysaccharide Monooxygenase by Cellobiose Dehydrogenase. *ACS Catalysis.* **10**(9), pp.4842-4853.

Caldararu, O., Oksanen, E., Ryde, U. and Hedegard, E.D. 2019. Mechanism of hydrogen peroxide formation by lytic polysaccharide monooxygenase. *Chemical Science.* **10**(2), pp.576-586.

Cannella, D., Hsieh, C.W., Felby, C. and Jorgensen, H. 2012. Production and effect of aldonic acids during enzymatic hydrolysis of lignocellulose at high dry matter content. *Biotechnology for Biofuels.* **5**(1), p26.

Cannella, D., Mollers, K.B., Frigaard, N.U., Jensen, P.E., Bjerrum, M.J., Johansen, K.S. and Felby, C. 2016. Light-driven oxidation of polysaccharides by photosynthetic pigments and a metalloenzyme. *Nature Communications.* **7**, p11134.

Chalak, A., Villares, A., Moreau, C., Haon, M., Grisel, S., d'Orlando, A., Herpoel-Gimbert, I., Labourel, A., Cathala, B. and Berrin, J.G. 2019. Influence of the carbohydrate-binding module on the activity of a fungal AA9 lytic polysaccharide monooxygenase on cellulosic substrates. *Biotechnology for Biofuels.* **12**, p206.

Chen, V.B., Arendall, W.B., 3rd, Headd, J.J., Keedy, D.A., Immormino, R.M., Kapral, G.J., Murray, L.W., Richardson, J.S. and Richardson, D.C. 2010. MolProbity: all-atom structure validation for macromolecular crystallography. *Acta Crystallographica Section D: Biological Crystallography.* **66**(1), pp.12-21.

Chinchetru, M.A., Cabezas, J.A. and Calvo, P. 1989. Purification and characterization of a broad specificity beta-glucosidase from sheep liver. *International Journal of Biochemistry.* **21**(5), pp.469-476.

Chiu, E., Hijnen, M., Bunker, R.D., Boudes, M., Rajendran, C., Aizel, K., Olieric, V., Schulze-Briese, C., Mitsuhashi, W., Young, V., Ward, V.K., Bergoin, M., Metcalf, P. and Coulibaly, F. 2015. Structural basis for the enhancement of virulence by viral spindles and their in vivo crystallization. *Proceedings of the National Academy of Sciences.* **112**(13), pp.3973-3978.

Ciano, L., Davies, G.J., Tolman, W.B. and Walton, P.H. 2018. Bracing copper for the catalytic oxidation of C–H bonds. *Nature Catalysis.* **1**(8), pp.571-577.

Collins, M.D. and Jones, D. 1981. Distribution of isoprenoid quinone structural types in bacteria and their taxonomic implication. *Microbiology Reviews.* **45**(2), pp.316-354.

Conchie, J. 1954. Beta-Glucosidase from rumen liquor; preparation, assay and kinetics of action. *Biochemical Journal.* **58**(4), pp.552-560.

Courtade, G., Forsberg, Z., Heggset, E.B., Eijsink, V.G.H. and Aachmann, F.L. 2018. The carbohydrate-binding module and linker of a modular lytic polysaccharide monooxygenase promote localized cellulose oxidation. *Journal of Biological Chemistry.* **293**(34), pp.13006-13015.

Courtade, G., Wimmer, R., Rohr, A.K., Preims, M., Felice, A.K., Dimarogona, M., Vaaje-Kolstad, G., Sorlie, M., Sandgren, M., Ludwig, R., Eijsink, V.G. and Aachmann, F.L. 2016. Interactions of a fungal lytic polysaccharide monooxygenase with beta-glucan substrates and cellobiose dehydrogenase. *Proceedings of the National Academy of Sciences.* **113**(21), pp.5922-5927.

Couturier, M., Ladeveze, S., Sulzenbacher, G., Ciano, L., Fanuel, M., Moreau, C., Villares, A., Cathala, B., Chaspoul, F., Frandsen, K.E., Labourel, A., Herpoel-Gimbert, I., Grisel, S., Haon, M., Lenfant, N., Rogniaux, H., Ropartz, D., Davies, G.J., Rosso, M.N., Walton, P.H., Henrissat, B. and Berrin, J.G. 2018. Lytic xylan oxidases from wood-decay fungi unlock biomass degradation. *Nature Chemical Biology.* **14**(3), pp.306-310.

Cowley, R.E., Tian, L. and Solomon, E.I. 2016. Mechanism of O2 activation and substrate hydroxylation in noncoupled binuclear copper monooxygenases. *Proceedings of the National Academy of Sciences.* **113**(43), pp.12035-12040.

Cowtan, K. 2006. The Buccaneer software for automated model building. 1. Tracing protein chains. *Acta Crystallographica D: Biological Crystallography.* **62**(9), pp.1002-1011.

Cowtan, K. 2010. Recent developments in classical density modification. *Acta Crystallographica D: Biological Crystallography.* **66**(4), pp.470-478.

Crouch, L.I., Labourel, A., Walton, P.H., Davies, G.J. and Gilbert, H.J. 2016. The Contribution of Non-catalytic Carbohydrate Binding Modules to the Activity of Lytic Polysaccharide Monooxygenases. *Journal of Biological Chemistry.* **291**(14), pp.7439-7449.

Davies, G.J., Wilson, K.S. and Henrissat, B. 1997. Nomenclature for sugar-binding subsites in glycosyl hydrolases. *Biochemical Journal.* **321**(2), pp.557-559.

Dimarogona, M., Topakas, E., Olsson, L. and Christakopoulos, P. 2012. Lignin boosts the cellulase performance of a GH-61 enzyme from *Sporotrichum thermophile*. *Bioresourse Technology.* **110**, pp.480-487.

Ding, S.Y., Liu, Y.S., Zeng, Y., Himmel, M.E., Baker, J.O. and Bayer, E.A. 2012. How does plant cell wall nanoscale architecture correlate with enzymatic digestibility? *Science.* **338**(6110), pp.1055-1060.

Divne, C., Stahlberg, J., Reinikainen, T., Ruohonen, L., Pettersson, G., Knowles, J.K., Teeri, T.T. and Jones, T.A. 1994. The three-dimensional crystal structure of the catalytic core of cellobiohydrolase I from *Trichoderma reesei*. *Science.* **265**(5171), pp.524-528.

Dupree, R., Simmons, T.J., Mortimer, J.C., Patel, D., Iuga, D., Brown, S.P. and Dupree, P. 2015. Probing the molecular architecture of *Arabidopsis thaliana* secondary cell walls using two- and three-dimensional (13)C solid state nuclear magnetic resonance spectroscopy. *Biochemistry.* **54**(14), pp.2335-2345.

El-Halfawy, O.M., Klett, J., Ingram, R.J., Loutet, S.A., Murphy, M.E., Martin-Santamaria, S. and Valvano, M.A. 2017. Antibiotic Capture by Bacterial Lipocalins Uncovers an Extracellular Mechanism of Intrinsic Antibiotic Resistance. *mBio.* **8**(2).

Emsley, P., Lohkamp, B., Scott, W.G. and Cowtan, K. 2010. Features and development of Coot. *Acta Crystallographica D: Biological Crystallography.* **66**(4), pp.486-501.

Evans, P.R. and Murshudov, G.N. 2013. How good are my data and what is the resolution? *Acta Crystallographica D: Biological Crystallography.* **69**(7), pp.1204-1214.

Fanuel, M., Garajova, S., Ropartz, D., McGregor, N., Brumer, H., Rogniaux, H. and Berrin, J.G. 2017. The *Podospora anserina* lytic polysaccharide monooxygenase PaLPMO9H catalyzes oxidative cleavage of diverse plant cell wall matrix glycans. *Biotechnology for Biofuels.* **10**, p63.

Farrell, A.E., Plevin, R.J., Turner, B.T., Jones, A.D., O'Hare, M. and Kammen, D.M. 2006. Ethanol can contribute to energy and environmental goals. *Science.* **311**(5760), pp.506-508.

Felice, A.K.G., Schuster, C., Kadek, A., Filandr, F., Laurent, C., Scheiblbrandner, S., Schwaiger, L., Schachinger, F., Kracher, D., Sygmund, C., Man, P., Halada, P., Oostenbrink, C. and Ludwig, R. 2021. Chimeric Cellobiose Dehydrogenases Reveal the Function of Cytochrome Domain Mobility for the Electron Transfer to Lytic Polysaccharide Monooxygenase. *ACS Catalysis.* **11**(2), pp.517-532.

Filiatrault-Chastel, C., Navarro, D., Haon, M., Grisel, S., Herpoel-Gimbert, I., Chevret, D., Fanuel, M., Henrissat, B., Heiss-Blanquet, S., Margeot, A. and Berrin, J.G. 2019. AA16, a new lytic polysaccharide monooxygenase family identified in fungal secretomes. *Biotechnology for Biofuels.* **12**, p55.

Forsberg, Z., Mackenzie, A.K., Sorlie, M., Rohr, A.K., Helland, R., Arvai, A.S., Vaaje-Kolstad, G. and Eijsink, V.G. 2014a. Structural and functional characterization of a conserved pair of bacterial cellulose-oxidizing lytic polysaccharide monooxygenases. *Proceedings of the National Academy of Sciences.* **111**(23), pp.8446-8451.

Forsberg, Z., Nelson, C.E., Dalhus, B., Mekasha, S., Loose, J.S., Crouch, L.I., Rohr, A.K., Gardner, J.G., Eijsink, V.G. and Vaaje-Kolstad, G. 2016. Structural and Functional Analysis of a Lytic Polysaccharide Monooxygenase Important for Efficient Utilization of Chitin in *Cellvibrio japonicus*. *Journal of Biological Chemistry.* **291**(14), pp.7300-7312.

Forsberg, Z., Rohr, A.K., Mekasha, S., Andersson, K.K., Eijsink, V.G., Vaaje-Kolstad, G. and Sorlie, M. 2014b. Comparative study of two chitin-active and two cellulose-active AA10-type lytic polysaccharide monooxygenases. *Biochemistry.* **53**(10), pp.1647-1656.

Forsberg, Z., Sorlie, M., Petrovic, D., Courtade, G., Aachmann, F.L., Vaaje-Kolstad, G., Bissaro, B., Rohr, A.K. and Eijsink, V.G. 2019. Polysaccharide degradation by lytic polysaccharide monooxygenases. *Current Opinion in Structural Biology.* **59**, pp.54-64.

Forsberg, Z., Vaaje-Kolstad, G., Westereng, B., Bunaes, A.C., Stenstrom, Y., MacKenzie, A., Sorlie, M., Horn, S.J. and Eijsink, V.G. 2011. Cleavage of cellulose by a CBM33 protein. *Protein Science.* **20**(9), pp.1479-1483.

Fowler, C.A., Sabbadin, F., Ciano, L., Hemsworth, G.R., Elias, L., Bruce, N., McQueen-Mason, S., Davies, G.J. and Walton, P.H. 2019. Discovery, activity and characterisation of an AA10 lytic polysaccharide oxygenase from the shipworm symbiont *Teredinibacter turnerae*. *Biotechnology for Biofuels.* **12**, p232.

Frandsen, K.E., Simmons, T.J., Dupree, P., Poulsen, J.C., Hemsworth, G.R., Ciano, L., Johnston, E.M., Tovborg, M., Johansen, K.S., von Freiesleben, P., Marmuse, L., Fort, S., Cottaz, S., Driguez, H., Henrissat, B., Lenfant, N., Tuna, F., Baldansuren, A., Davies, G.J., Lo Leggio, L. and Walton, P.H. 2016. The molecular basis of polysaccharide cleavage by lytic polysaccharide monooxygenases. *Nature Chemical Biology.* **12**(4), pp.298-303.

Frey, S. and Gorlich, D. 2014. A new set of highly efficient, tag-cleaving proteases for purifying recombinant proteins. *Journal of Chromatography A.* **1337**, pp.95-105.

Frommhagen, M., Sforza, S., Westphal, A.H., Visser, J., Hinz, S.W., Koetsier, M.J., van Berkel, W.J., Gruppen, H. and Kabel, M.A. 2015. Discovery of the combined oxidative cleavage of plant xylan and cellulose by a new fungal polysaccharide monooxygenase. *Biotechnology for Biofuels.* **8**, p101.

Garajova, S., Mathieu, Y., Beccia, M.R., Bennati-Granier, C., Biaso, F., Fanuel, M., Ropartz, D., Guigliarelli, B., Record, E., Rogniaux, H., Henrissat, B. and Berrin, J.G. 2016. Single-domain flavoenzymes trigger lytic polysaccharide monooxygenases for oxidative degradation of cellulose. *Scientific Reports.* **6**, p28276.

Gardner, J.G., Crouch, L., Labourel, A., Forsberg, Z., Bukhman, Y.V., Vaaje-Kolstad, G., Gilbert, H.J. and Keating, D.H. 2014. Systems biology defines the biological significance of redox-active proteins during cellulose degradation in an aerobic bacterium. *Molecular Microbiology.* **94**(5).

Gardner, J.G. and Keating, D.H. 2012. Genetic and functional genomic approaches for the study of plant cell wall degradation in Cellvibrio japonicus. *Methods Enzymol.* **510**, pp.331-347.

Gilbert, H.J., Knox, J.P. and Boraston, A.B. 2013. Advances in understanding the molecular basis of plant cell wall polysaccharide recognition by carbohydrate-binding modules. *Current Opinion in Structural Biology.* **23**(5), pp.669-677.

Greenfield, N.J. 2006a. Using circular dichroism collected as a function of temperature to determine the thermodynamics of protein unfolding and binding interactions. *Nature Protocols.* **1**(6), pp.2527-2535.

Greenfield, N.J. 2006b. Using circular dichroism spectra to estimate protein secondary structure. *Nature Protocols.* **1**(6), pp.2876-2890.

Gregory, R.C., Hemsworth, G.R., Turkenburg, J.P., Hart, S.J., Walton, P.H. and Davies, G.J. 2016. Activity, stability and 3-D structure of the Cu(ii) form of a chitin-active lytic polysaccharide monooxygenase from *Bacillus amyloliquefaciens*. *Dalton Transactions.* **45**(42), pp.16904-16912.

Gudmundsson, M., Kim, S., Wu, M., Ishida, T., Momeni, M.H., Vaaje-Kolstad, G., Lundberg, D., Royant, A., Stahlberg, J., Eijsink, V.G., Beckham, G.T. and Sandgren, M. 2014. Structural and electronic snapshots during the transition from a Cu(II) to Cu(I) metal center of a lytic polysaccharide monooxygenase by X-ray photoreduction. *Journal of Biological Chemistry.* **289**(27), pp.18782-18792.

Handa, N., Terada, T., Doi-Katayama, Y., Hirota, H., Tame, J.R., Park, S.Y., Kuramitsu, S., Shirouzu, M. and Yokoyama, S. 2005. Crystal structure of a novel polyisoprenoid-binding protein from *Thermus thermophilus* HB8. *Protein Science.* **14**(4), pp.1004-1010.

Hangasky, J.A., Iavarone, A.T. and Marletta, M.A. 2018. Reactivity of O2 versus H2O2 with polysaccharide monooxygenases. *Proceedings of the National Academy of Sciences.* **115**(19), pp.4915-4920.

Hangasky, J.A. and Marletta, M.A. 2018. A Random-Sequential Kinetic Mechanism for Polysaccharide Monooxygenases. *Biochemistry.* **57**(22), pp.3191-3199.

Harris, P.V., Welner, D., McFarland, K.C., Re, E., Navarro Poulsen, J.C., Brown, K., Salbo, R., Ding, H., Vlasenko, E., Merino, S., Xu, F., Cherry, J., Larsen, S. and Lo Leggio, L. 2010. Stimulation of lignocellulosic biomass hydrolysis by proteins of glycoside hydrolase family 61: structure and function of a large, enigmatic family. *Biochemistry.* **49**(15), pp.3305-3316.

Hatfield, R.D. and Nevins, D.J. 1987. Hydrolytic Activity and Substrate Specificity of an Endoglucanase from *Zea mays* Seedling Cell Walls. *Plant Physiology.* **83**(1), pp.203-207.

Hedegard, E.D. and Ryde, U. 2018. Molecular mechanism of lytic polysaccharide monooxygenases. *Chemical Science.* **9**(15), pp.3866-3880.

Hedison, T.M., Breslmayr, E., Shanmugam, M., Karnpakdee, K., Heyes, D.J., Green, A.P., Ludwig, R., Scrutton, N.S. and Kracher, D. 2020. Insights into the H2O2-driven catalytic mechanism of fungal lytic polysaccharide monooxygenases. *The FEBS Journal.*

Hemsworth, G.R., Henrissat, B., Davies, G.J. and Walton, P.H. 2014. Discovery and characterization of a new family of lytic polysaccharide monooxygenases. *Nature Chemical Biology.* **10**(2), pp.122-126.

Hemsworth, G.R., Johnston, E.M., Davies, G.J. and Walton, P.H. 2015. Lytic Polysaccharide Monooxygenases in Biomass Conversion. *Trends in Biotechnology.* **33**(12), pp.747-761.

Hemsworth, G.R., Taylor, E.J., Kim, R.Q., Gregory, R.C., Lewis, S.J., Turkenburg, J.P., Parkin, A., Davies, G.J. and Walton, P.H. 2013. The copper active site of CBM33 polysaccharide oxygenases. *Journal of the American Chemical Society.* **135**(16), pp.6069-6077.

Higham, C.W., Gordon-Smith, D., Dempsey, C.E. and Wood, P.M. 1994. Direct 1H NMR evidence for conversion of beta-D-cellobiose to cellobionolactone by cellobiose dehydrogenase from *Phanerochaete chrysosporium*. *FEBS Letters.* **351**(1), pp.128-132.

Himmel, M.E., Ding, S.Y., Johnson, D.K., Adney, W.S., Nimlos, M.R., Brady, J.W. and Foust, T.D. 2007. Biomass recalcitrance: engineering plants and enzymes for biofuels production. *Science.* **315**(5813), pp.804-807.

Holm, L. 2019. Benchmarking fold detection by DaliLite v.5. *Bioinformatics.* **35**(24), pp.5326-5327.

Horn, S.J., Sikorski, P., Cederkvist, J.B., Vaaje-Kolstad, G., Sorlie, M., Synstad, B., Vriend, G., Varum, K.M. and Eijsink, V.G. 2006. Costs and benefits of processivity in enzymatic degradation of recalcitrant polysaccharides. *Proceedings of the National Academy of Sciences.* **103**(48), pp.18089-18094.

Horn, S.J., Sorlie, M., Varum, K.M., Valjamae, P. and Eijsink, V.G. 2012a. Measuring processivity. *Methods in Enzymology.* **510**, pp.69-95.

Horn, S.J., Vaaje-Kolstad, G., Westereng, B. and Eijsink, V.G. 2012b. Novel enzymes for the degradation of cellulose. *Biotechnology for Biofuels.* **5**(1), p45.

Horne, J.E., Walko, M., Calabrese, A.N., Levenstein, M.A., Brockwell, D.J., Kapur, N., Wilson, A.J. and Radford, S.E. 2018. Rapid Mapping of Protein Interactions Using Tag-Transfer Photocrosslinkers. *Angewandte Chemie International Edition English.* **57**(51), pp.16688-16692.

Humphry, D.R., Black, G.W. and Cummings, S.P. 2003. Reclassification of '*Pseudomonas fluorescens* subsp. *cellulosa*' NCIMB 10462 (Ueda *et al*. 1952) as *Cellvibrio japonicus* sp. nov. and revival of *Cellvibrio vulgaris* sp. nov., nom. rev. and *Cellvibrio fulvus* sp. nov., nom. rev. *International Journal of Systematic and Evolutionary Microbiology.* **53**(2), pp.393-400.

Hyde, S.M. and Wood, P.M. 1997. A Mechanism for Production of Hydroxyl Radicals by the Brown-Rot Fungus *Coniophora Puteana*: Fe(III) Reduction by Cellobiose Dehydrogenase and Fe(II) Oxidation at a Distance from the Hyphae. *Microbiology.* **143**(1), pp.259-266.

Isaksen, T., Westereng, B., Aachmann, F.L., Agger, J.W., Kracher, D., Kittl, R., Ludwig, R., Haltrich, D., Eijsink, V.G. and Horn, S.J. 2014. A C4-oxidizing lytic polysaccharide monooxygenase cleaving both cellulose and cello-oligosaccharides. *Journal of Biological Chemistry.* **289**(5), pp.2632-2642.

Jensen, M.S., Klinkenberg, G., Bissaro, B., Chylenski, P., Vaaje-Kolstad, G., Kvitvang, H.F., Naerdal, G.K., Sletta, H., Forsberg, Z. and Eijsink, V.G.H. 2019. Engineering chitinolytic activity into a cellulose-active lytic polysaccharide monooxygenase provides insights into substrate specificity. *Journal of Biological Chemistry.* **294**(50), pp.19349-19364.

Johansen, K.S. 2016. Lytic Polysaccharide Monooxygenases: The Microbial Power Tool for Lignocellulose Degradation. *Trends in Plant Science.* **21**(11), pp.926-936.

Jordan, D.B., Bowman, M.J., Braker, J.D., Dien, B.S., Hector, R.E., Lee, C.C., Mertens, J.A. and Wagschal, K. 2012. Plant cell walls to ethanol. *Biochemical Journal.* **442**(2), pp.241-252.

Kabsch, W. 2010. Xds. *Acta Crystallographica D: Biological Crystallography.* **66**(2), pp.125-132.

Kim, S., Stahlberg, J., Sandgren, M., Paton, R.S. and Beckham, G.T. 2014. Quantum mechanical calculations suggest that lytic polysaccharide monooxygenases use a copper-oxyl, oxygen-rebound mechanism. *Proceedings of the National Academy of Sciences.* **111**(1), pp.149-154.

Kittl, R., Kracher, D., Burgstaller, D., Haltrich, D. and Ludwig, R. 2012. Production of four *Neurospora crassa* lytic polysaccharide monooxygenases in *Pichia pastoris* monitored by a fluorimetric assay. *Biotechnology for Biofuels.* **5**(1), p79.

Kjaergaard, C.H., Qayyum, M.F., Wong, S.D., Xu, F., Hemsworth, G.R., Walton, D.J., Young, N.A., Davies, G.J., Walton, P.H., Johansen, K.S., Hodgson, K.O., Hedman, B. and Solomon, E.I. 2014. Spectroscopic and computational insight into the activation of O2 by the mononuclear Cu center in polysaccharide monooxygenases. *Proceedings of the National Academy of Sciences.* **111**(24), pp.8797-8802.

Klock, H.E. and Lesley, S.A. 2009. The Polymerase Incomplete Primer Extension (PIPE) method applied to high-throughput cloning and site-directed mutagenesis. *Methods in molecular biology.* **498**, pp.91-103.

Kont, R., Pihlajaniemi, V., Borisova, A.S., Aro, N., Marjamaa, K., Loogen, J., Buchs, J., Eijsink, V.G.H., Kruus, K. and Valjamae, P. 2019. The liquid fraction from hydrothermal pretreatment of wheat straw provides lytic polysaccharide monooxygenases with both electrons and H2O2 co-substrate. *Biotechnology for Biofuels.* **12**, p235.

Kracher, D., Andlar, M., Furtmuller, P.G. and Ludwig, R. 2018. Active-site copper reduction promotes substrate binding of fungal lytic polysaccharide monooxygenase and reduces stability. *Journal of Biological Chemistry.* **293**(5), pp.1676-1687.

Kracher, D., Forsberg, Z., Bissaro, B., Gangl, S., Preims, M., Sygmund, C., Eijsink, V.G.H. and Ludwig, R. 2020. Polysaccharide oxidation by lytic polysaccharide monooxygenase is enhanced by engineered cellobiose dehydrogenase. *FEBS Journal.* **287**(5), pp.897-908.

Kracher, D., Scheiblbrandner, S., Felice, A.K., Breslmayr, E., Preims, M., Ludwicka, K., Haltrich, D., Eijsink, V.G. and Ludwig, R. 2016. Extracellular electron transfer systems fuel cellulose oxidative degradation. *Science.* **352**(6289), pp.1098-1101.

Kranz, R.G., Richard-Fogal, C., Taylor, J.S. and Frawley, E.R. 2009. Cytochrome c biogenesis: mechanisms for covalent modifications and trafficking of heme and for heme-iron redox control. *Microbiology and Molecular Biology Reviews.* **73**(3), pp.510-528.

Kremer, S.M. and Wood, P.M. 1992. Production of Fenton's reagent by cellobiose oxidase from cellulolytic cultures of *Phanerochaete chrysosporium*. *European Journal of Biochemistry.* **208**(3), pp.807-814.

Kroon-Batenburg, L.M. and Kroon, J. 1997. The crystal and molecular structures of cellulose I and II. *Glycoconjugate Journal.* **14**(5), pp.677-690.

Kurth, J.M., Brito, J.A., Reuter, J., Flegler, A., Koch, T., Franke, T., Klein, E.M., Rowe, S.F., Butt, J.N., Denkmann, K., Pereira, I.A., Archer, M. and Dahl, C. 2016. Electron Accepting Units of the Diheme Cytochrome c TsdA, a Bifunctional Thiosulfate Dehydrogenase/Tetrathionate Reductase. *Journal of Biological Chemistry.* **291**(48), pp.24804-24818.

Kuusk, S., Bissaro, B., Kuusk, P., Forsberg, Z., Eijsink, V.G.H., Sorlie, M. and Valjamae, P. 2018. Kinetics of H2O2-driven degradation of chitin by a bacterial lytic polysaccharide monooxygenase. *Journal of Biological Chemistry.* **293**(2), pp.523-531.

Kuusk, S., Kont, R., Kuusk, P., Heering, A., Sorlie, M., Bissaro, B., Eijsink, V.G.H. and Valjamae, P. 2019. Kinetic insights into the role of the reductant in H2O2-driven degradation of chitin by a bacterial lytic polysaccharide monooxygenase. *Journal of Biological Chemistry.* **294**(5), pp.1516-1528.

Langston, J.A., Shaghasi, T., Abbate, E., Xu, F., Vlasenko, E. and Sweeney, M.D. 2011. Oxidoreductive cellulose depolymerization by the enzymes cellobiose dehydrogenase and glycoside hydrolase 61. *Applied and Environmental Microbiology.* **77**(19), pp.7007-7015.

Laurent, C., Breslmayr, E., Tunega, D., Ludwig, R. and Oostenbrink, C. 2019. Interaction between Cellobiose Dehydrogenase and Lytic Polysaccharide Monooxygenase. *Biochemistry.* **58**(9), pp.1226-1235.

Levasseur, A., Drula, E., Lombard, V., Coutinho, P.M. and Henrissat, B. 2013. Expansion of the enzymatic repertoire of the CAZy database to integrate auxiliary redox enzymes. *Biotechnology for Biofuels.* **6**(1), p41.

Levasseur, A., Lomascolo, A., Chabrol, O., Ruiz-Duenas, F.J., Boukhris-Uzan, E., Piumi, F., Kues, U., Ram, A.F., Murat, C., Haon, M., Benoit, I., Arfi, Y., Chevret, D., Drula, E., Kwon, M.J., Gouret, P., Lesage-Meessen, L., Lombard, V., Mariette, J., Noirot, C., Park, J., Patyshakuliyeva, A., Sigoillot, J.C., Wiebenga, A., Wosten, H.A., Martin, F., Coutinho, P.M., de Vries, R.P., Martinez, A.T., Klopp, C., Pontarotti, P., Henrissat, B. and Record, E. 2014. The genome of the white-rot fungus *Pycnoporus cinnabarinus*: a basidiomycete model with a versatile arsenal for lignocellulosic biomass breakdown. *BMC Genomics.* **15**, p486.

Li, X., Beeson, W.T.t., Phillips, C.M., Marletta, M.A. and Cate, J.H. 2012. Structural basis for substrate targeting and catalysis by fungal polysaccharide monooxygenases. *Structure.* **20**(6), pp.1051-1061.

Lo Leggio, L., Simmons, T.J., Poulsen, J.C., Frandsen, K.E., Hemsworth, G.R., Stringer, M.A., von Freiesleben, P., Tovborg, M., Johansen, K.S., De Maria, L., Harris, P.V., Soong, C.L., Dupree, P., Tryfona, T., Lenfant, N., Henrissat, B., Davies, G.J. and Walton, P.H. 2015. Structure and boosting activity of a starch-degrading lytic polysaccharide monooxygenase. *Nature Communications.* **6**, p5961.

Loose, J.S., Forsberg, Z., Kracher, D., Scheiblbrandner, S., Ludwig, R., Eijsink, V.G. and Vaaje-Kolstad, G. 2016. Activation of bacterial lytic polysaccharide monooxygenases with cellobiose dehydrogenase. *Protein Science.* **25**(12), pp.2175-2186.

Lynd, L.R., Weimer, P.J., van Zyl, W.H. and Pretorius, I.S. 2002. Microbial cellulose utilization: fundamentals and biotechnology. *Microbiology and Molecular Biology Reviews.* **66**(3), pp.506-577.

Mandels, M., Parrish, F.W. and Reese, E.T. 1962. Sophorose as an inducer of cellulase in *Trichoderma viride*. *Journal of Bacteriology.* **83**, pp.400-408.

Mandels, M. and Reese, E.T. 1957. Induction of Cellulase in *Trichoderma viride* as influenced by carbon sources and metals. *Journal of Bacteriology.* **73**(2), pp.269-278.

Mandels, M. and Reese, E.T. 1960. Induction of cellulase in fungi by cellobiose. *Journal of Bacteriology.* **79**, pp.816-826.

Mansfield, S.D., Mooney, C. and Saddler, J.N. 1999. Substrate and Enzyme Characteristics that Limit Cellulose Hydrolysis. *Biotechnology Progress.* **15**(5), pp.804-816.

Marcaida, M.J., Schlarb-Ridley, B.G., Worrall, J.A., Wastl, J., Evans, T.J., Bendall, D.S., Luisi, B.F. and Howe, C.J. 2006. Structure of cytochrome c6A, a novel dithio-cytochrome of *Arabidopsis thaliana*, and its reactivity with plastocyanin: implications for function. *Journal of Molecular Biology.* **360**(5), pp.968-977.

Matthews, B.W. 1968. Solvent content of protein crystals. *Journal of Molecular Biology.* **33**(2), pp.491-497.

McCoy, A.J., Grosse-Kunstleve, R.W., Adams, P.D., Winn, M.D., Storoni, L.C. and Read, R.J. 2007. Phaser crystallographic software. *Journal of Applied Crystallography.* **40**(4), pp.658-674.

Moore, G.P., G. 1990. *Cytochromes c.* Springer-Verlag Berlin Heidelberg.

Morton, R.A. 1958. Ubiquinone. *Nature.* **182**(4652), pp.1764-1767.

Muller, G., Chylenski, P., Bissaro, B., Eijsink, V.G.H. and Horn, S.J. 2018. The impact of hydrogen peroxide supply on LPMO activity and overall saccharification efficiency of a commercial cellulase cocktail. *Biotechnology for Biofuels.* **11**, p209.

Muller, S., Hoege, C., Pyrowolakis, G. and Jentsch, S. 2001. SUMO, ubiquitin's mysterious cousin. *Nature Reviews Molecular Cell Biology.* **2**(3), pp.202-210.

Munzone, A., El Kerdi, B., Fanuel, M., Rogniaux, H., Ropartz, D., Reglier, M., Royant, A., Simaan, A.J. and Decroos, C. 2020. Characterization of a bacterial copper-dependent lytic polysaccharide monooxygenase with an unusual second coordination sphere. *FEBS Journal.* (287).

Murshudov, G.N., Skubak, P., Lebedev, A.A., Pannu, N.S., Steiner, R.A., Nicholls, R.A., Winn, M.D., Long, F. and Vagin, A.A. 2011. REFMAC5 for the refinement of macromolecular crystal structures. *Acta Crystallographica D: Biological Crystallography.* **67**(4), pp.355-367.

Nisizawa, K. and Hashimoto, Y. 1959. Cellulose-splitting enzymes. VI. Difference in the specificites of cellulase and beta-glucosidase from *Irpex lacteus*. *Archives of Biochemistry and Biophysics.* **81**(1), pp.211-222.

O'Dell, W.B., Agarwal, P.K. and Meilleur, F. 2017. Oxygen Activation at the Active Site of a Fungal Lytic Polysaccharide Monooxygenase. *Angewandte Chemie International Edition English.* **56**(3), pp.767-770.

Padilla, J.E. and Yeates, T.O. 2003. A statistic for local intensity differences: robustness to anisotropy and pseudo-centering and utility for detecting twinning. *Acta Crystallographica D: Biological Crystallography.* **59**(7), pp.1124-1130.

Paradisi, A., Johnston, E.M., Tovborg, M., Nicoll, C.R., Ciano, L., Dowle, A., McMaster, J., Hancock, Y., Davies, G.J. and Walton, P.H. 2019. Formation of a Copper(II)-Tyrosyl Complex at the Active Site of Lytic Polysaccharide Monooxygenases Following Oxidation by H2O2. *Journal of the American Chemical Society.* **141**(46), pp.18585-18599.

Pauly, M. and Keegstra, K. 2008. Cell-wall carbohydrates and their modification as a resource for biofuels. *Plant Journal.* **54**(4), pp.559-568.

Payne, C.M., Knott, B.C., Mayes, H.B., Hansson, H., Himmel, M.E., Sandgren, M., Stahlberg, J. and Beckham, G.T. 2015. Fungal cellulases. *Chemical Reviews.* **115**(3), pp.1308-1448.

Petrovic, D.M., Bissaro, B., Chylenski, P., Skaugen, M., Sorlie, M., Jensen, M.S., Aachmann, F.L., Courtade, G., Varnai, A. and Eijsink, V.G.H. 2018. Methylation of the N-terminal histidine protects a lytic polysaccharide monooxygenase from auto-oxidative inactivation. *Protein Science.* **27**(9), pp.1636-1650.

Petrovic, D.M., Varnai, A., Dimarogona, M., Mathiesen, G., Sandgren, M., Westereng, B. and Eijsink, V.G.H. 2019. Comparison of three seemingly similar lytic polysaccharide monooxygenases from *Neurospora crassa* suggests different roles in plant biomass degradation. *Journal of Biological Chemistry.* **294**(41), pp.15068-15081.

Phillips, C.M., Beeson, W.T., Cate, J.H. and Marletta, M.A. 2011. Cellobiose dehydrogenase and a copper-dependent polysaccharide monooxygenase potentiate cellulose degradation by *Neurospora crassa*. *ACS Chemical Biology.* **6**(12), pp.1399-1406.

Potterton, L., Agirre, J., Ballard, C., Cowtan, K., Dodson, E., Evans, P.R., Jenkins, H.T., Keegan, R., Krissinel, E., Stevenson, K., Lebedev, A., McNicholas, S.J., Nicholls, R.A., Noble, M., Pannu, N.S., Roth, C., Sheldrick, G., Skubak, P., Turkenburg, J., Uski, V., von Delft, F., Waterman, D., Wilson, K., Winn, M. and Wojdyr, M. 2018. CCP4i2: the new graphical user interface to the CCP4 program suite. *Acta Crystallographica D: Structral Biology.* **74**(2), pp.68-84.

Quinlan, R.J., Sweeney, M.D., Lo Leggio, L., Otten, H., Poulsen, J.C., Johansen, K.S., Krogh, K.B., Jorgensen, C.I., Tovborg, M., Anthonsen, A., Tryfona, T., Walter, C.P., Dupree, P., Xu, F., Davies, G.J. and Walton, P.H. 2011. Insights into the oxidative degradation of cellulose by a copper metalloenzyme that exploits biomass components. *Proceedings of the National Academy of Sciences.* **108**(37), pp.15079-15084.

Raghothama, S., Simpson, P.J., Szabo, L., Nagy, T., Gilbert, H.J. and Williamson, M.P. 2000. Solution structure of the CBM10 cellulose binding module from *Pseudomonas xylanase* A. *Biochemistry.* **39**(5), pp.978-984.

Reese, E.T. 1956. A microbiological process report; enzymatic hydrolysis of cellulose. *Applied Microbiology.* **4**(1), pp.39-45.

Reese, E.T. and Levinson, H.S. 1952. A Comparative Study of the Breakdown of Cellulose by Microorganisms. *Physiologia Plantarum.* **5**(3), pp.345-366.

Richter, O.M. and Ludwig, B. 2009. Electron transfer and energy transduction in the terminal part of the respiratory chain - lessons from bacterial model systems. *Biochimica et Biophysica Acta.* **1787**(6), pp.626-634.

Sabbadin, F., Hemsworth, G.R., Ciano, L., Henrissat, B., Dupree, P., Tryfona, T., Marques, R.D.S., Sweeney, S.T., Besser, K., Elias, L., Pesante, G., Li, Y., Dowle, A.A., Bates, R., Gomez, L.D., Simister, R., Davies, G.J., Walton, P.H., Bruce, N.C. and McQueen-Mason, S.J. 2018. An ancient family of lytic polysaccharide monooxygenases with roles in arthropod development and biomass digestion. *Nature Communications.* **9**(1), p756.

Sheldon, R.A. 2014. Green and sustainable manufacture of chemicals from biomass: state of the art. *Green Chemistry.* **16**(3), pp.950-963.

Sheldrick, G.M. 2008. A short history of SHELX. *Acta Crystallographica A.* **64**(1), pp.112-122.

Simmons, T.J., Frandsen, K.E.H., Ciano, L., Tryfona, T., Lenfant, N., Poulsen, J.C., Wilson, L.F.L., Tandrup, T., Tovborg, M., Schnorr, K., Johansen, K.S., Henrissat, B., Walton, P.H., Lo Leggio, L. and Dupree, P. 2017. Structural and electronic determinants of lytic polysaccharide monooxygenase reactivity on polysaccharide substrates. *Nature Communications.* **8**(1), p1064.

Solomon, E.I., Heppner, D.E., Johnston, E.M., Ginsbach, J.W., Cirera, J., Qayyum, M., Kieber-Emmons, M.T., Kjaergaard, C.H., Hadt, R.G. and Tian, L. 2014. Copper active sites in biology. *Chemical Reviews.* **114**(7), pp.3659-3853.

Span, E.A., Suess, D.L.M., Deller, M.C., Britt, R.D. and Marletta, M.A. 2017. The Role of the Secondary Coordination Sphere in a Fungal Polysaccharide Monooxygenase. *ACS Chemical Biology.* **12**(4), pp.1095-1103.

Stancik, L.M., Stancik, D.M., Schmidt, B., Barnhart, D.M., Yoncheva, Y.N. and Slonczewski, J.L. 2002. pH-dependent expression of periplasmic proteins and amino acid catabolism in *Escherichia coli*. *Journal of Bacteriology.* **184**(15), pp.4246-4258.

Stein, N. 2008. CHAINSAW: a program for mutating pdb files used as templates in molecular replacement. *Journal of Applied Crystallography.* **41**(3), pp.641-643.

Stepnov, A.A., Forsberg, Z., Sørlie, M., Nguyen, G.-S., Wentzel, A., Røhr, Å.K. and Eijsink, V.G.H. 2021. Unraveling the roles of the reductant and free copper ions in LPMO kinetics. *Biotechnology for Biofuels.* **14**(1), p28.

Sygmund, C., Kracher, D., Scheiblbrandner, S., Zahma, K., Felice, A.K., Harreither, W., Kittl, R. and Ludwig, R. 2012. Characterization of the two *Neurospora crassa* cellobiose dehydrogenases and their connection to oxidative cellulose degradation. *Applied and Environmental Microbiology.* **78**(17), pp.6161-6171.

Takeda, K., Matsumura, H., Ishida, T., Samejima, M., Ohno, H., Yoshida, M., Igarashi, K. and Nakamura, N. 2015. Characterization of a novel PQQ-dependent quinohemoprotein pyranose dehydrogenase from *Coprinopsis cinerea* classified into auxiliary activities family 12 in carbohydrate-active enzymes. *PLoS One.* **10**(2), pe0115722.

Tan, T.C., Kracher, D., Gandini, R., Sygmund, C., Kittl, R., Haltrich, D., Hallberg, B.M., Ludwig, R. and Divne, C. 2015. Structural basis for cellobiose dehydrogenase action during oxidative cellulose degradation. *Nature Communications.* **6**, p7542.

Tandrup, T., Tryfona, T., Frandsen, K.E.H., Johansen, K.S., Dupree, P. and Lo Leggio, L. 2020. Oligosaccharide Binding and Thermostability of Two Related AA9 Lytic Polysaccharide Monooxygenases. *Biochemistry.* **59**(36), pp.3347-3358.

Teo, R.D., Wang, R., Smithwick, E.R., Migliore, A., Therien, M.J. and Beratan, D.N. 2019. Mapping hole hopping escape routes in proteins. *Proceedings of the National Academy of Sciences.* **116**(32), pp.15811-15816.

Tormo, J., Lamed, R., Chirino, A.J., Morag, E., Bayer, E.A., Shoham, Y. and Steitz, T.A. 1996. Crystal structure of a bacterial family-III cellulose-binding domain: a general mechanism for attachment to cellulose. *EMBO Journal.* **15**(21), pp.5739-5751.

Trott, O. and Olson, A.J. 2010. AutoDock Vina: improving the speed and accuracy of docking with a new scoring function, efficient optimization, and multithreading. *Journal of Computational Chemistry.* **31**(2), pp.455-461.

Tuveng, T.R., Arntzen, M.O., Bengtsson, O., Gardner, J.G., Vaaje-Kolstad, G. and Eijsink, V.G. 2016. Proteomic investigation of the secretome of *Cellvibrio japonicus* during growth on chitin. *Proteomics.* **16**(13), pp.1904-1914.

Underwood, W. 2012. The plant cell wall: a dynamic barrier against pathogen invasion. *Frontiers in Plant Science.* **3**, p85.

Vaaje-Kolstad, G., Houston, D.R., Riemen, A.H., Eijsink, V.G. and van Aalten, D.M. 2005. Crystal structure and binding properties of the *Serratia marcescens* chitin-binding protein CBP21. *Journal of Biological Chemistry.* **280**(12), pp.11313-11319.

Vaaje-Kolstad, G., Westereng, B., Horn, S.J., Liu, Z., Zhai, H., Sorlie, M. and Eijsink, V.G. 2010. An oxidative enzyme boosting the enzymatic conversion of recalcitrant polysaccharides. *Science.* **330**(6001), pp.219-222.

Varnai, A., Umezawa, K., Yoshida, M. and Eijsink, V.G.H. 2018. The Pyrroloquinoline-Quinone-Dependent Pyranose Dehydrogenase from *Coprinopsis cinerea* Drives Lytic Polysaccharide Monooxygenase Action. *Applied and Environmental Microbiology.* **84**(11).

Vincent, F., Molin, D.D., Weiner, R.M., Bourne, Y. and Henrissat, B. 2010. Structure of a polyisoprenoid binding domain from Saccharophagus degradans implicated in plant cell wall breakdown. *FEBS Letters.* **584**(8), pp.1577-1584.

Voet, D., Voet, J.G. and Pratt, C.W. 2008. *Principles of biochemistry.* [Hoboken, N.J.]: Wiley.

Vonrhein, C., Flensburg, C., Keller, P., Sharff, A., Smart, O., Paciorek, W., Womack, T. and Bricogne, G. 2011. Data processing and analysis with the autoPROC toolbox. *Acta Crystallographica D: Biological Crystallography.* **67**(Pt 4), pp.293-302.

Vu, V.V., Beeson, W.T., Phillips, C.M., Cate, J.H. and Marletta, M.A. 2014a. Determinants of regioselective hydroxylation in the fungal polysaccharide monooxygenases. *Journal of the American Chemical Society.* **136**(2), pp.562-565.

Vu, V.V., Beeson, W.T., Span, E.A., Farquhar, E.R. and Marletta, M.A. 2014b. A family of starch-active polysaccharide monooxygenases. *Proceedings of the National Academy of Sciences.* **111**(38), pp.13822-13827.

Wang, B., Johnston, E.M., Li, P., Shaik, S., Davies, G.J., Walton, P.H. and Rovira, C. 2018. QM/MM Studies into the H2O2-Dependent Activity of Lytic Polysaccharide Monooxygenases: Evidence for the Formation of a Caged Hydroxyl Radical Intermediate. *ACS Catalysis.* **8**(2), pp.1346-1351.

Wang, B., Walton, P.H. and Rovira, C. 2019. Molecular Mechanisms of Oxygen Activation and Hydrogen Peroxide Formation in Lytic Polysaccharide Monooxygenases. *ACS Catalysis.* **9**(6), pp.4958-4969.

Wang, Z., Feng, S., Rovira, C. and Wang, B. 2021. How Oxygen Binding Enhances Long-Range Electron Transfer: Lessons From Reduction of Lytic Polysaccharide Monooxygenases by Cellobiose Dehydrogenase. *Angewandte Chemie International Edition English.* **60**(5), pp.2385-2392.

Williams, C.J., Headd, J.J., Moriarty, N.W., Prisant, M.G., Videau, L.L., Deis, L.N., Verma, V., Keedy, D.A., Hintze, B.J., Chen, V.B., Jain, S., Lewis, S.M., Arendall, W.B., 3rd, Snoeyink, J., Adams, P.D., Lovell, S.C., Richardson, J.S. and Richardson, D.C. 2018. MolProbity: More and better reference data for improved all-atom structure validation. *Protein Science.* **27**(1), pp.293-315.

Winter, G., Waterman, D.G., Parkhurst, J.M., Brewster, A.S., Gildea, R.J., Gerstel, M., Fuentes-Montero, L., Vollmar, M., Michels-Clark, T., Young, I.D., Sauter, N.K. and Evans, G. 2018. DIALS: implementation and evaluation of a new integration package. *Acta Crystallographica D: Biological Crystallography.* **74**(Pt 2), pp.85-97.

Wong, E., Vaaje-Kolstad, G., Ghosh, A., Hurtado-Guerrero, R., Konarev, P.V., Ibrahim, A.F., Svergun, D.I., Eijsink, V.G., Chatterjee, N.S. and van Aalten, D.M. 2012. The *Vibrio cholerae* colonization factor GbpA possesses a modular structure that governs binding to different host surfaces. *PLoS Pathogens.* **8**(1), pe1002373.

Wood, T.M. 1988. Preparation of crystalline, amorphous, and dyed cellulase substrates. *Methods in Enzymology.* Academic Press, pp.19-25.

Wu, M., Beckham, G.T., Larsson, A.M., Ishida, T., Kim, S., Payne, C.M., Himmel, M.E., Crowley, M.F., Horn, S.J., Westereng, B., Igarashi, K., Samejima, M., Stahlberg, J., Eijsink, V.G. and Sandgren, M. 2013. Crystal structure and computational characterization of the lytic polysaccharide monooxygenase GH61D from the Basidiomycota fungus *Phanerochaete chrysosporium*. *Journal of Biological Chemistry.* **288**(18), pp.12828-12839.

Yadav, S.K., Archana, Singh, R., Singh, P.K. and Vasudev, P.G. 2019. Insecticidal fern protein Tma12 is possibly a lytic polysaccharide monooxygenase. *Planta.* **249**(6), pp.1987-1996.

Zamocky, M., Ludwig, R., Peterbauer, C., Hallberg, B.M., Divne, C., Nicholls, P. and Haltrich, D. 2006. Cellobiose dehydrogenase--a flavocytochrome from wood-degrading, phytopathogenic and saprotropic fungi. *Current Protein and Peptide Science.* **7**(3), pp.255-280.

Zander, U., Faust, A., Klink, B.U., de Sanctis, D., Panjikar, S., Quentmeier, A., Bardischewsky, F., Friedrich, C.G. and Scheidig, A.J. 2011. Structural basis for the oxidation of protein-bound sulfur by the sulfur cycle molybdohemo-enzyme sulfane dehydrogenase SoxCD. *Journal of Biological Chemistry.* **286**(10), pp.8349-8360.

Zhou, H., Zhang, Y., Li, T., Tan, H., Li, G. and Yin, H. 2020. Distinct Interaction of Lytic Polysaccharide Monooxygenase with Cellulose Revealed by Computational and Biochemical Studies. *Journal of Physical Chemistry Letters.* **11**, pp.3987-3992.

Zhou, M., Diwu, Z., Panchuk-Voloshina, N. and Haugland, R.P. 1997. A stable nonfluorescent derivative of resorufin for the fluorometric determination of trace hydrogen peroxide: applications in detecting the activity of phagocyte NADPH oxidase and other oxidases. *Analytical Biochemistry.* **253**(2), pp.162-168.